Computational Methods and Exploration of the Multivalued Painlevé Transcendents, with Special Emphasis on $\mathrm{P}_{\mathrm{III}}$

Marco Fasondini

Submitted in accordance with the requirements for the degree of

Philosophiae Doctor

in the

Faculty of Natural and Agricultural Sciences
Department of Mathematics and Applied Mathematics

at the

University of the Free State
Bloemfontein 9300
South Africa

September 2017

Supervisor: Prof. J.A.C. Weideman, Stellenbosch University

Co-supervisors: Prof. B. Fornberg, University of Colorado Boulder

Prof. J.H. Meyer, University of the Free State

Preface

The principal contributions to be presented in this thesis are summarized by the abstracts of the two papers from which it arose:

1. M. Fasondini, B. Fornberg, and J.A.C. Weideman. Methods for the computation of the multivalued Painlevé transcendents on their Riemann surfaces. *J. Comput. Phys.*, 344:36–50, 2017.

   Abstract. We extend the numerical pole field solver (B. Fornberg and J.A.C. Weideman, J. Comput. Phys. 230:5957–5973, 2011) to enable the computation of the multivalued Painlevé transcendents, which are the solutions to the third, fifth and sixth Painlevé equations, on their Riemann surfaces. We display, for the first time, solutions to these equations on multiple Riemann sheets. We also provide numerical evidence for the existence of solutions to the sixth Painlevé equation that have pole-free sectors, known as tronquée solutions.

2. M. Fasondini, B. Fornberg, and J.A.C. Weideman. A computational exploration of the McCoy–Tracy–Wu solutions of the third Painlevé equation. Submitted to *Physica D*[1], 2017.

   Abstract. The method recently developed by the authors for the computation of the multivalued Painlevé transcendents on their Riemann surfaces (J. Comput. Phys. 344:36–50, 2017) is used to explore families of solutions to the third Painlevé equation that were identified by McCoy, Tracy and Wu (J. Math. Phys. 18:1058–1092, 1977) and which contain a pole-free sector. Limiting cases, in which the solutions are singular functions of the parameters, are also investigated and it is shown that a particular set of limiting solutions is expressible in terms of special functions. Solutions that are single-valued, logarithmically (infinitely) branched and algebraically branched, with any number of distinct sheets, are encountered. The algebraically branched solutions have multiple pole-free sectors on their Riemann surfaces that are accounted for by using asymptotic formulae and Bäcklund transformations.

[1]Submission history of the manuscript at the time of submission of the present thesis, September 2017: submitted, 14/06/2017; minor revision requested, 02/08/2017; revised manuscript submitted, 23/08/2017; final decision, pending.

Key words. Painlevé transcendents, P_{III} equation, P_V equation, P_{VI} equation, Riemann surface, Padé approximation, pole field solver, tronquée solutions, connection formulas, Bäcklund transformations

Declaration

1. I, Marco Fasondini, declare that the thesis that I hereby submit for the Doctoral Degree in Applied Mathematics at the University of the Free State, is my independent work, and that I have not previously submitted it for a qualification at another institution of higher education.

2. I hereby declare that I am aware that the copyright is vested in the University of the Free State.

3. I declare that all royalties as regards intellectual property that was developed during the course of and/or in connection with the study at the University of the Free State, will accrue to the University.

Signature: MF

Date: 20/09/2017

Acknowledgements

I am indebted to the following people who, through direct or indirect means, influenced the development of this thesis and my postgraduate studies:

- André Weideman, my supervisor, for
  - introducing me to some of his research collaborators (Nick Hale, Bengt Fornberg and Nick Trefethen), Chebfun and a number of new research topics, including differential equations in the complex plane and Hermite–Padé approximation;
  - bringing the paper [54], which plays a critical role in this thesis, to my attention;
  - his hospitality during a visit to Stellenbosch in 2015 and
  - his guidance, encouragement and insightful suggestions.
- Bengt Fornberg, my co-supervisor, for
  - contributing his and Natasha Flyer's node placement algorithm in [31], which is an essential component of the new computational methods presented in this thesis;
  - hosting my visit to Boulder, Colorado in 2017 and
  - his guidance, encouragement and insightful suggestions.
- Prof. J.H. Meyer, the present head of the Department of Mathematics and Applied Mathematics at the University of the Free State, for his full support and encouragement throughout my employment in his department.
- Nick Trefethen, for
  - inviting me for a six-week visit with the Chebfun team at the University of Oxford in 2016 and
  - highly thought-provoking discussions.
- Peter Clarkson, whose remark during a lecture at a 2015 workshop at Banff, Alberta, regarding the number of arbitrary parameters of the P_{III} equation, initiated this thesis by convincing me and my supervisors that the research topic of the thesis could be feasible.

I am also indebted to the workshop organisers for making the lecture available online[2], which is how I, as someone who was not in attendance at the workshop, accessed the lecture.

- Jinho Baik, Thomas Bothner and Peter Miller, the organisers of Painlevé Equations and Applications: A Workshop in Memory of A.A. Kapaev, in Ann Arbor, August 2017, for inviting me. Discussions at this workshop with Rodica Costin, Davide Guzzetti and Oleg Lisovyi are gratefully acknowledged and lead to some of the ideas for future research which are given in section 6.2.

- The anonymous referees of the two papers mentioned in the above Preface, for many helpful suggestions.

- Señor Thomas Mende, acquaintance of my late father and maternal grandmother, for being my mentor and for his supererogatory efforts in providing me with a wider education.

- My family, for their support.

[2] http://www.birs.ca/events/2015/5-day-workshops/15w5052/videos/watch/201501131449-Clarkson.html

Contents

List of symbols, abbreviations and special terms

Symbol, abbreviation or special term	**Description**
$\mathrm{P_J}$	The J-th Painlevé equation, $\mathrm{J} = \mathrm{I}, \mathrm{II}, \mathrm{III}, \mathrm{IV}, \mathrm{V}, \mathrm{VI}$, see p. 2.
$\widetilde{\mathrm{P}}_{\mathrm{III}}$	The modified third Painlevé equation, see p. 23.
$\widetilde{\mathrm{P}}_{\mathrm{V}}$	The modified fifth Painlevé equation, see p. 24.
$\mathrm{P}_{\mathrm{III}}^{(\mathrm{i})}$	$\mathrm{P_{III}}$ with $\gamma = 1 = -\delta$.
$\mathrm{P}_{\mathrm{III}}^{(\mathrm{ii})}$	$\mathrm{P_{III}}$ with $\alpha = 1$, $\gamma = 0$ and $\delta = -1$.
$\mathrm{P}_{\mathrm{III}}^{(7)}$	$\mathrm{P}_{\mathrm{III}}^{(\mathrm{ii})}$ with $z = \tau^3$, see p. 41.
$T_0(c_1, c_2)$	The scaling Bäcklund transformation for $\mathrm{P_{III}}$, see p. 48.
T_ε, $\varepsilon^2 = 1$	A rational Bäcklund transformation for $\mathrm{P}_{\mathrm{III}}^{(\mathrm{i})}$, see p. 66.
x	Real independent variable values
z	Complex independent variable values
$\mathbb{R}^+$	Positive real axis
$\mathbb{R}^-$	Negative real axis
PFS	Pole field solver
BVP	Boundary value problem
IVP	Initial value problem
ODE	Ordinary differential equation
PDE	Partial differential equation
ICs	Initial conditions
LDT	Lin, Dai and Tibboel
MTW	McCoy, Tracy and Wu
Tronquée solution	A solution characterized by an asymptotic expansion that is valid near infinity in a sector of the complex plane. A tronquée solution is pole-free on this region of validity.

Chapter 1

Introduction

1.1 History of the Painlevé equations

In 1889 Picard [75] posed the following problem: find differential equations of the form

$$\frac{d^2u}{dz^2} = R\Big(z, u, \frac{du}{dz}\Big), \qquad z \in \mathbb{C}, \tag{1.1}$$

where R is a rational function of its arguments, that possess what has become known as the Painlevé property. An equation is said to have the Painlevé property if its solutions are free from movable branch point singularities and a singularity of a solution is movable if its location depends on the initial conditions (ICs). Picard's problem was solved by the pioneering work of the politician and mathematician, Paul Painlevé, and by subsequent contributions of Gambier and Fuchs in papers published from 1895–1910, see [36] for original references. The remarkable result they discovered is that there are 50 equations of the form (1.1) that have the Painlevé property; 44 of these can be reduced to linear equations, solved in terms of elliptic functions or in terms of the solutions of the remaining six equations. These six equations, known as the

Painlevé equations, are

$$
\begin{aligned}
\mathrm{P_I} \quad &: \quad \frac{d^2u}{dz^2} = 6u^2 + z, \\
\mathrm{P_{II}} \quad &: \quad \frac{d^2u}{dz^2} = 2u^3 + zu + \alpha, \\
\mathrm{P_{III}} \quad &: \quad \frac{d^2u}{dz^2} = \frac{1}{u}\left(\frac{du}{dz}\right)^2 - \frac{1}{z}\frac{du}{dz} + \frac{\alpha u^2 + \beta}{z} + \gamma u^3 + \frac{\delta}{u}, \\
\mathrm{P_{IV}} \quad &: \quad \frac{d^2u}{dz^2} = \frac{1}{2u}\left(\frac{du}{dz}\right)^2 + \frac{\beta}{u} + 2(z^2 - \alpha)u + 4zu^2 + \frac{3}{2}u^3, \\
\mathrm{P_V} \quad &: \quad \frac{d^2u}{dz^2} = \left(\frac{1}{2u} + \frac{1}{u-1}\right)\left(\frac{du}{dz}\right)^2 - \frac{1}{z}\frac{du}{dz} + \frac{(u-1)^2}{z^2}\left(\alpha u + \frac{\beta}{u}\right) + \gamma\frac{u}{z} + \delta\frac{u(u+1)}{u-1}, \\
\mathrm{P_{VI}} \quad &: \quad \frac{d^2u}{dz^2} = \frac{1}{2}\left(\frac{1}{u} + \frac{1}{u-1} + \frac{1}{u-z}\right)\left(\frac{du}{dz}\right)^2 - \left(\frac{1}{z} + \frac{1}{z-1} + \frac{1}{u-z}\right)\left(\frac{du}{dz}\right) \\
&\qquad + \frac{u(u-1)(u-z)}{z^2(z-1)^2}\left(\alpha + \beta\frac{z}{u^2} + \gamma\frac{z-1}{(u-1)^2} + \delta\frac{z(z-1)}{(u-z)^2}\right),
\end{aligned}
$$

where α, β, γ and δ are arbitrary constants. The solutions of the Painlevé equations are known as the Painlevé transcendents since they generally cannot be expressed in terms of previously known functions. Painlevé's [72] proof of this result was disputed but more rigorous proofs were given in the 1980s by Nishioka [62] and Umemura [84, 85].

Two papers in the late 1970s lead to a resurgence of interest in the Painlevé transcendents. In the one, Ablowitz and Segur [1] found a connection between integrable nonlinear PDEs that are solvable by inverse scattering and the Painlevé equations. In the other, McCoy, Tracy and Wu [59] derived asymptotic connection formulae for a one-parameter family of $\mathrm{P_{III}}$ solutions. This family of solutions, which we call the MTW solutions, is of particular interest to us since we shall use our numerical method presented in Chapter 3 to perform a computational survey of these solutions in Chapter 5. A particular instance of the MTW solutions arose in earlier works on the spin-spin correlation functions of the 2D Ising model [11, 91], which is a model of ferromagnetism in statistical mechanics. The significance of McCoy, Tracy and Wu's paper is highlighted in [30], which calls it "the first rigorous study on the Painlevé connection formulae." Furthermore, the earlier works on the Ising model, which inspired the derivation of the connection formulae, are referred to in [30] as perhaps the first appearance of the Painlevé equations in a physical application. The Painlevé transcendents have since appeared in numerous and varied additional applications, some of which include random matrix theory [23, § 32.14], orthogonal polynomials [23, § 32.15], statistical physics [23, § 32.16], string theory [79], general relativity [74], the scattering of electromagnetic radiation [61], the quantum

sine-Gordon model [57], interaction models of fermions [25] and the study of two-dimensional polymers [93].

The role that the Painlevé transcendents started to play in nonlinear physics since the 1970s has been likened to that of the classical special functions, such as the Bessel functions, the Airy function and the hypergeometric functions in linear physics in the 18th and 19th centuries [30, 36]. The Painlevé transcendents have thus been referred to as nonlinear special functions [16, 30]. Their increasing importance has been recognised by the inclusion of a chapter on the Painlevé transcendents in the 2010 edition of the *NIST Handbook of Mathematical Functions* [23]. This is the successor to the very influential book of the same title, edited by Abramowitz and Stegun [8], that was first published in 1964 and in which no mention was made of the Painlevé transcendents.

The algebraic, analytical, asymptotic and numerical properties of the classical special functions were collated in the earlier *Handbook* [8] and a similar compilation was desired for the Painlevé transcendents, an initiative dubbed The Painlevé Project[1]. By 2010, much was known about the algebraic, analytic and asymptotic properties of the Painlevé transcendents, largely due to the isomonodromy method, introduced in the early 1980s [28, 45] (the authoritative reference on the isomonodromy or Riemann–Hilbert approach to the Painlevé equations is [30]). However, numerical methods for the Painlevé equations that had been used up to 2010 were limited in applicability and effectiveness. Consequently, in 2010 a workshop titled Numerical Solution of the Painlevé Equations was held at the International Centre for the Mathematical Sciences in Edinburgh. B. Fornberg and J.A.C. Weideman, who were in attendence at the workshop, subsequently introduced the pole field solver (PFS) [32] which is the only method yet presented that is capable of computing the pole fields of the Painlevé transcendents accurately and efficiently on extended regions of the complex plane. With the exceptions of [63] and [71], numerical studies preceding the PFS were limited to smooth solutions, of which examples are [13, 42, 47, 50]. In [63] Novokshenov computed pole fields of $\mathrm{P_I}$ and $\mathrm{P_{II}}$ on small regions using an expensive high-precision Padé approximant at a single point. In [71] Olver computed solutions of $\mathrm{P_{II}}$ with poles by solving Riemann–Hilbert problems numerically. However, solutions were presented only on a real interval whose length had to be limited due to a loss of accuracy.

[1] http://math.nist.gov/~DLozier/PainleveProject/

More comprehensive accounts of the intellectual history of the Painlevé equations can be found in [16, 30, 36]. Algebraic and geometric studies of the Painlevé equations [65–68] are some of the many additional developments that are discussed in these references.

1.2 Motivation for and aims of the thesis

Since the Painlevé equations possess the Painlevé property, their solutions are free from movable branch points. This implies that branch points can only occur at the fixed singularities of the equations. The P_I, P_{II} and P_{IV} equations have no fixed singularities in the finite complex plane and their solutions are meromorphic and thus single-valued [36, Ch. 1], [39, 82]. That is, the first, second and fourth Painlevé transcendents are analytic on the entire complex plane except at isolated points where they have poles. In the finite plane, P_{III} and P_V both have a fixed singularity at $z = 0$, and P_{VI} has fixed singularities at $z = 0$ and $z = 1$. Hence, the third, fifth and sixth Painlevé transcendents are generally multivalued with branch points at their fixed singularities. Essential singularities of the Painlevé transcendents can only occur at the fixed singularities of the equations [53, p. 128], [30]. The property of movable poles is a ubiquitous feature of generic solutions to all the Painlevé equations.

Closed-form solutions to the Painlevé equations are known for special parameter values, see [23], but the PFS brought within reach explorations of the entire solution spaces of the meromorphic Painlevé transcendents. Hence, the PFS enabled the survey of unexplored P_I, P_{II} and P_{IV} solutions, as reported in [32–34, 76–78], in which new solution features and structures in the solution spaces were discovered. The motivation behind this thesis is to begin to expand this enterprise to the multivalued Painlevé transcendents. Hence, one aim of this thesis is to extend the PFS method to the computation of P_{III}, P_V and P_{VI} solutions on multiple sheets of their Riemann surfaces, thus making unexplored solutions of these equations amenable to numerical exploration. Another aim is to use this extended PFS method to conduct a systematic computational exploration of a certain class of multivalued solutions of the third Painlevé equation.

1.3 Outline of the thesis

From a computational point of view, the two most important properties that distinguish the multivalued Painlevé transcendents from the single-valued Painlevé transcendents are the presence of branch points and, as we shall see, highly variable pole densities in the complex plane. These properties are the computational challenges that must be met to allow for the extension of the PFS to the computation of the multivalued Painlevé transcendents. In Chapter 2 we deal with the challenge of dense pole fields by developing and testing methods for an ODE whose known solution has a variable pole density but no branch points. In Chapter 3, which is adapted from the first paper mentioned in the Preface, [27], we combine these methods with computational approaches that accommodate the structure and geometry of the Riemann surfaces of the multivalued Painlevé transcendents. We demonstrate the efficacy and utility of our methods by displaying solutions to the third, fifth and sixth Painlevé equations on multiple Riemann sheets and by providing numerical evidence for the as yet unproved existence of solutions to the sixth Painlevé equation that have pole-free sectors, known as tronquée solutions.

Whereas Chapters 2 and 3 are concerned with computational issues for the multivalued Painlevé transcendents, Chapters 4 and 5 are devoted to the study of certain tronquée solutions of $\mathrm{P_{III}}$. Chapter 4 introduces existing results regarding $\mathrm{P_{III}}$ solutions, the symmetries of the $\mathrm{P_{III}}$ equation and the existence and uniqueness of certain tronquée $\mathrm{P_{III}}$ solutions. In the same chapter, closed-from cases of tronquée $\mathrm{P_{III}}$ solutions are studied (rational solutions and special cases of Bessel function solutions) and more detailed asymptotic expansions are derived for use in Chapter 5. In Chapter 5, which is based on the second paper in the Preface, [26], the new numerical method presented in Chapter 3 is used to survey systematically the above-mentioned MTW solutions, which is a subset of the tronquée $\mathrm{P_{III}}$ solutions introduced in Chapter 4. Solution features will be encountered in Chapter 5 which were not observed in the earlier PFS-enabled computational studies of the meromorphic Painlevé transcendents in [32–34, 76–78]. The most significant computational discovery in Chapter 5 is numerical evidence for the existence of multiple pole-free sectors on the Riemann sheets of the MTW solutions, which have not been identified before. A comprehensive analytical account of these pole-free sectors is given which also conclusively clears up a misconception in the literature regarding the types of algebraic branch points admitted by $\mathrm{P_{III}}$ solutions. Chapter 6 summarizes the principal new contributions of the thesis and lists related research projects that could be undertaken.

Chapter 2

The computation of variable density pole fields

In preparation for the computation of the multivalued Painlevé transcendents with pole fields of highly variable density on multiple Riemann sheets, we first consider a simpler computational problem: an ODE with a single-valued solution that has a variable pole density. This problem has the added advantage of a known exact solution which we use to test the accuracy of the numerical methods.

2.1 The test problem

Consider the test ODE initial value problem (IVP),

$$\frac{du}{dz} = z^2 + u^2, \qquad u(0) = 0, \tag{2.1}$$

which has a solution expressible in terms of Bessel functions,

$$u(z) = z\frac{J_{3/4}(z^2/2)}{J_{-1/4}(z^2/2)} = z\frac{\displaystyle\sum_{n=0}^{\infty} c_{n,3/4}\left(\frac{z^2}{4}\right)^{2n+3/4}}{\displaystyle\sum_{n=0}^{\infty} c_{n,-1/4}\left(\frac{z^2}{4}\right)^{2n-1/4}} = \frac{z^3}{4}\frac{\displaystyle\sum_{n=0}^{\infty} c_{n,3/4}\left(\frac{z^2}{4}\right)^{2n}}{\displaystyle\sum_{n=0}^{\infty} c_{n,-1/4}\left(\frac{z^2}{4}\right)^{2n}}, \tag{2.2}$$

where

$$c_{n,\alpha} = \frac{(-1)^n}{n!\Gamma(n+\alpha+1)}.$$

The solution is meromorphic and its poles, which are of first order with residue -1, are confined to the real and imaginary axes. Throughout we let z denote complex values and x real values.

We consider numerical methods for computing the solution to (2.1) on the positive real axis ($\mathbb{R}^+$), on which the pole density increases with x, see Figure 2.1. In fact, the decreasing distance between consecutive poles on $\mathbb{R}^+$ is asymptotic to π/x for $x \to +\infty$. This can be shown as follows. Let $j_{\alpha,m}$ denote the m-th zero of $J_\alpha(z)$, $\alpha \in \mathbb{R}$ on $\mathbb{R}^+$, then [69, p. 247]

$$j_{\alpha,m} = \left(m + \frac{\alpha}{2} - \frac{1}{4}\right)\pi + \mathcal{O}\left(m^{-1}\right), \qquad m \to \infty.$$

Hence, it follows from (2.2) that the m-th pole of the solution on $\mathbb{R}^+$ is at $x_m^2/2 := j_{-1/4,m}$ and

$$j_{-1/4,m+1} - j_{-1/4,m} = \frac{1}{2}\left(x_{m+1}^2 - x_m^2\right) = \frac{1}{2}\left(x_{m+1} - x_m\right)\left(x_{m+1} + x_m\right) = \pi + \mathcal{O}\left(m^{-1}\right), \quad m \to \infty,$$

from which we obtain an asymptotic formula for the distance between consecutive poles,

$$x_{m+1} - x_m = \frac{\pi}{x_m} + \mathcal{O}\left(m^{-3/2}\right), \qquad m \to \infty. \tag{2.3}$$

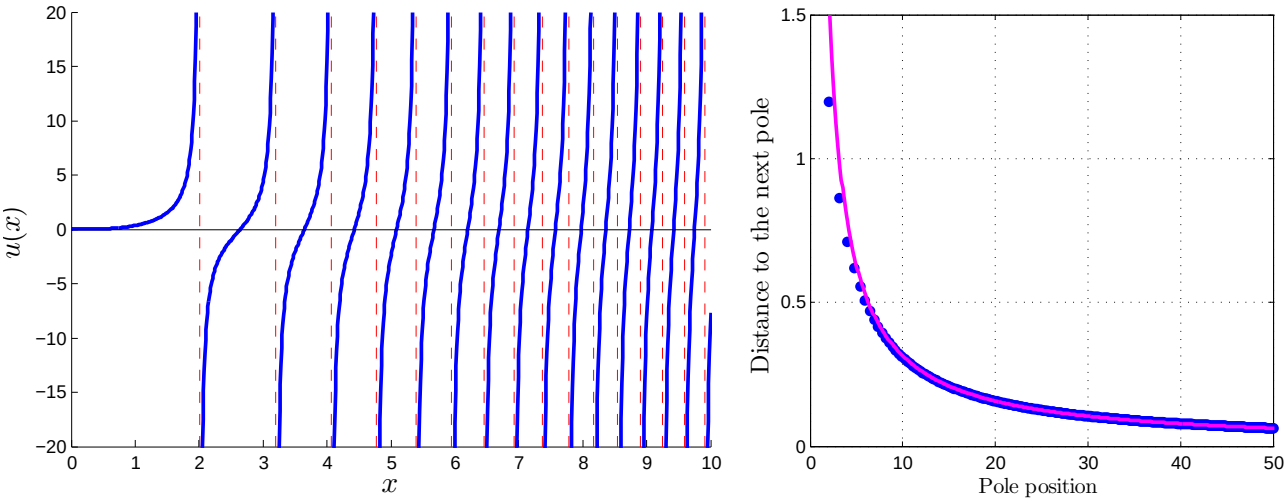

Figure 2.1: The solution (2.2) to the test problem (2.1) (left frame). The distance between consecutive poles on $\mathbb{R}^+$ (blue dots in the right frame) decreases as π/x (purple curve) for $x \to +\infty$, as indicated by (2.3).

2.2 Stepping through poles

2.2.1 Standard numerical methods

Well-known standard numerical methods for ODEs, e.g., high order Taylor methods, Runge–Kutta methods and linear multistep methods, all approximate the solution locally using polynomials. Hence, these methods will lose accuracy close to a pole unless very small step sizes

are used. This is illustrated in Figure 2.2 by the error of the Taylor method and the inbuilt MATLAB multistep method `ode113` [80] for the test problem (2.1). The method `ode113` is used, instead of the more standard `ode45`, since it is suited to problems with small error tolerances. Unsurprisingly, these polynomial-based methods are unable to integrate accurately beyond the first pole. The method `ode113` reduces the step sizes to around 10^{-14} close to the pole, but Figure 2.2 shows step sizes only down to 10^{-6}.

2.2.2 Fixed step size Padé method

One requires a method that uses local rational approximation instead of polynomials to compute solutions close to poles. The rational approximation employed by our methods is the Padé approximant, for which the Taylor coefficients of the solution are required. Suppose the ODE solution u is analytic at z, then it has the convergent Taylor expansion

$$u(z+h) = \sum_{j=0}^{\infty} c_j h^j, \qquad c_j = \frac{u^{(j)}(z)}{j!}, \tag{2.4}$$

provided $h \in \mathbb{C}$ is such that $|h|$ is smaller than the radius of convergence of the series. The ODE can be used to generate the coefficients c_j recursively. Substituting (2.4) into (2.1), we find that $c_0 = u(z)$ and

$$c_{j+1} = \frac{1}{j+1}\Big(\sum_{k=0}^{j} c_k c_{j-k} + t_j\Big), \qquad j \geq 0, \tag{2.5}$$

where $t_0 = z^2$, $t_1 = 2z$, $t_2 = 1$ and $t_j = 0$, $j \geq 3$. We remark that for ODEs such as the test problem (2.1) and the Painlevé equations, for which the right-hand sides are rational functions, it is straightforward to derive the exact recursive equations for the Taylor coefficients (such as (2.5)) by hand or by using symbolic algebra systems. However, this approach is problem-specific and can become cumbersome for systems of differential equations with complicated right-hand sides. In these cases the Taylor coefficients can be computed efficiently using the numerical methods presented in [12] or [18].

The Taylor method of order n approximates $u(z+h)$ by truncating (2.4) after $n+1$ terms; for the Taylor method in Figure 2.1, $n = 14$. The type (n_1, n_2) Padé approximant, if it exists, matches the first n_1+n_2+1 terms of the Taylor expansion (2.4) using a rational function, where n_1 and n_2 specify the degrees of the numerator polynomial, $p(h)$, and denominator polynomial,

$q(h)$, respectively. We let $n_1 = n_2 = \nu = n/2$, where n is even and thus we require

$$u(z+h) = \frac{p(h)}{q(h)} + \mathcal{O}\left(h^{n+1}\right) := \frac{a_0 + a_1 h + \cdots + a_\nu h^\nu}{b_0 + b_1 h + \cdots + b_\nu h^\nu} + \mathcal{O}\left(h^{n+1}\right). \tag{2.6}$$

To ensure that the Padé approximant $p(h)/q(h)$ does not have a pole at $h = 0$, we require $q(0) = b_0 \neq 0$ and thus we can normalize b_0 by setting $b_0 = 1$. In linearised form, (2.6) is

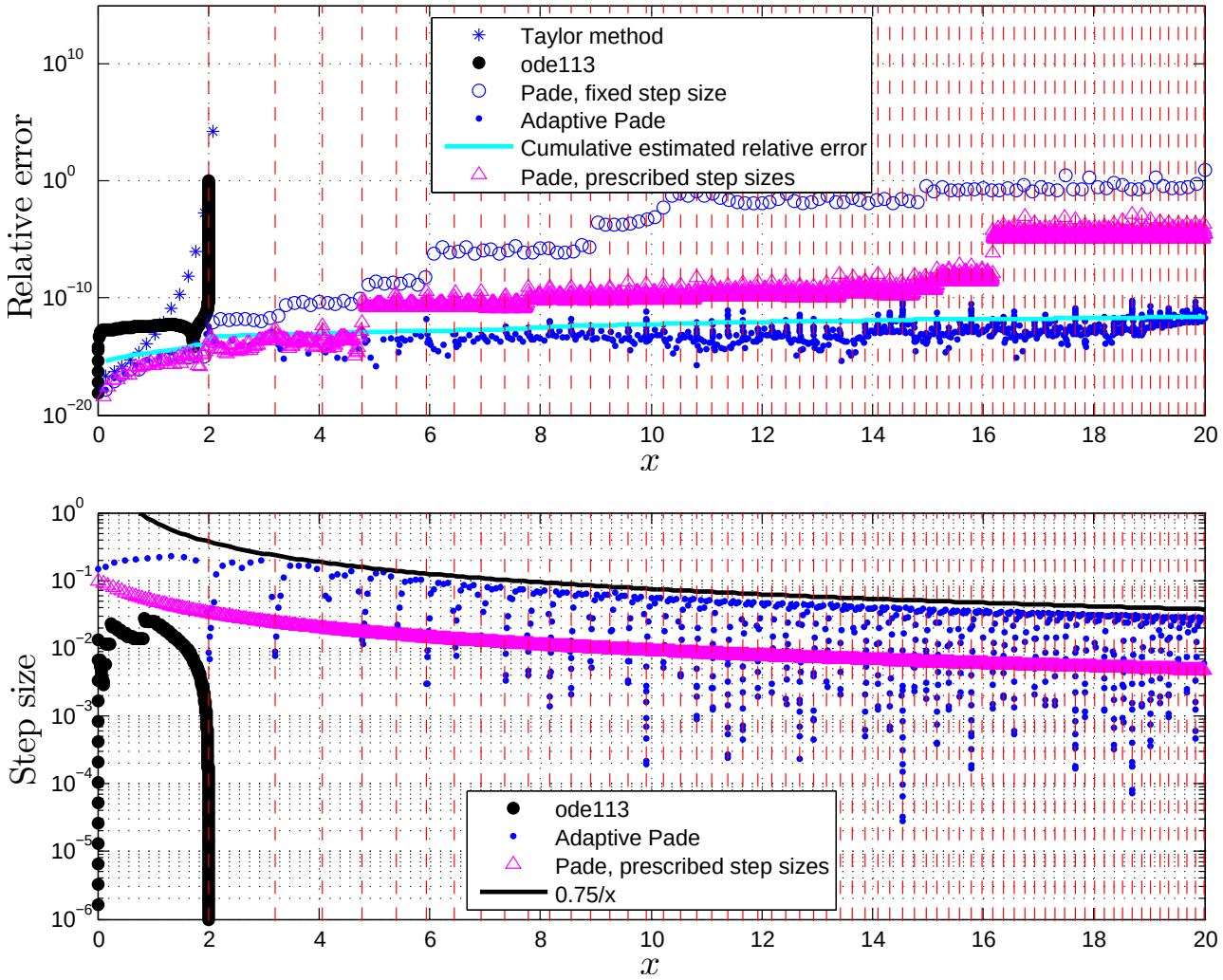

Figure 2.2: The relative error (top frame) and step sizes (bottom frame) of various methods used to approximate the solution to the problem (2.1). The vertical dashed lines indicate the locations of the poles of the solution (2.2). The Taylor method and the three Padé methods are all of 14th order. The Taylor method and fixed step size Padé method use a step size of $h = 4/27$. For the adaptive Padé method, $Tol =$ 1e-13 and $k =$ 1e-2 (see 2.11). The step sizes of the prescribed step size Padé method are specified by the function $h(x) = 0.1/(1+x)$.

$$q(h)u(z+h) - p(h) = (1 + b_1 h + \cdots + b_\nu h^\nu) \sum_{j=0}^{\infty} c_j h^j - (a_0 + a_1 h + \cdots + a_\nu h^\nu) \quad (2.7)$$

$$= \mathcal{O}\left(h^{n+1}\right). \quad (2.8)$$

To be clear, (2.8) means that the coefficients of h^j in (2.7) are zero for $j = 0, \ldots, n$. This condition can be satisfied by solving the Toeplitz system

$$\begin{pmatrix} c_\nu & c_{\nu-1} & \cdots & c_1 \\ c_{\nu+1} & c_\nu & \cdots & c_2 \\ \vdots & & \ddots & \vdots \\ c_{2\nu-1} & c_{2\nu-2} & \cdots & c_\nu \end{pmatrix} \begin{pmatrix} b_1 \\ b_2 \\ \vdots \\ b_\nu \end{pmatrix} = - \begin{pmatrix} c_{\nu+1} \\ c_{\nu+2} \\ \vdots \\ c_{2\nu} \end{pmatrix}, \quad (2.9)$$

and then setting

$$\begin{pmatrix} a_0 \\ a_1 \\ \vdots \\ a_\nu \end{pmatrix} = \begin{pmatrix} c_0 & 0 & \cdots & 0 \\ c_1 & c_0 & & 0 \\ \vdots & & \ddots & \vdots \\ c_\nu & c_{\nu-1} & \cdots & c_0 \end{pmatrix} \begin{pmatrix} 1 \\ b_1 \\ \vdots \\ b_\nu \end{pmatrix}.$$

We use MATLAB's backslash command to solve the system (2.9), which requires $\mathcal{O}(\nu^3)$ operations. As discussed in [32], there are faster $\mathcal{O}(\nu^2)$ algorithms for computing Padé approximants [86, 90, 92] but, in practice, for the small values of $\nu = n/2$ that we use (no more than 20), these algorithms are no faster than the backslash command. If the Toeplitz system is singular then, as in [32], we remove the final row of the matrix in (2.9), in which case the backslash command computes the minimum 2-norm solution of the underdetermined system.

For the fixed step size Padé method in Figure 2.2, the solution is approximated at every step using the Padé approximant $p(h)/q(h)$ defined in (2.6) with $\nu = n/2 = 7$ and $h = 4/27$. Unlike the polynomial-based methods, the Padé method can step through poles and maintain accuracy. However, the method eventually loses accuracy because the error increases by orders of magnitude, which appears as jumps in Figure 2.2, as it steps through certain poles. As discussed in [32], the Padé method loses accuracy when it steps from a position high up on a pole wall (i.e., very close to a pole) to some point much lower down due to finite-precision-arithmetic cancellation errors.

2.2.3 Adaptive Padé method

A variable step size Padé method is required to compute solutions with variable pole densities. We consider two variable step size methods, starting with an adaptive Padé method, which chooses an appropriate step size based on a local error estimate. It follows from (2.7) that

$$q(h)u(z+h) - p(h) = \sum_{j=n+1}^{\infty} \epsilon_j h^j, \qquad \epsilon_j = c_j + \sum_{k=1}^{\nu} b_k c_{j-k},$$

and thus the relative error incurred by a single Padé step can be estimated by

$$\left| \frac{u(z+h) - p(h)/q(h)}{p(h)/q(h)} \right| = \left| \frac{1}{p(h)} \sum_{j=n+1}^{\infty} \epsilon_j h^j \right| \approx \left| \frac{\epsilon_{n+1} h^{n+1}}{p(h)} \right| := T(h). \tag{2.10}$$

If $T(h) > Tol$, then a smaller step size, say ch, where $0 < c < 1$, must be chosen to meet the local error tolerance. We estimate the rescaling factor c as follows:

$$T(ch) = \left| \frac{\epsilon_{n+1}[ch]^{n+1}}{p(ch)} \right| \approx c^{n+1} \left| \frac{\epsilon_{n+1} h^{n+1}}{p(h)} \right| = c^{n+1} T(h) \leq Tol.$$

To ensure that the rescaled step size ch is sufficiently small, we choose

$$c = \left(\frac{k \cdot Tol}{T(h)} \right)^{1/(n+1)}, \qquad 0 < k \ll 1. \tag{2.11}$$

Two cases arise in our implementation of the adaptive Padé method:

- Case 1: $T(h) \leq Tol$. Accept the Padé approximation, i.e., set $u(z+h) \approx p(h)/q(h)$, and let $h := ch$, where c is defined in (2.11), be the step size to be used for the next Padé step.

- Case 2: $T(h) > Tol$. Reject the Padé step, re-evaluate the Padé approximation and the local error estimate $T(h)$ using the rescaled step size $h := ch$.

The top frame of Figure 2.2 shows that the adaptive Padé method can step through poles and maintain accuracy. The light blue line in the top frame was obtained by adding up the local error estimates, $T(h)$, at every step. This line shows that the cumulative sum of the error estimates along the interval is a reasonable model of the actual error, which is shown as blue dots. The bottom frame shows the small step sizes that are required close to the poles by the adaptive Padé method. The step sizes further away from the poles (midway between the vertical dashed lines), however, decrease as $\mathcal{O}(x^{-1})$, the same rate at which the distance

between consecutive poles decreases. This is illustrated by the close proximity of the black line and the topmost blue dots.

In Figure 2.3 the numerical experiment of Figure 2.2 is repeated with the adaptive Padé method but on a longer interval. The method can maintain accuracy on $[0, 20]$, on which there are 64 poles, but on the interval $[0, 80]$, with more than 1000 poles—1018 to be exact—the method loses accuracy. The method fails for the same reason mentioned for the fixed step size Padé method: eventually the adaptive Padé method is so close to a pole that finite precision rounding errors render the error estimate and the Padé approximant inaccurate.

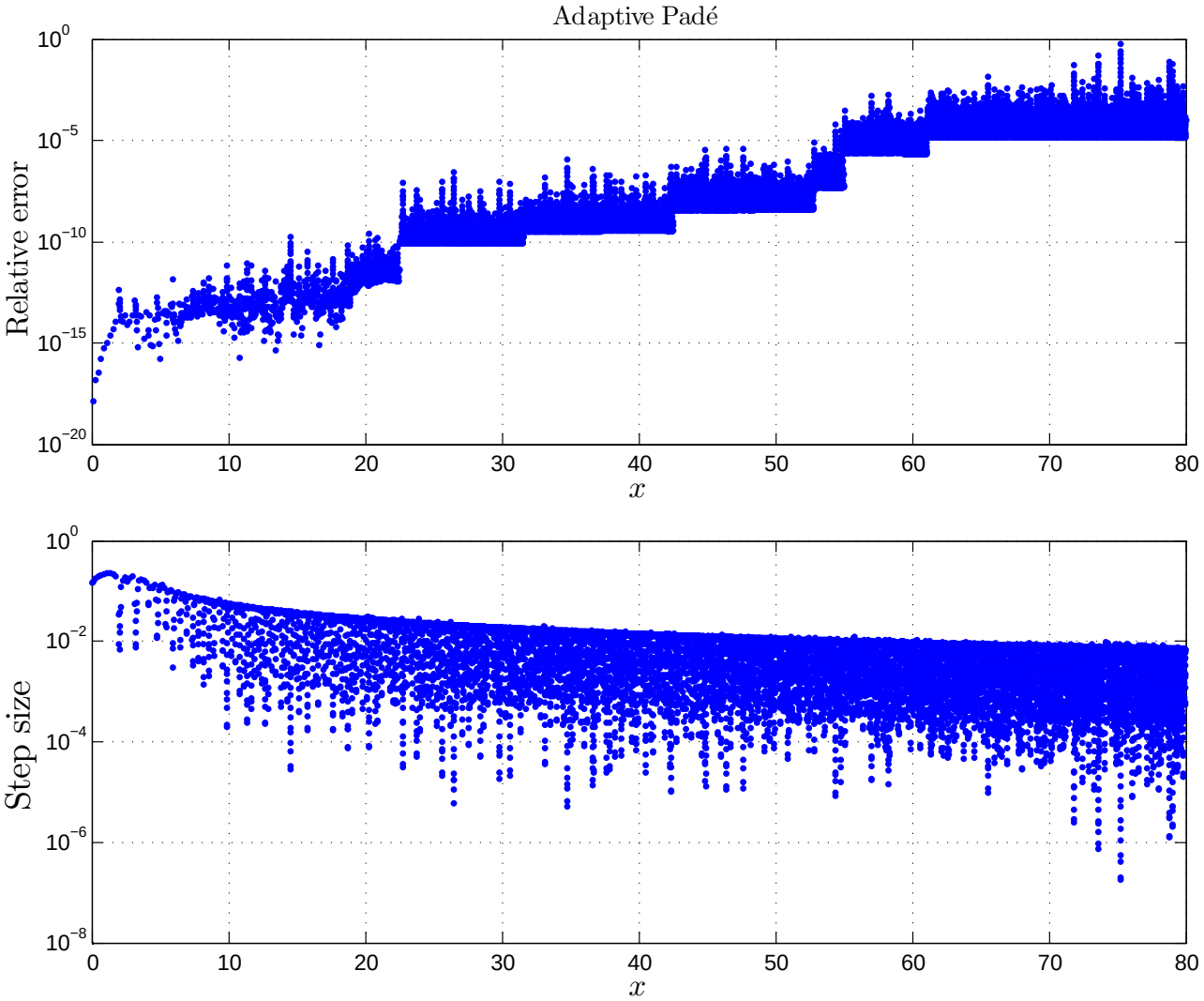

Figure 2.3: The adaptive Padé method that steps through poles is not very robust since it eventually loses accuracy if it steps through many poles. The parameters of the method are the same as in Figure 2.2.

We have unsuccessfully tried simple ad hoc measures to improve the robustness of the method, such as setting a minimum step size, including more terms of the series in (2.10)

to estimate the relative error and experimenting with different parameter values such as *Tol*, the order n and the value of k in (2.11). The robustness of the adaptive Padé method could probably be improved with more investigation. However, in section 2.3.3 we present a different adaptive Padé approach that has similar accuracy but more robustness than the adaptive Padé method presented in this section.

2.2.4 Prescribed step size Padé method

Another variable step size method, which we refer to as the prescribed step size Padé method, uses step sizes according to some predetermined step size function. For example, for the prescribed step size method in Figure 2.2, the Padé step size at x is specified by the function $h(x) = 0.1/(1 + x)$, see the purple triangles in the bottom frame of that figure. The step sizes of the adaptive Padé method was used to inform the choice of the step size function. The top frame of Figure 2.2 shows that the prescribed step size method is subject to the same loss of accuracy as the fixed step size Padé method, for the same reason given above. In section 2.3.4 we shall find that a different implementation of the prescribed step size method can yield accurate results.

2.3 Avoiding poles

The adaptive Padé method that steps through poles is inefficient since it requires very small step sizes, as shown in the bottom frame of Figure 2.2. More importantly, as we found in Figure 2.3, the method can lose accuracy if it steps too close to a pole, error control notwithstanding. A more efficient and robust approach, shown in Figure 2.4, is to avoid poles by allowing the Padé steps to enter the complex plane and run around poles. This allows for larger step sizes and it prevents the numerical instability that can occur close to poles. The details of the pole avoidance approach used in Figure 2.4 will be discussed later in this section.

2.3.1 History

The idea of letting integration paths of ODE methods venture into the complex plane around singularities, even when the solution is only sought on the real axis, was first proposed in 1980 by Corliss [17], who called this approach 'pole vaulting'. However, in that paper the polynomial-

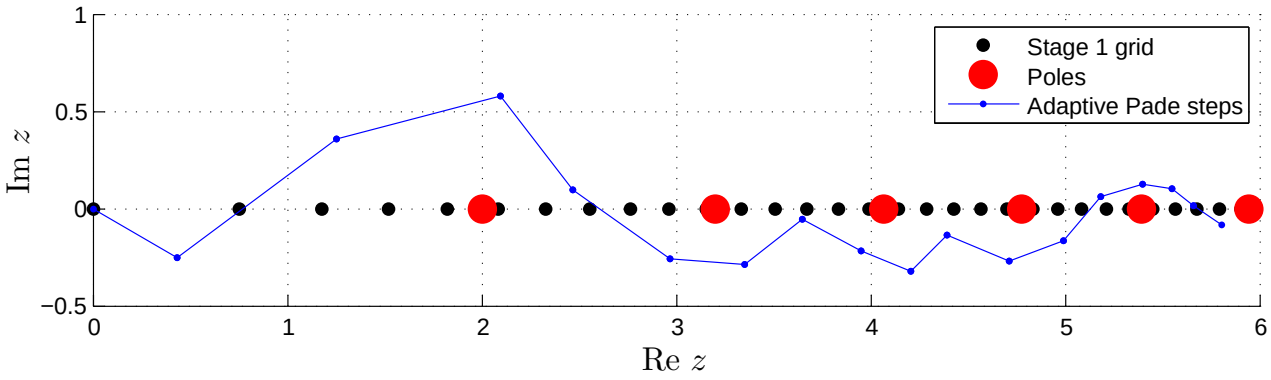

Figure 2.4: The steps taken by a 30th order adaptive Padé method during Stage 1 of the PFS method. The node separation function of the Stage 1 grid is $R(z) = 0.75/(1 + \text{Re } z)$.

based Taylor method was used, which, in order to maintain accuracy close to poles, requires much smaller step sizes (and is therefore much more expensive) than the Padé method. An illustration of this can be seen on the interval $[0, 2]$ in the top frame of Figure 2.2 in which the error of the Taylor method increases rapidly as the pole is approached, while the fixed step size Padé method, which uses the same step size as the Taylor method, remains accurate on $[0, 2]$. The additional step of converting a truncated Taylor expansion into a Padé approximant in an ODE approximation method was first introduced in 1974 by Willers [90]. Fornberg and Weideman's PFS method [32], the details of which we shall introduce shortly, combines the pole vaulting and Padé approximation ideas with a pole avoidance path selection strategy in the complex plane. As mentioned in section 1.3, the PFS method was a breakthrough that enabled the accurate and efficient computation of the single-valued Painlevé transcendents, which are characterized by movable poles, i.e., poles whose (generally unknown) locations in the complex plane depend on the ICs.

2.3.2 Fixed step size PFS method

We now describe the PFS method, as implemented in [32–34, 76–78]. The PFS computes solutions with poles in the complex plane using the following two-stage approach:

Stage 1: A node set is generated on the region where the solution is to be computed; for the single-valued Painlevé transcendents, a uniform coarse grid on a rectangle in the complex plane was used. Starting from the point where the ICs are supplied, the Taylor coeffi-

cients of the solution are recursively generated using the ODE, as discussed below (2.5)[1]. Then the type (ν, ν) Padé approximant is computed, where $\nu = n/2$ and n is even, in the manner described below (2.6). A target node is randomly chosen, and the Padé approximant is evaluated in five directions at a distance $|h|$ from the current point: one pointing straight at the target node as well as 15° and 30° on either side of this direction. The Padé step is taken in the direction in which the modulus of the solution is smallest among the five directions. Padé steps are taken in this fashion until the target node is within a distance of $|h|$. This ensures that the paths avoid poles. All the while the Padé coefficients, u (and u' for the second order Painlevé equations) are stored along the path. A different target node is chosen randomly and, starting from the closest point where the Padé coefficients are available, Padé steps are taken along the minimum modulus directions until the $|h|$-neighbourhood of that target node is reached. This is repeated until paths have been run to the neighbourhoods of all the nodes of the Stage 1 node set.

Stage 2: The solution is computed at all points on a fine grid (for the single-valued Painlevé transcendents, the fine grid was a uniform grid on the rectangular domain that was much more closely spaced than the Stage 1 coarse grid). This is accomplished as follows. Let the z_i, $1 \leq i \leq N$, denote the points where Padé coefficients are available from Stage 1. Padé steps are taken from each z_i to the points on the fine grid to which it is the closest point among the z_i.

The test calculations for the PFS in [32] were performed on an ODE whose solution (the Weierstrass $\wp$-function [23, Ch. 23]) has a constant pole density. For such pole fields the PFS methodology is numerically very stable, with test experiments reported in [32] (using standard double precision arithmetic) maintaining high accuracy even for integration distances in the 10^5–10^6 range.

The pole densities of the single-valued Painlevé transcendents, however, are not constant. For example, the number of poles of $\mathrm{P_I}$ solutions in a disc of radius R centred at the origin grows as $\mathcal{O}\left(R^{5/2}\right)$ [38]. Nevertheless, satisfactory accuracy was achieved with a uniform Stage 1 grid

[1]For first order problems such as the test problem (2.1), an approximation to the solution $u(z)$ (obtained from the Padé approximant) is required to initialize the generation of the Taylor coefficients while for the second order Painlevé equations, approximations to $u(z)$ and $u'(z)$ (obtained by differentiating the Padé approximant) are required.

and constant Stage 1 Padé step sizes in the numerical studies of the meromorphic Painlevé transcendents in [32–34, 76–78] since there was not much variation in the pole density on the domain. However, if the PFS is implemented with constant Stage 1 step sizes for the test problem (2.1), accuracy is lost sufficiently far out on $\mathbb{R}^+$, as shown in Figure 2.5, since the pole density increases with Re z.

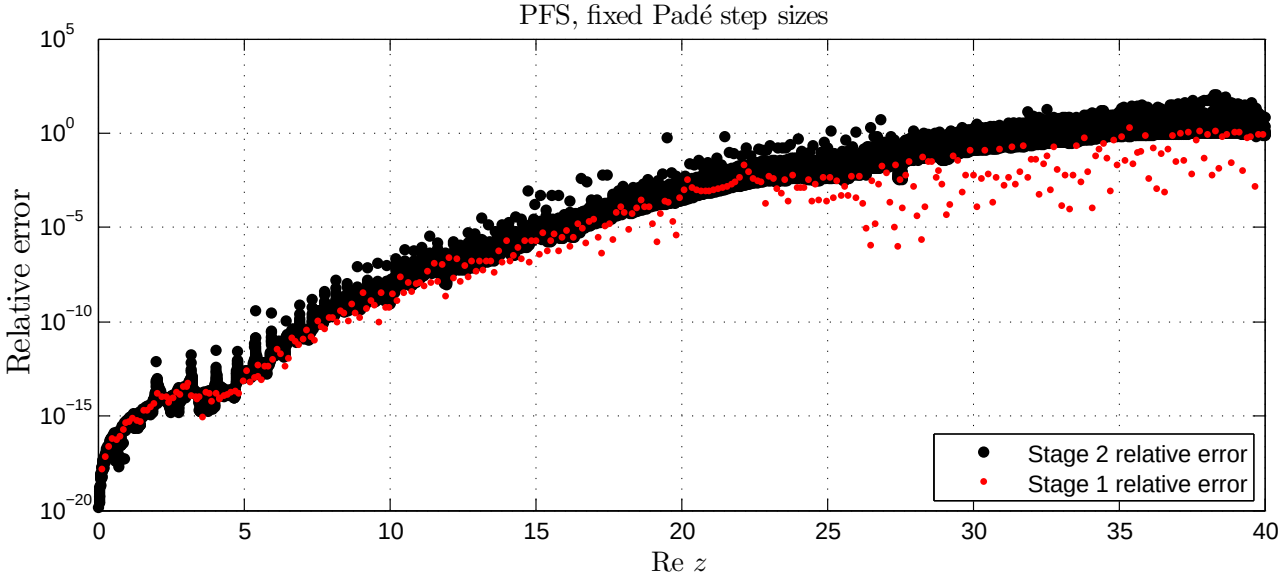

Figure 2.5: The PFS method with constant 14th order Padé step lengths of 4/27 for Stage 1 loses accuracy since the pole density of the solution (2.2) increases on $\mathbb{R}^+$. The Stage 1 and Stage 2 grids used are given in the caption of Figure 2.6.

To compute solutions with variable pole densities using the PFS approach, we use a Stage 1 node set that conforms to the pole density of the solution and variable Padé step lengths during Stage 1. For the test problem (2.1), the distance between consecutive poles on $\mathbb{R}^+$ decreases as $\mathcal{O}\left(1/\text{Re } z\right)$ (see (2.3)). Hence, we let the node separation function, which specifies the distance between consective Stage 1 nodes, be an inverse-linear function of Re z. For example, the node separation function of the Stage 1 grid depicted in Figure 2.4 is $R(z) = 0.75/(1 + \text{Re } z)$.

2.3.3 Adaptive Padé PFS method

As in section 2.2, we consider two variable step size methods: adaptive and prescribed step size Padé methods. We use the adaptive Padé method only in Stage 1 of the PFS, as follows. After a Padé step is taken in the minimum modulus direction in the manner described above, the error is estimated using $T(h)$, which is defined in (2.10). If $T(h) > Tol$, then h is replaced by

ch, where c is given in (2.11), the Padé approximant is again evaluated in the five directions, the minimum modulus direction is found again, and $T(h)$ is computed. This is repeated until $T(h) \leq Tol$. If $T(h) \leq Tol$, then u (and u' for the second Painlevé equations), the Padé coefficients and the scaled step length $|ch|$ are stored at the point. The initial step length is always the scaled step length stored at the current point; if the current point is the initial point, a user-specified step length is used. Variable step size Padé steps are taken in this manner until the target node is within a distance of $|ch|$. Paths are run in this fashion to reach close to all the Stage 1 nodes, after which Stage 2 is implemented as described above. Figure 2.4 shows the Stage 1 paths taken by the adaptive Padé method. Note how the poles are avoided and how the step lengths vary depending on the proximity of the paths to the poles.

Figure 2.6 shows the performance of the PFS method with an adaptive Padé Stage 1 implementation for the test problem (2.1) on the interval $[0, 80]$ with 1018 poles. The cumulative estimated relative error during Stage 1, shown in light blue in the top frame, is a reasonable model of the actual Stage 1 error. It is to be expected that the Stage 2 error will be larger than the Stage 1 error since error control is applied only in Stage 1. As expected, the step sizes taken during Stage 1 by the adaptive Padé method in Figure 2.6 that avoids poles are much larger than those taken by the adaptive Padé method in Figure 2.3 that steps through poles. Pole avoidance resolves the robustness problems of the adaptive Padé method in the previous section since we have found that accuracy is maintained on the entire interval, with results similar to those in Figure 2.6, for a wide range of choices of the parameters of the method (e.g., Stage 1 and Stage 2 grids, order, Tol and k).

2.3.4 Prescribed step size PFS method

If we use the prescribed step size method, the length of each Padé step in Stage 1 is usually chosen to be $|h(z)| = cR(z)$, where c is a positive constant, and $R(z)$ is the node separation function. Paths are run to within a distance $|h(z)|$ of each Stage 1 node. Otherwise, the implementation of the prescribed step size and adaptive step size methods are the same.

As before, the steps taken by the adaptive Padé method informs the choice of Stage 1 step sizes to be used in the prescribed step size method (shown in purple in Figure 2.6). The accuracy of the prescribed step size method, shown in Figure 2.7, is similar to that of adaptive method since similar step sizes are used in Stage 1.

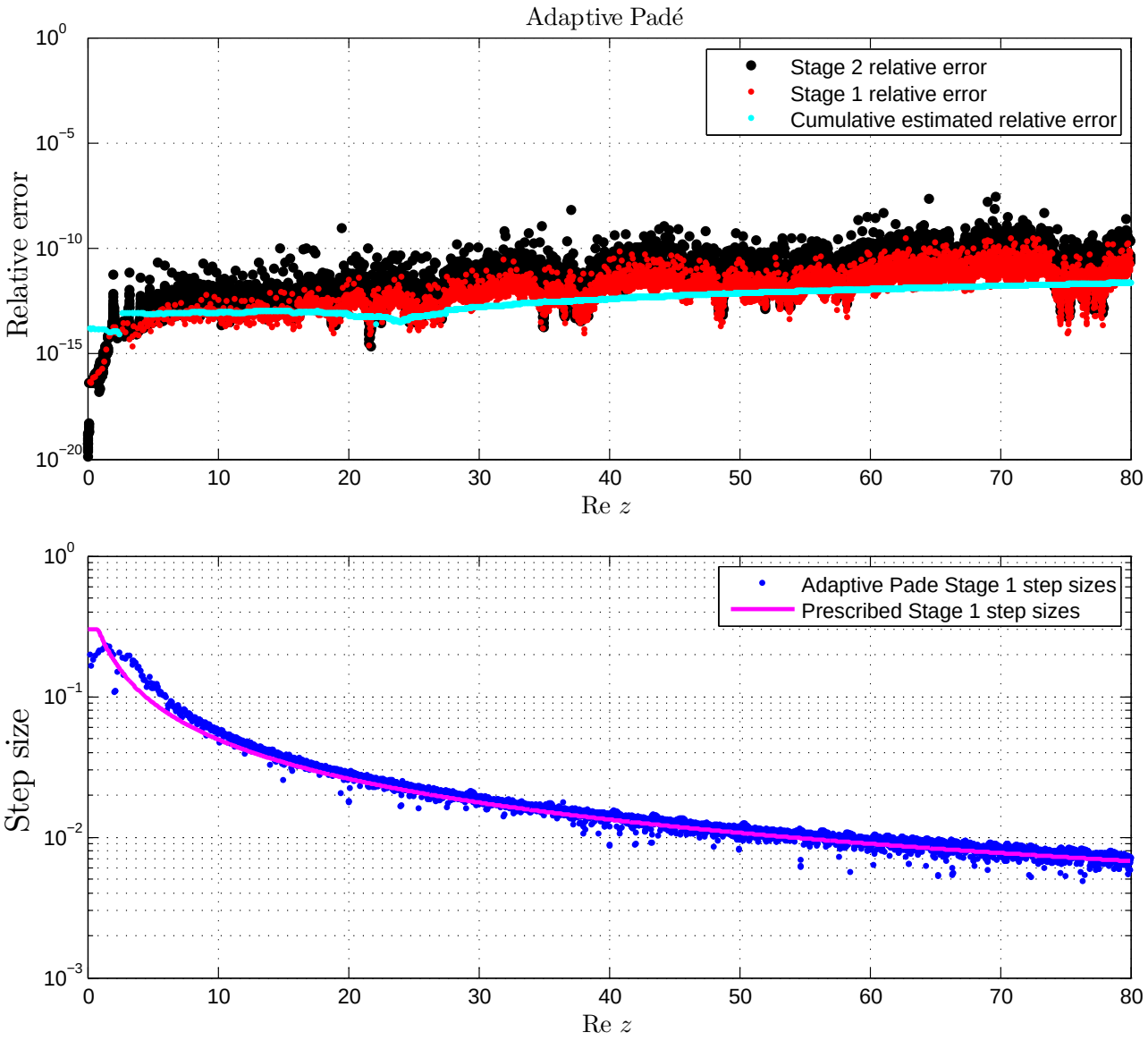

Figure 2.6: The error (top frame) and Stage 1 step sizes (bottom frame) of the PFS method with an adaptive Padé Stage 1 implementation for the test problem (2.1). The node separation function of the Stage 1 grid, which is confined to the real axis, is $R(z) = 0.75/(1 + \text{Re } z)$, and the Stage 2 grid is an equispaced grid on $\mathbb{R}^+$ with spacing $\pi/800 \approx 0.004$. The same Stage 1 and Stage 2 grids are used in Figures 2.5, 2.7 and 2.8. The other parameters of the method are $n = 14$, i.e., 14th order Padé steps are taken in Stage 1 and Stage 2, $Tol =$ 1e-13 and $k =$ 1e+2 (see (2.11)). The function specifying the prescribed step sizes of the method in Figure 2.7 is $\min\{0.3, 0.5475/(1 + \text{Re } z)\}$ (purple curve).

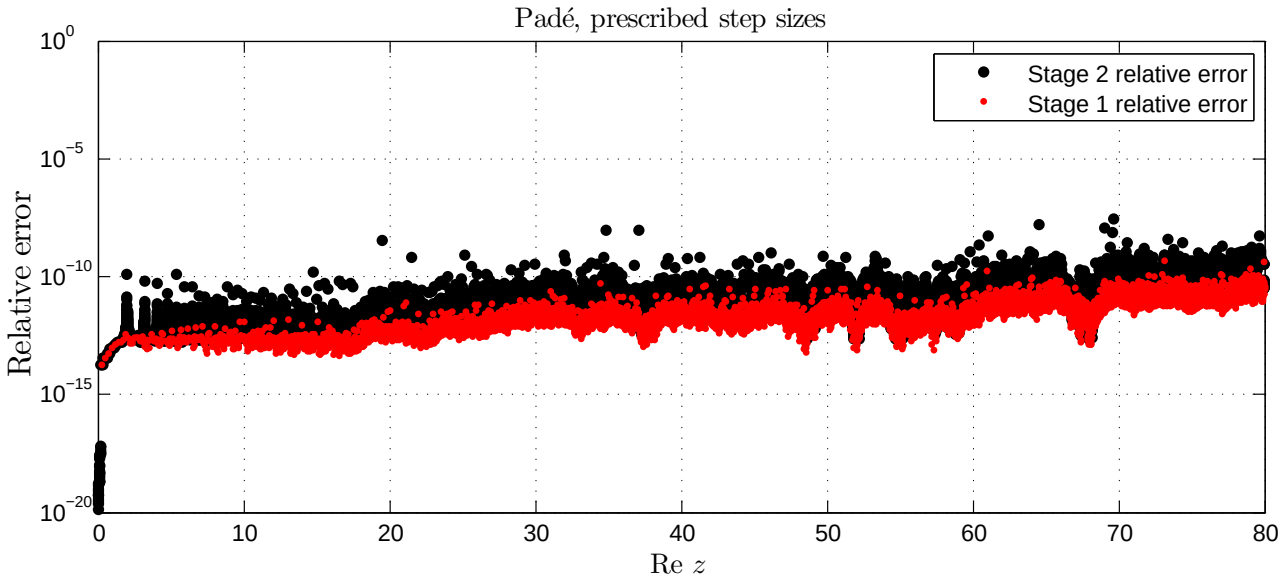

Figure 2.7: The error of the 14th order prescribed step size method whose step sizes are given by the purple curve in the bottom frame of Figure 2.6, i.e., the function $\min\{0.3, 0.5475/(1+\text{Re } z)\}$. Quantitative comparisons between the methods in this figure and Figure 2.6 are made in Table 2.1.

Table 2.1 gives a detailed comparison between the adaptive and prescribed step size methods. The difference in execution time between these methods is due to the error control overhead of the adaptive Padé method. Stage 2 of the PFS method requires very little execution time compared to Stage 1. Since all the Padé coefficients are computed in Stage 1, what is required in Stage 2 is (i) to find, for each point on the fine grid, the closest point z_i (recall that the points z_i denote the points where Padé coefficients are available from Stage 1) and (ii) to take Padé steps from each point z_i to the points on the fine grid identified in (i). In MATLAB, (i) is accomplished for all the points on the fine grid with a single call to the function `knnsearch`, a function in the Statistics Toolbox for finding nearest neighbours in data. The evaluation of the Padé steps in (ii) for each z_i is vectorized in MATLAB and can be further speeded up with parallelization since the steps from the different z_i to the points on the Stage 2 grid are independent.

Table 2.1: Statistics for the PFS methods used in Figures 2.6 and 2.7 for the computation of the solution to the test problem (2.1), which has 1018 poles on the interval $[0, 80]$. The Stage 1 grid, Stage 2 grid and other parameters of the methods used in these numerical experiments are given in the caption of Figure 2.6. The execution times were recorded on a machine with a clock speed of 3.6 GHz using only one core.

	Stage 1 adaptive step sizes	Stage 1 prescribed step sizes
Stage 1 nodes	4452	
Stage 2 fine grid points	20372	
Stage 1 Padé steps	8671	8645
Stage 1 execution time	3.22 seconds	2.54 seconds
Stage 2 execution time	0.1 seconds	

2.3.5 The instability of IVP methods on smooth regions

Figure 2.8 illustrates a counter-intuitive aspect of computing solutions with poles. We forced the paths shown in the top frame of the figure to move off the pole-infested real axis and into the smooth region off the real axis by making the paths run from the vicinity of a Stage 1 node at $z = 10$ to a Stage 1 node at $20 + i/2$. The red dots on the interval $\text{Re}\, z \in [10, 20]$ in the bottom frame of Figure 2.8 shows that the solution is computed almost to machine precision on this path in the smooth region from $z = 10$ to $z = 20 + i/2$. However, as the paths return towards the real axis from the path in the smooth region, the error increases rapidly, as shown by the vertical rows of red dots in the bottom frame. We emphasize that the increase in the error occurs within the smooth region, as soon as the paths move from the smooth region towards $\mathbb{R}$. The Stage 2 fine grid is confined to the real axis and thus the black dots in the bottom frame show the error on $\mathbb{R}$.

The paradoxical fact that the accuracy of the PFS method decreases on smooth pole-free regions was noted in [32]. The explanation given in [32] for the P_I equation ($u'' = 6u^2 + z$) is that in smooth regions, the left-hand side of the equation is small, the terms on the right-hand side balance and small numerical errors in the solution lead to large relative errors in u'', which

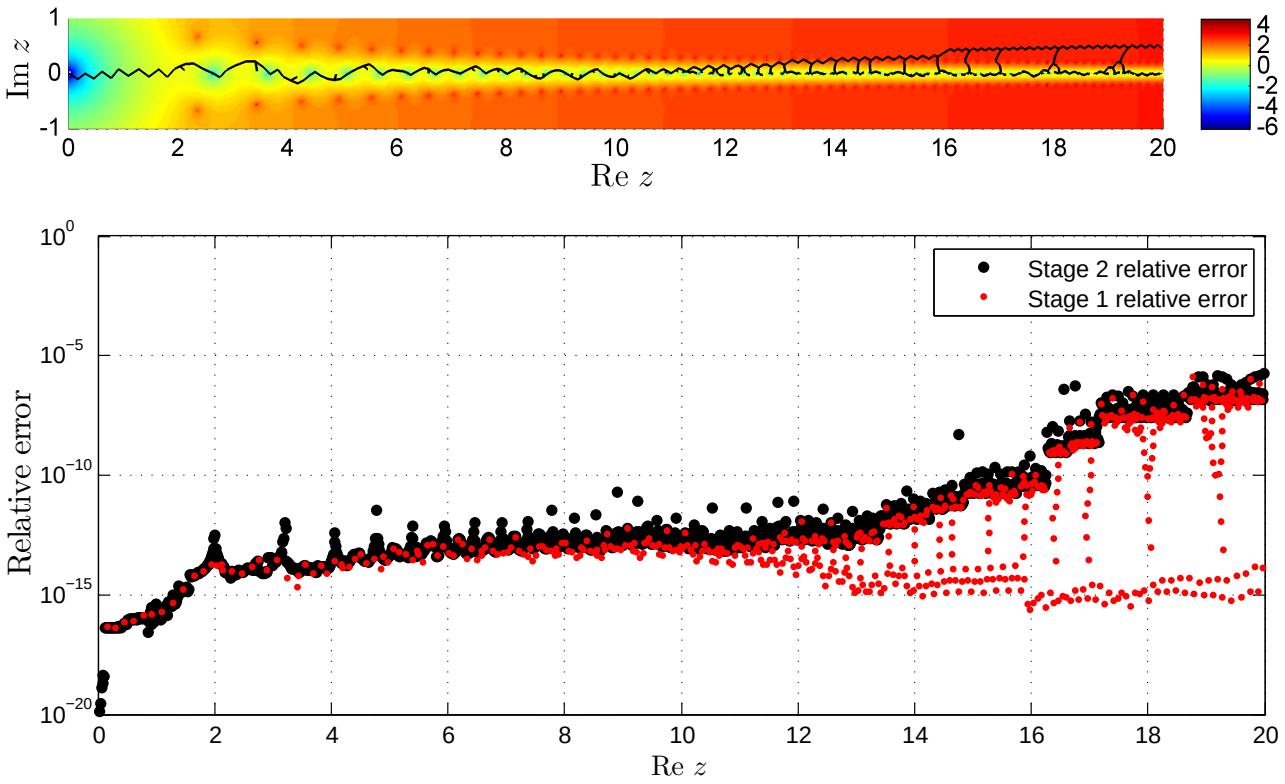

Figure 2.8: Top frame: a contour plot of $\log_{10}(\kappa_r)$ with its colour bar on the right, where κ_r, defined in (2.12), is the 'relative condition number' of the differential equation (2.1). The Stage 1 paths taken by the adaptive Padé method is superimposed on the plot. The bottom frame shows that the error increases rapidly as the paths move from the smooth region off the real axis, with large condition number κ_r, towards the real axis.

renders IVP methods unstable as they step through smooth regions. Boundary-value problem (BVP) solvers were suggested as more well-conditioned methods for computing solutions on smooth regions. This approach will be illustrated in section 3.3.2. Here we quantify the sensitivity of the test equation (2.1) to numerical errors.

Let u be the exact solution to the test problem (2.1) and let $\widetilde{u}$ be the numerical solution. If we set $u \approx \widetilde{u} + \epsilon$, where ϵ is constant, then the relative error in the right-hand side of the equation, the relative defect, can be estimated by

$$\left|\frac{u' - \widetilde{u}'}{\widetilde{u}'}\right| \approx \left|\frac{(\widetilde{u}+\epsilon)^2 + z^2 - (\widetilde{u}^2 + z^2)}{\widetilde{u}'}\right| = \left|\frac{2\widetilde{u}\epsilon + \epsilon^2}{\widetilde{u}'}\right| = \left|\frac{2\widetilde{u}^2}{\widetilde{u}'}\right| \left|\frac{\epsilon}{\widetilde{u}}\right| + \mathcal{O}\left(\epsilon^2\right).$$

Hence, the relative defect is given approximately by the relative error of the numerical solution, $|\epsilon/\widetilde{u}|$, multiplied by the factor

$$\left|\frac{2\widetilde{u}^2}{\widetilde{u}'}\right| := \kappa_r, \tag{2.12}$$

which we interpret as a relative condition number of the equation. The top frame of Figure 2.8 is a contour plot of $\log_{10}(\kappa_r)$ from which we see that the equation is well conditioned (κ_r is not much greater than 1) within a narrow strip about the pole-laden real axis while κ_r increases on the smooth region where u' is small. Note in Figure 2.8 that the error is small on Re $z \in [0, 13]$ while the paths in the top frame are confined to the yellow region, and the error increases on the rest of the interval after the paths have veered into the smooth region and returned to $\mathbb{R}$. To obtain the results in Figures 2.6 and 2.7 we had to prevent the paths from moving into the smooth regions. This was achieved by first running paths to Stage 1 nodes at $z = 1, 2, \ldots, 80$, which are sufficiently close together to prevent paths from moving too far into the smooth regions. After this paths were run to the remaining Stage 1 nodes in a random order. The maximum value of κ_r along the Stage 1 paths for the experiments in Figures 2.6, 2.7 and 2.8 are, respectively, 7.0, 6.7 and 3e+3, confirming that the paths in Figures 2.6 and 2.7 were confined to well-conditioned regions.

2.3.6 Postscript: eliminating poles

Finally, we mention that an alternative to using methods that avoid poles is to devise methods that eliminate poles. Peltonen [73], under the supervision of L.N. Trefethen, attempted to eliminate poles of ODE solutions by mapping the solution to the Riemann sphere. However, it was demonstrated that it is not always possible to eliminate poles in this fashion. After the introduction of the PFS, another method for computing the Painlevé transcendents was introduced by Abramov and Yukhno [2–7]. Their method eliminates poles by making certain changes of variables in the neighbourhoods of poles. Hence, their method can employ any of the standard polynomial-based numerical methods for ODEs. The numerical solutions presented in [2–7] are however confined to the real axis.

Chapter 3

The computation of the multivalued Painlevé transcendents

The multivalued Painlevé transcendents present more formidable computational challenges than the problem considered in the previous chapter. This is not only because of the presence of branch points but also because the exact solutions are generally not available and the pole densities are unknown, parameter dependent (recall from section 1.1 that the $\mathrm{P_{III}}$, $\mathrm{P_V}$ and $\mathrm{P_{VI}}$ equations each has four arbitrary parameters) and vary on a two-dimensional domain.

Our computational approaches to the $\mathrm{P_{III}}$, $\mathrm{P_V}$ and $\mathrm{P_{VI}}$ equations are determined by the possible locations of the branch points of their solutions. Recall from section 1.2 that, in the finite plane, $z = 0$ is the only point at which $\mathrm{P_{III}}$ and $\mathrm{P_V}$ can have a branch point while $z = 0$ and $z = 1$ are the only points where branch points of $\mathrm{P_{VI}}$ can occur. Hence, our computational methods for $\mathrm{P_{III}}$ and $\mathrm{P_V}$ are similar, while $\mathrm{P_{VI}}$ requires a different approach.

3.1 Computing $\mathrm{P_{III}}$ and $\mathrm{P_V}$ solutions

For $\mathrm{P_{III}}$ and $\mathrm{P_V}$ one can use an exponential transformation to map the fixed singularity at $z = 0$ out of the finite complex plane and then obtain equations whose solutions are meromorphic and thus single-valued. Specifically, setting $z = e^{\zeta/2}$ and $u(z) = e^{-\zeta/2}w(\zeta)$ in $\mathrm{P_{III}}$ results in a modified third Painlevé equation,

$$\widetilde{\mathrm{P}}_{\mathrm{III}}: \qquad \frac{d^2w}{d\zeta^2} = \frac{1}{w}\left(\frac{dw}{d\zeta}\right)^2 + \frac{1}{4}\left(\alpha w^2 + \gamma w^3 + \beta e^{\zeta} + \frac{\delta e^{2\zeta}}{w}\right),$$

whose solutions are meromorphic [41]. Likewise, setting $z = e^{\zeta}$ and $u(z) = w(\zeta)$ in $\mathrm{P_V}$ yields a modified fifth Painlevé equation,

$$\widetilde{\mathrm{P}}_{\mathrm{V}}: \qquad \frac{d^2w}{d\zeta^2} = \left(\frac{1}{2w} + \frac{1}{w-1}\right)\left(\frac{dw}{d\zeta}\right)^2 + (w-1)^2\left(\alpha w + \frac{\beta}{w}\right) + \gamma e^{\zeta} w + \frac{\delta e^{2\zeta} w(w+1)}{w-1},$$

whose solutions are meromorphic [40]. One may thus obtain multivalued $\mathrm{P_{III}}$ and $\mathrm{P_V}$ solutions u in the z-plane by computing the single-valued solutions w of $\widetilde{\mathrm{P}}_{\mathrm{III}}$ and $\widetilde{\mathrm{P}}_{\mathrm{V}}$ in the ζ-plane. We have reduced the computation of $\mathrm{P_{III}}$ and $\mathrm{P_V}$ solutions to the same problem as in the previous chapter, viz. the computation of meromorphic functions with variable pole densities. We therefore employ the two effective methods we developed in the previous chapter: the PFS with a variable density Stage 1 node set and either an adaptive Padé method or prescribed step size Padé method for Stage 1. We refer to any one of these two methods as the enhanced PFS method.

3.1.1 An illustration of the enhanced PFS method in the ζ-plane

Recall from the previous chapter that the Stage 1 node set is determined by a node separation function $R(\zeta)$ that specifies the distance between a node at ζ and its neighbouring nodes. In the previous chapter the Stage 1 nodes were confined to the real axis (see Figure 2.4) and the known pole density of the solution could be used to choose a suitable node separation function. The generation and selection of a Stage 1 node set is more challenging for the $\widetilde{\mathrm{P}}_{\mathrm{III}}$ and $\widetilde{\mathrm{P}}_{\mathrm{V}}$ equations for two reasons. Firstly, a node set is required on a two-dimensional domain and, secondly, the pole densities of $\mathrm{P_{III}}$ and $\mathrm{P_V}$ solutions (which could be translated to those of $\widetilde{\mathrm{P}}_{\mathrm{III}}$ and $\widetilde{\mathrm{P}}_{\mathrm{V}}$ solutions) are not known.

We use Fornberg and Flyer's node placement algorithm [31] to generate, for a given node separation function $R(\zeta)$, a Stage 1 node set on a two-dimensional domain. The non-uniform Stage 1 node set should reflect at least the general trend in the pole densities of $\widetilde{\mathrm{P}}_{\mathrm{III}}$ and $\widetilde{\mathrm{P}}_{\mathrm{V}}$ solutions. We have not found any results concerning the pole densities of $\mathrm{P_{III}}$ and $\mathrm{P_V}$ solutions, but our experiments indicate that they are not only highly non-uniform functions of ζ but also of the parameters and ICs. This makes it difficult to choose a Stage 1 node set that conforms to the pole densities of all $\widetilde{\mathrm{P}}_{\mathrm{III}}$ and $\widetilde{\mathrm{P}}_{\mathrm{V}}$ solutions. Nevertheless, it is to be expected from the exponential transformations used to arrive at $\widetilde{\mathrm{P}}_{\mathrm{III}}$ and $\widetilde{\mathrm{P}}_{\mathrm{V}}$ that the pole density will increase rapidly on the region $\mathrm{Re}\,\zeta \gg 0$. For simplicity we have therefore chosen Stage 1 node sets

with a node separation function $R(\zeta)$ that decreases linearly with Re ζ. For example, the first column of Figure 3.1 shows a Stage 1 node set in a rectangular domain on the ζ-plane with a node separation function given by $R(\zeta) = (8-\text{Re }\zeta)/20$.

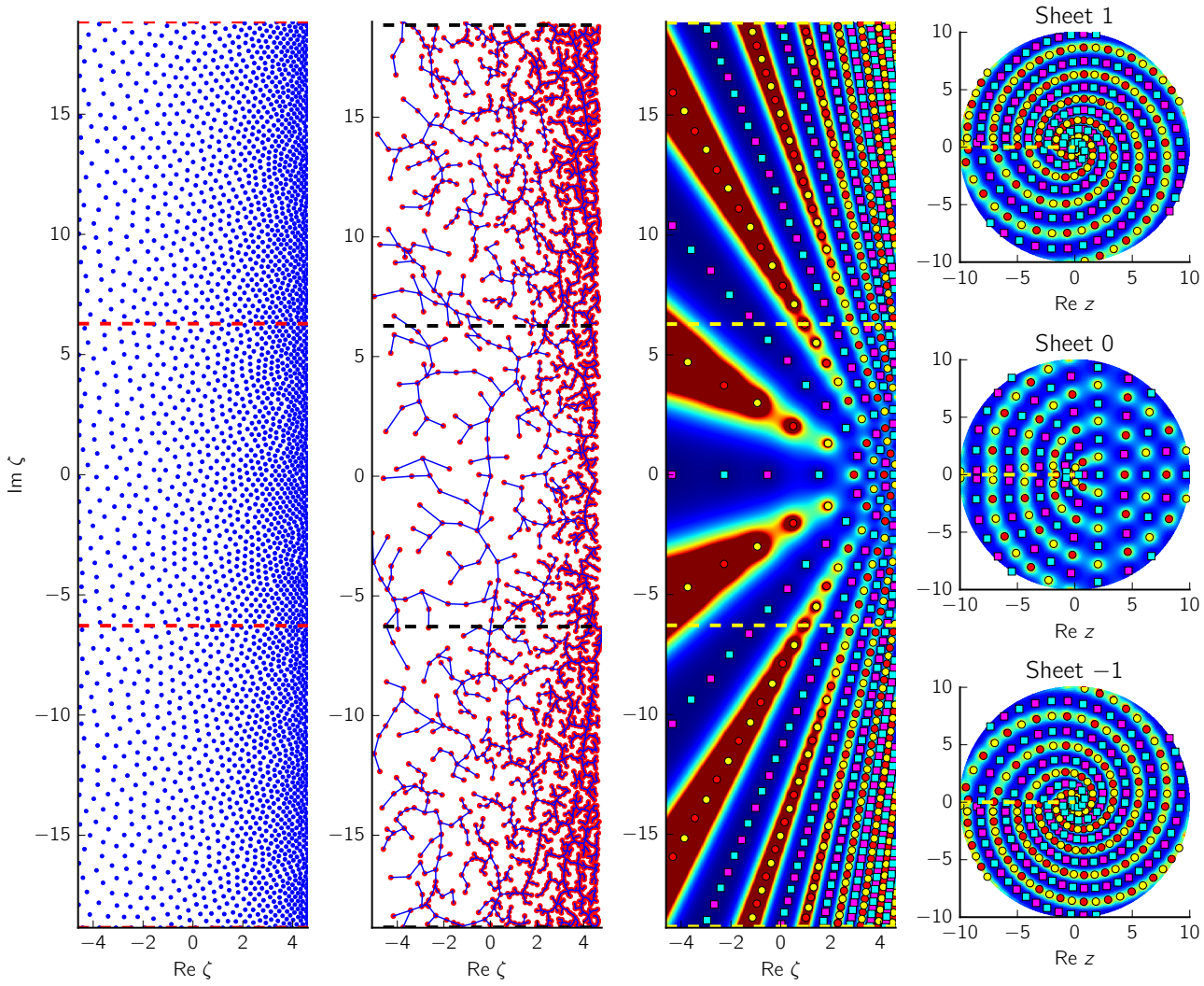

Figure 3.1: A P_{III} solution on three sheets of its Riemann surface, as computed by the enhanced PFS method. Left to right: The Stage 1 node set with node separation function $R(\zeta) = (8-\text{Re }\zeta)/20$; the Padé steps taken by the adaptive step size method in Stage 1; a P_{III} solution in the ζ-plane and on the corresponding sheets of its Riemann surface in the z-plane ($z = e^{\zeta/2}$). This solution has parameter values $(\alpha, \beta, \gamma, \delta) = (-1/2, -1/2, 1, -1)$ and ICs $(u(1), u'(1)) = (1/4, 1)$ in the z-plane.

The second column of Figure 3.1 shows the Padé steps taken by the adaptive step size method in the first stage of the PFS. At each of the 2701 points in the second column, w, w' and the Padé coefficients are available and each of the 3041 nodes in the first column is within a distance of $|ch|$, where c is defined in (2.11), to a point in the second column. To compute the solution shown in the third column, we used a 571×140 uniform grid with spacing 1/15 on the ζ-plane domain as our Stage 2 fine grid. Thus, the Padé coefficients at the 2701 points in the second column were used to compute Padé approximations to the solution w at the $571 \times 140 = 79940$ points of the fine grid.

The third column of Figure 3.1 is a plot of the modulus of a $\mathrm{P_{III}}$ solution, i.e., a plot of $|e^{-\zeta/2}w(\zeta)| = |u|$, where w is the solution computed on the Stage 2 grid mentioned above. We map the $\widetilde{\mathrm{P}}_{\mathrm{III}}$ solution w on the strip $-2\pi < \mathrm{Im}\ \zeta - 4\pi s \le 2\pi$, $s \in \mathbb{Z}$ to the $\mathrm{P_{III}}$ solution u on the s-th sheet of the Riemann surface in the z-plane according to $u(z) = u(e^{\zeta/2}) = e^{-\zeta/2}w(\zeta)$. The strips with $s = -1, 0, 1$ are indicated by dashed horizontal lines in Figure 3.1. The fourth column is another plot of $|u|$, but mapped to the $s = -1, 0, 1$ sheets of the Riemann surface. According to Table 3.1 all the poles of the solution in Figure 3.1 are of first order with residue $+\sqrt{\gamma} = +1$ or $-\sqrt{\gamma} = -1$ in the z-plane, indicated by red and yellow circles, respectively. Similarly, all the zeros are simple, and u' either has the value $\sqrt{-\delta} = +1$ (purple squares) or $-\sqrt{-\delta} = -1$ (light blue squares) at each zero in the z-plane. Note how the lengths of the Padé steps taken in the second column by the adaptive step size method conform to the pole density of the solution in the third column. The modulus of the solution in Figure 3.1 has an up-down symmetry in the ζ-plane since the solution in the upper and lower half planes are conjugate; this is a consequence of the real valued parameters and real ICs on the real ζ-axis. The distinctive spirals of poles whirling around the branch point $z = 0$ in the fourth column is a pole field pattern that has not been observed before: the pole fields of the single-valued Painlevé transcendents shown in [32–34, 77, 78] have very different characteristics.

One could compute $\mathrm{P_{III}}$ and $\mathrm{P_V}$ solutions in the z-plane instead of the ζ-plane by making the Padé steps run around the possible branch point at $z = 0$ in clockwise and counterclockwise directions (and thus onto the $s \le 0$ and $s \ge 0$ sheets, respectively). We shall illustrate this approach for the computation of $\mathrm{P_{VI}}$ solutions in section 3.2. We have found that the pole densities of $\mathrm{P_{III}}$ and $\mathrm{P_V}$ solutions can also be highly non-uniform in the z-plane, as Figure 3.1 illustrates for $\mathrm{P_{III}}$ (solutions of $\mathrm{P_V}$ in the z-plane will be shown in section 3.3). Thus, variable

Table 3.1: The labels indicating the poles and zeros of the P_{III} solution in Figure 3.1. For every solution displayed in this chapter we give a table similar to this one to describe the types of poles and zeros of the solution. The coefficients c_k in this table and the similar Tables 3.3–3.6 are derived as follows. In a neighbourhood of a pole or zero at z_0 we have $u \approx c_k(z-z_0)^k$ with $k<0$ or $k>0$, respectively. Making this substitution in the relevant equation and taking the limit $z \to z_0$ readily yields the order k of the pole or zero as well as the leading order coefficient c_k. We assume that z_0 is not a fixed singularity of the equation. The coefficients c_k in the transformed plane, e.g., the ζ-plane in Figure 3.1, can be derived similarly or by applying the appropriate transformation to the poles and zeros in the z-plane.

		Poles		Zeros	
P_{III}, $\gamma\delta \neq 0$	z-plane	$c_{-1} = +1/\sqrt{\gamma}$	●	$c_1 = +\sqrt{-\delta}$	■
		$c_{-1} = -1/\sqrt{\gamma}$	●	$c_1 = -\sqrt{-\delta}$	■
	ζ-plane	$c_{-1} = +2e^{-\zeta_0/2}/\sqrt{\gamma}$	●	$c_1 = +e^{\zeta_0/2}\sqrt{-\delta}/2$	■
		$c_{-1} = -2e^{-\zeta_0/2}/\sqrt{\gamma}$	●	$c_1 = -e^{\zeta_0/2}\sqrt{-\delta}/2$	■

density Stage 1 node sets and a variable step size Padé method are also required in the z-plane. We have not found that there is any advantage, in terms of accuracy or speed, to computing P_{III} and P_V solutions in the z-plane as opposed to the ζ-plane. If anything, the implementation of our method in the z-plane is more complicated because of the need to impose certain directions on the integration paths.

3.1.2 Experiments

In practice we choose specific parameters in our numerical method (e.g., $R(\zeta)$, the value of c for the prescribed step sizes $|h(\zeta)| = cR(\zeta)$, the value of k in (2.11), the order n of the Padé approximations) based on experimentation, for which error estimates are essential. Solutions of $\widetilde{P}_{III}$ and $\widetilde{P}_V$ with real parameter values and real ICs on the real axis satisfy $w(\overline{\zeta}) = \overline{w(\zeta)}$. If we do not make use of this symmetry in our numerical method but, instead, compute the Padé steps in the upper and lower halves of the ζ-plane independently, as is the case in the second column of Figure 3.1, then we can estimate the relative numerical error by

calculating $E(\zeta) = |w(\overline{\zeta}) - \overline{w(\zeta)}|/|w(\zeta)|$. By plotting $E(\zeta)$ and recording the execution time for different choices of the parameters, we can experimentally determine parameter choices that give satisfactory results.

In Table 3.2 we compare the performance of the adaptive and prescribed step size methods for two different situations: when high accuracy is required (Experiment 1), e.g., for the verification of theoretical asymptotic formulae and known closed-form solutions, and when efficiency is essential (Experiment 2), e.g., in a survey of a large number of solutions. As expected, the adaptive step size method is more accurate but slower than the prescribed step size method since it incorporates error control. Similar to what we found for the actual error in the previous chapter, the estimated error in Table 3.2 is orders of magnitude greater than *Tol* for the adaptive step size method since error control is only applied in Stage 1 but not in Stage 2. In addition, *Tol* is only a bound on the local error that accumulates with the number of Padé steps on the domain, which also accounts for the fact that the error on sheets $+1$ and -1 is larger than on the 0th sheet. The efficiency of both methods can be increased by using the up-down symmetry in the ζ-plane (for real-valued ICs and parameter values) and by parallelizing the implementation of Stage 1 and Stage 2. The parallelization of Stage 2 was discussed in section 2.3. Here we note that Stage 1 can be parallelized by partitioning the domain, running a path to a point in each sub-domain from the initial point and then computing the solution independently on each partition. As we shall point out again in Chapter 5, we used parallel computation to produce animations of solutions of $\mathrm{P_{III}}$ on multiple Riemann sheets for a large number of different parameter values, which lead to the discovery and analysis of certain symmetry properties of the solutions.

Table 3.2: Statistics for the computation of the solution shown in Figure 3.1. In Experiment 1 and Experiment 2 both methods used a Stage 1 node set with a node separation function given by $R_1(\zeta) = (8 - \text{Re } \zeta)/40$ and $R_2(\zeta) = (8 - \text{Re } \zeta)/10$, respectively, and both used 30th order Padé steps. The adaptive step size method used $k = 10^{-3}$ (see (2.11)) in both experiments and $Tol = 10^{-14}$ in Experiment 1 and $Tol = 10^{-11}$ in Experiment 2. The step sizes of the prescribed step size method were $|h(\zeta)| = 1.85R_1(\zeta)$ in Experiment 1 and $|h(\zeta)| = 0.6R_2(\zeta)$ in Experiment 2. The third column refers to the number of Padé steps taken in Stage 1; the fine grid used for Stage 2, a 571×140 uniform grid with spacing 1/15 on the ζ-plane domain, were the same in both experiments. The execution times include Stage 1 and Stage 2 and were recorded on a machine with a clock speed of 3.6 GHz using only one core. The first and second relative errors in each row are for the solution on the regions $-2\pi < \text{Im } \zeta \leq 2\pi$ (corresponding to the 0th sheet) and $|\text{Im } \zeta - 4\pi| \leq 2\pi$ (-1th and $+1$th sheets), respectively. These errors were estimated using the symmetry-based method discussed above.

		Number of steps	Time (seconds)	Relative error
Experiment 1	Adaptive step sizes	4259	5.43	4e-10, 4e-8
	Prescribed step sizes	4270	4.52	8e-6, 4e-3
Experiment 2	Adaptive step sizes	1324	2.27	1e-6, 8e-2
	Prescribed step sizes	1314	1.48	2e-6, 4e-2

3.2 Computing $\mathrm{P_{VI}}$ solutions

An exponential transformation mapped the fixed singular point of $\mathrm{P_{III}}$ and $\mathrm{P_V}$ at $z = 0$ out of the finite plane since the exponential function is entire and never assumes the value zero. This allowed us to avoid the possible branch point of $\mathrm{P_{III}}$ and $\mathrm{P_V}$ solutions at $z = 0$. In general we cannot avoid the branch points of $\mathrm{P_{VI}}$ solutions because the $\mathrm{P_{VI}}$ equation has fixed singular points at $z = 0$ and $z = 1$ and, by Picard's theorem, no non-constant entire function can avoid two different values, as would be required to map these points out of the finite plane. Thus it is generally necessary to steer the integration paths of the PFS around branch points of $\mathrm{P_{VI}}$ solutions. However, it is possible to use transformations to avoid branch points on restricted parts of the Riemann surfaces of $\mathrm{P_{VI}}$ solutions. We illustrate both of these approaches, starting with the latter.

3.2.1 Avoiding branch points

The transformation $z = e^\zeta$ maps the fixed singularity of $\mathrm{P_{VI}}$ at $z = 0$ out of the finite ζ-plane, and it maps the fixed singularity at $z = 1$ to $\zeta = 2i\pi k$, $k \in \mathbb{Z}$. These points are the fixed singularities of the equation

$$\begin{aligned}\frac{d^2w}{d\zeta^2} &= \frac{1}{2}\left(\frac{1}{w} + \frac{1}{w-1} + \frac{1}{w-e^\zeta}\right)\left(\frac{dw}{d\zeta}\right)^2 - \left(\frac{e^\zeta}{e^\zeta - 1} + \frac{e^\zeta}{w - e^\zeta}\right)\frac{dw}{d\zeta} \\ &\quad + \frac{w(w-1)(w-e^\zeta)}{(e^\zeta-1)^2}\left(\alpha + \frac{\beta e^\zeta}{w^2} + \frac{\gamma(e^\zeta - 1)}{(w-1)^2} + \frac{\delta e^\zeta(e^\zeta-1)}{(w-e^\zeta)^2}\right),\end{aligned} \tag{3.1}$$

obtained by setting $u(z) = w(\zeta)$, $z = e^\zeta$ in $\mathrm{P_{VI}}$. Another exponential transformation, $\zeta = e^\eta$, maps the fixed singularity at $\zeta = 0$ out of the finite η-plane, and it maps the remaining fixed singularities to

$$\eta = \log|2\pi k| + i\arg(2\pi i k), \qquad |k| \geq 1, \tag{3.2}$$

which are the fixed singularities of the equation obtained by setting $w(\zeta) = v(\eta)$, $\zeta = e^\eta$ in (3.1), i.e.,

$$\begin{aligned}\frac{d^2v}{d\eta^2} &= \frac{1}{2}\left(\frac{1}{v} + \frac{1}{v-1} + \frac{1}{v-e^{e^\eta}}\right)\left(\frac{dv}{d\eta}\right)^2 - \left(\frac{e^\eta e^{e^\eta}}{e^{e^\eta}-1} + \frac{e^\eta e^{e^\eta}}{v-e^{e^\eta}} - 1\right)\frac{dv}{d\eta} \\ &\quad + \frac{v(v-1)(v-e^{e^\eta})e^{2\eta}}{(e^{e^\eta}-1)^2}\left(\alpha + \frac{\beta e^{e^\eta}}{v^2} + \frac{\gamma(e^{e^\eta}-1)}{(v-1)^2} + \frac{\delta e^{e^\eta}(e^{e^\eta}-1)}{(v-e^{e^\eta})^2}\right).\end{aligned} \tag{3.3}$$

We conclude from (3.2) that the region $\mathrm{Re}\,\eta < \log 2\pi$ is branch point-free. The first column of Figure 3.2 shows a $\mathrm{P_{VI}}$ solution computed within this region. This solution was computed by

applying the enhanced PFS method to (3.3). The solution within the region $-3\pi \leq \text{Im } \eta \leq -\pi$, not shown in Figure 3.2, is the conjugate of the displayed solution contained in $\pi \leq \text{Im } \eta \leq 3\pi$; as before, this follows from the real-valued parameters and real ICs on the real η-axis. The η-plane region in Figure 3.2 corresponds to the following two rectangular sheets of the Riemann surface that winds around the branch point at $\zeta = 0$ in the second column of Figure 3.2:

$$\{\zeta \in \mathbb{C} \,:\, \log(1/100) \leq \text{Re } \zeta \leq \log(10), -\pi \leq \text{Im } \zeta \leq \pi,\ -\pi \leq \arg \zeta \leq 3\pi\}.$$

The asymptotic behaviours of the solution close to its poles and zeros are given in Table 3.3.

Table 3.3: The poles and zeros of the P_{VI} solutions in Figures 3.2, 3.3 and 3.5.

		Poles		Zeros	
P_{VI}, $\alpha\beta \neq 0$	η-plane	$c_{-1} = +e^{-\eta_0}(e^{e^{\eta_0}} - 1)/\sqrt{2\alpha}$	●	$c_1 = +e^{\eta_0}e^{e^{\eta_0}}\sqrt{-2\beta}/(e^{e^{\eta_0}} - 1)$	■
		$c_{-1} = -e^{-\eta_0}(e^{e^{\eta_0}} - 1)/\sqrt{2\alpha}$	●	$c_1 = -e^{\eta_0}e^{e^{\eta_0}}\sqrt{-2\beta}/(e^{e^{\eta_0}} - 1)$	■
	ζ-plane	$c_{-1} = +(e^{\zeta_0} - 1)/\sqrt{2\alpha}$	●	$c_1 = +e^{\zeta_0}\sqrt{-2\beta}/(e^{\zeta_0} - 1)$	■
		$c_{-1} = -(e^{\zeta_0} - 1)/\sqrt{2\alpha}$	●	$c_1 = -e^{\zeta_0}\sqrt{-2\beta}/(e^{\zeta_0} - 1)$	■
	z-plane	$c_{-1} = +z_0(z_0 - 1)/\sqrt{2\alpha}$	●	$c_1 = +\sqrt{-2\beta}/(z_0 - 1)$	■
		$c_{-1} = -z_0(z_0 - 1)/\sqrt{2\alpha}$	●	$c_1 = -\sqrt{-2\beta}/(z_0 - 1)$	■

3.2.2 Circumambulating branch points

Unlike the branch point at $\zeta = 0$, the branch point at $\zeta = 2\pi i$ in the second column of Figure 3.2 is not mapped out of the finite η-plane. Hence, this branch point cannot be avoided by computing in the η-plane. The approach we follow to compute the solution in the neighbourhood of $\zeta = 2\pi i$ is to apply the enhanced PFS method to (3.1). The only modification of the method that is required is to steer the Padé paths in the appropriate directions around the branch points in the ζ-plane, as shown in the third column of Figure 3.2. In the bottom-right frame, the Stage 1 Padé paths run in clockwise and counterclockwise directions around the branch point at $\zeta = 0$. Note that, as required, none of the paths overstep the branch cuts, indicated by solid lines, on a given sheet. To move onto the sheet in the top-right frame the

paths move through the branch cut by running only in a counterclockwise direction around $\zeta = 0$, as indicated by the arrows. The paths then run in both directions around the branch point at $\zeta = 2\pi i$. The dots on which the paths are superimposed are the points of the Stage 1 node set. We chose a node set that becomes increasingly dense close to the branch points since our numerical experiments have shown that there can be high pole densities in the neighbourhoods of the branch points, which is evidently the case for the solution in the top-center frame of Figure 3.2. Note from the bottom-right frame that the adaptive step size method chose a few, relatively large steps on the pole-free sheet, while the step sizes in the top-right frame reflect the increasing pole densities close to the branch points.

Figure 3.3 again depicts the $\mathrm{P_{VI}}$ solution in the ζ-plane but also on the corresponding sheets in the z-plane. The second and third columns show phase portraits [88] of the solution, i.e., plots of $\mathrm{Arg}[w(\zeta)] \in (-\pi, \pi]$ and $\mathrm{Arg}[u(z)]$, respectively. The phase of the solution is indicated according to the colour wheel at the top of Figure 3.3 and so, for example, positive real solution values are indicated by red. The branch cuts in the second column are unmistakable and clearly indicate the manner in which the two sheets in the ζ-plane are connected through the branch cut or, equivalently, the directions in which the PFS integration paths must have run. The traversal of the paths through the branch cut in the bottom-center frame corresponds to a traversal through the branch cut $z \in (0, 1)$ on the 0th sheet in the z-plane. The movement of the paths across the dotted line in the top-center frame corresponds to a movement across the branch cut on the negative real axis on the 1st sheet in the z-plane. Hence, the paths in the ζ-plane correspond to counterclockwise revolutions around the branch points at $z = 0$ and $z = 1$, and thus the sheets in the z-plane are parametrized by

$$\text{sheet } k = \{z \in \mathbb{C} \,:\, 1/100 \leq |z| \leq 10,\ z = re^{i\theta_k},\ z = 1 + \rho e^{i\phi_k},\ \rho \geq 1/100\},$$

where

$$\begin{aligned} -\pi < \theta_0 \leq \pi, \qquad & -\pi < \phi_0 \leq \pi, \\ -\pi < \theta_1 \leq \pi, \qquad & \pi < \phi_1 \leq 3\pi, \\ \pi < \theta_2 \leq 3\pi, \qquad & \pi < \phi_2 \leq 3\pi. \end{aligned}$$

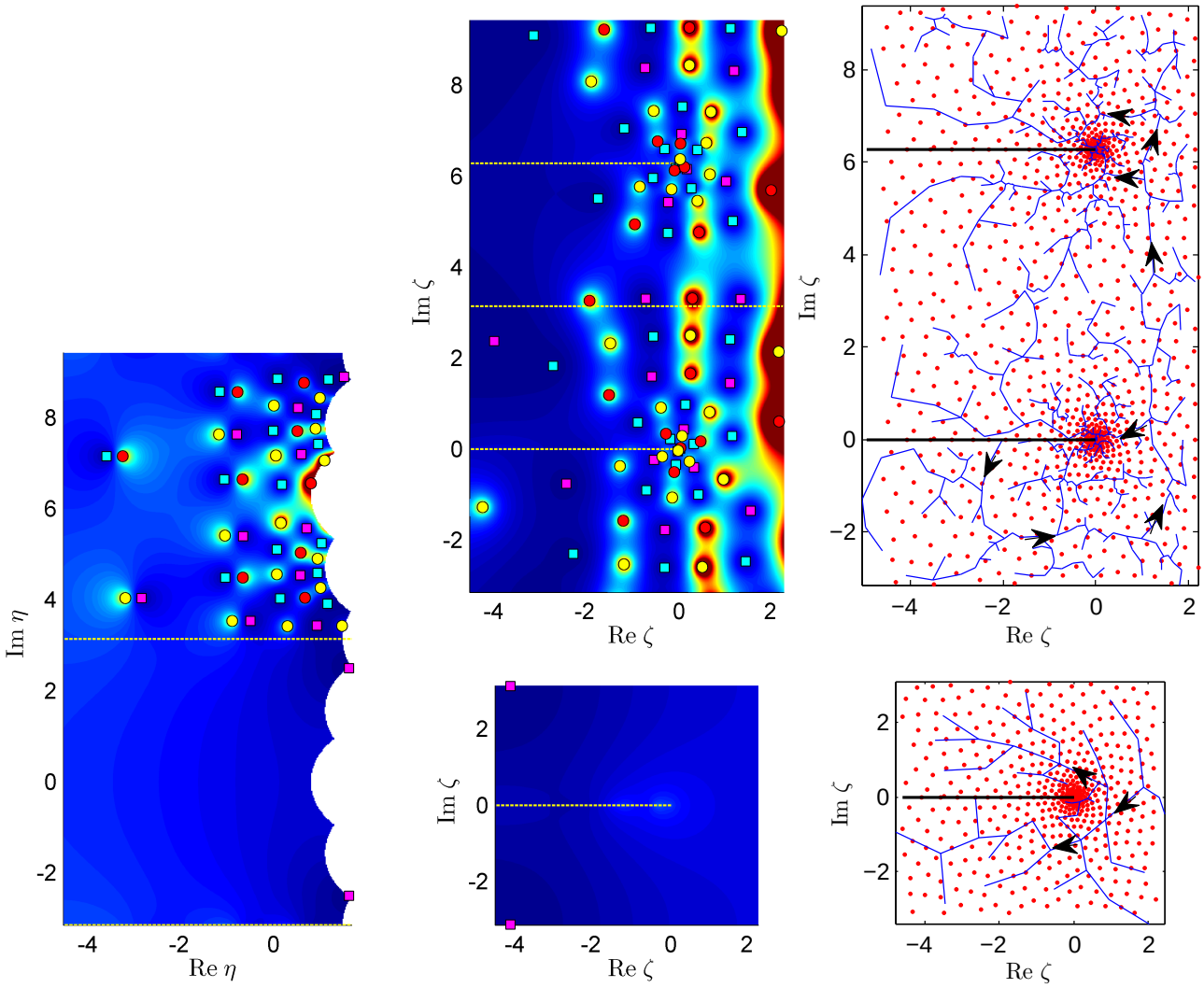

Figure 3.2: Two approaches to the computation of a P_{VI} solution: computing on a region in the η-plane that is branch point-free (first column) and computing in the ζ-plane by making the PFS paths run around the branch points (second and third columns). This P_{VI} solution has parameters $(\alpha, \beta, \gamma, \delta) = (4, -4, 8, -8)$ and ICs $u(10) = 0.429534600325223$ and $u'(10) = -1.61713114374804\text{e-}3$ in the z-plane. The symmetry-based error estimates for the η-plane method are 4e-7 and 3e-6 for the solution contained in the regions $-\pi < \text{Im } \eta \leq \pi$ and $\pi < \text{Im } \eta \leq 3\pi$, respectively; those for the ζ-plane method are 6e-7, for the solution shown in the bottom-centre frame, and 6e-4 and 5e-4 for the solution within the strips $-\pi < \text{Im } \zeta \leq \pi$ and $\pi < \text{Im } \zeta \leq 3\pi$, respectively, in the top-center frame.

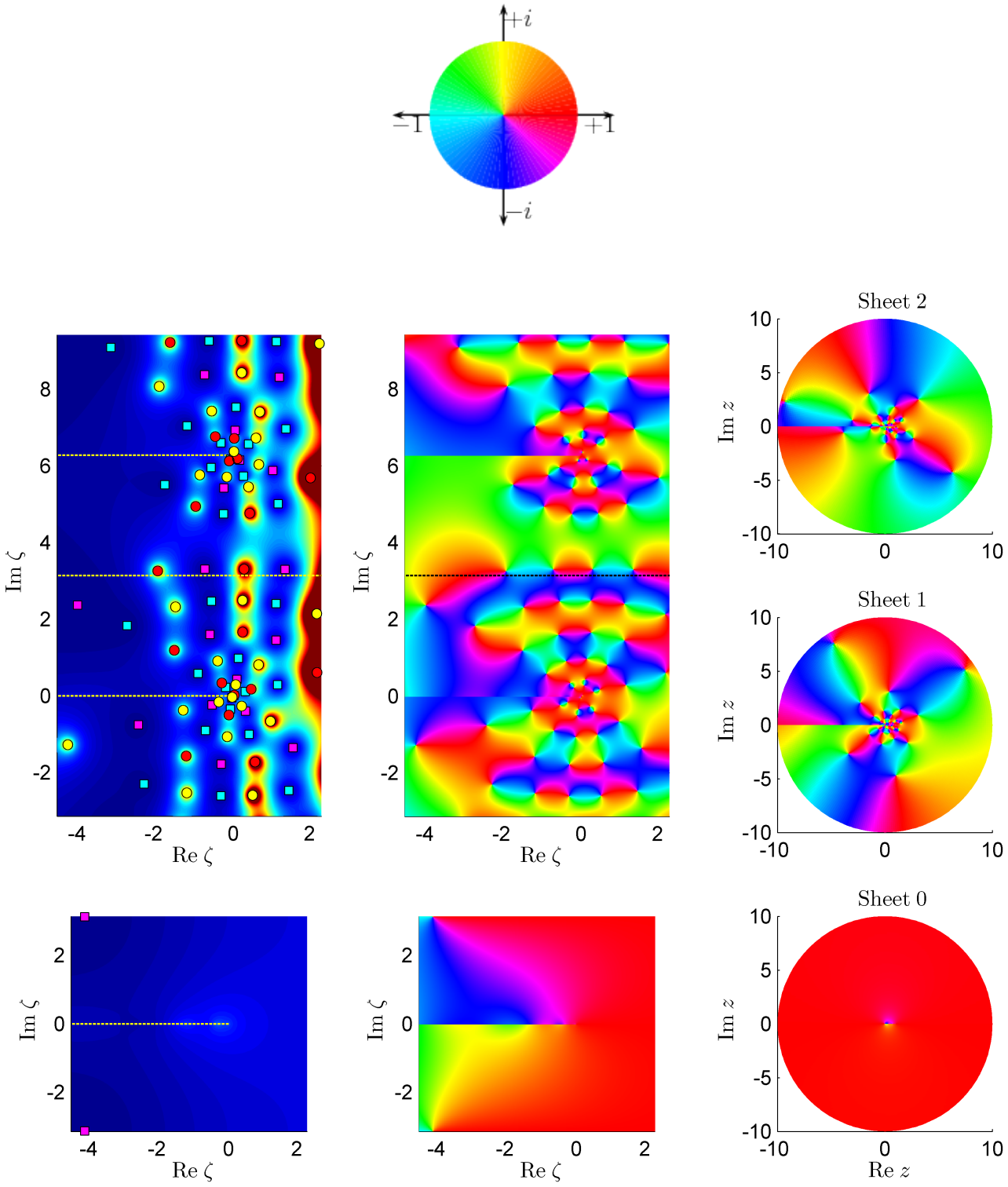

Figure 3.3: The phase of the P_{VI} solution shows the structure of the Riemann surfaces in the ζ and z planes (recall that $z = e^{\zeta}$). The phase of the solution is depicted according to the colour wheel, taken from `http://dlmf.nist.gov/help/vrml/aboutcolour`. The phase portraits suggest that the pole-free 0th sheet in the z-plane only has a branch cut on $z \in (0, 1)$, whereas the other sheets have branch cuts on $z \in (0, 1)$ and the negative real z-axis.

3.2.3 Evidence for a tronquée $\mathrm{P_{VI}}$ solution

The most striking feature of the solution in Figures 3.2 and 3.3 is its large pole-free sector. Tronquée solutions are characterized by asymptotic expansions near infinity that are valid in certain sectors of the complex plane. Tronquée solutions are pole-free on these regions of validity. The ICs of the solution in Figures 3.2 and 3.3, given in the caption to Figure 3.2, were obtained by substituting the formal asymptotic expansion $u = \sum_{n=0}^{\infty} a_n z^{-n}$ into $\mathrm{P_{VI}}$, generating the coefficients a_n recursively and evaluating the expansion by optimal truncation far out on the positive real axis. Based on the pole-free region in Figure 3.3, we conjecture that the formal asymptotic expansion is valid for $z \to \infty$, $-\pi < \arg z \leq \pi$. That is, we conjecture that this $\mathrm{P_{VI}}$ solution is a tronquée solution.

Tronquée solutions of $\mathrm{P_I}$–$\mathrm{P_V}$ have been studied, see [9,21,46–49,54], but we are not aware of any results concerning tronquée solutions of $\mathrm{P_{VI}}$. It is known [37], however, that $\mathrm{P_{VI}}$ admits an expansion of the above form, $u = \sum_{n=0}^{\infty} a_n z^{-n}$, at $z = \infty$ but the region of validity of the expansion is not given in [37].

A tronquée solution is pole-free on a certain sector of the complex plane as $z \to \infty$. Another notable feature of the solution in Figure 3.3 is that it also appears to be pole-free for all *finite* z on the region $-\pi < \arg z \leq \pi$. Tronquée solutions, in particular their asymptotics and their pole-free regions in the finite plane, will be investigated in greater detail in Chapters 4 and 5.

3.3 More examples of $\mathrm{P_{III}}$, $\mathrm{P_V}$ and $\mathrm{P_{VI}}$ solutions

In this section we use the methods discussed above to compute more examples of the multi-valued Painlevé transcendents on multiple sheets of their Riemann surfaces. In addition, we derive a condition number for $\mathrm{P_{III}}$ (similar to the condition number derived in section 2.3.5 for the model problem (2.1)) which shows that in pole-free regions the solution can be sensitive to perturbations. In these regions we enhance the method by solving the equation by boundary-value techniques, a remedy originally suggested in [32].

3.3.1 A tronquée $\mathrm{P_V}$ solution

Figure 3.4 shows a $\mathrm{P_V}$ solution computed in the same manner as the $\mathrm{P_{III}}$ solution in Figure 3.1. The solution on sheets -1 and -2 (not shown) are the conjugates of the solution on sheets $+1$

Table 3.4: The poles and zeros of the P_V solution in Figure 3.4.

		Poles		Zeros
P_V, $\alpha \neq 0$, $\beta = 0$	z-plane	$c_{-1} = +z_0/\sqrt{2\alpha}$ $c_{-1} = -z_0/\sqrt{2\alpha}$	● ●	$c_2 = k \in \mathbb{C}$
	ζ-plane	$c_{-1} = +1/\sqrt{2\alpha}$ $c_{-1} = -1/\sqrt{2\alpha}$	● ●	$c_2 = e^{2\zeta_0} k$

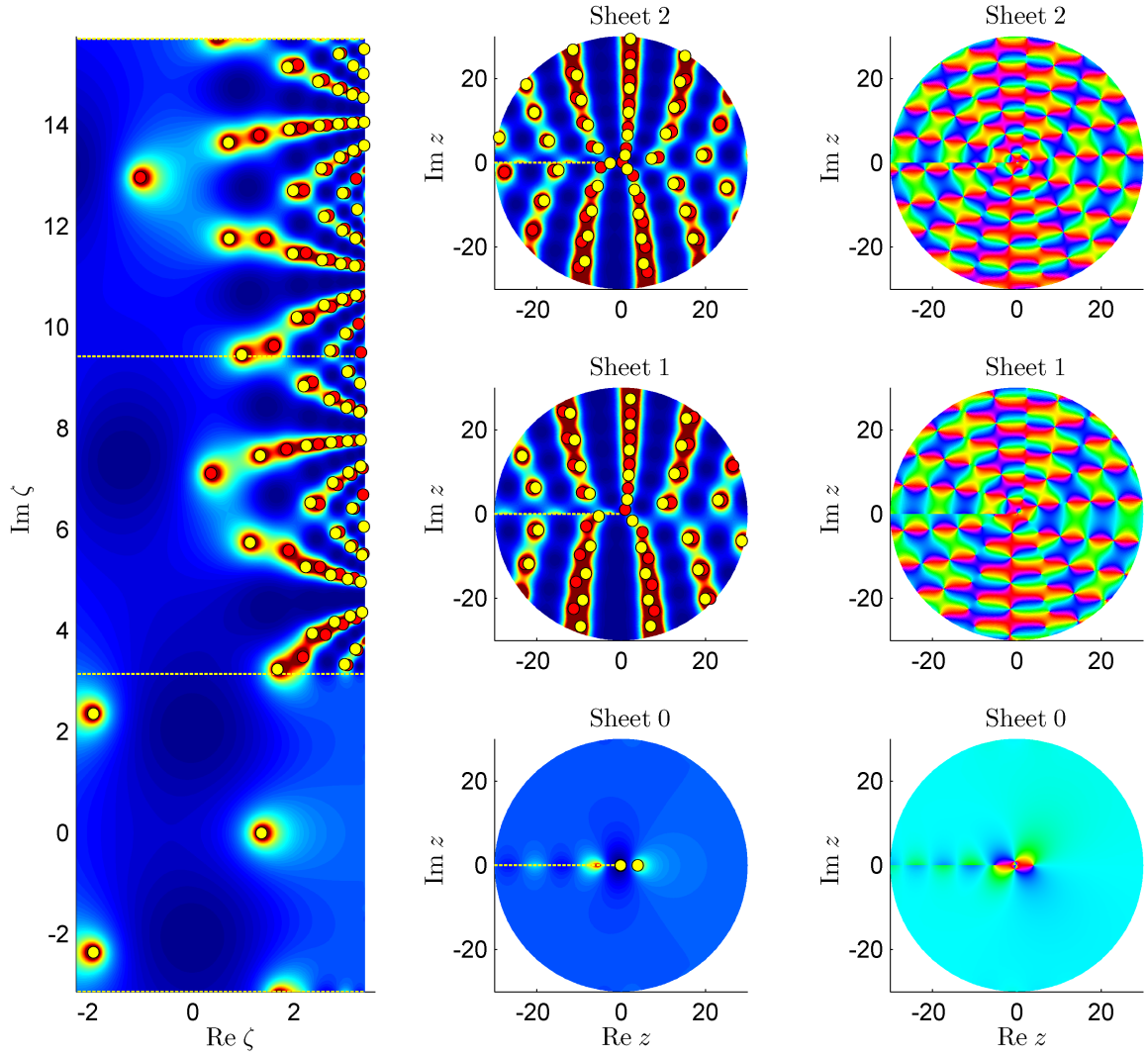

Figure 3.4: A tronquée P_V solution in the ζ and z planes with parameters $(\alpha, \beta, \gamma, \delta) = (1, 0, 1/4, -1/2)$ and ICs $u(30) = -1.05294551349665$ and $u'(30) = 2.47019460566845\text{e-}3$ in the z-plane. The third column is a phase portrait of the solution shown in the second column. The symmetry-based error estimates for the solution on sheets 0–2 are 3e-10, 7e-7 and 1e-6, respectively.

and +2, respectively. According to Table 3.4, all the zeros of the solution have double multiplicity. They can be identified on the phase portraits in the third column as points around which each colour is assumed twice in the order indicated by the colour wheel above Figure 3.3 (red→yellow→green etc. for a counterclockwise traversal around the point).

It is shown in Proposition 2 of [9] that for a given set of parameters $\alpha, \beta, \gamma, \delta$ with $\delta \neq 0$, there is a unique tronquée $\mathrm{P_V}$ solution with

$$u(z) \sim -1 + \sum_{n=1}^{\infty} a_n z^{-n}, \qquad z \to \infty, \qquad -\pi < \arg z < \pi, \tag{3.4}$$

where the coefficients a_n are obtained by substitution into the $\mathrm{P_V}$ equation. Up to numerical error, the solution in Figure 3.4 is an example of such a tronquée solution. Its ICs were obtained by evaluating the (optimally truncated) expansion (3.4) far out on the positive real axis and the pole-free sector of the solution evidently corresponds to the region indicated in (3.4). From the first column of Figure 3.4 we observe that there are three poles on sheet 0 of the solution. Thus, in contrast to the solutions in Figures 3.3 and 3.5, the tronquée solution in Figure 3.4 does not contain a sector that is pole-free for all finite z.

3.3.2 A tronquée $\mathrm{P_{III}}$ solution

The first and second columns of Figure 3.5 show a tronquée $\mathrm{P_{III}}$ solution that is pole-free on the region $-3\pi/4 < \arg z < 9\pi/4$ (column 1), which in the ζ-plane corresponds to the region $-3\pi/2 < \operatorname{Im} \zeta < 9\pi/2$ (column 2). In the z-plane the asymptotic behaviour of the solution on the pole-free region is $u \sim \sqrt[3]{z}$, $z \to \infty$, which in the ζ-plane is equivalent to $u \sim (e^{\zeta/2})^{1/3} = e^{\zeta/6}$, $\operatorname{Re} \zeta \to +\infty$. This solution is an example of the following set of tronquée $\mathrm{P_{III}}$ solutions, the existence of which is proved in [54]: for $\gamma = 0$, $\alpha = 1 = -\delta$, β arbitrary and any of the branches of $z^{1/3}$, there is a unique tronquée $\mathrm{P_{III}}$ solution with the behaviour $u \sim z^{1/3}$, $z \to \infty$ on a certain region with angular width 3π.

As discussed in [32], the accurate computation of the solution of a Painlevé equation on a pole-free region requires that it be solved as a boundary value problem (BVP) on that region. For the tronquée solutions in Figures 3.2 and 3.4, we achieved satisfactory accuracy without the use of a BVP solver. However, the tronquée solution in Figure 3.5 has a much larger pole-free sector, and thus a BVP solver greatly improves the accuracy of the solution. Indeed, if the enhanced PFS method is used without a BVP solver to compute the tronquée $\mathrm{P_{III}}$ solution, then

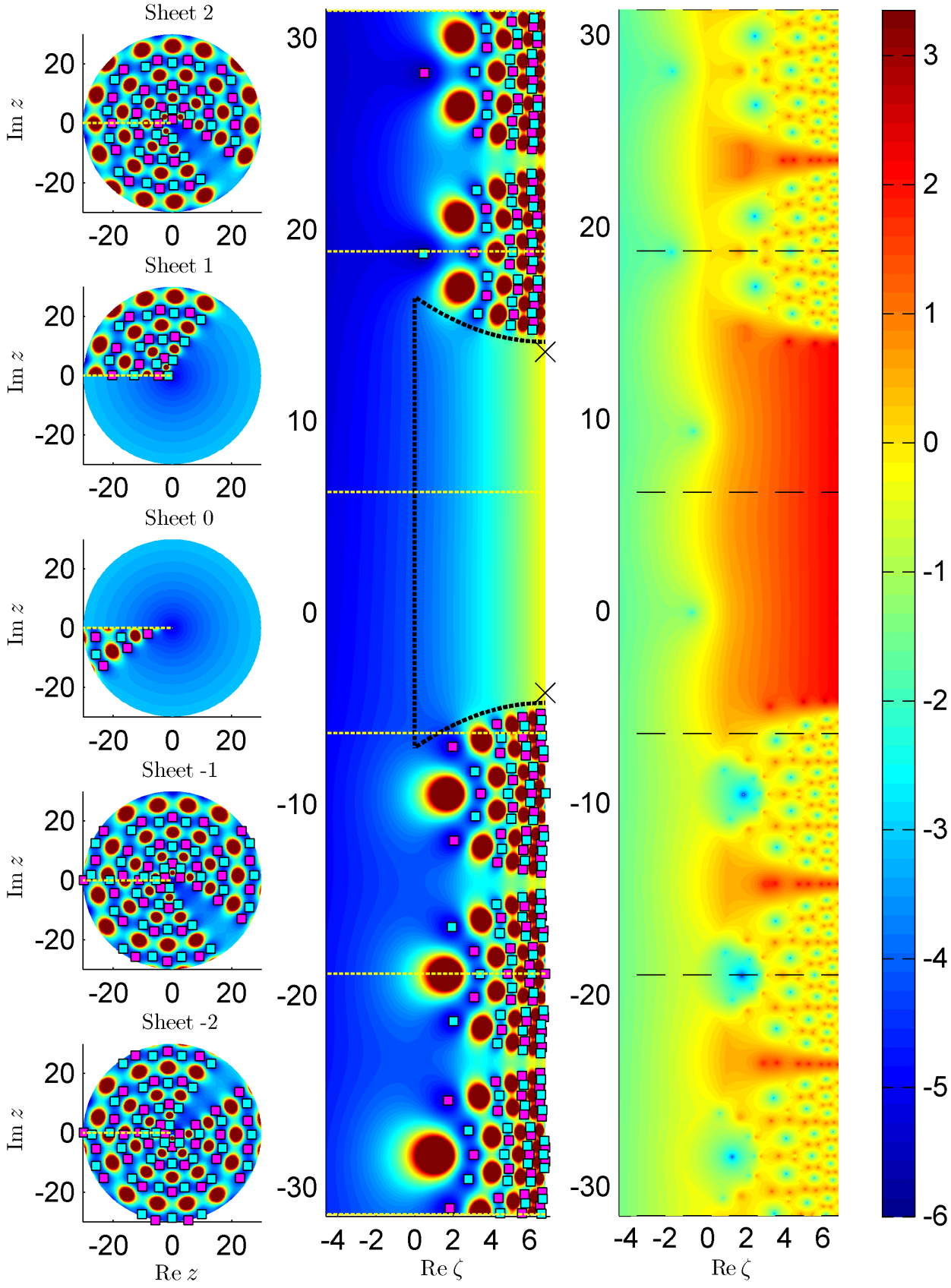

Figure 3.5: A tronquée $\mathrm{P_{III}}$ solution (left) and a contour plot of $\log_{10}(\min\{\kappa_r, \kappa_a\})$, where κ_r is defined in (3.7) and $\kappa_a = \kappa_r|\widetilde{w}''|$; κ_r and κ_a are interpreted as relative and absolute condition numbers of the $\widetilde{\mathrm{P}}_{\mathrm{III}}$ equation, indicating its sensitivity to numerical errors. This solution has parameters $(\alpha, \beta, \gamma, \delta) = (1, -1/20, 0, -1)$ and its ICs in the z-plane are given in (3.6). The error estimates for the solution on each of the strips, indicated by the dashed horizontal lines, are, from bottom to top: 4e-6, 3e-7, 2e-8, 3e-9, 4e-8.

the error is on the order of 10^{-1}. If we use a BVP solver, then we achieve the much smaller errors reported in the caption of Figure 3.5. We now describe how we used a BVP solver to compute the tronquée $\mathrm{P_{III}}$ solution, how the error of the computed solution was estimated and why the PFS method is unstable on the smooth region.

According to Theorem 2 and equation (3.13) of [54], in the z-plane the tronquée solution in Figure 3.5 satisfies

$$u \sim \sqrt[3]{z}\left[1+\sum_{n=1}^{\infty} a_n (\sqrt[3]{z})^{-2n}\right], \qquad z\to\infty, \qquad -\frac{3\pi}{4} < \arg z < \frac{9\pi}{4}. \tag{3.5}$$

Substituting this expansion into the $\mathrm{P_{III}}$ equation, generating the coefficients a_n recursively and evaluating the optimally truncated expansion (and its derivative) at two points close to the boundary of the pole-free sector at $\arg z = -3\pi/4$ and $\arg z = 9\pi/4$, we find that

$$\begin{aligned}
&z_1 = 30e^{9\pi i/4 - i\pi/12}, && z_2 = 30e^{-3\pi i/4 + i\pi/12},\\
&u(z_1) = -2.000735432319 + 2.376177147900i, && u(z_2) = 2.384379236170 - 1.993845650158i,\\
&u'(z_1) = -5.939523100\text{e-}3 + 3.402038641\text{e-}2i, && u'(z_2) = 6.050817704\text{e-}3 + 3.398020750\text{e-}2i,
\end{aligned} \tag{3.6}$$

for the parameter values given in the caption of Figure 3.5. We translate these ICs at z_1 and z_2 to ICs for the $\widetilde{\mathrm{P}}_{\mathrm{III}}$ equation at the corresponding points in the ζ-plane: the two points indicated by crosses in the second column of Figure 3.5. The enhanced PFS method is launched from these points to compute the solution everywhere on the rectangular domain except on the region inscribed on the pole-free sector in the second column. The solution values computed on the two curved boundaries of the inscribed region are used as boundary conditions for the BVP solver that is used to compute the solution on the pole-free sector. As in [32], we use the DMSUITE package [89] to implement a Chebyshev spectral collocation method as BVP solver.

We estimate the error on the pole-free region (computed with the BVP solver) and on the rest of the domain (computed with the enhanced PFS method) using different methods. The error of the PFS-computed solution in Figure 3.5 cannot be estimated using the symmetry-based method discussed in section 3.1.2 since the solution does not have the up-down symmetry in the ζ-plane. Instead, we use the following method. Recall from section 2.3 that the PFS method selects the target nodes in Stage 1 in a random order. Hence, if we compute the same solution twice, different paths will be run in Stage 1, resulting in solutions that should differ by approximately the numerical error. We therefore use the relative difference between two

independently calculated solutions as an error estimate. The error of the solution computed by the BVP solver can be estimated using the method discussed in [32]: by measuring the difference between the derivative values of the PFS-computed solution and the BVP solver-computed solution at the boundaries. We increase the number of collocation points of the BVP solver until the derivative values match to the desired accuracy. We also use the difference between BVP solver-computed solutions with different numbers of collocation points as an error estimate. For the solution in Figure 3.5, we increased the number of collocation points until error estimates for the BVP solver-computed solution were smaller than the error estimate for the PFS-computed solution.

The instability of the computation of $\widetilde{\mathrm{P}}_{\mathrm{III}}$ solutions as initial-value problems on pole-free regions can be demonstrated as follows[1]. Let the exact solution to the $\widetilde{\mathrm{P}}_{\mathrm{III}}$ equation be w and let $\widetilde{w}$ be the approximate (numerical) solution. Let $w(\zeta) \approx \widetilde{w}(\zeta) + \epsilon$, where ϵ is constant. Making these substitutions in the $\widetilde{\mathrm{P}}_{\mathrm{III}}$ equation, we find that

$$\begin{aligned} \left|\frac{w'' - \widetilde{w}''}{\widetilde{w}''}\right| &\approx \left|\frac{1}{\widetilde{w}''}\left[-\frac{(\widetilde{w}')^2}{\widetilde{w}} + \frac{1}{4}\left(2\alpha\widetilde{w}^2 + 3\gamma\widetilde{w}^3 - \frac{\delta e^{2\zeta}}{\widetilde{w}}\right)\right]\right| \left|\frac{\epsilon}{\widetilde{w}}\right| + \mathcal{O}\left(\epsilon^2\right) \\ &:= \kappa_r \left|\frac{\epsilon}{\widetilde{w}}\right| + \mathcal{O}\left(\epsilon^2\right), \ \kappa_r = \left|\frac{1}{\widetilde{w}''}\left[-\frac{(\widetilde{w}')^2}{\widetilde{w}} + \frac{1}{4}\left(2\alpha\widetilde{w}^2 + 3\gamma\widetilde{w}^3 - \frac{\delta e^{2\zeta}}{\widetilde{w}}\right)\right]\right|. \end{aligned} \tag{3.7}$$

Thus, we interpret κ_r as a 'relative condition number' of the $\widetilde{\mathrm{P}}_{\mathrm{III}}$ equation. It gives the approximate factor with which the relative error of the solution ($|\epsilon/\widetilde{w}|$) is amplified to give the relative error in the evaluation of the right-hand side of the $\widetilde{\mathrm{P}}_{\mathrm{III}}$ equation ($|w'' - \widetilde{w}''|/|\widetilde{w}|$). Since the $\widetilde{\mathrm{P}}_{\mathrm{III}}$ equation is used to generate the Taylor coefficients that are converted to Padé coefficients in the PFS method, we expect the error of the PFS-computed solution to grow rapidly on regions where κ_r is large. That is, we expect the PFS method to be unstable where κ_r is large. On the pole-free sector of the solution in the second column of Figure 3.5, $\widetilde{w} \approx w = e^{\zeta/2}u \sim e^{\zeta/2}e^{\zeta/6} = e^{2\zeta/3}$, $\mathrm{Re}\ \zeta \to +\infty$, in which case κ_r simplifies to

$$\kappa_r \sim \frac{27}{16} e^{2\mathrm{Re}\ \zeta/3}, \qquad \mathrm{Re}\ \zeta \to +\infty,$$

for the parameter values of the solution in Figure 3.5. This shows that computation on the smooth region is exponentially unstable. For the $\mathrm{P}_{\mathrm{III}}$ solution in Figure 3.5, $\mathrm{Re}\ \zeta \leq 2\log 30$ and thus the maximum value of κ is approximately $27/16(30)^{4/3} \approx 157$. By contrast, the equation

[1] Although we only consider this instability for the $\widetilde{\mathrm{P}}_{\mathrm{III}}$ equation, it is also present in the computation of $\mathrm{P}_{\mathrm{III}}$ solutions in the z-plane. Recall that we obtain $\mathrm{P}_{\mathrm{III}}$ solutions u by computing $\widetilde{\mathrm{P}}_{\mathrm{III}}$ solutions w (with $w = e^{\zeta/2}u$).

is well-conditioned in the neighbourhood of a pole or zero. For the solution in Figure 3.5, the behaviour in the neighbourhood of a pole at ζ_0 is (see Table 3.5) $\widetilde{w} \approx w = e^{\zeta/2}u \sim e^{\zeta_0/2}c_{-2}(\zeta-\zeta_0)^{-2}$. Similarly, in the neighbourhood of a zero, $\widetilde{w} \approx w = e^{\zeta/2}u \sim e^{\zeta_0/2}c_1(\zeta-\zeta_0)$. For the parameter values of the solution in Figure 3.5, κ_r and the absolute condition number, $\kappa_a = \kappa_r|\widetilde{w}''|$, simplify to

$$\kappa_r \sim \frac{e^{2\text{Re }\zeta_0}}{1536}|\zeta-\zeta_0|^6 \qquad \text{and} \qquad \kappa_a \sim \frac{e^{2\text{Re }\zeta_0}}{32}|\zeta-\zeta_0|^2, \qquad \zeta \to \zeta_0,$$

in the neighbourhood of a pole and

$$\kappa_r \sim 10e^{2\text{Re }\zeta_0}|\zeta-\zeta_0|^2 \qquad \text{and} \qquad \kappa_a \sim \frac{e^{2\text{Re }\zeta_0}}{8}|\zeta-\zeta_0|^2, \qquad \zeta \to \zeta_0,$$

in the neighbourhood of a zero. The third column of Figure 3.5 shows a plot of the condition number for the tronquée P_{III} solution. The plot clearly shows the exponential increase of the condition number on the pole-free region with Re ζ as well as the comparatively well-conditioned nature of the pole fields. However, we also observe isolated points inside and between the pole fields with large condition numbers. These are the points at which the second derivative is small.

Table 3.5: The poles and zeros of the solution in Figure 3.5.

		Poles	Zeros	
P_{III}, $\gamma = 0$, $\alpha\delta \neq 0$	z-plane	$c_{-2} = 2/\alpha$	$c_1 = +\sqrt{-\delta}/2$	■
			$c_1 = -\sqrt{-\delta}/2$	■
	ζ-plane	$c_{-2} = 8e^{-\zeta_0/2}/\alpha$	$c_1 = +e^{\zeta_0/2}\sqrt{-\delta}/2$	■
			$c_1 = -e^{\zeta_0/2}\sqrt{-\delta}/2$	■

As we shall find in section 4.1, for the P_{III} equation with $\gamma = 0$ and $\alpha\delta \neq 0$, one can set $\alpha = 1 = -\delta$ without loss of generality, an equation which we denote by $\text{P}_{\text{III}}^{(\text{ii})}$. The solution in Figure 3.5 is a $\text{P}_{\text{III}}^{(\text{ii})}$ solution. As the expansion (3.5) in powers of $\sqrt[3]{z}$ suggests, it may be convenient to let $z = \tau^3$ and $u(z) = y(\tau)$ in $\text{P}_{\text{III}}^{(\text{ii})}$. The resulting equation, which we denote by $\text{P}_{\text{III}}^{(7)}$, as in [15], is given by

$$\text{P}_{\text{III}}^{(7)}: \qquad \frac{d^2y}{d\tau^2} = \frac{1}{y}\left(\frac{dy}{d\tau}\right)^2 - \frac{1}{\tau}\frac{dy}{d\tau} + 9\tau(y^2+\beta) - \frac{9\tau^4}{y},$$

and has been the subject of numerous studies (see the references in [15]). Roughly speaking, the main difference between the solutions of $\mathrm{P}_{\mathrm{III}}^{(\mathrm{ii})}$ and $\mathrm{P}_{\mathrm{III}}^{(7)}$ is that every three sheets of the Riemann surface of a $\mathrm{P}_{\mathrm{III}}^{(\mathrm{ii})}$ solution are 'rolled up' into one sheet of the Riemann surface of a $\mathrm{P}_{\mathrm{III}}^{(7)}$ solution. However, the solutions to both equations generally have a branch point at the origin since each has a fixed singularity at the origin. Therefore, for the same reasons given below Table 3.1, we have found that, compared to the ζ-plane method used in Figure 3.5, there is no advantage to computing the solution to $\mathrm{P}_{\mathrm{III}}^{(7)}$ in the τ-plane.

3.3.3 Generic $\mathrm{P_V}$ and $\mathrm{P_{VI}}$ solutions

We close with $\mathrm{P_V}$ and $\mathrm{P_{VI}}$ solutions in Figures 3.6 and 3.7, respectively. These solutions were computed by applying the enhanced PFS method to the $\widetilde{\mathrm{P}}_{\mathrm{V}}$ equation and the transformed $\mathrm{P_{VI}}$ equation (3.3). It follows from Table 3.3 that for a $\mathrm{P_{VI}}$ solution with a pole at z_0, where $|z_0| > 1$, the residue of the pole in the z-plane is larger than the corresponding residues in the η and ζ planes by a factor of at least $|z_0|$. We therefore found it necessary to plot $\log_{10}|u|$ in the z-plane in Figure 3.7 (column 3), instead of $|u|$, which is what we plot in the η and ζ planes (columns 1 and 2, respectively).

The generic solutions in Figures 3.6 and 3.7 and the generic $\mathrm{P_{III}}$ solution in the third column of Figure 3.1 share a common feature: they have poles and zeros along oblique lines in the transformed planes. These sloping lines of poles and zeros are mapped to spirals in z-plane (for the $\mathrm{P_{III}}$ and $\mathrm{P_V}$ solutions) or ζ-plane (for the $\mathrm{P_{VI}}$ solution). As we remarked above, spirals of poles and zeros were not observed in the single-valued Painlevé transcendents in [32–34,77,78].

Table 3.6: The poles and zeros of the solutions in Figures 3.6 and 3.7.

			Poles		Zeros	
Figure 3.6	$\mathrm{P_V}$, $\alpha\beta \neq 0$	z-plane	$c_{-1} = +z_0/\sqrt{2\alpha}$	●	$c_1 = +\sqrt{-2\beta}/z_0$	■
			$c_{-1} = -z_0/\sqrt{2\alpha}$	●	$c_1 = -\sqrt{-2\beta}/z_0$	■
		ζ-plane	$c_{-1} = +1/\sqrt{2\alpha}$	●	$c_1 = +\sqrt{-2\beta}$	■
			$c_{-1} = -1/\sqrt{2\alpha}$	●	$c_1 = -\sqrt{-2\beta}$	■
Figure 3.7	$\mathrm{P_{VI}}$, $\alpha\beta \neq 0$	η, ζ and z planes	See Table 3.3			

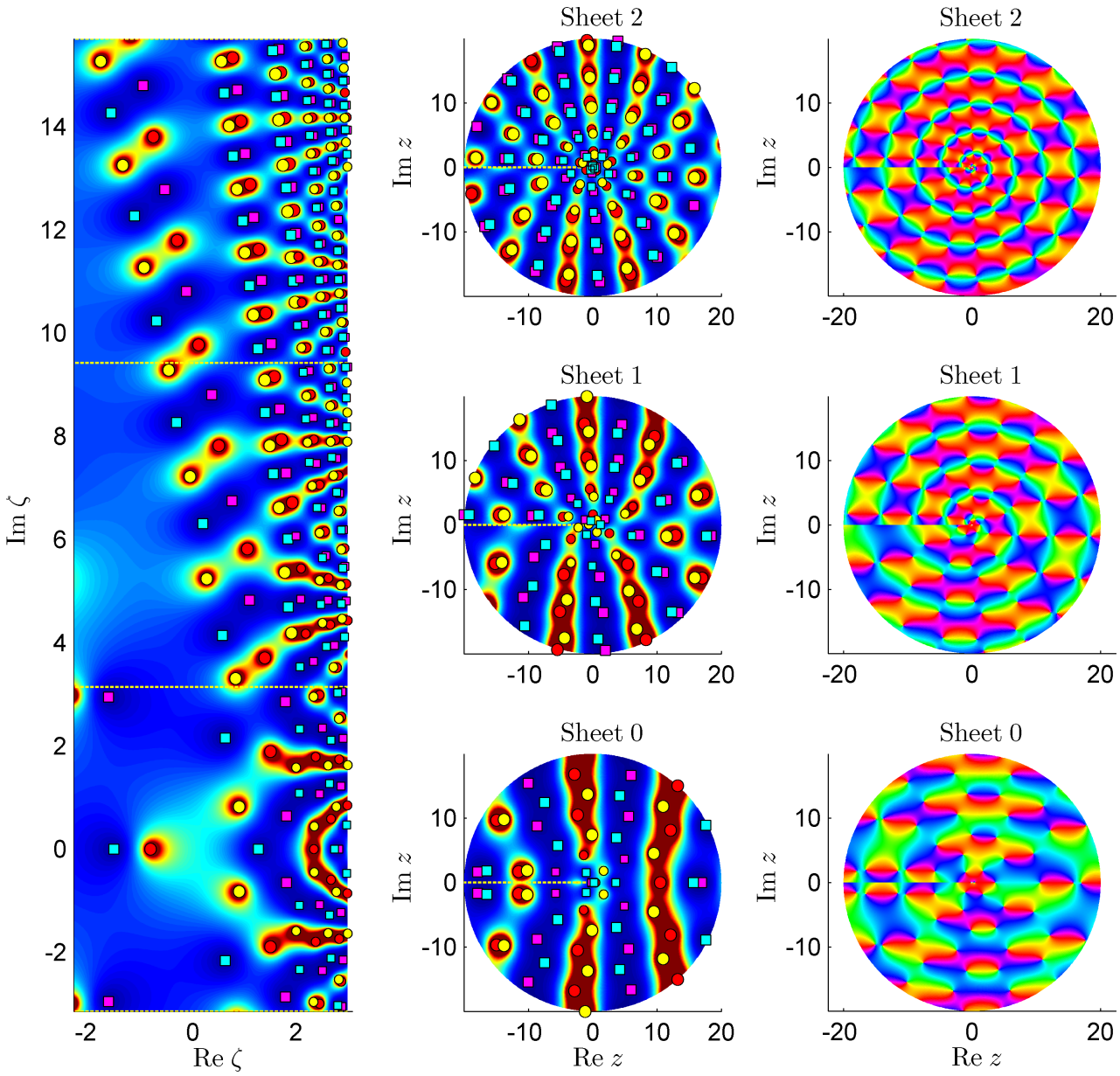

Figure 3.6: A generic P_V solution in the ζ and z planes ($z = e^{\zeta}$). The solution has parameter values $(\alpha, \beta, \gamma, \delta) = (1, -1, 1, -1/2)$ and ICs $z_0 = 1$, $u(z_0) = 2$ and $u'(z_0) = -1$. The error estimates for the solution on sheets 0–2 are 3e-9, 7e-6 and 2e-5, respectively.

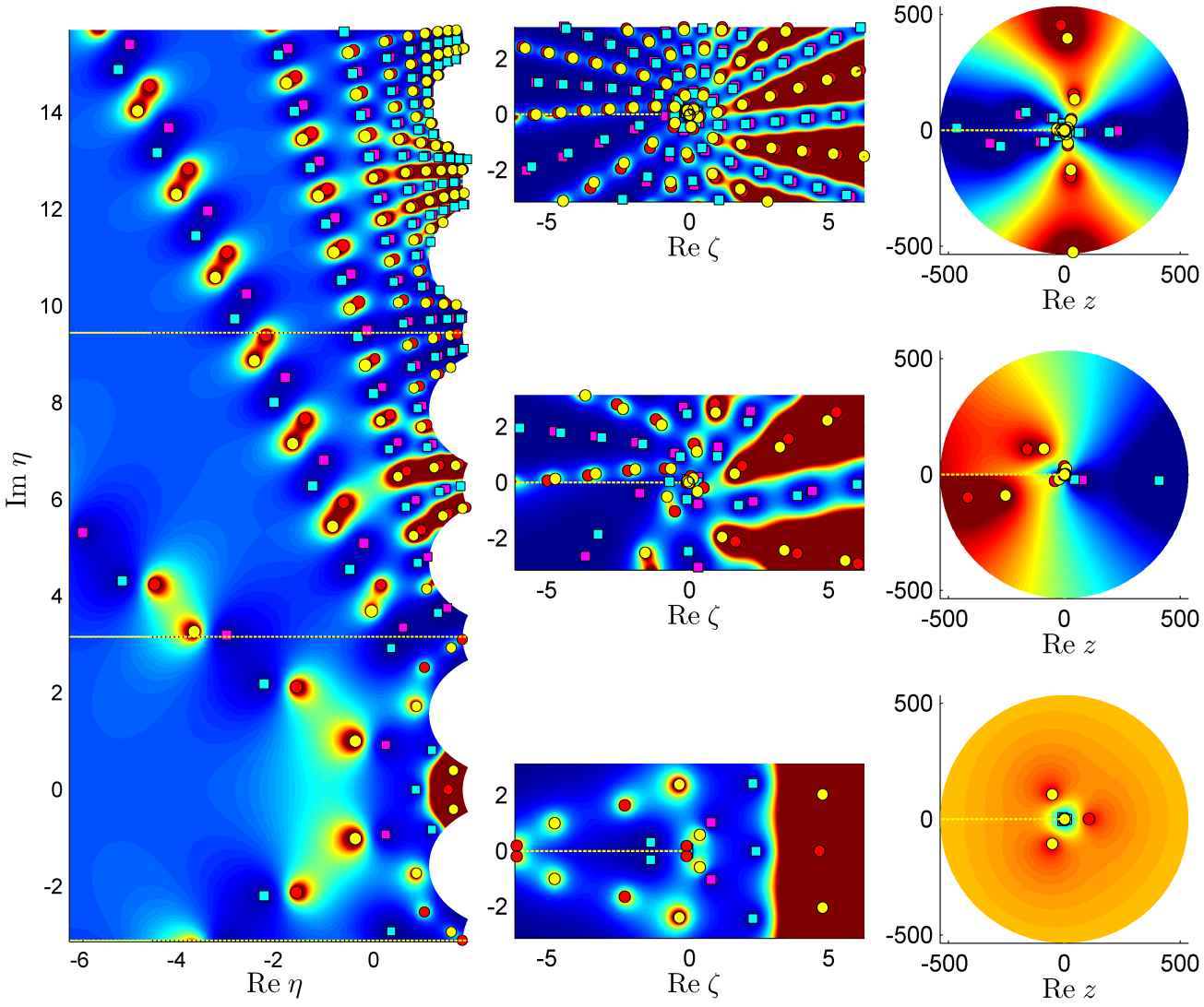

Figure 3.7: A generic P_{VI} solution in the η, ζ and z planes ($\zeta = e^{\eta}$, $z = e^{\zeta}$). The solution has parameters $(\alpha, \beta, \gamma, \delta) = (1, -1, 3/4, -3/2)$ and ICs $z_0 = 2$, $u(z_0) = 3/2$ and $u'(2) = -1$. The error estimates for the solution on the strips indicated in the η-plane are, from bottom to top: 5e-8, 4e-4 and 8e-4.

3.4 Conclusions

We have presented (here and in [27]) the first numerical method for computing multivalued P_{III}, P_V and P_{VI} solutions on multiple sheets of their Riemann surfaces. In the process we have displayed pole field patterns of generic and tronquée solutions to P_{III} and P_V, solutions that had been studied only theoretically before. We also displayed a generic P_{VI} solution as well as what appears to be a tronquée P_{VI} solution, which seems not to have been proposed in the literature as yet. In short, our numerical experiments have agreed with theory, offered finer detail, and yielded hypotheses for theory to confirm.

We extended the capabilities of the PFS method for the single-valued Painlevé transcendents. In particular, the enhanced PFS method can compute highly non-uniform pole fields accurately and efficiently and it can move onto the desired sheets of the Riemann surfaces of the multivalued Painlevé transcendents by following appropriate paths around the branch points.

The methods we have presented in this chapter are applicable to any ODE that possesses the Painlevé property. Our methods could be used to explore ODEs that do not possess the Painlevé property if they are used in conjunction with methods for singularity detection, see [17, 43, 83], so that movable branch points can be identified. However, our methods are not applicable beyond natural boundaries, which are closed curves in the complex plane beyond which the solution cannot be analytically continued. The Chazy equation is a well-known example of an ODE whose solutions have such a movable natural boundary.

Chapter 4

Tronquée solutions of $\mathrm{P}_{\mathrm{III}}^{(\mathrm{i})}$

In this chapter and the next we shift our attention from the computation of the multivalued Painlevé transcendents to the (computationally-aided) study of a class of solutions of $\mathrm{P}_{\mathrm{III}}$. We recapitulate some basic facts regarding $\mathrm{P}_{\mathrm{III}}$ solutions. The origin is the only point in the finite plane where a branch point of a $\mathrm{P}_{\mathrm{III}}$ solution can occur. Solutions of $\mathrm{P}_{\mathrm{III}}$ may have any number of distinct Riemann sheets: we shall encounter algebraically branched solutions with any finite number of distinct sheets (including single-valued solutions) as well as solutions that have infinitely many distinct sheets (logarithmically branched solutions). In all these cases the $\mathrm{P}_{\mathrm{III}}$ solution is meromorphic on each Riemann sheet, which is a covering of the punctured plane.

The $\mathrm{P}_{\mathrm{III}}$ equation has a vast solution space, represented by $\mathbb{C}^6$, since the equation has four arbitrary complex parameters (see section 1.1) and two free initial conditions. Nevertheless, we shall find that the equation possesses certain symmetries that justify the consideration of restricted parts of separate two-dimensional and one-dimensional parameter spaces.

This chapter and the next are devoted to the study of certain tronquée solutions of $\mathrm{P}_{\mathrm{III}}$. Hence we also recall some of their properties and motivate their selection, out of the vast solution space of $\mathrm{P}_{\mathrm{III}}$, as a class of solutions to be explored by the enhanced PFS method.

The solutions of the Painlevé equations typically have poles all over their domains, as we found in the plots of the generic solutions in the previous chapter (Figures 3.1, 3.6 and 3.7). Solutions that contain pole-free sectors are therefore atypical and were identified as early as 1913 by Boutroux [14] who called them tronquée (truncated) solutions. Tronquée solutions are defined by generally divergent asymptotic expansions near infinity in certain sectors. We have

seen examples of tronquée solutions and their asymptotic expansions in Figures 3.4 and 3.5 and equations (3.4) and (3.5). Tronquée solutions of P_I–P_V and related equations have been studied recently [9, 21, 46–49, 54, 81] and the numerical evidence we presented in section 3.2 suggests that tronquée solutions of P_{VI} also exist.

We shall see that tronquée P_{III} solutions fall into a broad category of solutions that includes rational and particular special function solutions (for which closed-form expressions are available) as special cases. Tronquée solutions can be thought of as lying between generic and closed-form solutions on a spectrum of available analytical information: Prior to the computation of a generic solution of a Painlevé equation, only the parameter values and initial conditions at a point are known; for a tronquée solution it is known that an asymptotic expansion is satisfied near infinity on a sector in the complex plane while for a closed-form solution exact information is known on the entire complex plane. Hence, computation reveals more new information about generic solutions than about tronquée solutions but tronquée solutions are more amenable to analysis than generic solutions since more information is available.

The PFS is particularly effective in elucidating the properties of tronquée solutions in the finite plane, a region about which the asymptotic expansions give limited or no information. For example, based on the pole field plots in [32], it was conjectured in [24] and later proved in [19] that the unique tritronquée solution of P_I[1] is pole-free in the full sector $\arg z \in [-\frac{3\pi}{5}, \pi]$ and the disk $|z| < 37/20$. In the next chapter we shall use the enhanced PFS method to study tronquée solutions of P_{III} in the finite plane on multiple sheets and in the process discover and then analyse additional pole-free sectors that have not been identified before. We hope to illustrate in this chapter and the next that a computational approach aids and complements the analysis of tronquée solutions.

As pointed out in [54], there are two main directions of research on the asymptotic properties of the Painlevé transcendents. The one avenue is the study of their asymptotics in the complex plane, where tronquée solutions are of particular interest since they satisfy asymptotic expansions near infinity on certain sectors in the complex plane. The other avenue of research concerns the study of asymptotic connection formulae, which relate the solution at two endpoints of an interval (see, for example, [10, 22, 44, 51, 52, 58, 59]). In the next chapter we combine

[1] It is shown in [24] that this solution is related to the critical behaviour of the nonlinear Schrödinger equation.

the two directions of asymptotic research when we make use of connection formulae for a set of tronquée solutions of $\mathrm{P_{III}}$ (that relate solutions at 0 and at $+\infty$ on the real axis) for numerical computation and for the proof of certain properties of the tronquée solutions. As pointed out in section 1.1, the connection formulae we shall use occupy an eminent position in the history of the Painlevé equations and are also notable for their appearance in the 2D Ising model. It is to be expected that if a solution of a Painlevé equation describes a nonlinear physical phenomenon, it should be in the form of a tronquée solution since physical phenomena are more likely to be described by smooth solutions than by solutions with poles.

To summarize, we regard tronquée solutions of the Painlevé equations as interesting and worthy of computationally-aided study because of their atypical pole-free sectors, their known asymptotic expansions which facilitate their analysis, their special, closed-form cases and their likely appearance in applications.

4.1 Bäcklund transformations and two canonical cases of $\mathrm{P_{III}}$

Let $u(z;\alpha,\beta,\gamma,\delta)$ denote a solution of $\mathrm{P_{III}}$. The following Bäcklund transformations relate $\mathrm{P_{III}}$ solutions with (generally) different parameter values [36, p. 150]:

$$T_0(c_1,c_2): \qquad u(z;\widetilde{\alpha},\widetilde{\beta},\widetilde{\gamma},\widetilde{\delta}) = c_1^{-1}u(c_2z;\alpha,\beta,\gamma,\delta), \tag{4.1}$$

$$\widetilde{\alpha} = c_1c_2\alpha, \qquad \widetilde{\beta} = c_1^{-1}c_2\beta, \qquad \widetilde{\gamma} = c_1^2c_2^2\gamma, \qquad \widetilde{\delta} = c_1^{-2}c_2^2\delta, \tag{4.2}$$

$$R: \qquad u(z;-\beta,-\alpha,-\delta,-\gamma) = \left[u(z;\alpha,\beta,\gamma,\delta)\right]^{-1}, \tag{4.3}$$

$$S: \qquad u\Big(\frac{z^2}{2},\gamma,\delta,0,0\Big) = \left[u\left(z,0,0,\gamma,\delta\right)\right]^2. \tag{4.4}$$

These Bäcklund transformations lend themselves to the consideration of the following cases of $\mathrm{P_{III}}$:

(i) $\gamma\delta \neq 0$,

(ii) $\gamma = 0$, $\alpha\delta \neq 0$ or $\delta = 0$, $\beta\gamma \neq 0$,

(iii) $\gamma = \delta = 0$, $\alpha\beta \neq 0$,

(iv) $\alpha = \gamma = 0$ or $\beta = \delta = 0$.

The $\mathrm{P_{III}}$ equation is fully integrable in case (iv) [55]. For the sub-case $\beta = \delta = 0$ of case (iv), the general solution is [60]

$$u(z; 2a, 0, b^2 - 4ad, 0) = \frac{1}{z(a \ln^2 z + b \ln z + d)},$$

or (depending on the value of an arbitrary integration constant)

$$u(z; -\lambda^2 B, 0, \lambda^2 B - 4AD\lambda^2, 0) = \frac{z^{\lambda-1}}{Az^{2\lambda} + Bz^{\lambda} + D}.$$

The general solution for the sub-case $\alpha = \gamma = 0$ can be obtained by applying the reciprocal transformation R to these solutions, see (4.3). These general solutions illustrate the different types of branch points mentioned above: logarithmic and algebraic of any order. In the next chapter we shall find more examples of these types of branch points for solutions for which closed-form expressions are not available.

The transformation S in (4.4) relate solutions for the case (i) to the case (iii). The reciprocal transformation relate solutions between the sub-cases of case (ii). Hence, it suffices to consider case (i) and the sub-case $\gamma = 0$, $\alpha\delta \neq 0$ of case (ii). For these cases the scaling transformation $T_0(c_1, c_2)$ in (4.1)–(4.2) implies that, without loss of generality, we may set $\gamma = 1 = -\delta$ and $\alpha = 1 = -\delta$. We conclude that it is sufficient to consider two cases of $\mathrm{P_{III}}$:

- $\mathrm{P_{III}}$ with $\gamma = 1 = -\delta$, an equation denoted by $\mathrm{P_{III}^{(i)}}$, as in [54], and
- $\mathrm{P_{III}}$ with $\alpha = 1$, $\gamma = 0$, $\delta = -1$, an equation denoted by $\mathrm{P_{III}^{(ii)}}$.

Hence, in $\mathrm{P_{III}^{(i)}}$ the number of arbitrary parameters is reduced to two and $\mathrm{P_{III}^{(ii)}}$ only has one arbitrary parameter. Figures 3.1 and 3.5 are examples of solutions of $\mathrm{P_{III}^{(i)}}$ and $\mathrm{P_{III}^{(ii)}}$, respectively, and the poles and zeros admitted by these equations at $z \neq 0$ are given in Tables 3.1 and 3.5.

Necessary and sufficient conditions for the existence of $\mathrm{P_{III}}$ solutions with a pole at the origin are derived in [36, pp. 151–153]. Here we note that if $\mathrm{P_{III}}$ admits a pole at $z = 0$, then $\alpha\gamma \neq 0$ (hence $\mathrm{P_{III}^{(ii)}}$ does not admit a pole at $z = 0$) and the pole is simple with residue

$$c_{-1} = -\frac{\alpha}{\gamma}. \tag{4.5}$$

A consequence of this fact and the reciprocal transformation (4.3) is that if $\mathrm{P_{III}}$ has a zero at $z = 0$, then $\beta\delta \neq 0$ and the zero is simple with derivative value

$$c_1 = -\frac{\delta}{\beta}. \tag{4.6}$$

For the remainder of the thesis we study solutions of $\mathrm{P_{III}^{(i)}}$. Solutions of $\mathrm{P_{III}^{(ii)}}$ are discussed in section 6.2 in the context of possible future research projects.

4.2 Bäcklund transformations for $\mathrm{P}_{\mathrm{III}}^{(\mathrm{i})}$

Let $u(z;\alpha,\beta)$ denote a $\mathrm{P}_{\mathrm{III}}^{(\mathrm{i})}$ solution. It follows from (4.2) that for $\mathrm{P}_{\mathrm{III}}^{(\mathrm{i})}$ solutions to be closed under $T_0(c_1,c_2)$, i.e., for the conditions $\widetilde{\gamma}=\gamma=1$ and $\widetilde{\delta}=\delta=-1$ to be satisfied, we require that c_1 and c_2 each be a fourth root of unity, with either c_1 and c_2 both real or both imaginary. Hence, only the following scaling transformations need to be considered for $\mathrm{P}_{\mathrm{III}}^{(\mathrm{i})}$:

$$T_0(\pm1,\pm1): \qquad u(z;\alpha,\beta)=\pm u(\pm z;\alpha,\beta), \tag{4.7}$$

$$T_0(\pm1,\mp1): \qquad u(z;-\alpha,-\beta)=\pm u(\mp z;\alpha,\beta), \tag{4.8}$$

$$T_0(\pm i,\pm i): \qquad u(z;-\alpha,\beta)=\mp iu(\pm iz;\alpha,\beta), \tag{4.9}$$

$$T_0(\pm i,\mp i): \qquad u(z;\alpha,-\beta)=\mp iu(\mp iz;\alpha,\beta). \tag{4.10}$$

Transformations such as (4.7) that preserve parameter values are known as auto-Bäcklund transformations. Generally, auto-Bäcklund transformations relate *different* solutions with the same parameters. However, in section 5.6, when we study the properties of a set of multivalued $\mathrm{P}_{\mathrm{III}}^{(\mathrm{i})}$ solutions, we shall make extensive use of auto-Bäcklund transformations that relate the solution on different Riemann sheets of the *same* solution.

Solutions of $\mathrm{P}_{\mathrm{III}}^{(\mathrm{i})}$ are closed under R, see (4.3):

$$R: \qquad u(z;-\beta,-\alpha)=[u(z;\alpha,\beta)]^{-1}. \tag{4.11}$$

The following nontrivial Bäcklund transformations can also be used to generate solutions of $\mathrm{P}_{\mathrm{III}}^{(\mathrm{i})}$ [23, 29, 35]:

$$\mathcal{T}_1: \quad u(z,\alpha+2,\beta+2)=\frac{zu'+zu^2-\beta u-u+z}{u(zu'+zu^2+\alpha u+u+z)},$$

$$\mathcal{T}_2: \quad u(z,\alpha-2,\beta+2)=-\frac{zu'-zu^2-\beta u-u+z}{u(zu'-zu^2-\alpha u+u+z)}, \tag{4.12}$$

$$\mathcal{T}_3: \quad u(z,\alpha+2,\beta-2)=-\frac{zu'+zu^2+\beta u-u-z}{u(zu'+zu^2+\alpha u+u-z)}, \tag{4.13}$$

$$\mathcal{T}_4: \quad u(z,\alpha-2,\beta-2)=\frac{zu'-zu^2+\beta u-u-z}{u(zu'-zu^2-\alpha u+u-z)},$$

where $u:=u(z;\alpha,\beta)$ on the right-hand sides.

Figure 4.2, to which we shall frequently return, depicts the real parameter space of $\mathrm{P}_{\mathrm{III}}^{(\mathrm{i})}$. Here we mention that, in principle, the transformations (4.7)–(4.10), (4.11) and $\mathcal{T}_1$–$\mathcal{T}_4$ justify the consideration of only the parameter values in the shaded triangular region in Figure 4.2,

known as the fundamental domain, since, by translating the fundamental domain, these transformations can be used to cover the entire parameter space. However, since it is nontrivial to deduce the solution features of solutions that result from the application of $\mathcal{T}_1$–$\mathcal{T}_4$, we shall not make use of these transformations to reduce the number of solutions that we consider. Nevertheless, we shall use $\mathcal{T}_1$–$\mathcal{T}_4$ and their related transformations in sections 4.4.1, 4.5.2 and the next chapter to construct closed-form solutions or for asymptotic analysis. However, we shall use the scaling transformations (4.7)–(4.10) and the reciprocal transformation (4.11) to reduce the size of the region of the parameter space that we consider since their action upon solutions are straightforward to understand and visualize.

We shall require the following result on the action of the scaling transformation upon the poles and zeros of $\mathrm{P}_{\mathrm{III}}^{(\mathrm{i})}$ solutions. It follows from Table 3.1 that in the neighbourhood of a pole or zero of $\mathrm{P}_{\mathrm{III}}^{(\mathrm{i})}$ at $z_0 \neq 0$, $u(z;\alpha,\beta) \sim \varepsilon/(z-z_0)$ or $u(z;\alpha,\beta) \sim \varepsilon(z-z_0)$, $\varepsilon^2=1$, for $z \to z_0$. Then, for the transformed solution,

$$u(z;\widetilde{\alpha},\widetilde{\beta}) = T_0(c_1,c_2)u(z;\alpha,\beta) \sim \frac{\varepsilon c_1^{-1}c_2^{-1}}{z-c_2^{-1}z_0}, \qquad z \to c_2^{-1}z_0, \tag{4.14}$$

or

$$u(z;\widetilde{\alpha},\widetilde{\beta}) = T_0(c_1,c_2)u(z;\alpha,\beta) \sim \varepsilon c_1^{-1}c_2(z-c_2^{-1}z_0), \qquad z \to c_2^{-1}z_0, \tag{4.15}$$

where (c_1,c_2) denotes any of the ordered pairs on the left-hand sides of (4.7)–(4.10). Hence, $T_0(c_1,c_2)$ transforms a pole (or zero) of $u(z;\alpha,\beta)$ at z_0 to a pole (or zero) of $u(z;\widetilde{\alpha},\widetilde{\beta})$ at $c_2^{-1}z_0$ whose residue (or derivative value) is of the same or opposite sign, depending on the values of c_1 and c_2 in (4.7)–(4.10).

4.3 The LDT tronquée solutions of $\mathrm{P}_{\mathrm{III}}^{(\mathrm{i})}$

The existence and uniqueness of tronquée solutions of $\mathrm{P}_{\mathrm{III}}^{(\mathrm{i})}$, $\mathrm{P}_{\mathrm{III}}^{(\mathrm{ii})}$ and P_{IV} were recently proved for the first time by Lin, Dai and Tibboel in [54]. We adumbrate their proof for $\mathrm{P}_{\mathrm{III}}^{(\mathrm{i})}$ in this section. The proofs in [54], and also the earlier proofs of the existence and uniqueness of tronquée solutions of P_{I} [47] and P_{II}-related equations [48], are based on a result of Wasow [87, Theorem 12.1], which is stated below in Theorem 1 and also in [54, Theorem 4]. It is remarked in [54] that compared to other methods of proving the existence of tronquée solutions, e.g., the isomonodromy deformation method used for P_{V} in [9], the method based on Wasow's

theorem is simpler. Prompted by the numerical evidence for tronquée $\mathrm{P_{VI}}$ solutions presented in section 3.2, we applied Wasow's theorem to $\mathrm{P_{VI}}$. However, as we shall demonstrate in this section, we were unable to prove the existence of tronquée $\mathrm{P_{VI}}$ solutions because we could not find a formulation of $\mathrm{P_{VI}}$ that satisfies all the conditions of Wasow's theorem.

Theorem 1. Wasow's theorem [87, Theorem 12.1]

Let S be an open sector in the complex plane with vertex at the origin and a positive central angle not exceeding $\pi/(q+1)$, where q is a nonnegative integer. Let the N-dimensional vector function $\boldsymbol{f}(z,\boldsymbol{w}) : \mathbb{C}\times\mathbb{C}^N \to \mathbb{C}^N$ have the following properties.

(1) $\boldsymbol{f}(z,\boldsymbol{w})$ is a polynomial in the components w_j of $\boldsymbol{w}$, $j = 1,\dots,N$, with coefficients that are holomorphic in z in the region $0 < z_0 \le |z| < \infty$, $z \in S$, where z_0 is a constant.

(2) The coefficients of the polynomial $\boldsymbol{f}(z,\boldsymbol{w})$ have asymptotic series in powers of z^{-1}, as $z \to \infty$, in S.

(3) If $f_j(z,\boldsymbol{w})$ denotes the components of $\boldsymbol{f}(z,\boldsymbol{w})$ then all the eigenvalues λ_j, $j = 1,2,\dots,N$ of the Jacobian matrix

$$\left\{ \lim_{z\to\infty, z\in S} \left(\frac{\partial f_j}{\partial w_k}\Big|_{\boldsymbol{w}=\boldsymbol{0}} \right) \right\}, \tag{4.16}$$

are different from zero.

(4) The differential equation

$$z^{-q}\boldsymbol{w}' = \boldsymbol{f}(z,\boldsymbol{w}), \tag{4.17}$$

is formally satisfied by a power series of the form

$$\sum_{n=1}^{\infty} \boldsymbol{a}_n z^{-n}. \tag{4.18}$$

Then there exists, for sufficiently large z in S, a solution $\boldsymbol{w} = \boldsymbol{\phi}(z)$ of (4.17) such that, in every proper subsector of S,

$$\boldsymbol{\phi}(z) \sim \sum_{n=1}^{\infty} \boldsymbol{a}_n z^{-n}, \qquad z \to \infty.$$

We now apply Wasow's theorem to $\mathrm{P_{III}^{(i)}}$ (as presented in [54]) and $\mathrm{P_{VI}}$. Since the right-hand sides of $\mathrm{P_I}$ and $\mathrm{P_{II}}$ are polynomial functions of u, see section 1.1, Wasow's theorem was applied directly to these equations in [47] and [48]. Since the right-hand sides of $\mathrm{P_{III}^{(i)}}$ and

$\mathrm{P_{VI}}$ are not polynomial functions of u, we consider first-order systems of differential equations that are equivalent to these equations. Equivalent first-order formulations of $\mathrm{P_{III}^{(i)}}$ and $\mathrm{P_{VI}}$ are, respectively, [36, p. 149]

$$\begin{aligned} u' &= 1 + (1-\beta)\frac{u}{z} + u^2 U \\ U' &= \frac{\alpha}{z} + u - (2-\beta)\frac{U}{z} - uU^2 \end{aligned} \tag{4.19}$$

and [36, p. 218]

$$\begin{aligned} u' &= \frac{1}{z(z-1)}\left\{\eta_2 z + \left[(\eta_3-\eta_2)z - (1+\eta_2+\eta_4)\right]u + C_2 u^2 + C_1 u(u-1)(u-z)U\right\} \\ U' &= \frac{1}{z(z-1)}\left\{\frac{2\alpha - C_2^2}{2C_1} - \left[(\eta_3-\eta_2)z - (1+\eta_2+\eta_4)\right]U - 2C_2 uU \right. \\ &\qquad \left. - \frac{C_1}{2}(3u^2 - 2zu - 2u + z)U^2\right\}, \end{aligned} \tag{4.20}$$

where

$$\eta_2^2 = -2\beta, \qquad \eta_3^2 = 2\gamma, \qquad \eta_4^2 = 1 - 2\delta, \qquad C_1 \neq 0, \qquad C_2 = 1 + \eta_2 - \eta_3 + \eta_4. \tag{4.21}$$

Note that each system is a polynomial function of the dependent variables. The $\mathrm{P_{III}^{(i)}}$ system (4.19) admits the formal expansions

$$u^{(m)}(z) = \sum_{j=0}^{\infty} a_j^{(m)} z^{-j} \qquad \text{and} \qquad U^{(m)}(z) = \sum_{j=0}^{\infty} A_j^{(m)} z^{-j}, \tag{4.22}$$

where

$$a_0^{(m)} = e^{\frac{m\pi i}{2}}, \qquad m = 0, 1, 2, 3, \tag{4.23}$$

and $A_0^{(m)} = -(a_0^{(m)})^2$. The equations for $a_j^{(m)}$, $A_j^{(m)}$, $j \geq 1$ are given [54] but these coefficients will not be required to proceed with the proof. Similarly, the $\mathrm{P_{VI}}$ system (4.20) admits the formal expansions

$$u(z) = \sum_{j=0}^{\infty} a_j z^{-j} \qquad \text{and} \qquad U(z) = \sum_{j=0}^{\infty} A_j z^{-j}, \tag{4.24}$$

where

$$a_0 = \frac{\eta_2}{\eta_2 + \eta_3}, \qquad \eta_2 + \eta_3 \neq 0, \qquad A_0 = -\frac{2(\eta_2 + \eta_3)}{C_1},$$

and the equations for a_j, A_j, $j \geq 1$ will not be required hereafter. Note that for the numerical evidence of tronquée $\mathrm{P_{VI}}$ solutions presented in Figures 3.2 and 3.3, $\beta = -4$ and $\gamma = 8$ and thus $\eta_2 + \eta_3 \neq 0$, see (4.21).

Corollary 1. [54, **Proposition 1**]

In any sector of angle less than π*, there exists a solution* $u(z)$ *of* $\mathrm{P}_{\mathrm{III}}^{(\mathrm{i})}$ *whose asymptotic behaviour as* $z \to \infty$ *is given by* $u^{(m)}(z)$ *in* (4.22) *with* $m = 0, 1, 2, 3$.

Proof. The system (4.19) and expansions in (4.22) can be put into the standard forms (4.17) and (4.18) in Wasow's theorem by making the change of variables $v(z) = u(z) - a_0^{(m)}$ and $V(z) = U(z) - A_0^{(m)}$ in (4.19) and (4.22). It is straightforward to verify that the resulting system satisfies the first, second and fourth conditions in Theorem 1 with $q = 0$. The third condition is also satisfied since the Jacobian matrix (4.16) of the transformed system is [54]

$$\begin{pmatrix} -2(a_0^{(m)})^3 & (a_0^{(m)})^2 \\ 0 & 2(a_0^{(m)})^3 \end{pmatrix},$$

whose eigenvalues are

$$\lambda_{1,2} = \pm 2(a_0^{(m)})^3 = \pm 2e^{-\frac{m\pi i}{2}} \neq 0, \qquad m = 0, 1, 2, 3, \tag{4.25}$$

which, by Wasow's theorem, concludes the proof. □

To prove a similar result for P_{VI}, we also set $v(z) = u(z) - a_0$ and $V(z) = U(z) - A_0$ in (4.20) and (4.24) and find that the resulting system satisfies the first, second and fourth conditions in Theorem 1 with $q = 0$. However, the Jacobian matrix of the resulting system is the zero matrix since, in the limit $z \to \infty$, the denominators of the right-hand sides of (4.20) contain z^2 which strictly dominates all the terms in the numerators. Hence, the third condition of Theorem 1 is not satisfied and thus we are unable to draw any conclusions regarding the existence of tronquée solutions of P_{VI}.

The first-order formulations of $\mathrm{P}_{\mathrm{III}}^{(\mathrm{i})}$ in (4.19) and P_{VI} in (4.20) are not unique; alternative systems are given in [36, p. 150, p. 219]. However, we were unable to find a first-order formulation of P_{VI} (or a suitable manipulation thereof) that satisfies the third condition in Theorem 1. An alternative method of proving tronquée solutions of P_{VI}, which we have not attempted, is the isomonodromy method that was used in [9] to establish tronquée P_{V} solutions.

Theorem 2. Tronquée solutions of $\mathrm{P}_{\mathrm{III}}^{(\mathrm{i})}$ [54, **Theorem 1**]

For $n \in \mathbb{Z}$ *and a* $z_0 \neq 0$ *of sufficiently large modulus, the following two statements hold.*

(1) There exist one-parameter solutions of $\mathrm{P}_{\mathrm{III}}^{(\mathrm{i})}$ *in the sectors*

$$S_n^{(m)} = \begin{cases} \left\{ z \in \mathbb{C} : |z| > |z_0|, -\frac{\pi}{2} + n\pi < \arg z < \frac{\pi}{2} + n\pi \right\}, & \text{for } m = 0, 2, \\ \left\{ z \in \mathbb{C} : |z| > |z_0|, n\pi < \arg z < (n+1)\pi \right\}, & \text{for } m = 1, 3, \end{cases} \tag{4.26}$$

with the following asymptotic expansion

$$u^{(m)}(z) \sim a_0^{(m)} + \sum_{j=1}^{\infty} a_j^{(m)} z^{-j}, \qquad z \to \infty. \tag{4.27}$$

Substituting the expansion (4.27) into $\mathrm{P}_{\mathrm{III}}^{(\mathrm{i})}$ *shows that* $a_0^{(m)}$ *is given by (4.23) and for a fixed* m*, the remaining coefficients are unique polynomial functions of* α *and* β*, thus* $a_j^{(m)} = a_j^{(m)}(\alpha, \beta)$.

(2) There exists a unique solution of $\mathrm{P}_{\mathrm{III}}^{(\mathrm{i})}$ *in each of the following sectors*

$$\Omega_n^{(m)} = \begin{cases} \left\{ z \in \mathbb{C} : |z| > |z_0|, -\dfrac{\pi}{2} + n\pi < \arg z < \dfrac{3\pi}{2} + n\pi \right\}, & \text{for } m = 0, 2, \\ \{ z \in \mathbb{C} : |z| > |z_0|, n\pi < \arg z < (n+2)\pi \}, & \text{for } m = 1, 3, \end{cases} \tag{4.28}$$

with the asymptotic expansion given in (4.27).

Proof. Let $\widehat{u}(z)$ be a small perturbation of a solution described in Corollary 1, then it is shown in [54] that the leading order behaviour of $\widehat{u}(z)$ on the pole-free sector is

$$\widehat{u}(z) \sim k_1 z^{d_1} e^{\lambda_1 z} + k_2 z^{d_2} e^{\lambda_2 z}, \qquad z \to \infty, \tag{4.29}$$

where k_1 and k_2 are arbitrary constants and λ_1 and λ_2 are defined in (4.25). For the perturbation to remain small, at most one of the arbitrary constants may be nonzero in which case the perturbation remains small on the regions $S_n^{(m)}$ defined in (4.26). This concludes the proof of part (1).

Let $\epsilon > 0$ be small and let

$$S_{n,\pm\epsilon}^{(m)} = \begin{cases} \left\{ z \in \mathbb{C} \mid |z| > |z_0|, \ -\dfrac{\pi}{2} + n\pi \pm \epsilon < \arg z < \dfrac{\pi}{2} + n\pi \pm \epsilon \right\}, & \text{for } m = 0, 2, \\ \{ z \in \mathbb{C} \mid |z| > |z_0|, \ n\pi \pm \epsilon < \arg z < (n+1)\pi \pm \epsilon \}, & \text{for } m = 1, 3. \end{cases}$$

Let u_1 and u_2 be solutions whose asymptotic behaviour is given by (4.22) on the sectors $S_{n,\epsilon}^{(m)}$ and $S_{n+1,-\epsilon}^{(m)}$, respectively (the existence of such solutions is assured by Corollary 1). Consider the difference of these solutions,

$$w := u_1 - u_2,$$

on the intersection of their pole-free sectors,

$$\begin{aligned} \widehat{S}_{n,\epsilon}^{(m)} &= S_{n,\epsilon}^{(m)} \cap S_{n+1,-\epsilon}^{(m)} \\ &= \begin{cases} \left\{ z \in \mathbb{C} \mid |z| > |z_0|, \ \dfrac{\pi}{2} + n\pi - \epsilon < \arg z < \dfrac{\pi}{2} + n\pi + \epsilon \right\}, & \text{for } m = 0, 2, \\ \{ z \in \mathbb{C} \mid |z| > |z_0|, \ (n+1)\pi - \epsilon < \arg z < (n+1)\pi + \epsilon \}, & \text{for } m = 1, 3. \end{cases} \end{aligned}$$

Since u_1 and u_2 both satisfy the same algebraic expansion (4.22) on $\widehat{S}_{n,\epsilon}^{(m)}$, it follows that

$$w(z) = \mathcal{O}\left(z^{-j}\right), \qquad j \in \mathbb{N}, \qquad z \to \infty, \qquad z \in \widehat{S}_{n,\epsilon}^{(m)}. \tag{4.30}$$

It is shown in [54] that the leading order behaviour of $w(z)$ is also given by (4.29):

$$w(z) \sim k_1 z^{d_1} e^{\lambda_1 z} + k_2 z^{d_2} e^{\lambda_2 z}, \qquad z \to \infty, \qquad z \in \widehat{S}_{n,\epsilon}^{(m)}.$$

The only way to ensure that (4.30) is satisfied to choose $k_1 = k_2 = 0$. Hence, $u_1 = u_2$ for $z \in \widehat{S}_{n,\epsilon}^{(m)}$ and by letting $\epsilon \to 0$ we obtain the regions of validity $\Omega_n^{(m)}$ in (4.28). This concludes the proof of part (2). □

Henceforth, we shall refer to the solutions in Theorem 2 as the LDT solutions, after Lin, Dai and Tibboel. It follows from the above proof that the one-parameter families in part (1) of Theorem 2 satisfy (cf. (4.27) and (4.29))

$$u^{(m)}(z;\alpha,\beta,k) \sim a_0^{(m)} + \sum_{j=1}^{\infty} a_j^{(m)}(\alpha,\beta) z^{-j} - k z^d e^{\lambda z}, \qquad z \to \infty, \tag{4.31}$$

where k is an arbitrary parameter and d is a constant that depends on m, α and β and which can be determined by substitution into $\mathrm{P}_{\mathrm{III}}^{(\mathrm{i})}$. Furthermore, $\lambda = -2$ in right half-planes ($S_n^{(m)}$, $m = 0, 2$, n even); $\lambda = 2$ in left half-planes ($S_n^{(m)}$, $m = 0, 2$, n odd); $\lambda = 2i$ in upper half-planes ($S_n^{(m)}$, $m = 1, 3$, n even) and $\lambda = -2i$ in lower half-planes ($S_n^{(m)}$, $m = 1, 3$, n odd). The unique solutions in part (2) of Theorem 2 are the solutions for which $k = 0$. Hence, the $k = 0$ LDT solutions are defined by the algebraic asymptotic expansion (4.27) while the one-parameter LDT solutions have an algebraic expansion with exponential-order correction terms containing an arbitrary parameter, see (4.31).

4.4 The $k = 0$ LDT solutions

The following theorem shows that for the $k = 0$ LDT solutions $u^{(m)}(z;\alpha,\beta,0)$, it is sufficient to consider only the $m = 0$ solution since the solutions with $m = 1, 2, 3$ are related to the $m = 0$ solution through simple scaling Bäcklund transformations.

Theorem 3. *The $k = 0$ LDT solutions in part (2) of Theorem 2 are related as follows,*

$$u^{(0)}(z; -\alpha, -\beta, 0) = T_0(1, -1)u^{(0)}(z; \alpha, \beta, 0) = u^{(0)}(-z; \alpha, \beta, 0), \tag{4.32}$$

$$u^{(0)}(z; -\beta, -\alpha, 0) = Ru^{(0)}(z; \alpha, \beta, 0) = \left[u^{(0)}(z; \alpha, \beta, 0)\right]^{-1}, \tag{4.33}$$

$$u^{(2)}(z; \alpha, \beta, 0) = T_0(-1, -1)u^{(0)}(z; \alpha, \beta, 0) = -u^{(0)}(-z; \alpha, \beta, 0), \tag{4.34}$$

$$u^{(1)}(z; \alpha, -\beta, 0) = T_0(-i, i)u^{(0)}(z; \alpha, \beta, 0) = iu^{(0)}(iz; \alpha, \beta, 0), \tag{4.35}$$

$$u^{(3)}(z; -\alpha, \beta, 0) = T_0(i, i)u^{(0)}(z; \alpha, \beta, 0) = -iu^{(0)}(iz; \alpha, \beta, 0). \tag{4.36}$$

Proof. These relationships follow from the definitions of the Bäcklund transformations T_0 in (4.1) and (4.2) and R in (4.3) and the fact that the solutions on the left and right-hand sides of (4.32)–(4.36) each has a unique expansion in powers of z^{-1}, as stated in Theorem 2 (recall from (4.31) that the $k = 0$ solutions are defined to all orders by the algebraic asymptotic expansion (4.27)). Alternatively, these relationships can be proved directly by showing that the algebraic expansions of the solutions on the left and right-hand sides of (4.32)–(4.36) match to all orders. This is done (except for (4.33)) in the proof following Lemma 1 in section 4.6. □

Figure 4.1 shows two independently computed solutions, $u^{(0)}(z; \alpha, \beta, 0)$ (first and third columns) and $u^{(3)}(z; -\alpha, \beta, 0)$ (second and fourth columns) that, according to (4.36), are shifted and scaled versions of each other. The solutions are depicted in the ζ-plane (recall that $z = e^{\zeta/2}$) since it more clearly illustrates the relationship (4.36) on multiple sheets than the corresponding plots in the z-plane. In the ζ-plane, the pole-free sectors of the solutions $u^{(0)}(z; \alpha, \beta, 0)$ and $u^{(3)}(z; -\alpha, \beta, 0)$ are within the respective strips

$$-\pi \le \text{Im } \zeta \le 3\pi, \qquad \text{and} \qquad -2\pi \le \text{Im } \zeta \le 2\pi.$$

These regions correspond to the z-plane sectors $\Omega_0^{(0)}$ and $\Omega_{-1}^{(3)}$, respectively, defined in (4.28). The initial conditions of the solutions were obtained by evaluating the optimally truncated algebraic expansions (4.27) in the centre of their pole-free regions at $|z| = 10$ (i.e., $z = 10i$ for $u^{(0)}(z; \alpha, \beta, 0)$ and $z = 10$ for $u^{(3)}(z; -\alpha, \beta, 0)$) from whence the enhanced PFS was initialized in the ζ-plane.

Since α and β have imaginary values in Figure 4.1, $u^{(3)}(z; -\alpha, \beta, 0)$ is imaginary on the real axis and it satisfies $u^{(3)}(\overline{z}; -\alpha, \beta, 0) = -\overline{u^{(3)}(z; -\alpha, \beta, 0)}$. This can be proved by using the equations in Lemma 1 to show that the defining asymptotic expansion (4.27) (and hence its derivative) is imaginary on the real axis and noting from the $\text{P}_{\text{III}}^{(\text{i})}$ equation that if u, u', α and β

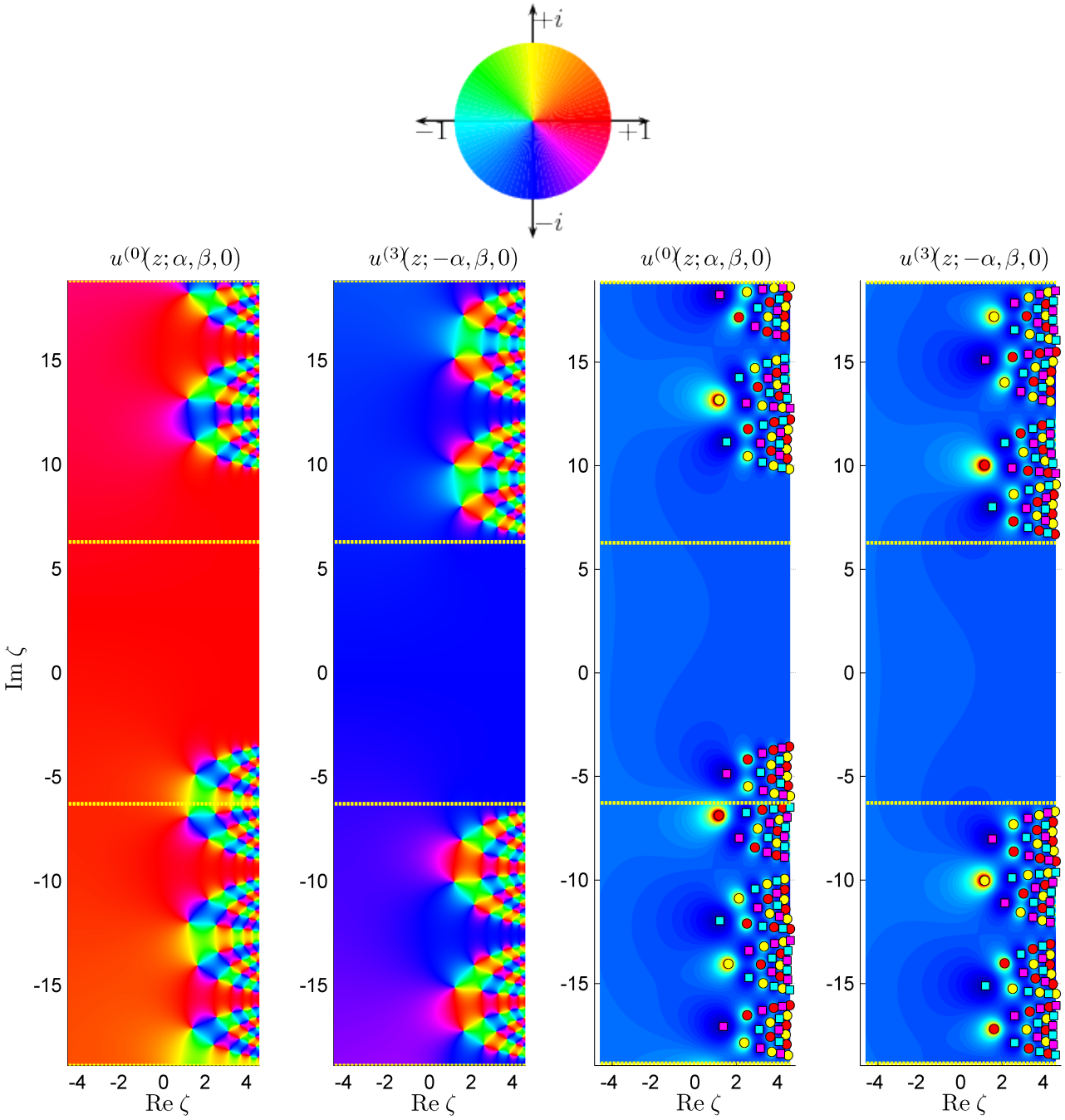

Figure 4.1: An illustration of the relationship $u^{(3)}(z;-\alpha,\beta,0) = -iu^{(0)}(iz;\alpha,\beta,0)$ from Theorem 3 in the ζ-plane ($z = e^{\zeta/2}$) with $\alpha = i/3$, $\beta = -i/2$. The colour wheel above the figure indicates that the conspicuous red and blue in the phase portraits in the first and second columns indicate positive real and negative imaginary values, respectively. The error estimates for $u^{(3)}(z;-\alpha,\beta,0)$ are 4.1e-8 and 1.0e-6 on sheets 0 and ± 1, respectively. The 'relative transformation error', $|u^{(3)}(z;-\alpha,\beta,0)+iu^{(0)}(iz;\alpha,\beta,0)|/|u^{(3)}(z;-\alpha,\beta,0)|$, is 8.2e-8 on the pole-free sectors and 3.6e-5 on the rest of the overlapping domains of the solutions. The modulus plots in the third and fourth columns illustrate that the corresponding poles of the solutions have residues of opposite signs while the derivative values at the zeros have the same signs, as shown in (4.37).

are imaginary, then so are the derivatives of all orders. Hence, the error estimates in the caption of Figure 4.1 were obtained by computing the maximum of

$$\frac{\left|u^{(3)}(\overline{e^{\zeta/2}};-\alpha,\beta,0)+\overline{u^{(3)}(e^{\zeta/2};-\alpha,\beta,0)}\right|}{|u^{(3)}(e^{\zeta/2};-\alpha,\beta,0)|},$$

for the numerical solution. Note that the error reported in the caption of Figure 4.1 for the relationship (4.36) is comparable to the error estimate for $u^{(3)}(z;-\alpha,\beta,0)$, which confirms the validity of (4.36).

It follows from (4.36) and (4.14)–(4.15) that if $u^{(0)}(z;\alpha,\beta,0)$ has a pole or zero at z_0 with residue or derivative value ε, where $\varepsilon^2=1$, then for the corresponding pole or zero of $u^{(3)}(z;-\alpha,\beta,0)$ at $-iz_0$:

$$u^{(3)}(z;-\alpha,\beta,0)\sim\frac{-\varepsilon}{z+iz_0}\qquad\text{and}\qquad u^{(3)}(z;-\alpha,\beta,0)\sim\varepsilon(z+iz_0),\qquad z\to-iz_0. \tag{4.37}$$

Hence, comparing poles and zeros in the third and fourth columns of Figure 4.1 whose vertical positions differ by π in the ζ-plane, we find that the residues have opposite signs and the derivative values at the zeros are the same, in accordance with (4.37).

4.4.1 Rational solutions

The $\mathrm{P}_{\mathrm{III}}^{(\mathrm{i})}$ equation has rational solutions if and only if [56], [36, p. 174]

$$\alpha+\varepsilon\beta=4n,\qquad \varepsilon^2=1,\qquad n\in\mathbb{Z}. \tag{4.38}$$

These parameter values are depicted in Figure 4.2 as blue lines in parameter space. Rational solutions are single-valued tronquée solutions whose pole-free sectors have angular width 2π. Thus, as pointed out in [54], the unique $k=0$ solutions in part (2) of Theorem 2 with $\alpha\pm\beta=4n$ correspond to rational solutions. It follows from (4.27) and (4.23) that rational solutions asymptote to ±1 or $\pm i$ for $z\to\infty$ and thus they must be of type (m,m), i.e., the numerator and denominator polynomials must have the same degrees.

The simplest rational solutions that are admitted by $\mathrm{P}_{\mathrm{III}}^{(\mathrm{i})}$ are

$$u^{(m)}(z;\alpha,\beta,0)=a_0^{(m)},\qquad\text{with}\qquad\begin{cases}\alpha=-\beta, & \text{if } m=0,2,\\ \alpha=\beta, & \text{if } m=1,3,\end{cases} \tag{4.39}$$

where the conditions on the parameter values follow from substitution into $\mathrm{P}_{\mathrm{III}}^{(\mathrm{i})}$. These solutions can be used as seed solutions from which more complicated rational solutions can be

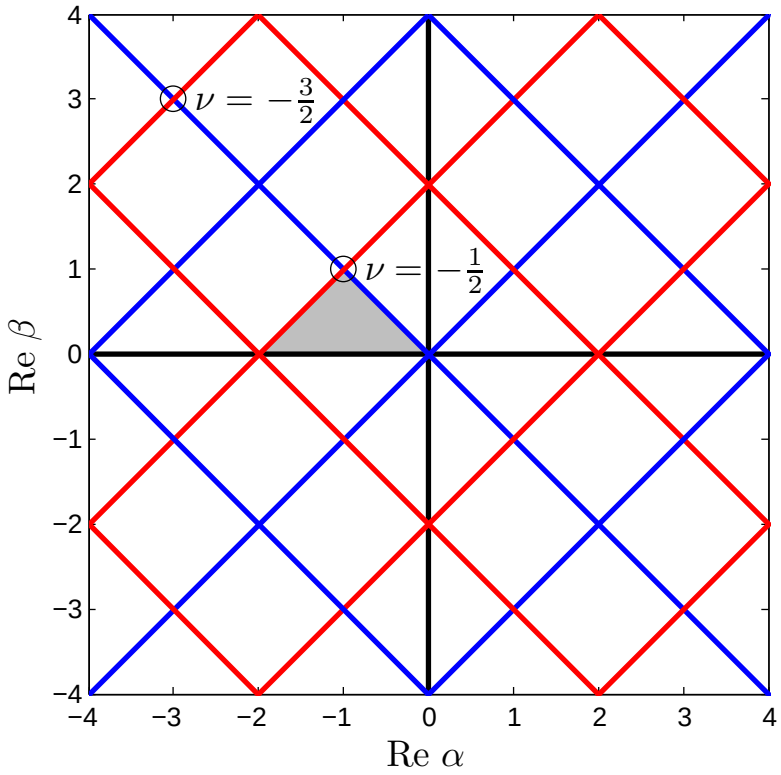

Figure 4.2: The blue lines ($\alpha + \varepsilon\beta = 4n$, $\varepsilon^2 = 1$) and red lines ($\varepsilon_1\alpha + \varepsilon_2\beta = 4n + 2$, $\varepsilon_1^2, \varepsilon_2^2 = 1$) indicate points in the parameter space of $\mathrm{P}_{\mathrm{III}}^{(\mathrm{i})}$ at which, respectively, rational solutions (section 4.4.1) and one-parameter Bessel function solutions (section 4.5) are admitted. The shaded triangle is the fundamental domain (section 4.1). The solutions located at the open circles will be discussed in sections 4.5.2 and 5.5.2.

constructed by repeated application of the Bäcklund transformations $\mathcal{T}_1$–$\mathcal{T}_4$, defined below (4.11). Note that the two real-valued seed solutions in (4.39) lie on the line of negative slope through the origin in Figure 4.2. It is straightforward to confirm that applying any composition of the $\mathcal{T}_j$, $j = 1, 2, 3, 4$ to the real-valued seeds yields a rational solution on some line $\alpha + \beta = 4n$ (some line with negative slope in Figure 4.2) that asymptotes to a real value for $z \to \infty$, i.e., $u \sim a_0^{(m)}$ with $m = 0$ or $m = 2$. Similarly, applying any composition of the $\mathcal{T}_j$, $j = 1, 2, 3, 4$ to the imaginary seeds in (4.39) yields a rational solution on some line $\alpha - \beta = 4n$ (some line with positive slope in Figure 4.2) that asymptotes to an imaginary value for $z \to \infty$, i.e., $u \sim a_0^{(m)}$ with $m = 1$ or $m = 3$. However, it is sufficient to consider the $m = 0$ solutions, which lie on lines of negative slope in Figure 4.2, since the solutions with $m \neq 0$ are related to the $m = 0$ solutions according to the simple relationships in Theorem 3. Furthermore, (4.32)

implies that it is sufficient to consider $m = 0$ rational solutions on the lines $\alpha + \beta = 4n$, $n \geq 0$.

It is shown in [15] that rational solutions of $\mathrm{P}_{\mathrm{III}}^{(\mathrm{i})}$ with $m = 0$ on the line $\alpha + \beta = 4n$ in parameter space can be expressed as

$$u_n^{(0)}(z;\mu) := u^{(0)}(z;\alpha_n(\mu),\beta_n(\mu),0) = \frac{S_n(z;\mu-1)S_{n-1}(z;\mu)}{S_n(z;\mu)S_{n-1}(z;\mu-1)}, \tag{4.40}$$

where

$$\alpha_n(\mu) = 2n + 2\mu - 1, \qquad \beta_n(\mu) = 2n - 2\mu + 1 \qquad \Rightarrow \qquad \alpha_n + \beta_n = 4n, \tag{4.41}$$

and where the polynomials $S_n(z;\mu)$ are generated from the recursion

$$S_{n+1}S_{n-1} = -z\left[S_n\frac{d^2S_n}{dz^2} - \left(\frac{dS_n}{dz}\right)^2\right] - S_n\frac{dS_n}{dz} + (z+\mu)S_n^2, \qquad S_{-1} = S_0 = 1.$$

We find that

$$u_0^{(0)}(z;\mu) = 1, \tag{4.42}$$

$$u_1^{(0)}(z;\mu) = 1 - \frac{1}{z+\mu}, \tag{4.43}$$

$$u_2^{(0)}(z;\mu) = 1 + \frac{1}{z+\mu-1} - \frac{3(z+\mu)^2}{(z+\mu)^3-\mu}, \tag{4.44}$$

$$u_3^{(0)}(z;\mu) = 1 + \frac{3(z+\mu-1)^2}{(z+\mu-1)^3-\mu+1} - \frac{6(z+\mu)^5 - 15\mu(z+\mu)^2 + 9\mu}{(z+\mu)^6 - 5\mu(z+\mu)^3 + 9\mu(z+\mu) - 5\mu^2}. \tag{4.45}$$

An alternative method of generating these solutions is by multiple applications of $\mathcal{T}_1$ to the seed solution, i.e., $u_n^{(0)}(z;\mu) = \mathcal{T}_1^n u_0^{(0)}(z;\mu)$ (throughout we let $\mathcal{T}^n$ denote n applications of the transformation $\mathcal{T}$). Figure 4.3 depicts examples of $u_n^{(0)}$ for $n = 1,2,3,4$. Note how the pole field pattern of $u_{n-1}^{(0)}$ is nested within that of $u_n^{(0)}$ and that $u_n^{(0)}$ is of type (n^2,n^2) (see also (4.42)–(4.45) for confirmation of the latter fact).

Figure 4.4 shows the typical pole field dynamics of $u_n^{(0)}(z;\mu)$ as μ is varied, for the case $n = 3$. As μ is increased, the pole field moves horizontally to the left. Poles and zeros coalesce at the origin when $\mu = -1,0,1,2$. However, for $\mu = -1,0$, all the zeros that coalesce have opposite derivative values and for $\mu = 1,2$, all the poles that coalesce have opposite residues and thus they cancel each other out. The net result is that poles coalesce at $z = 0$ if $\mu = -1,0$ and zeros coalesce at the origin if $\mu = 1,2$. We conclude from (4.5) and (4.6) that for the coalesced poles and zeros at the origin in Figure 4.4, the residues and derivative values are, respectively,

$$c_{-1} = -\frac{\alpha}{\gamma} = -(5+2\mu), \qquad \mu = -1,0, \qquad \text{and} \qquad c_1 = -\frac{\delta}{\beta} = \frac{1}{7-2\mu}, \qquad \mu = 1,2. \tag{4.46}$$

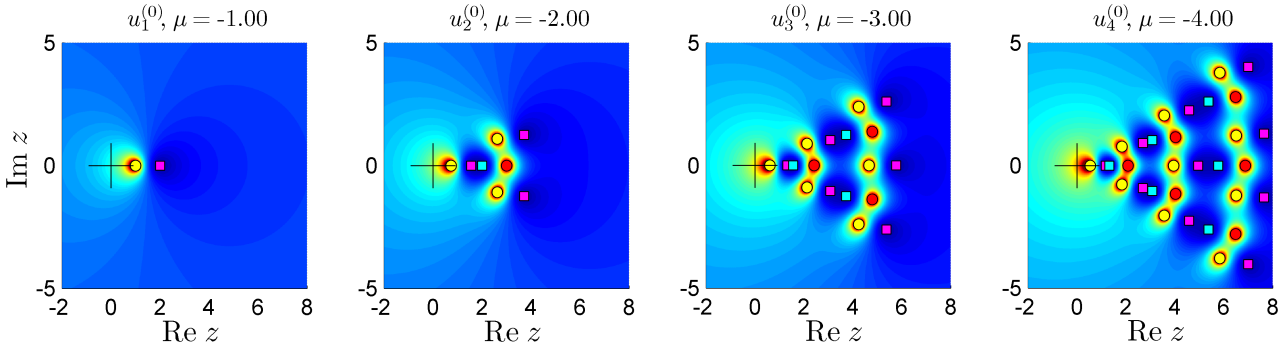

Figure 4.3: Examples of rational solutions of $\mathrm{P}_{\mathrm{III}}^{(\mathrm{i})}$, defined in (4.40), see also (4.42)–(4.45).

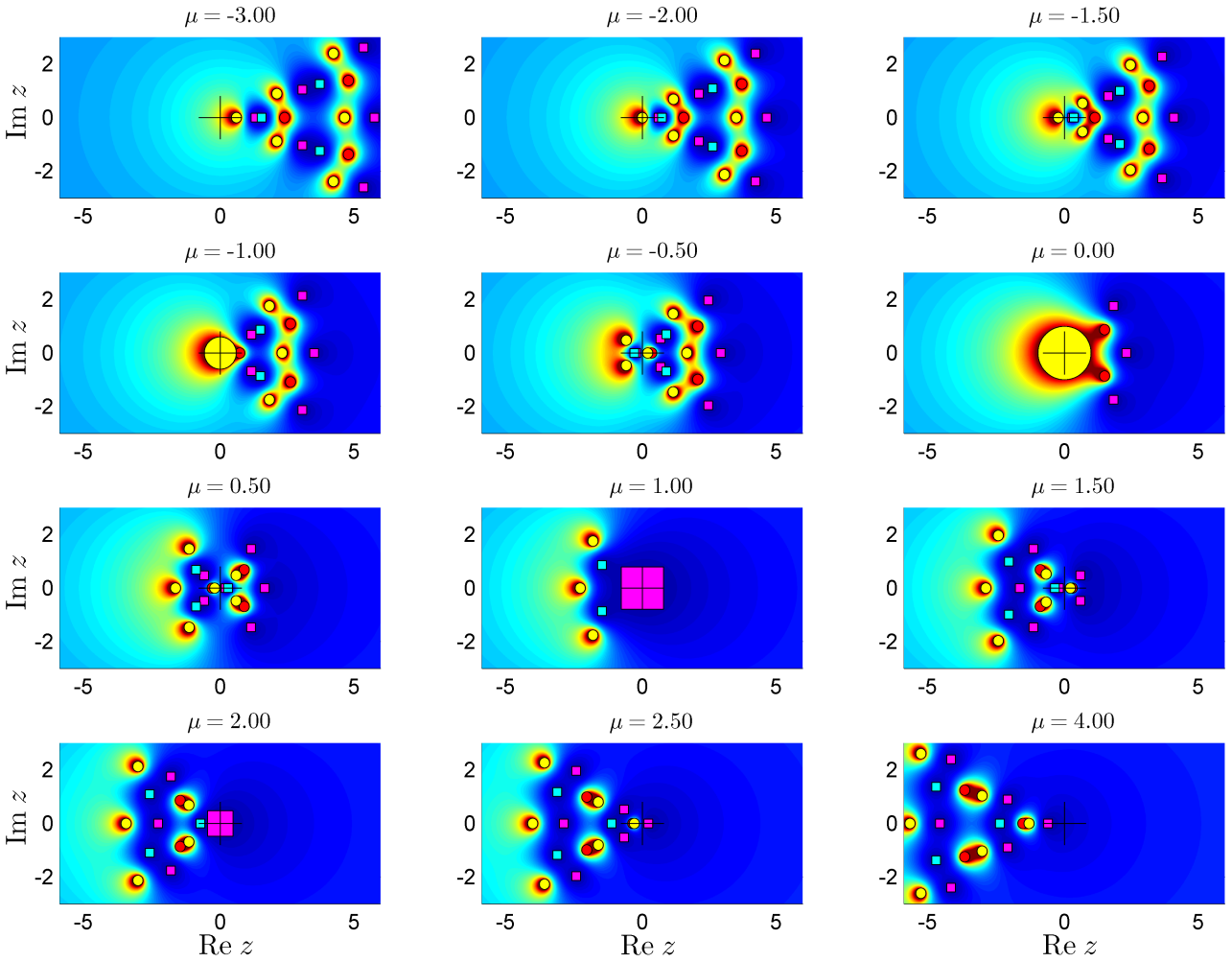

Figure 4.4: The typical evolution of a rational $\mathrm{P}_{\mathrm{III}}^{(\mathrm{i})}$ solution along the line $\alpha + \beta = 4n$ in parameter space. The parameter values are given by (4.41) with $n = 3$: $\alpha = 5 + 2\mu$, $\beta = 7 - 2\mu$. The coalesced poles and zeros at the origin in the frames with $\mu = -1, 0, 1, 2$ are indicated by enlarged markers (circles or squares) whose sizes vary in proportion to the number of coalesced poles or zeros.

Hence, five poles of residue -1 coalesce in the $\mu = 0$ frame in Figure 4.4 to form a pole of residue -5 and five zeros with $c_1 = +1$ coalesce in the $\mu = 1$ frame to form a zero with $c_1 = +1/5$. By comparing the frames before and after a coalescence occurs, e.g., the $\mu = 0.5$ and $\mu = 1.5$ frames, we find that the poles and zeros that coalesced are rotated through an angle of π in the two frames.

These observations for Figure 4.4 generalize in a straightforward manner. For example, for rational solutions with $m = 0$ on the line $\alpha + \beta = 4n$, poles coalesce at the origin when $\mu = -(n-2), \ldots, 0$ and these poles have residues (cf. (4.46))

$$c_{-1} = -\frac{\alpha}{\gamma} = -(2n + 2\mu - 1), \qquad \mu = -(n-2), \ldots, 0. \tag{4.47}$$

These poles result from the coalescence of $4n + 2\mu - 1$ poles of residue -1.

The intriguing pole and zero coalescences at the origin are not unique to rational $\mathrm{P}_{\mathrm{III}}^{(\mathrm{i})}$ solutions. We shall find similar coalescences for another set of single-valued solutions in section 4.5 and for multivalued solutions in section 5.4.2. This is one of a number of solution features of $\mathrm{P}_{\mathrm{III}}^{(\mathrm{i})}$ that were not found in the computational studies of the meromorphic Painlevé transcendents in [32–34, 76–78].

By comparing the first and final frames of Figure 4.4, it appears that the two solutions are related through a rotation and a reciprocal transformation. In fact, it follows from (4.32) and (4.33) that the relationship

$$\begin{aligned} u_3^{(0)}(z; \alpha_3(\mu_2), \beta_3(\mu_2), 0) &= R \circ T_0(1,-1) u_3^{(0)}(z; \alpha_3(\mu_1), \beta_3(\mu_1), 0) \\ &= \left[u_3^{(0)}(-z; \alpha_3(\mu_1), \beta_3(\mu_1), 0) \right]^{-1}, \end{aligned} \tag{4.48}$$

holds in Figure 4.4 for any two solutions for which $\alpha_3(\mu_1) = \beta_3(\mu_2)$ and $\beta_3(\mu_1) = \alpha_3(\mu_2)$, i.e., solutions for which

$$\mu_1 + \mu_2 = 1.$$

Hence, the first and final frames in Figure 4.4, for which $\mu_1 = -3$ and $\mu_2 = 4$, is one of five pairs of frames for which this relationship holds. It follows from (4.14)–(4.15) that $T_0(1,-1)$ changes the signs of the residues and derivative values of the transformed poles and zeros and thus under the transformation $R \circ T(1,-1)$ in (4.48), poles with residue ± 1 are mapped to zeros with $c_1 = \mp 1$ and vice versa. The frame $\mu = 0.5$ in Figure 4.4 is the special case for which (4.48) is an auto-Bäcklund transformation since then the parameters on the left and right-hand

sides of (4.48) are the same. Since there is a unique rational solution which asymptotes to 1 if $\alpha + \beta = 4n$ (this is a consequence of part (2) of Theorem 2), it follows that not only the parameters but also the solutions on the left and right-hand sides of (4.48) are the same if $\mu = 0.5$. Hence (4.48) gives the relationship between the same solution if $\mu_1 = \mu_2 = 0.5$ and different solutions if $\mu_1, \mu_2 \neq 0.5$ with $\mu_1 + \mu_2 = 1$.

4.5 The one-parameter LDT solutions with $\alpha = \pm\beta$

The next chapter is dedicated to the MTW solutions, which are one-parameter LDT solutions with $m = 0$ and $\lambda = -2$ (i.e., they asymptote to 1 in a right half-plane, see (4.31)) on the line $\alpha = -\beta$ in parameter space. In this section we show that the MTW solutions are related to the other one-parameter LDT solutions in (4.31) on the two lines through the origin in parameter space. Hereafter, we set $\alpha = -\beta = 2\nu$ or $\alpha = \beta = 2\nu$ on these lines. We shall find that the MTW solutions, which are on the line $\alpha = -\beta = 2\nu$, are undefined for negative half-integer ν values. In parameter space these ν values correspond to the points indicated by open circles in Figure 4.2. Therefore, in this section we also investigate one-parameter LDT solutions with negative half-integer ν values. It will be demonstrated in this section and the next chapter that these one-parameter LDT solutions with $\nu = -\frac{1}{2} - n$ stand out for a number of special properties: they are closed-form, meromorphic solutions that are examples of Bessel function solutions of $\mathrm{P}_{\mathrm{III}}^{(\mathrm{i})}$ and they can be considered as a set of limiting MTW solutions.

4.5.1 Asymptotics

On the lines in parameter space considered in this section ($\alpha = -\beta$ and $\alpha = \beta$), the unique tronquée solutions in part (2) of Theorem 2 are the rational solutions $a_0^{(m)}$, with $m = 0, 2$ (see (4.39) and (4.23)) if $\alpha = -\beta$ and $m = 1, 3$ if $\alpha = \beta$. Hence, in these cases the algebraic part of the asymptotic expansion (4.31) converges to $a_0^{(m)}$. This observation also follows from the first, third, fourth and fifth properties of the coefficients in Lemma 1. To obtain higher order terms for our numerical work in the next chapter, we multiply the exponential order term in (4.31) by an algebraic series. That is, we use the ansatz

$$u^{(m)}(z; 2\nu, -2\nu, k) \sim a_0^{(m)} - kz^d e^{\lambda z}\Big(1 + \sum_{j=1}^{\infty} c_j^{(m)}(\nu) z^{-j}\Big), \qquad z \to \infty, \tag{4.49}$$

for $m = 0, 2$ (note that $\alpha = -\beta$) and

$$u^{(m)}(z; 2\nu, 2\nu, k) \sim a_0^{(m)} - kz^d e^{\lambda z}\Big(1 + \sum_{j=1}^{\infty} c_j^{(m)}(\nu) z^{-j}\Big), \qquad z \to \infty, \tag{4.50}$$

for $m = 1, 3$ (note that $\alpha = \beta$). As before, $\lambda = \pm 2$ in (4.49) (in left and right half-planes, respectively) and $\lambda = \pm 2i$ in (4.50) (in upper and lower half-planes, respectively).

The following theorem, whose results are similar to those in Theorem 3 for the $k = 0$ solutions, shows that, of the one-parameter solutions represented by (4.49) and (4.50), it is sufficient to consider the solutions in (4.49) with $m = 0$, $k > 0$ and $\lambda = -2$. This is because all the other solutions are related to this solution through simple Bäcklund transformations.

Theorem 4. *The one-parameter LDT solution in (4.49) with $m = 0$ and $\lambda = -2$ satisfies*

$$u^{(0)}(z; 2\nu, -2\nu, k) \sim 1 - kz^{-\nu-1/2} e^{-2z}\Big(1 + \sum_{j=1}^{\infty} c_j^{(0)}(\nu) z^{-j}\Big), \qquad z \to \infty, \tag{4.51}$$

where z is in a right half-plane (i.e., $z \in S_n^{(0)}$, n even, and $S_n^{(0)}$ is defined in (4.26)) and

$$c_{j+1}^{(0)}(\nu) = -\frac{(2\nu + 2j + 1)^2}{16(j+1)} c_j^{(0)}(\nu), \qquad j \geq 0, \qquad c_0^{(0)}(\nu) = 1. \tag{4.52}$$

Furthermore, the one-parameter LDT solutions in (4.49) and (4.50) are related as follows to the solution in (4.51), at least up to $\mathcal{O}\left(e^{-2z}\right)$ terms for $z \to \infty$, with $z \in S_n^{(0)}$, n even:

$$u^{(0)}(z; -2\nu, 2\nu, (-1)^{\nu-1/2}k) = T_0(1, -1)u^{(0)}(z; 2\nu, -2\nu, k) = u^{(0)}(-z; 2\nu, -2\nu, k), \tag{4.53}$$

$$u^{(0)}(z; 2\nu, -2\nu, -k) = Ru^{(0)}(z; 2\nu, -2\nu, k) = \left[u^{(0)}(z; 2\nu, -2\nu, k)\right]^{-1}, \tag{4.54}$$

$$u^{(2)}(z; 2\nu, -2\nu, (-1)^{\nu+1/2}k) = T_0(-1, -1)u^{(0)}(z; 2\nu, -2\nu, k) = -u^{(0)}(-z; 2\nu, -2\nu, k), \tag{4.55}$$

$$u^{(1)}(z; 2\nu, 2\nu, i^{\nu+1/2}k) = T_0(-i, i)u^{(0)}(z; 2\nu, -2\nu, k) = iu^{(0)}(iz; 2\nu, -2\nu, k), \tag{4.56}$$

$$u^{(3)}(z; -2\nu, -2\nu, i^{\nu+1/2}k) = T_0(i, i)u^{(0)}(z; 2\nu, -2\nu, k) = -iu^{(0)}(iz; 2\nu, -2\nu, k). \tag{4.57}$$

Proof. Multiplying the $\mathrm{P}_{\mathrm{III}}^{(\mathrm{i})}$ equation with $\alpha = -\beta = 2\nu$ by u and substituting (4.49) with $m = 0$, $\lambda = -2$ and letting z be in a right half-plane with $z \to \infty$, we find that

$$d = -\nu - \frac{1}{2}$$

and

$$kz^{-\nu-1/2}e^{-2z} \sum_{j=0}^{\infty} \Big[-4(j+1)c_{j+1}^{(0)}(\nu) - \frac{1}{4}(2\nu + 2j + 1)^2 c_j^{(0)}(\nu)\Big] z^{-j-2} + \mathcal{O}\left(e^{-4z}\right) = 0,$$

from which (4.51) and (4.52) follow.

The proof of the relationships (4.53)–(4.57) is similar to the proof of Theorem 3. These relationships follow from (4.51), the definitions of the Bäcklund transformations T_0 in (4.1) and (4.2) and R in (4.3) and the fact that for a fixed m, the coefficients $c_j^{(m)}(\nu)$ in (4.49) and (4.50) are unique functions of ν.

The relationships can also be proved directly, which we illustrate for (4.56). Substituting (4.50) into $\mathrm{P}_{\mathrm{III}}^{(\mathrm{i})}$ with $m = 1$, $\lambda = 2i$ and letting z be in an upper half-plane, we find that

$$d = \nu - \frac{1}{2}, \qquad \text{and} \qquad c_j^{(1)}(\nu) = (-i)^{-j} c_j^{(0)}(-\nu), \qquad j \geq 1. \tag{4.58}$$

Hence, it follows from (4.58) that for z in an upper half-plane and $z \to \infty$,

$$\begin{aligned}
u^{(1)}(z; 2\nu, 2\nu, k) &\sim i - k z^{\nu-1/2} e^{2iz} \left(1 + \sum_{j=1}^{\infty} c_j^{(1)}(\nu) z^{-j} \right), \\
&= i - k z^{\nu-1/2} e^{2iz} \left(1 + \sum_{j=1}^{\infty} c_j^{(0)}(-\nu)(-iz)^{-j} \right) \\
&= i - i^{\nu-1/2} k (-iz)^{\nu-1/2} e^{2iz} \left(1 + \sum_{j=1}^{\infty} c_j^{(0)}(-\nu)(-iz)^{-j} \right) \\
&= i \left[1 - i^{\nu-3/2} k (-iz)^{\nu-1/2} e^{2iz} \left(1 + \sum_{j=1}^{\infty} c_j^{(0)}(-\nu)(-iz)^{-j} \right) \right] \\
&\sim i u^{(0)}(-iz; -2\nu, 2\nu, i^{\nu-3/2} k), \qquad (4.59) \\
&\sim i u^{(0)}(iz; 2\nu, -2\nu, i^{-\nu-1/2} k). \qquad (4.60)
\end{aligned}$$

where the steps (4.59) and (4.60) follow from (4.51) and (4.53), respectively. This shows that the relationship (4.56) holds at least up to $\mathcal{O}\left(e^{-2z}\right)$ for the asymptotic expansions of the solutions on their pole-free sectors. □

In section 4.5.2 and the next chapter we shall require a Bäcklund transformation that maps a $\mathrm{P}_{\mathrm{III}}^{(\mathrm{i})}$ solution with parameters $\alpha = -\beta = 2\nu$ to one with parameters $\alpha = -\beta = 2(\nu + \varepsilon)$, $\varepsilon^2 = 1$. We obtain such Bäcklund transformations by applying the reciprocal transformation (4.11) to $\mathcal{T}_2$, (4.12), and $\mathcal{T}_3$, (4.13), with $\alpha = -\beta = 2\nu$, then we obtain[2]

$$T_\varepsilon : \quad u(z; 2(\nu+\varepsilon), -2(\nu+\varepsilon)) = -\frac{u(zu' + \varepsilon z u^2 + 2\nu\varepsilon u + u - \varepsilon z)}{zu' + \varepsilon z u^2 - 2\nu\varepsilon u - u - \varepsilon z}, \qquad \varepsilon^2 = 1, \tag{4.61}$$

[2]Note from (4.54) that the reciprocal transformation is an auto-Bäcklund transformation for solutions with parameters $\alpha = -\beta = 2\nu$ but, for one-parameter solutions, it has the effect of changing the sign of the arbitrary parameter.

where $u := u(z; 2\nu, -2\nu)$ on the right-hand side.

Note from (4.52) that the algebraic series multiplying the exponential term in (4.51) converges to a finite sum only if ν has negative half-integer values,

$$\nu = -\frac{1}{2} - n, \qquad n \geq 0, \tag{4.62}$$

since then $c_j^{(0)}(\nu) = 0$, $j \geq n+1$. In this case, (4.51) becomes, for $z \to \infty$ in a right half-plane,

$$\begin{aligned} u^{(0)}(z; -2n-1, 2n+1, k) &\sim 1 - kz^n e^{-2z}\Big(1 + \sum_{j=1}^{n} c_j^{(0)}(-1/2-n) z^{-j}\Big), \\ &= 1 - kp_n(z)e^{-2z}, \qquad p_n(z) = \sum_{j=0}^{n} c_j^{(0)}(-1/2-n) z^{n-j}. \end{aligned} \tag{4.63}$$

The parameter values at the open circles in Figure 4.2, which correspond to negative half-integer ν values, are special since both the algebraic series that defines the $k = 0$ solution, (4.27), and the algebraic series multiplying the exponential order term converge to a finite sum. We now show that the one-parameter LDT solutions corresponding to the negative half-integer ν values are meromorphic Bessel function solutions of $\mathrm{P}_{\mathrm{III}}^{(\mathrm{i})}$.

4.5.2 Bessel function one-parameter LDT solutions with $\nu = -\frac{1}{2} - n$

The $\mathrm{P}_{\mathrm{III}}^{(\mathrm{i})}$ equation has Bessel function solutions if and only if [23, 36, 55, 56]

$$\varepsilon_1\alpha + \varepsilon_2\beta = 4n + 2, \qquad \varepsilon_1^2, \varepsilon_2^2 = 1, \qquad n \in \mathbb{Z}. \tag{4.64}$$

These parameter values correspond to the red lines in parameter space in Figure 4.2. Just as for the rational $\mathrm{P}_{\mathrm{III}}^{(\mathrm{i})}$ solutions, we first consider seed solutions on the lines for which $n = 0$, from which solutions on the lines $n \neq 0$ may be generated by the application of suitable Bäcklund transformations.

It is shown in [60] that the seed solutions on the two lines with $\varepsilon_1 = -\varepsilon_2$ and $n = 0$ in Figure 4.2 (lines with positive slopes) can be expressed in terms of modified Bessel functions of the first and second kinds (I_α and K_α, respectively). Specifically,

$$u(z; 1-c, -c-1) = -\frac{\phi'(z)}{\phi(z)}, \qquad u(z; c-1, c+1) = \frac{\phi'(z)}{\phi(z)}, \tag{4.65}$$

where

$$\phi(z) = C_1 z^{(1-c)/2} I_{(c-1)/2}(\pm z) + C_2 z^{(1-c)/2} K_{(c-1)/2}(\pm z), \tag{4.66}$$

and C_1 and C_2 are arbitrary constants. Note that we use the notation $u(z;\alpha,\beta)$ (for generic solutions of $\mathrm{P}_{\mathrm{III}}^{(\mathrm{i})}$) instead of $u^{(m)}(z;\alpha,\beta,k)$ (for LDT $\mathrm{P}_{\mathrm{III}}^{(\mathrm{i})}$ solutions) since we are yet to demonstrate that (4.65) can be expressed as LDT solutions. The solutions on the two lines with $\varepsilon_1=\varepsilon_2$ and $n=0$ (lines with negative slopes) can be expressed in terms of Bessel functions of the first and second kinds [60]:

$$u(z;1-c,c+1)=-\frac{\phi'(z)}{\phi(z)},\qquad u(z;c-1,-c-1)=\frac{\phi'(z)}{\phi(z)},\tag{4.67}$$

where

$$\phi(z)=C_1z^{(1-c)/2}J_{(c-1)/2}(\pm z)+C_2z^{(1-c)/2}Y_{(c-1)/2}(\pm z).\tag{4.68}$$

Since we restrict ourselves to the one-parameter solutions on the blue lines through the origin in Figure 4.2, we only consider the points at which the red lines intersect these blue lines. The seed solutions in (4.66) and (4.68) intersect the lines through the origin only if $c=0$. In this case, the (spherical) Bessel functions in (4.66) and (4.68) are elementary functions [8],

$$J_{-1/2}(z)=\sqrt{\frac{2}{\pi z}}\cos z,\quad Y_{-1/2}(z)=\sqrt{\frac{2}{\pi z}}\sin z,\quad I_{-1/2}(z)=\sqrt{\frac{2}{\pi z}}\cosh z,\quad K_{-1/2}(z)=\sqrt{\frac{\pi}{2z}}e^{-z},$$

and hence the seed solutions (4.66) and (4.68) can be expressed as, respectively, [60]

$$u(z;\varepsilon,-\varepsilon)=-\varepsilon\frac{a\cosh z+b\sinh z}{a\sinh z+b\cosh z},\qquad \varepsilon^2=1,\tag{4.69}$$

and

$$u(z;\varepsilon,\varepsilon)=-\varepsilon\frac{a\cos z-b\sin z}{a\sin z+b\cos z},\qquad \varepsilon^2=1.\tag{4.70}$$

The four different seed solutions represented by (4.69) and (4.70) are scaled and rotated versions of each other since $\cosh z=\cos iz$ and $\sinh z=-i\sin iz$. Hence, we need to consider only one seed solution. Recall that our aim is to show that a set of Bessel function solutions coincides with the LDT solutions (4.63), which have negative half-integer ν values that are located at the open circles in Figure 4.2. We therefore choose the seed solution whose parameter values and leading order asymptotic behaviour far out in the right half-plane coincides with that of the LDT solution (4.63) with $n=0$. That is, we consider the seed solution (4.69) with $\varepsilon=-1$, which, in parameter space, is located at the first open circle in Figure 4.2. By multiple applications of T_{-1}, defined in (4.61), to this seed solution we obtain solutions whose parameter values coincide with the LDT solutions (4.63):

$$u(z;-1-2n,1+2n)=T_{-1}^{n}u(z;-1,1).\tag{4.71}$$

The first two of these solutions (those for which $n = 0, 1$) are at the two open circles in Figure 4.2. By an appropriate relabelling of the constants in (4.69), the seed solution can be expressed in the form of the LDT one-parameter solution (4.63):

$$u(z;-1,1) = \frac{1-\left(\frac{b-a}{a+b}\right)e^{-2z}}{1+\left(\frac{b-a}{a+b}\right)e^{-2z}} = \frac{1-(C/2)e^{-2z}}{1+(C/2)e^{-2z}} := u(z;-1,1,C) \tag{4.72}$$

$$= 1 - Ce^{-2z} + \mathcal{O}\left(e^{-4z}\right), \tag{4.73}$$

for $z \to \infty$ in the right half-plane. Since $p_0(z) = 1$ in (4.63), the large-z expansions in (4.63) and (4.73) match up to $\mathcal{O}\left(e^{-2z}\right)$ terms if $k = C$. A similar conclusion holds for the special function solutions (4.71) with $n > 0$, as we show in Lemma 2 in section 4.6:

$$u(z;-1-2n,1+2n,C) = T_{-1}^n u(z;-1,1,C) = 1 - CP_n(z)e^{-2z} + \mathcal{O}\left(e^{-4z}\right), \tag{4.74}$$

where $P_n(z) = \frac{(-4)^n}{n!}p_n(z)$, for $z \to \infty$, $-\frac{\pi}{2} < \arg z < \frac{\pi}{2}$. Hence, the expansions (4.63) and (4.74) match up to $\mathcal{O}\left(e^{-2z}\right)$ terms if $k = \frac{(-4)^n}{n!}C$. If the ansatz in (4.51) (which reduces to (4.63) if ν has negative half-integer values) is appropriately generalized to include higher order exponential terms,

$$u^{(0)}(z;2\nu,-2\nu,k) \sim 1 - \sum_{m=1}^{\infty}\left(kz^{-\nu-1/2}e^{-2z}\right)^m\left(1+\sum_{j=1}^{\infty}c_{j,m}^{(0)}(\nu)z^{-j}\right), \qquad z\to\infty, \tag{4.75}$$

then the expansions (4.63) and (4.74) match to all orders since the expansion (4.75) is unique. Hence, the special function solutions at the open circles, (4.74), coincide with the one-parameter LDT solutions (4.63):

$$u(z;-1-2n,1+2n,C) = u^{(0)}\left(z;-1-2n,1+2n,\frac{(-4)^n}{n!}C\right). \tag{4.76}$$

Figure 4.5 shows the meromorphic elementary function $\mathrm{P}_{\mathrm{III}}^{(\mathrm{i})}$ solutions defined by (4.74) for $n = 0, 1, 2$. Letting $x := (C/2)e^{-2z}$ for brevity, these solutions are given by

$$u(z;-1,1,C) = \frac{1-x}{1+x}, \tag{4.77}$$

$$u(z;-3,3,C) = u(z;-1,1,C)\,\frac{x^2-4zx-1}{x^2+4zx-1}, \tag{4.78}$$

$$u(z;-5,5,C) = \frac{u(z;-3,3,C)}{u(z;-1,1,C)}\,\frac{-x^3+(8z^2+4z+1)x^2+(8z^2-4z+1)x-1}{x^3+(8z^2+4z+1)x^2-(8z^2-4z+1)x-1}. \tag{4.79}$$

Since the solutions with $C > 0$ and $C < 0$ are related through the reciprocal transformation, see (4.54) and (4.77)–(4.79), we let $C > 0$ in Figure 4.5. The fact that the solutions in

Figure 4.5 have infinitely many poles is in accordance with a result in [56]: if $\alpha\gamma \neq 0$, then every meromorphic solution of $\mathrm{P_{III}}$ that is not rational will have an infinite number of poles.

We find similar coalescences of poles and zeros in Figure 4.5 that we found for the rational solutions in Figure 4.4. Besides the poles and zeros of opposite residues and derivative values that cancel when they coalesce, we find that if n is even (first and third rows of Figure 4.5), a zero is admitted at the origin when $C = 2$ with a derivative value, according to (4.6), of

$$c_1 = -\frac{\delta}{\beta} = \frac{1}{2n+1},$$

which results from the coalescence of $2n+1$ zeros with $u' = 1$. Similarly, if n is odd (second row of Figure 4.5), then a pole at the origin with residue, according to (4.5), of

$$c_{-1} = -\frac{\alpha}{\gamma} = 2n+1,$$

results from the coalescence of $2n+1$ poles of residue $+1$ if $C = 2$. By comparing the leftmost and rightmost frames in the first to third rows of Figure 4.5, we find that the poles and zeros that coalesce are rotated through an angle of π in the two frames.

The fourth row shows phase portraits of the solutions in the third row. These figures illustrate that the solutions have positive real values far out in the right half-plane, as expected from (4.74), and negative real values far out in the left half-plane. These phase portraits suggest that the auto-Bäcklund transformation

$$u(z; -1-2n, 1+2n, C) = -u(-z; -1-2n, 1+2n, 4/C) \tag{4.80}$$

holds, which can be verified in (4.77)–(4.79). This auto-Bäcklund transformation describes the relationship between different solutions if $C \neq 4/C$ (e.g., those in the leftmost and rightmost frames in Figure 4.5) and same solution if $C = 4/C$ (e.g., the central frames in Figure 4.5).

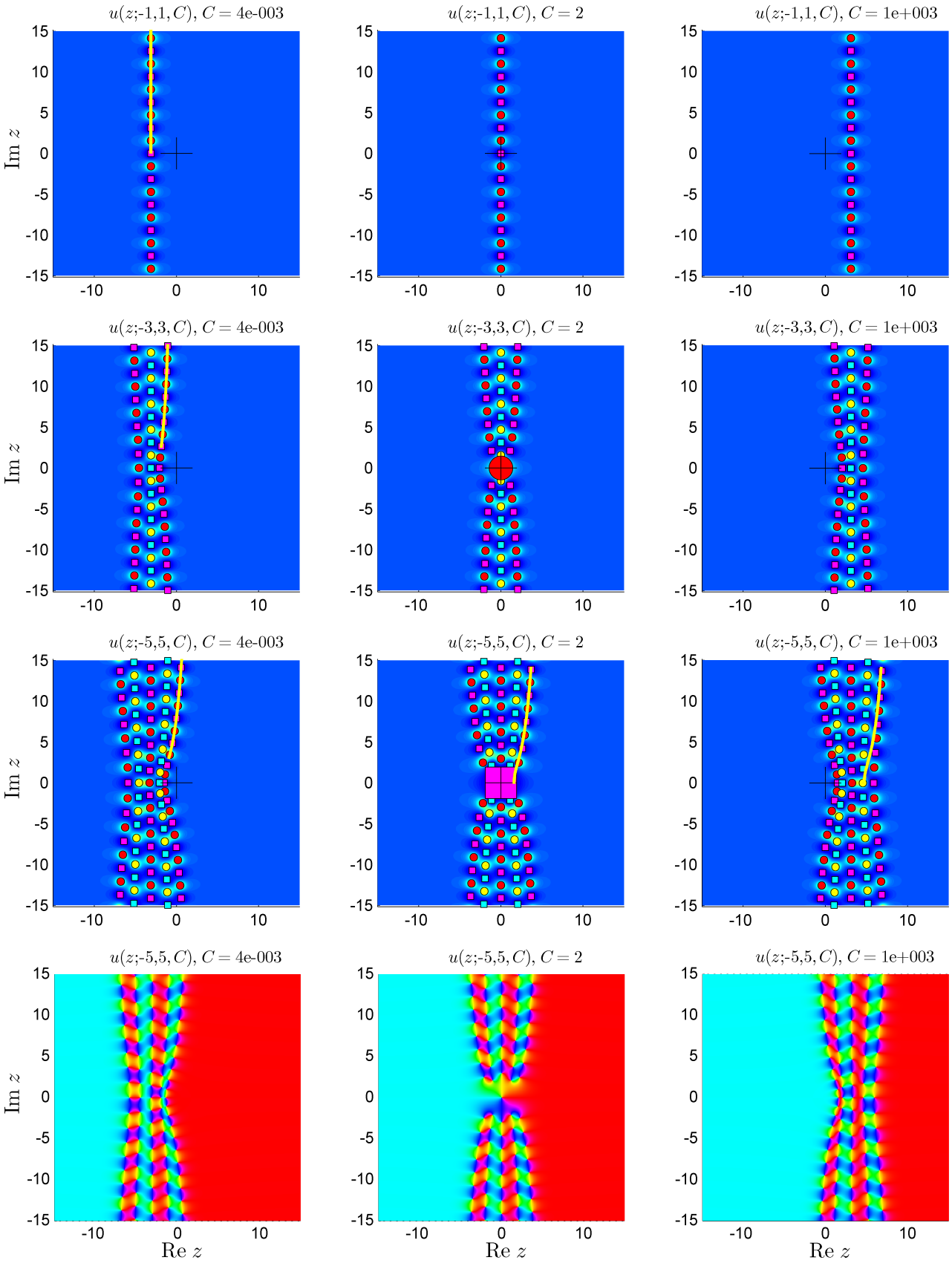

Figure 4.5: The pole field dynamics of the meromorphic, elementary-function, one-parameter LDT solutions in (4.77)–(4.79) that are special cases of Bessel function $\mathrm{P}_{\mathrm{III}}^{(\mathrm{i})}$ solutions. The fourth row shows phase portraits (whose colour wheel is above Figure 4.1) of the solutions in the third row. The purpose of the yellow curves in the first to third rows will be clarified in section 4.5.3. The solutions in the left and right columns of each row are related according to (4.80), while (4.80) relates the left and right half-planes of the solutions in the central frames.

4.5.3 Pole-free regions

The distinctive feature of the one-parameter LDT solutions satisfying (4.51) is their pole-free regions in the right half-plane. The solution is pole-free sufficiently far out along any ray $z = re^{i\theta}$ with $|\theta| < \frac{\pi}{2}$ since the exponential-order terms of (4.51) can be made arbitrarily small for sufficiently large r. Nevertheless, a great variety of pole-free regions are admitted by solutions satisfying (4.51). For example, Figure 4.5 shows[3] significant variation in the pole-free region as a function of the parameters with right half-planes that are entirely pole-free (top-left frame) or that contain infinitely many poles within a strip Re $z < a$, $a > 0$ (right column).

The dependence of the pole-free regions on the parameters can be understood intuitively and analytically by considering only the second term of the asymptotic expansion (4.51):

$$m(z;\nu,k) := kz^{-\nu-1/2}e^{-2z}, \tag{4.81}$$

from which a $\mathcal{O}\left(m(z;\nu,k)/z\right)$ estimate of the solution can be constructed,

$$1 + m(z;\nu,k) = u^{(0)}(z;2\nu,-2\nu,k) + \mathcal{O}\left(\frac{m(z;\nu,k)}{z}\right), \qquad -\frac{\pi}{2} < \arg z < \frac{\pi}{2}, \qquad z \to \infty. \tag{4.82}$$

On the region $|\theta| > \frac{\pi}{2}$, the error of the estimate (4.82) becomes unbounded as $z \to \infty$. However, we shall find that in the finite plane, the estimates derived from (4.82) can also be reasonably accurate in the left half-plane.

In the finite plane, especially close to the imaginary axis (where the modulus of e^{-2z} is not very small), the modulus of $m(z;\nu,k)$ can be non-negligible if k is large or ν is negative, which accounts for the presence of poles in the right half-plane in the right column of Figure 4.5. Furthermore, close the imaginary axis, the modulus of $m(z;\nu,k)$, and thus the pole-free regions, can vary greatly as a function of k and ν. For example, in each row of Figure 4.5, $k = \frac{(-4)^n}{n!}C$ (see (4.76)) varies through almost six orders of magnitude, which results in noticeable horizontal displacements of the pole-free regions. Down each column of Figure 4.5, n increases (see (4.74)), thus ν decreases (see (4.62)), which increases the modulus of $m(z;\nu,k)$ and results in a decrease of the angular width of the pole-free regions in the finite plane. In this section we derive estimates of these changes in the pole-free regions as functions of the parameters.

[3] Recall from (4.76) that the solutions in Figure 4.5 are special cases of the one-parameter LDT solutions in (4.51).

Horizontal displacement

If ν is fixed and k is scaled by e^{2t}, $t \in \mathbb{R}$, then

$$\begin{aligned} m(z;\nu,e^{2t}k) &= kz^{-\nu-1/2}e^{-2(z-t)} = \left(\frac{z}{z-t}\right)^{-\nu-1/2} m(z-t;\nu,k), \\ &= \left(1-\frac{t}{z}\right)^{\nu+1/2} m(z-t;\nu,k), \\ &= m(z-t;\nu,k) + \mathcal{O}\left(\frac{t}{z}\right), \qquad |z| \gg |t|. \end{aligned} \tag{4.83}$$

We conclude from (4.83) and (4.82) that the pole-free region is displaced horizontally by approximately t units if k is scaled by e^{2t} and this approximation improves as $|z|$ increases.

In each row of Figure 4.5, $k = \frac{(-4)^n}{n!}C$ is scaled by 5×10^2 from one frame to the next and thus we expect an approximate horizontal displacement of the pole-free region by

$$t = \frac{1}{2}\log(5 \times 10^2) \approx 3.11. \tag{4.84}$$

For the solution in the first row of Figure 4.5, this estimate is exact since it follows from (4.77) that

$$u(z;-1,1,e^{2t}C) = u(z-t;-1,1,C).$$

Figure 4.6 shows the error of the estimate (4.84) for the horizontal displacement of the pole-free regions for the solutions in the second and third rows of Figure 4.5. These errors are computed as follows:

1. Represent the boundary of the pole-free region in the left column (of the second and third rows in Figure 4.5) by an interpolant through the rightmost poles and zeros. We let the interpolant be a cubic spline.

2. Translate the interpolant to the right by t units (for the solution in the middle frame) or $2t$ units (for the solution in the right frame), where t is given by (4.84). The translated interpolants are shown in row 3, columns 2 and 3 of Figure 4.5. Then measure the horizontal differences between the translated interpolants and the rightmost poles and zeros of the solutions in the second and third columns of Figure 4.5. For example, the 9 blue stars in Figure 4.6 represent the differences between the real parts of the 9 rightmost poles and zeros (on $\mathbb{R}$ and in the upper half-plane) of the solution in row 3, column 2 of Figure 4.6 and the translated interpolant.

The dotted line in Figure 4.6 shows the expected $\mathcal{O}(z^{-1})$ asymptotic error decay that follows from (4.82) and (4.83). Figure 4.6 shows that the error of the estimate increases from column 2 to column 3 for a given row and from row 2 to row 3 for a given column. This is consistent with (4.82) since the modulus of $m(z;\nu,k)$ increases along the rows and columns.

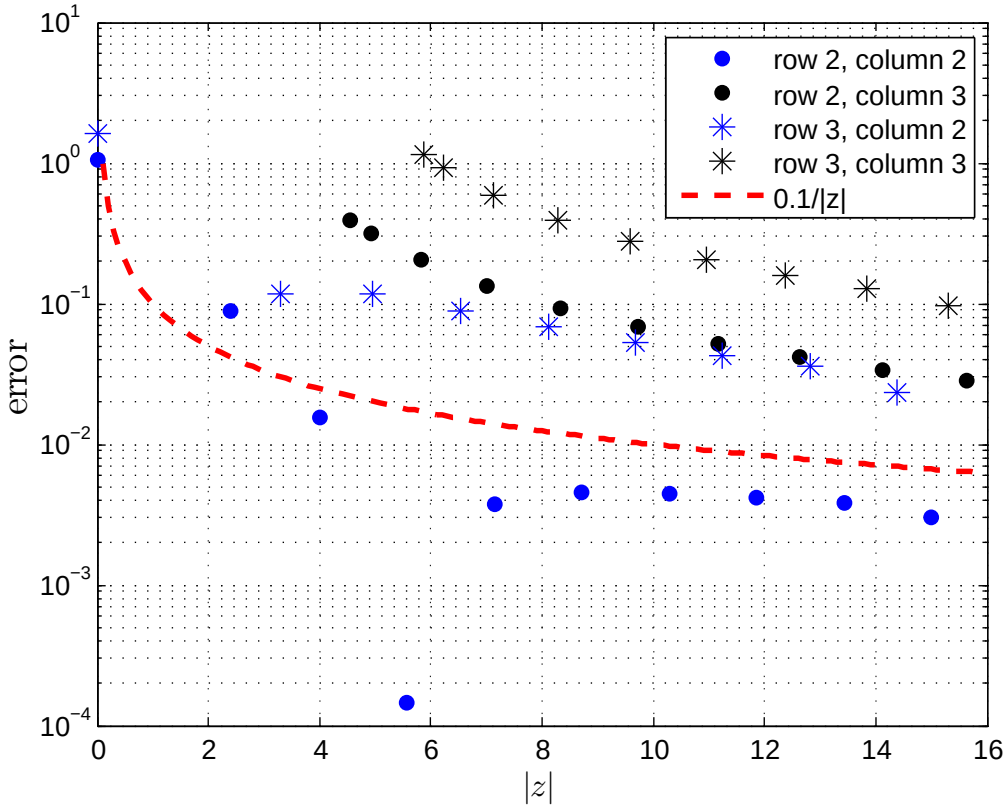

Figure 4.6: The error of the estimate (4.84) of the horizontal displacement of the pole-free regions in the second and third rows of Figure 4.5.

Angular displacement

Down a given column in Figure 4.5, C is fixed, n (see (4.76)) increases by increments of one, $k = \frac{(-4)^n}{n!}C$ (see (4.76)) and $\nu = -\frac{1}{2} - n$ (see (4.62)). Hence, the angular displacement of the modulus of $m(z;\nu,k)$, defined in (4.81), between successive rows in each column of Figure 4.5

can be found by solving the following equation for δ:

$$\begin{aligned}\frac{\left|m(re^{i(\theta+\delta)};-n-\frac{3}{2},\frac{(-4)^{n+1}}{(n+1)!}C)\right|}{\left|m(re^{i\theta};-n-\frac{1}{2},\frac{(-4)^{n}}{n!}C)\right|} &= \frac{\left|\frac{(-4)^{n+1}}{(n+1)!}C\right| r^{n+1}\exp[-2r\cos(\theta+\delta)]}{\left|\frac{(-4)^{n}}{n!}C\right| r^{n}\exp[-2r\cos\theta]},\\ &= \frac{4r}{n+1}\exp[-2r(\cos(\theta+\delta)-\cos\theta)], \qquad (4.85)\\ &= 1.\end{aligned}$$

We find that

$$\delta=\delta(r,\theta,n)=\cos^{-1}\left\{-\frac{1}{2r}\log\left[\frac{n+1}{4r}\right]+\cos\theta\right\}-\theta, \qquad \theta\in[0,\pi]. \qquad (4.86)$$

Due to the up-down symmetry of the modulus of the solutions in Figure 4.5, it is sufficient to consider $\theta\geq 0$ in (4.86). It follows from (4.81) and (4.82) that (4.86) is a valid estimate for the angular displacement of the modulus of the solution in the limit $r\to\infty$ only if $-\frac{\pi}{2}<\theta<\frac{\pi}{2}$; in this limit there is no angular displacement,

$$\lim_{r\to\infty}\delta(r,\theta,n)=0, \qquad 0\leq\theta<\frac{\pi}{2}.$$

In the finite plane, we shall estimate the angular displacement of the pole-free regions using (4.86), not only for $|\theta|<\frac{\pi}{2}$ but also for $|\theta|\geq\frac{\pi}{2}$.

Close to the imaginary axis, i.e., for $\theta=\frac{\pi}{2}-\epsilon$ with $0\leq|\epsilon|\ll 1$ (we also consider $\epsilon\leq 0$ since we allow $|\theta|\geq\frac{\pi}{2}$ in the finite plane), (4.86) can be simplified by noting in (4.85) that

$$\cos(\theta+\delta)-\cos\theta=\cos(\tfrac{\pi}{2}-\epsilon+\delta)-\cos(\tfrac{\pi}{2}-\epsilon)=\sin(\epsilon-\delta)-\sin\epsilon=-\delta+\mathcal{O}[(\epsilon-\delta)^3-\epsilon^3],$$

from which we obtain (cf. (4.86))

$$\delta\approx\frac{1}{2r}\log\left[\frac{n+1}{4r}\right], \qquad \theta=\frac{\pi}{2}-\epsilon, \qquad 0\leq|\epsilon|\ll 1 \qquad (4.87)$$

If $\theta=\frac{\pi}{2}$, then $\epsilon=0$ and it can be seen from (4.85) that (4.86) becomes

$$\delta=\sin^{-1}\left\{\frac{1}{2r}\log\left[\frac{n+1}{4r}\right]\right\}.$$

The estimate (4.87) shows that $\delta<0$ for $4r>n+1$. This is consistent with what is observed down each column of Figure 4.5 since there is a negative angular displacement of the pole-free regions. The first two rows of Figure 4.7 show the estimated angular displacements (4.86) of the boundaries of the pole-free regions in Figure 4.5 and the third row of Figure 4.7 gives the errors of the resulting approximations to the boundaries of the pole-free regions. The results in Figure 4.7 were obtained as follows.

1. Represent the boundary of the pole-free region of each solution in the first row of Figure 4.5 by constructing an interpolant through the rightmost poles and zeros on $\mathbb{R}$ and in the upper half-plane. The interpolant for the solution in the top-left frame is shown in Figure 4.5 as a yellow curve.

2. Angularly displace every point of the interpolant in the first row by $\delta(r, \theta, n)$, which is defined in (4.86), with $n = 0$, to obtain an approximation of the boundary of the pole-free region in the second row. Angularly displace every point of this (already angularly displaced) interpolant by $\delta(r, \theta, n)$, with $n = 1$, to approximate the pole-free region in the third row. Examples of these angularly displaced interpolants are shown in column 1, rows 2 and 3 of Figure 4.5. The angular displacements of the interpolants in the first and second rows of Figure 4.5 are shown in blue in the corresponding rows of Figure 4.7. As expected from (4.87), which is plotted as red dotted lines in Figure 4.7, these angular displacements are negative and decrease monotonically for sufficiently large r.

3. Measure the horizontal differences between the angularly displaced interpolants and the rightmost poles and zeros. For example, the 9 blue dots in the bottom-left frame of Figure 4.6 are the horizontal differences between the yellow curve in row 2, column 1 of Figure 4.5 and its 9 overlapping poles and zeros. The magnitude of the errors in Figure 4.7 confirm that reasonable estimates of the changes of the pole-free regions down the columns in Figure 4.5 can be derived from (4.86).

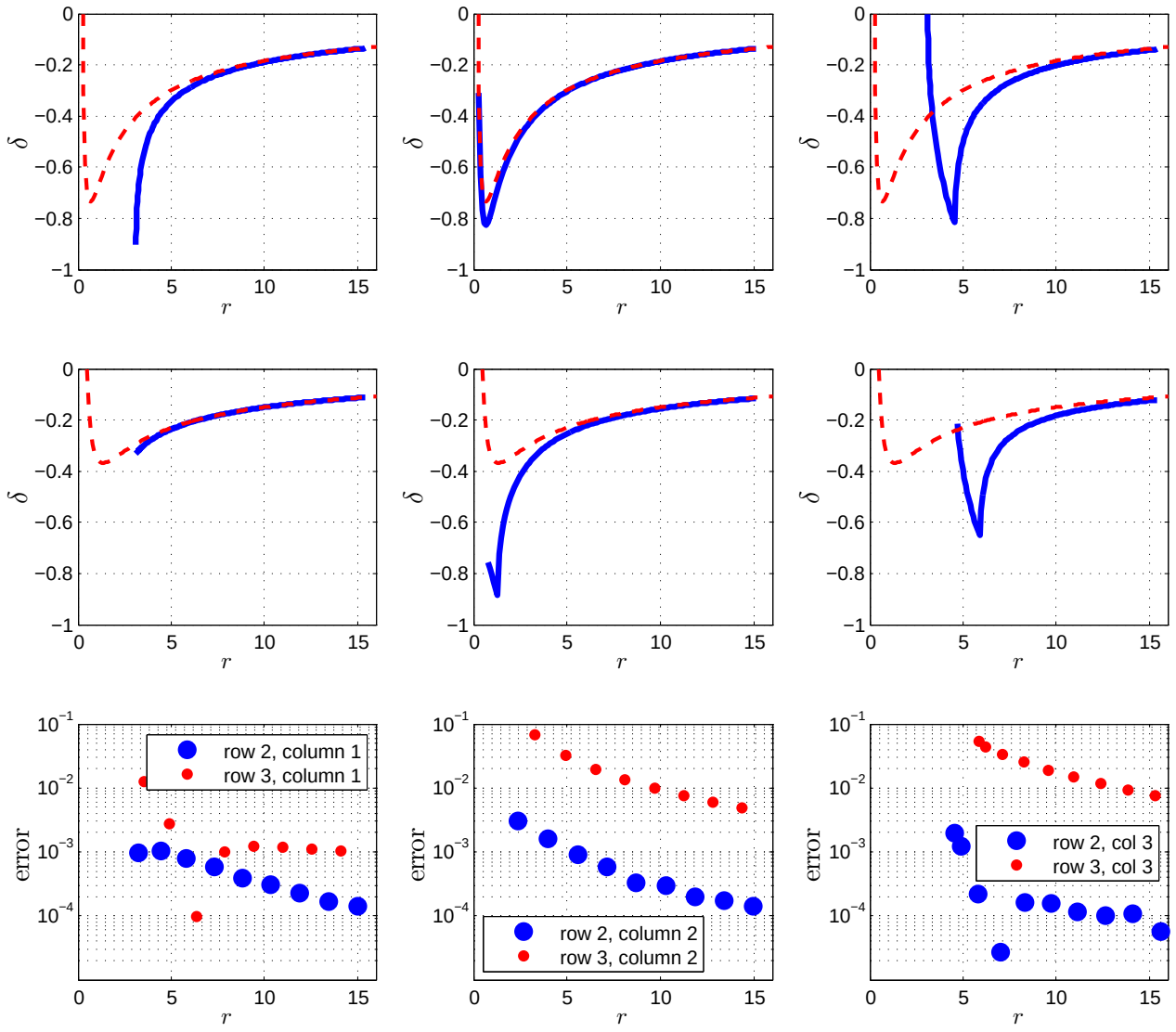

Figure 4.7: Rows 1 and 2: The angular displacements (4.86), shown in blue, of the estimated boundaries of the pole-free regions of the solutions in the corresponding rows in Figure 4.5 and the approximate angular displacements (4.87), shown in red. Row 3: The horizontal differences between the estimated boundaries of the pole-free regions and their overlapping poles and zeros.

4.6 Appendix

The following result will be used to give a direct proof of the relationships (4.32), (4.34)–(4.36).

Lemma 1. *The coefficients $a_j^{(m)}(\alpha,\beta)$ of the LDT algebraic expansion (4.27) have the following properties for $j \geq 0$:*

1. *If $\alpha = -\beta$, then $a_j^{(0)}(\alpha,\beta) = 0$, $j \geq 1$,*
2. $a_j^{(0)}(-\alpha,-\beta) = (-1)^j a_j^{(0)}(\alpha,\beta)$,
3. $a_j^{(2)}(\alpha,\beta) = (-1)^{j+1} a_j^{(0)}(\alpha,\beta)$,
4. $a_j^{(1)}(\alpha,-\beta) = i^{1-j} a_j^{(0)}(\alpha,\beta)$,
5. $a_j^{(3)}(-\alpha,\beta) = i^{1-j} a_j^{(0)}(\alpha,\beta)$.

Proof. Henceforth, we shall use the abbreviated notation $a_j^{(m)}$ for $a_j^{(m)}(\alpha,\beta)$. Substituting (4.27) into $\mathrm{P}_{\mathrm{III}}^{(\mathrm{i})}$, we find that $a_0^{(m)} = e^{\frac{m\pi i}{2}}$, $m = 0,1,2,3$ and we obtain the following formula for $a_j^{(m)}$, $j \geq 1$:

$$4\left(a_0^{(m)}\right)^3 a_j^{(m)} = T_{1,j}^{(m)} + T_{2,j}^{(m)} + T_{3,j}^{(m)} + T_{4,j}^{(m)} + T_{5,j}^{(m)}, \qquad j \geq 1, \tag{4.88}$$

$$T_{1,j}^{(m)} = T_{1,j}^{(m)}(\alpha,\beta) = -\sum_{k_3=0}^{j}\sum_{k_2=0}^{k_3}\sum_{k_1=0}^{k_2} a_{k_1}^{(m)} a_{k_2-k_1}^{(m)} a_{k_3-k_2}^{(m)} a_{j-k_3}^{(m)} + 4\left(a_0^{(m)}\right)^3 a_j^{(m)}, \; j \geq 2, \tag{4.89}$$

$$T_{2,j}^{(m)} = T_{2,j}^{(m)}(\alpha,\beta) = \sum_{k=3}^{j}(k-1)(k-2) a_{k-2}^{(m)} a_{j-k}^{(m)}, \qquad j \geq 3, \tag{4.90}$$

$$T_{3,j}^{(m)} = T_{3,j}^{(m)}(\alpha,\beta) = -\beta a_{j-1}^{(m)}, \qquad j \geq 1, \tag{4.91}$$

$$T_{4,j}^{(m)} = T_{4,j}^{(m)}(\alpha,\beta) = -\alpha\sum_{k_2=0}^{j-1}\sum_{k_1=0}^{k_2} a_{k_1}^{(m)} a_{k_2-k_1}^{(m)} a_{j-1-k_2}^{(m)}, \qquad j \geq 1, \tag{4.92}$$

$$T_{5,j}^{(m)} = T_{5,j}^{(m)}(\alpha,\beta) = -\sum_{k=2}^{j-1}(j-k)(k-1) a_{k-1}^{(m)} a_{j-1-k}^{(m)}, \qquad j \geq 3, \tag{4.93}$$

Note that the formula for $a_j^{(m)}$ is explicit, i.e., each term on the right-hand side of (4.88) is a function of coefficients $a_k^{(m)}$ with $k < j$.

To prove the first property of the coefficients, we set $j = 1,2$ in (4.88) and find, respectively,

$$4\left(a_0^{(m)}\right)^3 a_1^{(m)} = T_{3,1}^{(m)} + T_{4,1}^{(m)} = -\beta a_0^{(m)} - \alpha\left(a_0^{(m)}\right)^3, \tag{4.94}$$

and

$$4\left(a_0^{(m)}\right)^3 a_2^{(m)} = T_{1,2}^{(m)} + T_{3,2}^{(m)} + T_{4,2}^{(m)} = -6\left(a_0^{(m)}\right)^2\left(a_1^{(m)}\right)^2 - \beta a_1^{(m)} - 3\alpha\left(a_0^{(m)}\right)^2 a_1^{(m)}. \tag{4.95}$$

Setting $m = 0$ and $\alpha = -\beta$, it follows from (4.94) that $a_1^{(0)} = 0$ and then (4.95) implies that $a_2^{(0)} = 0$. Now it is easy to show by induction (or to see by inspection of (4.89)–(4.93)) that for $j \geq 3$, each term on the right-hand side of (4.88) is zero and hence $a_j^{(0)} = 0$, $j \geq 3$.

We now prove only the fourth property of the coefficients by induction since the proof of the remaining properties proceeds similarly. The fourth property holds for $j = 0, 1$ since $a_0^{(0)} = 1$, $a_0^{(1)} = i$ and (4.94) implies that $a_1^{(0)}(\alpha, \beta) = -(\alpha + \beta)/4$ and $a_1^{(1)}(\alpha, -\beta) = -(\alpha + \beta)/4 = a_1^{(0)}(\alpha, \beta)$. The induction hypothesis is that the fourth property holds for $0 \leq j - 1 \leq n$, for some $n \geq 0$ in which case it follows from (4.91) that

$$\begin{aligned}
T_{4,j}^{(1)}(\alpha, -\beta) &= -\alpha \sum_{k_2=0}^{j-1} \sum_{k_1=0}^{k_2} a_{k_1}^{(1)}(\alpha, -\beta) a_{k_2-k_1}^{(1)}(\alpha, -\beta) a_{j-1-k_2}^{(1)}(\alpha, -\beta) \\
&= -\alpha \sum_{k_2=0}^{j-1} \sum_{k_1=0}^{k_2} a_{k_1}^{(0)}(\alpha, \beta) a_{k_2-k_1}^{(0)}(\alpha, \beta) a_{j-1-k_2}^{(0)}(\alpha, \beta) i^{1-k_1+1-k_2+k_1+1-j+1+k_2} \\
&= -i^{-j}\alpha \sum_{k_2=0}^{j-1} \sum_{k_1=0}^{k_2} a_{k_1}^{(0)}(\alpha, \beta) a_{k_2-k_1}^{(0)}(\alpha, \beta) a_{j-1-k_2}^{(0)}(\alpha, \beta) \\
&= i^{-j} T_{4,j}^{(0)}(\alpha, \beta).
\end{aligned}$$

In a similar way it can be shown that the terms $T_{k,j}^{(1)}(\alpha, -\beta)$, $k = 1, 2, 3, 5$ have the same property, i.e.,

$$T_{k,j}^{(1)}(\alpha, -\beta) = i^{-j} T_{k,j}^{(0)}(\alpha, \beta), \qquad 1 \leq k \leq 5.$$

Then it follows from (4.88) that

$$\begin{aligned}
a_j^{(1)}(\alpha, -\beta) &= \frac{i}{4}\left[T_{1,j}^{(1)}(\alpha, -\beta) + T_{2,j}^{(1)}(\alpha, -\beta) + T_{3,j}^{(1)}(\alpha, -\beta) + T_{4,j}^{(1)}(\alpha, -\beta) + T_{5,j}^{(1)}(\alpha, -\beta)\right] \\
&= \frac{i^{1-j}}{4}\left[T_{1,j}^{(0)}(\alpha, \beta) + T_{2,j}^{(0)}(\alpha, \beta) + T_{3,j}^{(0)}(\alpha, \beta) + T_{4,j}^{(0)}(\alpha, \beta) + T_{5,j}^{(0)}(\alpha, \beta)\right] \\
&= i^{1-j} a_j^{(0)}(\alpha, \beta),
\end{aligned}$$

which completes the proof of the fourth property. □

Direct proof of (4.32), (4.34)–(4.36). We give the proof of (4.34) only since the proof of (4.32), (4.35)–(4.36) is, mutatis mutandis, the same.

It follows from the third property of the coefficients in Lemma 1 and Theorem 2 that for $z \in \Omega_n^{(2)}$ and $z \to \infty$,

$$u^{(2)}(z; \alpha, \beta, 0) \sim \sum_{j=0}^{\infty} a_j^{(2)}(\alpha, \beta) z^{-j} = -\sum_{j=0}^{\infty} a_j^{(0)}(\alpha, \beta)(-z)^{-j} \sim -u^{(0)}(-z; \alpha, \beta, 0). \tag{4.96}$$

The algebraic expansion in powers z^{-1} defines the $k = 0$ solutions to all orders (recall from (4.31) that the $k = 0$ solutions have no exponential-order terms). Hence, if the algebraic expansions of two $k = 0$ solutions match to all orders, then they must be identical since the asymptotic expansion in powers of z^{-1} is unique for a solution of $\mathrm{P}_{\mathrm{III}}^{(\mathrm{i})}$, as stated in Theorem 2. We conclude that $u^{(2)}(z;\alpha,\beta,0) = -u^{(0)}(-z;\alpha,\beta,0)$. □

Lemma 2. *Let $u(z;-1,1,C)$ be the solution defined in (4.72) and let $p_n(z)$ be the polynomial defined in (4.63). To simplify notation, this polynomial is henceforth denoted by $p_n(z) = \sum_{j=0}^{n} c_j z^{n-j}$, where the coefficients c_j are defined by (4.52) with $\nu = -\frac{1}{2} - n$, i.e.,*

$$c_{j+1} = -\frac{(n-j)^2}{4(j+1)} c_j, \qquad 0 \le j \le n-1, \qquad c_0 = 1. \tag{4.97}$$

Then

$$u(z;-1-2n,1+2n,C) = T_{-1}^{n} u(z;-1,1,C) = 1 - C P_n(z) e^{-2z} + \mathcal{O}\left(e^{-4z}\right), \tag{4.98}$$

for $z \to \infty$, $-\frac{\pi}{2} < \arg z < \frac{\pi}{2}$, where $P_n(z) = \frac{(-4)^n}{n!} p_n(z)$.

Proof. We prove the result by induction. Since $p_0(z) = c_0 = 1$, it follows from (4.63) and (4.73) that $P_0(z) = p_0(z)$ if we set $k = C$ and thus the result is valid for $n = 0$. Let $P_n(z) = \sum_{j=0}^{n} c_j^{(n)} z^{n-j}$ and suppose that (4.98) holds for some $n \ge 1$ with $P_n(z) = \frac{(-4)^n}{n!} p_n(z)$ if we set $k = C$. Then, substituting (4.98) into the Bäcklund transformation (4.61) with $\varepsilon = -1$, we find that

$$\begin{aligned} u(z;-1-2(n+1),1+2(n+1),C) &= T_{-1} u(z;-1-2n,1+2n,C) \\ &= 1 - C P_{n+1}(z) e^{-2z} + \mathcal{O}\left(e^{-4z}\right), \end{aligned}$$

for $z \to \infty$, $-\frac{\pi}{2} < \arg z < \frac{\pi}{2}$, where

$$P_{n+1}(z) = P_n(z) - \frac{z}{n+1}\left[4P_n(z) - P_n'(z)\right]. \tag{4.99}$$

The recurrence (4.99) implies that

$$c_{j+1}^{(n+1)} = c_j^{(n)} - \frac{4}{n+1} c_{j+1}^{(n)} + \frac{n-j}{n+1} c_j^{(n)}, \qquad 0 \le j \le n-1, \tag{4.100}$$

and

$$c_0^{(n+1)} = -\frac{4}{n+1} c_0^{(n)}, \qquad c_{n+1}^{(n+1)} = c_n^{(n)}. \tag{4.101}$$

Since the induction hypothesis is that $P_n(z) = \frac{(-4)^n}{n!} p_n(z)$, the formula (4.97) also holds for the coefficients of $P_n(z)$, except that $c_0^{(n)} = \frac{(-4)^n}{n!}$. Using this and (4.100) and (4.101), it is straightforward to show that

$$c_{j+1}^{(n+1)} = -\frac{(n+1-j)^2}{4(j+1)} c_j^{(n+1)}, \qquad 0 \le j \le n, \qquad c_0^{(n+1)} = \frac{(-4)^{n+1}}{(n+1)!}. \tag{4.102}$$

Comparing (4.102) and (4.97) with $n+1$ we deduce that $P_{n+1}(z) = \frac{(-4)^{n+1}}{(n+1)!} p_{n+1}(z)$, which concludes the proof. □

Chapter 5

A computational survey of the MTW tronquée solutions of $\mathrm{P}_{\mathrm{III}}^{(\mathrm{i})}$

In the introduction of the previous chapter we noted that there are two strands of research on the asymptotics of the Painlevé transcendents: one concerned with asymptotic expansions in the complex plane and the other with asymptotic connection formulae between two endpoints of an axis. The results of Lin, Dai and Tibboel in [54] that we presented in the previous chapter (on LDT solutions) fall into the former category of research whereas the results of McCoy, Tracy and Wu in [59] to be presented in this chapter (on the MTW solutions) are from the latter category. The relationship between the LDT and MTW solutions can be understood by comparing their asymptotic formulae.

It was shown in Theorem 4 that the one-parameter LDT solutions of $\mathrm{P}_{\mathrm{III}}^{(\mathrm{i})}$ (i.e., $\mathrm{P}_{\mathrm{III}}$ with $\gamma = 1 = -\delta$) on the line

$$\alpha = -\beta = 2\nu, \tag{5.1}$$

in parameter space that asymptote to 1 in the right half-plane satisfy, for $z \to \infty$,

$$u^{(0)}(z; 2\nu, -2\nu, k) \sim 1 - kz^{-\nu-1/2}e^{-2z}\Big(1 + \sum_{j=1}^{\infty} c_j^{(0)}(\nu) z^{-j}\Big), \qquad -\frac{\pi}{2} < \arg z < \frac{\pi}{2}, \tag{5.2}$$

where

$$c_{j+1}^{(0)}(\nu) = -\frac{(2\nu + 2j + 1)^2}{16(j+1)} c_j^{(0)}(\nu), \qquad j \geq 0, \qquad c_0^{(0)}(\nu) = 1. \tag{5.3}$$

The MTW solutions of $\mathrm{P}_{\mathrm{III}}^{(\mathrm{i})}$ have parameters (5.1) and their asymptotic behaviour far out on the positive real axis ($\mathbb{R}^+$) is [59]

$$u(x; \nu, \lambda) \sim 1 - \lambda\, \Gamma\big(\nu + \tfrac{1}{2}\big)\, 2^{-2\nu} x^{-\nu-1/2} e^{-2x}, \qquad x \to +\infty, \tag{5.4}$$

where λ is an arbitrary parameter that we restrict to real values in this chapter.

By comparing (5.4) and (5.2), note that by setting $k = \lambda\,\Gamma\big(\nu+\frac{1}{2}\big)\,2^{-2\nu}$ the two leading order terms of the expansions coincide on $\mathbb{R}^+$. Similar to what we did in the previous chapter (in obtaining (4.49) from (4.31)), to improve the accuracy of (5.4) for numerical purposes we use the ansatz

$$u(x;\nu,\lambda) \sim 1 - \lambda\,\Gamma\big(\nu+\tfrac{1}{2}\big)\,2^{-2\nu}x^{-\nu-1/2}e^{-2x}\Big(1+\sum_{j=1}^{\infty}c_j(\nu)x^{-j}\Big), \qquad x\to+\infty, \tag{5.5}$$

to obtain higher order terms. Hence, the initial conditions used to compute the MTW solutions in this chapter with the enhanced PFS method (in the ζ-plane, as described in section 3.1) are obtained by evaluating u and u' on $\mathbb{R}^+$ (which are then transplanted to the ζ-plane) from (5.5) by using the optimal truncation rule. Since the expansions (5.5) and (5.2) are identical upon setting $k = \lambda\,\Gamma\big(\nu+\frac{1}{2}\big)\,2^{-2\nu}$, the coefficients $c_j(\nu)$ are defined by (5.3) (with $c_j^{(0)}$ replaced by c_j). The gamma function, which features in (5.5), has simple poles at the non-positive integers, and thus the MTW solutions are undefined for negative half-integer ν values. Since the expansions (5.5) and (5.2) match to all orders on $\mathbb{R}^+$, we conclude that, except for negative half-integer ν values, the MTW solutions and the one-parameter LDT solutions in (5.2) coincide:

$$u^{(0)}\left(z;2\nu,-2\nu,\lambda\,\Gamma\big(\nu+\tfrac{1}{2}\big)\,2^{-2\nu}\right) = u(z;\nu,\lambda), \qquad \nu\neq-\frac{1}{2}-n, \qquad n\geq 0. \tag{5.6}$$

Hence, we may replace the expansion (5.5), which is valid on $\mathbb{R}^+$, by one that is valid far out in the right half-plane,

$$u(z;\nu,\lambda) \sim 1 - \lambda\,\Gamma\big(\nu+\tfrac{1}{2}\big)\,2^{-2\nu}z^{-\nu-1/2}e^{-2z}\Big(1+\sum_{j=1}^{\infty}c_j(\nu)z^{-j}\Big), \quad z\to\infty, \quad -\frac{\pi}{2}<\arg z<\frac{\pi}{2}. \tag{5.7}$$

The simple relationships between the LDT solutions in (5.2), which are the MTW solutions if $\nu\neq-\frac{1}{2}-n$, and other one-parameter LDT solutions on the lines $\alpha=-\beta=2\nu$ and $\alpha=\beta=2\nu$ in parameter space (see (4.49)–(4.50)) are given in Theorem 4. We shall illustrate that the Bessel function one-parameter LDT solutions with $\nu=-\frac{1}{2}-n$ that were studied in section 4.5.2 can be considered as a set of limiting MTW solutions.

For the MTW solutions we have additional asymptotic information that was not given in [54] for the LDT solutions: associated with every (ν,λ) in (5.7), where $\nu\neq-\frac{1}{2}-n$, there is a corresponding asymptotic connection formula, to be presented in section 5.1, that gives the solution behaviour in the small-z limit. In section 5.6, this formula will be crucial to proving

certain symmetry properties between different Riemann sheets of algebraically branched MTW solutions.

We reiterate that the paper [59] introducing the MTW solutions is cited in [30] as a major breakthrough in the study of the Painlevé equations since it was the first rigorous derivation of connection formulae for a Painlevé transcendent. In addition, these connection formulae arose in earlier work on the 2D Ising model in [11, 91], which may be the first appearance of a Painlevé transcendent in a physical application. It is remarked in [30] that the connection formulae in [59] were derived before the discovery of the Riemann-Hilbert, or isomonodromy, formalism for the Painlevé equations, which is a modern analytical tool that is used, inter alia, for the derivation of connection formulae. As pointed out in [16], an earlier analytical tool that has been superseded by the isomonodromy method, and that was also used, among other things, for the derivation of connection formulae, is the connection, discovered by Ablowitz and Segur in [1], between the Painlevé equations and nonlinear partial differential equations that are solvable by inverse scattering. However, this earlier analytical insight was not used to obtain the connection formulae in [59].

This chapter is structured as follows. The MTW small-z connection formulae are presented first. Then, since the MTW solutions are undefined for negative half-integer ν values, we divide the parameter space into the cases $\nu > -\frac{1}{2}$, $\nu < -\frac{1}{2}$ and the limiting cases $\nu = -\frac{1}{2} - n$. For each of these cases we let the arbitrary parameter λ in (5.7) be real, hence we survey a subset of $\mathbb{R}^2$ in the parameter space of the MTW solutions. We consider only $\lambda > 0$ since, as shown in [59],

$$u(z;\nu,-\lambda) = \frac{1}{u(z;\nu,\lambda)}, \tag{5.8}$$

which also follows from (4.54) since the MTW solutions are a set of LDT solutions. Recall from the previous chapter that if $\lambda = 0$ then we obtain the unique tronquée solution in part (2) of Theorem 2, which for the MTW solutions is the rational solution $u = 1$, as can be seen in (5.7). By using the enhanced PFS method, we first explore the MTW solutions for these cases on the 0th Riemann sheet, $-\pi/2 < \arg z \leq \pi/2$, and then on multiple sheets ($|\arg z| > \pi/2$).

5.1 The MTW small-z connection formulae

5.1.1 $0 < \lambda < 1/\pi$ or $0 < \sigma < 1$

The $\mathrm{P}_{\mathrm{III}}^{(\mathrm{i})}$ equation with MTW parameters (5.1) admits the formal small-z expansion [59]

$$u\left(z/2\right) \sim Bz^{\sigma}\left\{1+\sum_{j=1}^{\infty}\sum_{k=1}^{j+1} b_{j,k} z^{j-\sigma(j+2-2k)}\right\}, \qquad z\to 0, \qquad -1<\mathrm{Re}\ \sigma<1, \tag{5.9}$$

where B is arbitrary and the $b_{j,k}$ are unique functions of σ, ν and B. As stated in [59] and proved in Lemma 5 of section 5.8, it transpires that $b_{j,1}=0$, $j\geq 3$, which implies that there are no terms of the form $z^{n-n\sigma}$ for $n\geq 3$, and thus (5.9) becomes

$$u(z/2) = Bz^{\sigma}\left\{1+b_{1,1}z^{1-\sigma}+b_{1,2}z^{1+\sigma}+b_{2,1}z^{2-2\sigma}+\mathcal{O}\left(z^2\right)\right\}, \qquad -1<\mathrm{Re}\ \sigma<1, \tag{5.10}$$

where, as shown in (5.77) and (5.78) and reported in [59],

$$Bb_{1,1} = -\frac{\nu}{(1-\sigma)^2}, \qquad Bb_{1,2} = \frac{B^2\nu}{(\sigma+1)^2}, \qquad \text{and} \qquad Bb_{2,1} = \frac{1}{B}\left[\frac{4\nu^2-(\sigma-1)^2}{16(\sigma-1)^4}\right]. \tag{5.11}$$

For generic $\mathrm{P}_{\mathrm{III}}^{(\mathrm{i})}$ solutions, B is arbitrary and the only restriction on σ is given in (5.9). However, if the bounded large-z behaviour of the solution is given by (5.4), then σ and B are no longer arbitrary but they become functions of λ and ν. Specifically, as demonstrated in [59], the connection formulae relating the large-z behaviour, (5.4), and the small-z behaviour, (5.9), are given by

$$\sigma = \sigma(\lambda) = \frac{2}{\pi}\arcsin(\pi\lambda), \tag{5.12}$$

and

$$B = B(\sigma,\nu) = 2^{-3\sigma}\frac{\Gamma^2\left(\frac{1}{2}(1-\sigma)\right)\Gamma\left(\frac{1}{2}(1+\sigma)+\nu\right)}{\Gamma^2\left(\frac{1}{2}(1+\sigma)\right)\Gamma\left(\frac{1}{2}(1-\sigma)+\nu\right)}. \tag{5.13}$$

Since we let $\lambda>0$, we only consider (5.10)–(5.13) for $0<\sigma<1$, or $0<\lambda<1/\pi$. Hereafter we use the notations $u(z;\nu,\lambda)$ and $u(z;\nu,\sigma)$ interchangeably to denote the MTW solutions.

Note from (5.13) that $B(\sigma,\nu)$ vanishes when $\Gamma\left(\frac{1}{2}(1-\sigma)+\nu\right)$ is singular, i.e.,

$$B(\sigma,\nu)\to 0, \qquad \sigma\to\sigma_c = 2\nu+2n+1, \qquad -n-\frac{1}{2}<\nu<-n, \qquad n\geq 0, \tag{5.14}$$

where the inequality follows from the condition $0<\sigma_c<1$. Likewise, $B(\sigma,\nu)$ becomes unbounded if a pole of $\Gamma\left(\frac{1}{2}(1+\sigma)+\nu\right)$ is approached:

$$|B(\sigma,\nu)|\to\infty, \qquad \sigma\to\sigma_c = -2\nu-2n-1, \qquad -n-1<\nu<-n-\frac{1}{2}, \qquad n\geq 0. \tag{5.15}$$

The behaviour of the coefficients $B(\sigma,\nu)b_{1,1}$ and $B(\sigma,\nu)b_{1,2}$ in (5.11) in the limits (5.14) and (5.15) is clear. The coefficient $B(\sigma,\nu)b_{2,1}$, however, is bounded in the limit small-B (5.14) if $n=0$ but unbounded if $n>0$:

$$\lim_{\sigma\to 2\nu+1} B(\sigma,\nu)b_{2,1} = \frac{2^{6\nu}\Gamma^2(\nu)}{8\nu^2\Gamma^2(-\nu)\Gamma(2\nu)}, \qquad -\frac{1}{2}<\nu<0, \tag{5.16}$$

$$B(\sigma,\nu)b_{2,1} \sim -\frac{n(n+2\nu)}{64(n+\nu)^4}\frac{1}{B(\sigma,\nu)}, \qquad B(\sigma,\nu)\to 0, \tag{5.17}$$

where $\sigma\to 2\nu+2n+1$, $-n-\frac{1}{2}<\nu<-n$ and $n\geq 1$ in (5.17). In section 5.4.2 we shall find that pole and zero coalescences occur at $z=0$, similar to those in Figures 4.4 and 4.5, but generally on multiple sheets in the small-B (5.14) and large-B (5.15) limits.

5.1.2 $\lambda = 1/\pi$ or $\sigma = 1$

The following small-z asymptotic formulae for $\lambda\geq 1/\pi$ are valid on the positive real axis, which we indicate by using the variable x. It is shown in [59] that in the limit $\lambda\to 1/\pi$, or $\sigma\to 1$, (5.10)–(5.13) become

$$u(x/2;\nu,\pi^{-1}) \sim \frac{1}{2}x\left\{\nu\ln^2 x - C(\nu)\ln x + \frac{1}{4\nu}\left[C^2(\nu)-1\right]\right\}, \qquad x\to 0^+, \tag{5.18}$$

where

$$C(\nu) = 1+2\nu[3\ln 2 + 2\psi(1) - \psi(\nu+1)]. \tag{5.19}$$

Here ψ denotes the digamma function ($\psi=\Gamma'/\Gamma$) and $\lim_{\nu\to 0} 1/(4\nu)[C^2(\nu)-1] = 3\ln 2+\psi(1)$. The instances

$$\nu = -n, \qquad n\geq 1, \tag{5.20}$$

for which the constant $C(\nu)$ becomes unbounded will be discussed in section 5.4.2. The cases (5.20) can be considered as special cases of the large-B limit (5.15) with $\nu\to -n-1$ and thus $\sigma_c\to 1$.

5.1.3 $\lambda > 1/\pi$ or $\sigma = 1+2i\mu$

Small-x asymptotic formulae for $\lambda>1/\pi$ were derived in [59] only for $\nu=0$. Here we also consider the case $\nu\neq 0$, $\nu\in\mathbb{R}$. For $\lambda>1/\pi$, we let

$$\lambda = \cosh(\pi\mu)/\pi, \qquad \mu>0, \qquad \Longrightarrow \qquad \sigma = 1+2i\mu. \tag{5.21}$$

Using the properties $\Gamma(1+z) = z\Gamma(z)$ and $\Gamma(\overline{z}) = \overline{\Gamma(z)}$, (5.13) becomes

$$\begin{aligned} B(1+2i\mu,\nu) &= 2^{-3-6i\mu}\frac{\Gamma^2(-i\mu)\Gamma(1+\nu+i\mu)}{\Gamma^2(1+i\mu)\Gamma(\nu-i\mu)} \\ &= -\frac{(\nu+i\mu)}{8\mu^2}\exp\left\{2i\left[\arg\Gamma(\nu+i\mu) - 2\arg\Gamma(i\mu) - \mu\log 8\right]\right\} \end{aligned} \tag{5.22}$$

and for $x \to 0^+$, (5.10) and (5.11) simplify to

$$\begin{aligned} u(x/2;\nu,\cosh(\pi\mu)/\pi) &= B(1+2i\mu,\nu)x\left[b_{1,1} + x^{2i\mu} + b_{2,1}x^{-2i\mu}\right] + \mathcal{O}\left(x^3\right), \\ &= x\left[\frac{\nu}{4\mu^2} + B(1+2i\mu,\nu)x^{2i\mu} + \overline{B(1+2i\mu,\nu)x^{2i\mu}}\right] + \mathcal{O}\left(x^3\right), \\ &= \frac{x}{4\mu}\left\{\frac{\nu}{\mu}\left(1-\cos\left[\phi(x,\nu,\mu)\right]\right) + \sin\left[\phi(x,\nu,\mu)\right]\right\} + \mathcal{O}\left(x^3\right), \end{aligned} \tag{5.23}$$

where

$$\phi(x,\nu,\mu) = 2\mu\ln(x/8) - 4\arg\left[\Gamma(i\mu)\right] + 2\arg\left[\Gamma(\nu+i\mu)\right]. \tag{5.24}$$

5.2 An example of an MTW solution

The bottom-left frame of Figure 5.1 depicts the modulus of an MTW solution with parameters $\nu = \frac{1}{2}$ and $\mu = 2$ (see (5.21)) on the annulus $10^{-10} \le |z| \le 15$, $-\pi < \arg z \le \pi$. We shall find it instructive to depict some solutions in the ζ-plane, which is related to the z-plane according to $z = e^{\zeta/2}$. The ζ-plane region corresponding to the annulus in the z-plane is the rectangle $-2\pi < \mathrm{Im}\ \zeta \le 2\pi$, $2\log(10^{-10}) \le \mathrm{Re}\ \zeta \le 2\log(15)$, see the top frame of Figure 5.1. Since the branch point at $z = 0$ is mapped out of the finite ζ-plane, the solution is meromorphic in the ζ-plane [41]. We refer to the solution on the region $-\pi < \arg z - 2\pi s \le \pi$, or $-2\pi < \mathrm{Im}\ \zeta - 4\pi s \le 2\pi$, as the solution on the s-th sheet of the Riemann surface. Since the MTW solutions are solutions of $\mathrm{P}_{\mathrm{III}}^{(\mathrm{i})}$, for which $\gamma = 1 = -\delta$, it follows from Table 3.1 that at $z \neq 0$, the poles have residues $c_{-1} = \pm 1$ (indicated by red and yellow circles, respectively) and the zeros have derivative values $c_1 = \pm 1$ (indicated by purple and light blue squares, respectively). Conspicuous in the bottom-left frame is the pole-free sector contained in the right half-plane, in accordance with the large-z formula (5.7). The poles are arranged as spirals in the z-plane which, as noted in Chapter 3, appears to be a common feature of the multivalued (but not the meromorphic) Painlevé transcendents. The modulus of the solution has an up-down symmetry in the z and ζ planes since the solution in the upper and lower half planes are conjugate. This is a consequence of the fact that for real parameter values, the MTW solutions

are real on $\arg z = 0$ (which corresponds to the real ζ-axis), as indicated by the asymptotic formulae above.

The bottom-right frame of Figure 5.1 shows the solution on $\arg z = 0$ with the large-x (5.7) and small-x (5.23) asymptotic formulae; note how these formulae match the computed solution (shown in blue). As expected from (5.23), the solution is oscillatory with an infinite number of zeros accumulating on $\arg z = 0$ as $z \to 0$ for $\lambda > 1/\pi$. If $\lambda < -1/\pi$, infinitely many poles accumulate on $\mathbb{R}^+$, see (5.8), in which case the limit point $z = 0$ is a non-isolated singularity. For fixed ν, the poles or zeros become more closely spaced on the real ζ-axis as μ increases, see (5.23) and (5.24). For fixed ν and μ, the spacing of the poles or zeros on the real ζ-axis is uniform, see Figure 5.1 and (5.24) with $x = e^{\zeta/2}$, which implies that in the z-plane the spacing is (approximately) proportional to z and thus decreases exponentially as $z \to 0$ on $\arg z = 0$.

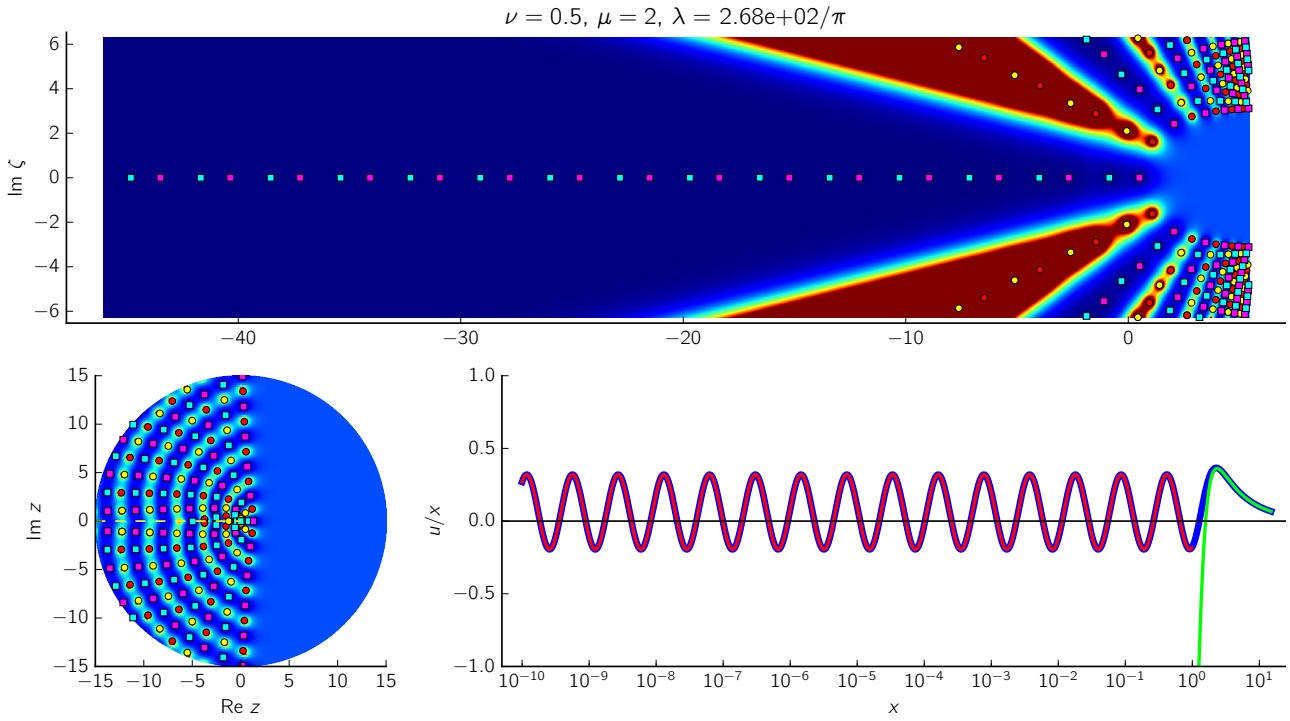

Figure 5.1: An MTW solution with $\nu > -\frac{1}{2}$ for the case $\lambda > 1/\pi$ on the annulus $10^{-10} \le |z| \le 15$ (bottom-left frame), its corresponding region in the ζ-plane (top frame, $z = e^{\zeta/2}$) and on the positive real axis of the z-plane (bottom-right frame). In the latter frame the small-x and large-x asymptotic approximations, (5.23) (red) and (5.7) (green), respectively, are divided by x and superimposed on the computed solution (blue), which is also divided by x.

5.3 MTW solutions with $\nu > -\frac{1}{2}$ on the 0th sheet

5.3.1 Fixed ν, varying λ

For MTW solutions with a fixed value of ν, where $\nu > -\frac{1}{2}$, the pole field dynamics on the 0th sheet can be divided into three stages: $0 < \lambda \leq \lambda_c$ (recall that $\lambda = 0$ corresponds to the solution $u = 1$), $\lambda_c < \lambda \leq 1/\pi$ and $\lambda > 1/\pi$. Figure 5.2 depicts pole fields in these stages. In the first stage, as λ is increased from zero, a pole field moves horizontally to the right from the left half-plane (leftmost frame). In the second stage, the moment λ exceeds λ_c (our computations indicate that $\lambda_c \approx 0.1/\pi$) then, in addition to the horizontal rightwards movement of the pole field for increasing λ, there is also a slight vertical movement upwards (in the upper half-plane) and downwards (in the lower half-plane) as poles from the neighbouring sheets (sheets $+1$ and -1) move through the branch cut (middle frame). In the third stage, as λ is increased beyond $1/\pi$, the branch point $z = 0$ acts as a 'zeros source' along $\mathbb{R}^+$ according to (5.23) and the movement of poles into the right half-plane along arcs that emerge through the branch cut is continued (rightmost frame). If we compare the middle frame of Figure 5.2 (for which $\mu = 0$), the bottom left frame of Figure 5.1 ($\mu = 2$) and the rightmost frame of Figure 5.2 ($\mu = 5$), we find that in the upper half-plane there are poles on five, six and eight arcs, respectively. In these frames the numbers of poles in the annulus $10^{-10} \leq |z| \leq 5$ are, respectively, 8, 37 and 172.

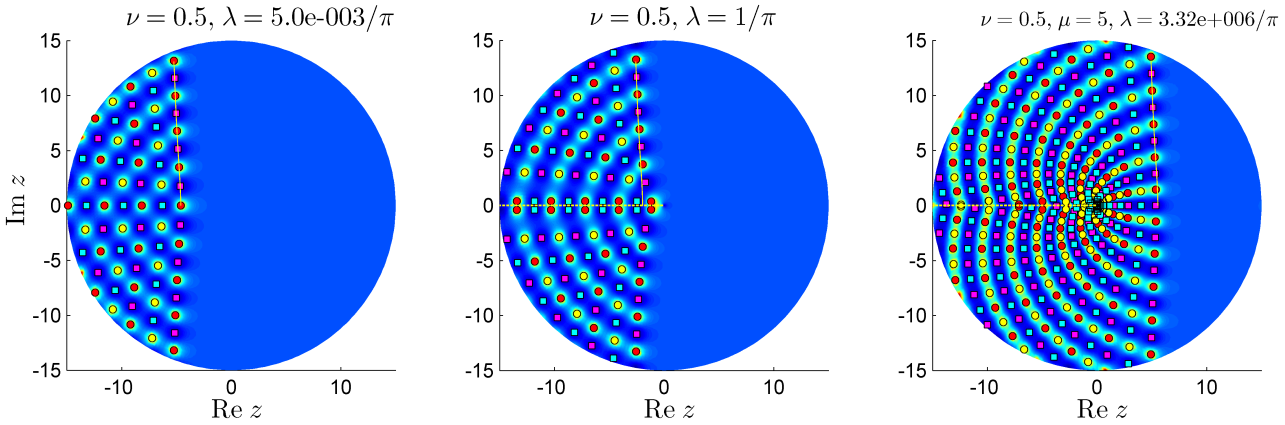

Figure 5.2: The typical evolution of an MTW solution for a fixed $\nu > -\frac{1}{2}$ on the 0th sheet as λ is increased. The bottom left frame of Figure 5.1 is also a member of this sequence, slotting between the second and third frames.

We emphasize that, unlike the creation of an infinity of zeros (for $\lambda > 1/\pi$) or poles (for

$\lambda < -1/\pi$) on $\mathbb{R}^+$, the profusion of poles away from $\mathbb{R}^+$ in the stage $\lambda > 1/\pi$ is not due to any pole creation process. Rather, as we shall observe in Figure 5.15, these are poles from sheets neighbouring the 0th sheet that move through the branch cut as the pole density on these sheets rapidly increases for $\lambda > 1/\pi$.

For solutions with $\nu \geq 0$, zeros appear on $\mathbb{R}^+$ only in the third stage when $\lambda > 1/\pi$. For solutions with $-\frac{1}{2} < \nu < 0$, however, a single zero appears on $\mathbb{R}^+$ for $\lambda < 1/\pi$ in the small-B limit (5.14) with $n = 0$ (this zero is visible in the top-left frame of Figure 5.4). As we shall find in section 5.4.2, *poles* appear on $\mathbb{R}^+$ in the small-B limit if $n > 0$. These facts are consequences of (5.16) and (5.17): the boundedness of $Bb_{2,1}$ for $n = 0$ and the unboundedness of $Bb_{2,1}$ for $n > 0$ in the small-B limit.

Note that the absence of a dotted line on $\mathbb{R}^-$ of the leftmost frame in Figure 5.2 indicates the absence of a branch cut and thus a single-valued solution. However, this solution cannot be exactly single-valued since it would require $\sigma = 0$ in (5.9) but $\lambda \neq 0$ and thus $\sigma \neq 0$. However, due to limited numerical accuracy, the branch cut of the computed solution is not resolved adequately.

Since the solution in the upper and lower half-planes are complex conjugates for real parameters, a single-valued solution is real-valued on $\mathbb{R}^-$. If a $\mathrm{P_{III}}$ solution with real parameters has a pole or a zero on $\mathbb{R}^-$, then the solution is real-valued on $\mathbb{R}^-$ within the radius of convergence of the Laurent or Taylor expansion about the pole or zero since all the Laurent or Taylor coefficients are real-valued. Hence, the presence of poles and zeros close to $\mathbb{R}^-$ in the left frame of Figure 5.2 indicates that the solution is nearly single-valued.

We have found that solutions with half-integer ν-values are the only solutions that are nearly single-valued during the first stage when $0 < \lambda \leq \lambda_c$, with poles and zeros close to the negative real axis. When λ exceeds λ_c, the poles and zeros on $\mathbb{R}^-$ 'split' in which case $\mathbb{R}^-$ is unambiguously a branch cut, as shown in the middle frame in Figure 5.2. Solutions for which ν is not a half-integer are multivalued for all $\lambda > 0$, with poles and zeros above and below the branch cut. We shall observe a similar phenomenon again in Figure 5.6, where solutions with (approximate) negative half-integer ν-values are nearly single-valued for $0 < \lambda \leq \lambda_c$, with poles close to $\mathbb{R}^-$, while the other solutions are multivalued for all $\lambda > 0$. Bessel function solutions with negative half-integer ν values that were studied in section 4.5.2, and which will be shown in section 5.5.2 to be limiting MTW solutions, are single-valued for all values of the arbitrary

parameter (see (4.77)–(4.79)). The small-z (5.9) or large-z (5.7) expansions give no indication why it should be that MTW solutions with half-integer ν values are nearly single-valued for small λ. In particular, $\sigma = \sigma(\lambda)$ in (5.12), which determines the type of branch point at $z = 0$, is independent of ν.

Recall from (4.83) and (4.82) that the pole fields in Figure 5.2 are displaced horizontally by approximately t units from one frame to the next if the arbitrary parameter is scaled by e^{2t}. The approximate horizontal displacements from the left to the middle fame and from the middle frame to the right frame in Figure 5.2 are, respectively,

$$t = \frac{1}{2}\log\left(\frac{1}{5\times 10^{-3}}\right) \approx 2.65 \qquad \text{and} \qquad t = \frac{1}{2}\log\left(\cosh(5\pi)\right) \approx 7.51. \tag{5.25}$$

The errors of these estimates are shown in Figure 5.3 and are computed using the same two-step approach described below (4.84). The interpolant that represents the boundary of the pole-free region in the left column, as well as the two translated interpolants, are depicted as yellow curves in Figure 5.2.

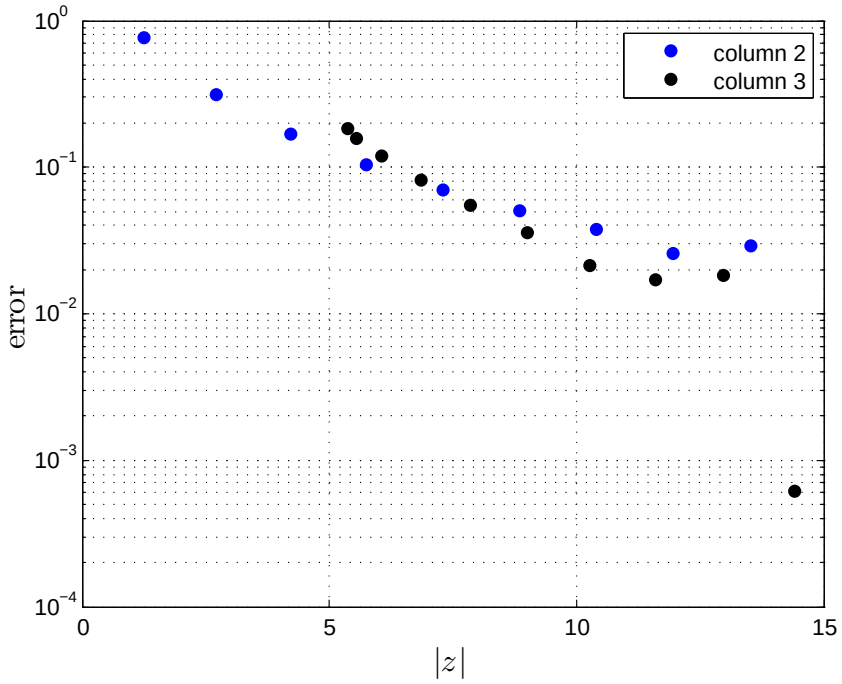

Figure 5.3: The error of the estimates (5.25) of the horizontal displacements of the pole-free regions in the second and third columns of Figure 5.2. Each dot represents the difference between the real part of a pole or zero on the boundary of the pole-free region in the second or third column of Figure 5.2 and the yellow curve.

5.3.2 Fixed λ, varying ν

In Figure 5.4, λ is fixed and as $\nu > -\frac{1}{2}$ increases, the angular widths of the pole-free regions in the finite plane increase. Specifically, let z^* be the location of the outermost pole or zero on the boundary of the pole-free region in the upper half-plane of a solution in Figure 5.4; z^* is indicated by a yellow open circle in the top-left and bottom-right frames of Figure 5.4. For the $\nu = -\frac{1}{4}$ (top-left frame) and $\nu = \frac{3}{2}$ (bottom-right frame) solutions, $\arg z^* = 0.51\pi$ and $\arg z^* = 0.60\pi$, respectively, which is an angular displacement of 0.09π.

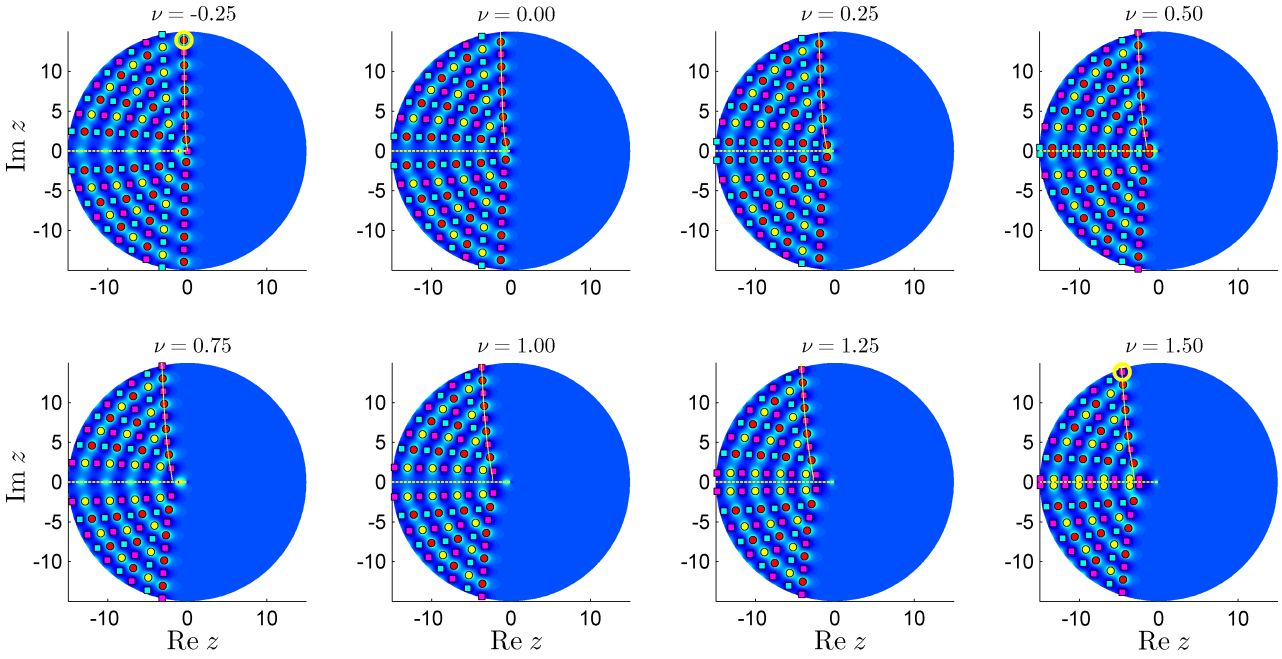

Figure 5.4: The typical variations between MTW solutions with $\nu > -\frac{1}{2}$ and a fixed λ ($\lambda = 1/\pi$ in this case). Note the slight differences in the pole fields close to the branch cut and how the angular width of the pole-free region increases with ν. The yellow curves are used to estimate the change in angular widths of the pole-free regions. The second solution in the top row ($\nu = 0$, $\lambda = 1/\pi$) is related to the correlation function of the 2D Ising model [59, 91].

As an in section 4.5.3, the changes in the pole-free regions can be understood intuitively and analytically by examining only the second term of the large-z expansion (5.7):

$$m(z;\nu,\lambda) = \lambda 2^{-2\nu}\,\Gamma\left(\nu+\tfrac{1}{2}\right) z^{-\nu-1/2} e^{-2z}.$$

This is based on the observation, which follows from (5.7), that a $\mathcal{O}\left(m(z;\nu,\lambda)/z\right)$ approximation to the solution can be constructed by considering only $m(z;\nu,\lambda)$:

$$1 + m(z;\nu,\lambda) = u(z;\nu,\lambda) + \mathcal{O}\left(\frac{m(z;\nu,\lambda)}{z}\right), \qquad z\to\infty, \qquad -\frac{\pi}{2} < \arg z < \frac{\pi}{2}. \tag{5.26}$$

As in section 4.5.3, we shall find that, in the finite plane, reasonable approximations of the changes in the pole-free regions can be derived from $m(z;\nu,\lambda)$, not only in the right half-plane but also in the left half-plane. The accuracy of the estimates in Figure 5.3 already illustrate this fact since the boundary of the pole-free region in the left frame of Figure 5.2 is in the left half-plane.

To estimate the angular displacement of the pole-free regions between the frames in Figure 5.4, we find the angular displacement of the modulus of $m(z;\nu,\lambda)$, for fixed λ and a change in ν of c, by solving the following equation for δ:

$$\frac{\left|m(re^{i(\theta+\delta)};\nu+c,\lambda)\right|}{|m(re^{i\theta};\nu,\lambda)|}=2^{-2c}\left|\frac{\Gamma\left(\nu+\frac{1}{2}+c\right)}{\Gamma\left(\nu+\frac{1}{2}\right)}\right|r^{-c}\exp[-2r(\cos(\theta+\delta)-\cos\theta)]=1.$$

We find that (cf. (4.86))

$$\delta=\delta(r,\theta,\nu,c)=\cos^{-1}\left\{-\frac{1}{2r}\log\left[(4r)^c\left|\frac{\Gamma\left(\nu+\frac{1}{2}\right)}{\Gamma\left(\nu+\frac{1}{2}+c\right)}\right|\right]+\cos\theta\right\}-\theta,\qquad\theta\in[0,\pi].\quad(5.27)$$

Due to the up-down symmetry of the modulus of the MTW solutions with real parameters, it is sufficient to consider $\theta\geq 0$ in (5.27). In the limit $r\to\infty$, it follows from (5.26) that (5.27) is a valid estimate for the angular displacement of the pole-free regions only if $-\frac{\pi}{2}<\theta<\frac{\pi}{2}$ and in this limit there is no angular displacement,

$$\lim_{r\to\infty}\delta(r,\theta,\nu,c)=0,\qquad 0\leq\theta<\frac{\pi}{2},\qquad \nu,\nu+c\neq-\frac{1}{2}-n,\qquad n\geq 0.$$

Close to the imaginary axis, in both the right and left half-planes, (5.27) can be simplified, with the same argument used to arrive at (4.87), to

$$\delta\approx\frac{1}{2r}\log\left[(4r)^c\left|\frac{\Gamma\left(\nu+\frac{1}{2}\right)}{\Gamma\left(\nu+\frac{1}{2}+c\right)}\right|\right],\qquad\theta=\frac{\pi}{2}-\epsilon,\qquad 0\leq|\epsilon|\ll 1,\qquad(5.28)$$

and if $\theta=\frac{\pi}{2}$, then (5.27) becomes

$$\delta=\sin^{-1}\left\{\frac{1}{2r}\log\left[(4r)^c\left|\frac{\Gamma\left(\nu+\frac{1}{2}\right)}{\Gamma\left(\nu+\frac{1}{2}+c\right)}\right|\right]\right\}.$$

Figure 5.5 shows plots of the angular displacements (5.27), in blue, and the approximate angular displacements (5.28), in red, for the solutions in the corresponding rows and columns of Figure 5.4. These results, and the errors in the bottom-right frame of Figure 5.5, were obtained using the same three-step method described below (4.87). The interpolant that represents the boundary of the pole-free region of the solution in the top-left frame, as well

as the angularly displaced versions of this interpolant that were obtained using (5.27), are depicted as yellow curves in Figure 5.4. Figure 5.5 confirms the expectation from Figure 5.4: that the estimated angular displacements of the pole-free regions are positive and decrease monotonically for sufficiently large r.

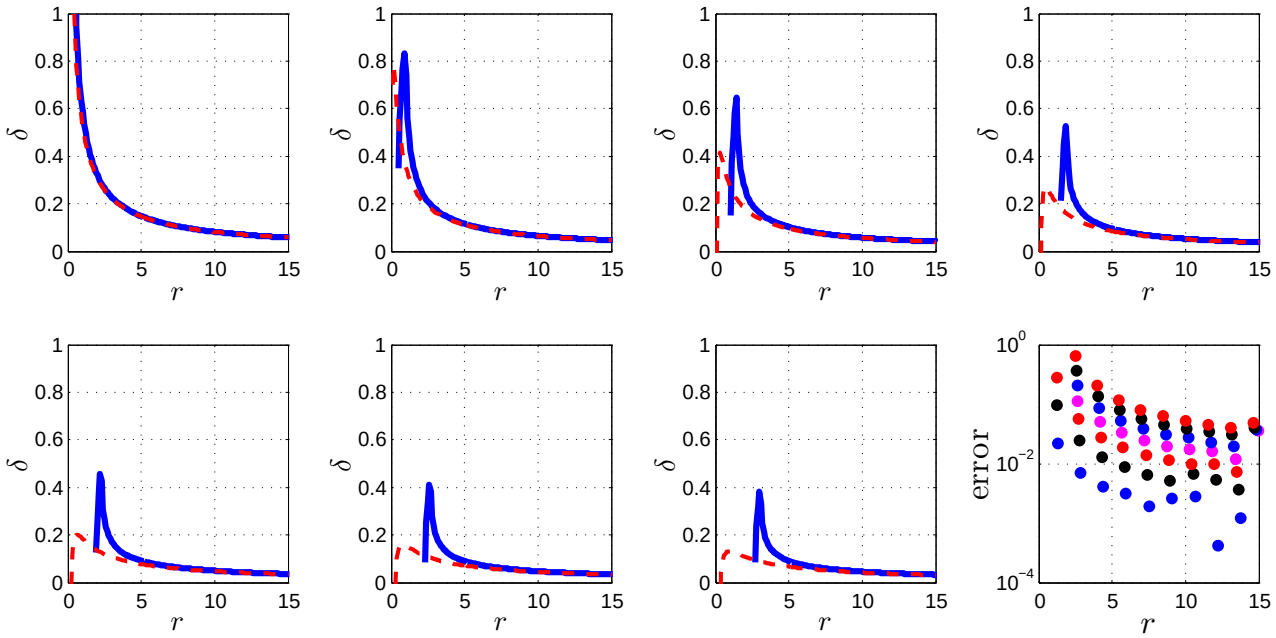

Figure 5.5: The angular displacements (5.27) (blue) of the estimated boundaries of the pole-free regions of the solutions in the corresponding rows and columns of Figure 5.4, as well as the approximate angular displacement (5.28) (red). The error of the estimated boundaries increases from frame to frame. Hence, the bottom row of dots in the bottom-right frame are the errors for the estimated pole-free boundary of the solution in row 1, column 2 of Figure 5.4 and the top row of dots are for the solution in row 2, column 4 of Figure 5.4.

5.4 MTW solutions with $\nu < -\frac{1}{2}$ on the 0th sheet

For the MTW solutions with $\nu < -\frac{1}{2}$, the large-z formula and the small-z formulas are discontinuous functions of the parameters; see (5.4) with $\nu = -\frac{1}{2} - n$, $n \geq 0$, (5.14), (5.15) and (5.20). However, we shall find that except for transitions through the critical parameter values, the pole dynamics of the MTW solutions with $\nu < -\frac{1}{2}$ are similar to those with $\nu > -\frac{1}{2}$.

5.4.1 $\sigma < \sigma_c$

As for the MTW solutions with $\nu > -\frac{1}{2}$, a pole field moves horizontally to the right from the left half-plane as σ (or λ, see (5.12)) is increased from zero. Figure 5.6 shows pole fields with $\sigma < \sigma_c$, where σ_c is defined in (5.14) and (5.15). We observe that $2\lfloor -\nu \rfloor + 1$ rows of poles are dislodged from the pole field on the left when $\nu \approx -\frac{1}{2} - n$ and that these rows of poles undergo a reciprocal transformation when ν transitions through the critical value $-\frac{1}{2} - n$. This can be ascribed to the sign change of the gamma function in the large-z formula (5.7) during this transition. As ν decreases in Figure 5.6, poles and zeros emerge through the branch cut and there are changes in the angular widths of the pole-free regions that can be quantified using (5.27).

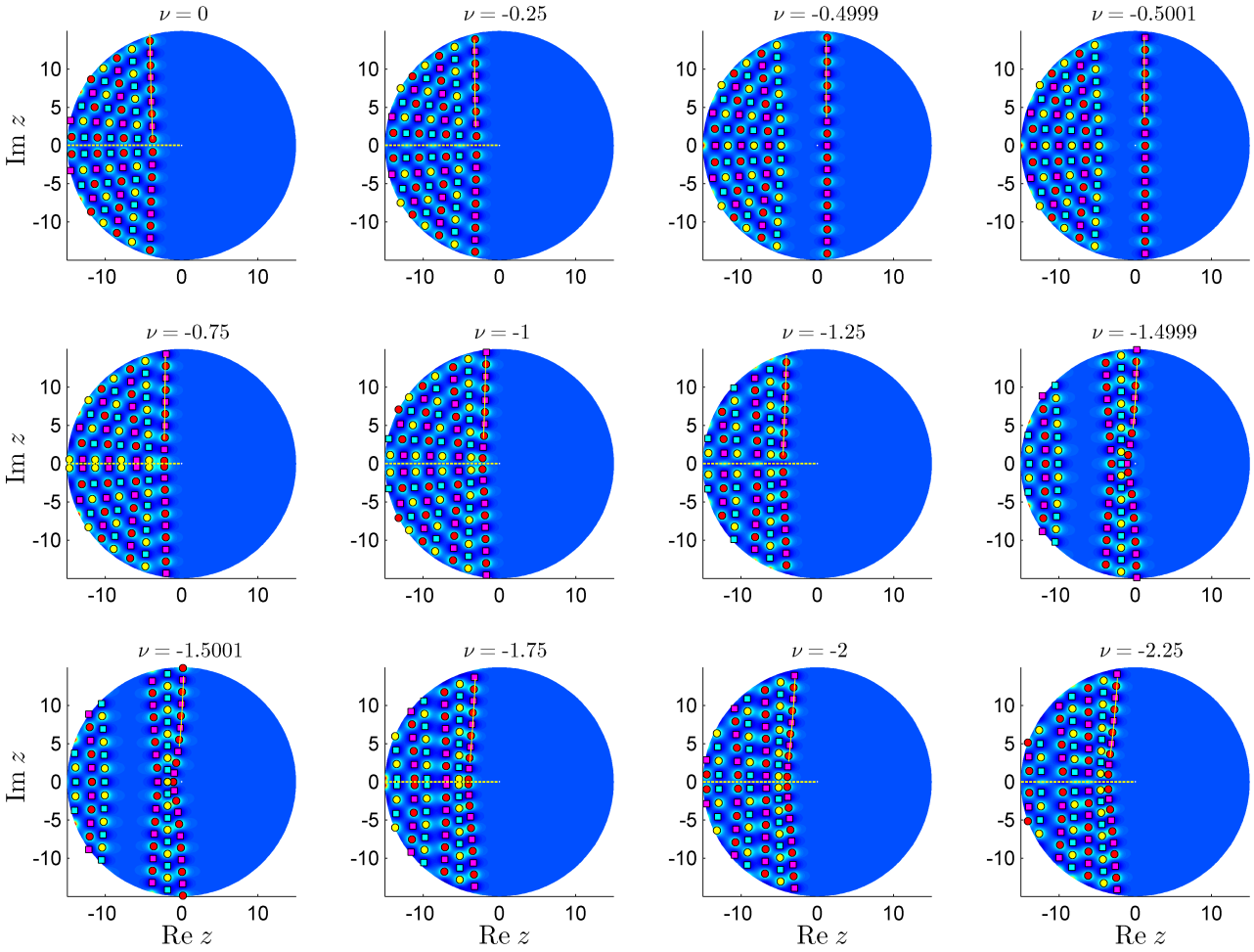

Figure 5.6: The pole dynamics of MTW solutions with $\nu < -\frac{1}{2}$ preceding the approach of the critical σ value, i.e., $\sigma < \sigma_c$. The solutions with $0 \leq \nu \leq -1$ and $\nu < -1$ have the parameter values $\sigma = 4.8 \cdot 10^{-5}$ and $\sigma = 4.8 \cdot 10^{-6}$, respectively.

The first six solutions in Figure 5.6 have a fixed value of σ (and thus of λ) and the final six

solutions in Figure 5.6 have a different fixed value of λ. Hence, we apply the formula (5.27) for the angular displacements of the estimated pole-free boundaries separately to the two sets of six solutions in Figure 5.6. The resulting angular displacements are shown in Figure 5.7, in blue, along with the approximate angular displacements (5.28), in red, as well as the errors of the estimated pole-free boundaries. Except for the solutions in the top-right and bottom-left frames of Figure 5.6, the angular displacements of the pole-free boundaries are negative (in Figure 5.4 the angular displacements are positive but ν increases between frames). Note that different vertical scales are used in Figure 5.7.

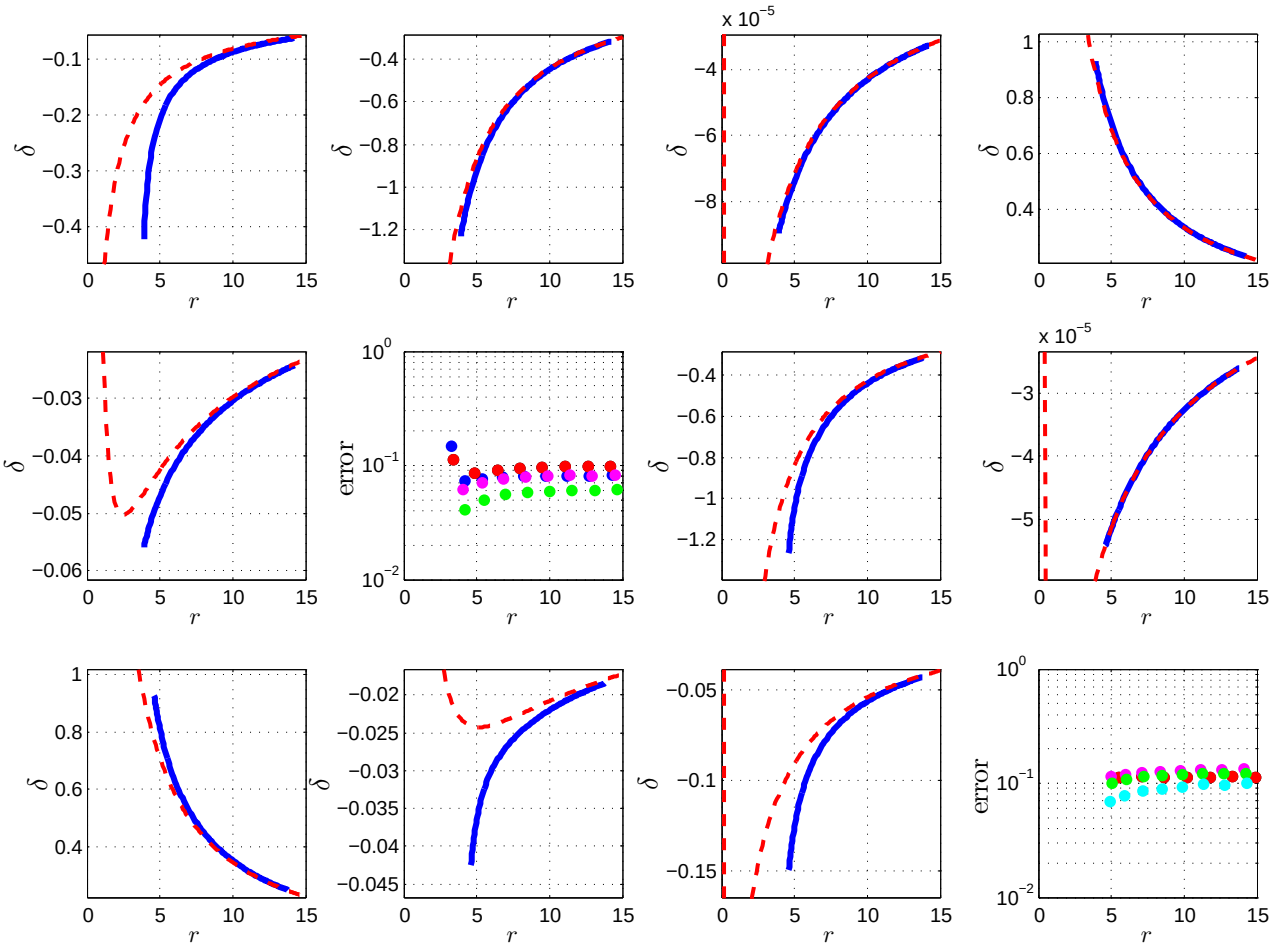

Figure 5.7: The angular displacements (5.27) (blue) of the estimated pole-free boundaries of the solutions in the corresponding rows and columns of Figure 5.6 along with the approximate angular displacement (5.28) (red). The errors (shown in row 2, column 2 and row 3, column 4) of the two sets of five angularly displaced estimated pole-free boundaries show that the yellow curves in Figure 5.6 are reasonable estimates of the actual pole-free boundaries.

5.4.2 $\sigma \to \sigma_c$

Numerical observations

As σ is increased from the small values in the caption of Figure 5.6, the rightward horizontal movement of the pole fields is continued. As σ increases through the critical value σ_c, a finite number of poles appear on $\mathbb{R}^+$ in the z-plane, which corresponds to $\mathbb{R}$ in the ζ-plane. Figure 5.8 shows the transition through σ_c in the ζ-plane for three of the solutions in Figure 5.6. The first row of Figure 5.8 shows a solution in the small-B limit (5.14) with $n = 1$; the second row shows a solution in the large-B limit (5.15) with $n = 1$ and the third row shows a solution with the critical parameter value (5.20) with $n = 2$ (which is a special case of the large-B limit (5.15) with $n = 1$ and $\nu \to -2$).

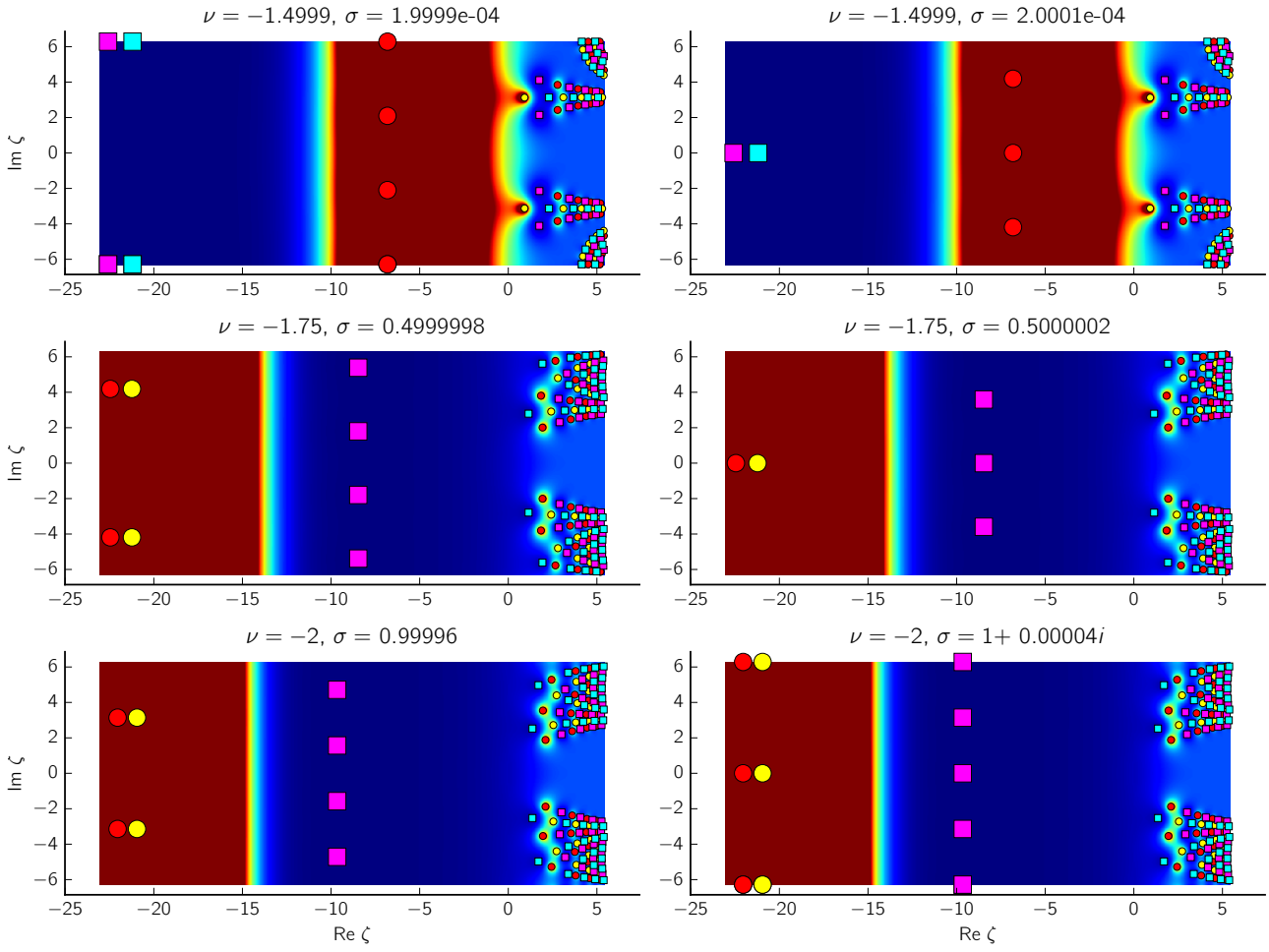

Figure 5.8: Round$(-\nu)$ poles appear on $\mathbb{R}^+$ in the z-plane, or $\mathbb{R}$ in the ζ-plane, as σ increases through σ_c, defined in (5.14) and (5.15).

In the left half ζ-plane we find that as $\sigma \to \sigma_c^-$ (left column of Figure 5.8) poles and zeros are equally spaced along vertical lines. The vertical spacing between the two pairs of zeros (first

row) or poles (second and third rows) is $2\pi/|\nu+1|$ and the spacing between the single vertical row of four poles (first row) or four zeros (second and third rows) is $2\pi/|\nu|$. Furthermore, the spacing is symmetric about Im $\zeta = 0$. Thus, the pairs of zeros or poles and the single vertical row of poles or zeros are at, respectively,

$$\zeta = x_1 + \frac{(2k+1)\pi i}{\nu+1} \qquad \text{and} \qquad \zeta = x_2 + \frac{(2k+1)\pi i}{\nu}, \qquad k \in \mathbb{Z}, \tag{5.29}$$

where x_1 and x_2 depend on σ and $x_1 < x_2 < 0$. Figure 5.8 shows the solution on the 0th sheet ($|\text{Im } \zeta| \leq 2\pi$), but we have found that the spacing (5.29) holds on all the sheets ($|\text{Im } \zeta| > 2\pi$).

As $\sigma \to \sigma_c^-$, the poles and zeros move infinitely far into the left half-plane, $x_1 < x_2 \to -\infty$ in (5.29). As σ increases through σ_c, the poles and zeros return from Re $\zeta = -\infty$ along

$$\zeta = x_1 + \frac{2k\pi i}{\nu+1} \qquad \text{and} \qquad \zeta = x_2 + \frac{2k\pi i}{\nu}, \qquad k \in \mathbb{Z}, \tag{5.30}$$

where $x_1 < x_2$, see the second column of Figure 5.8. In the z-plane (recall $z = e^{\zeta/2}$), the movement of the poles and zeros from (5.29) to (5.30) corresponds to a rotation through $\pi/(2\nu+2)$ (mod 2π) and $\pi/(2\nu)$ (mod 2π). The appearance of poles and zeros on Im $\zeta = 0$ as σ increases through σ_c, see (5.30) with $k = 0$, corresponds to the appearance of poles and zeros on $\mathbb{R}^+$ in the z-plane.

In Figure 5.8 there is no perceptible change in the pole fields in the right half-plane as σ transitions through σ_c. This is to be expected since the large-z formula (5.7), unlike the small-z formulae (5.10)–(5.13), is a continuous function of the parameters in the limit $\sigma \to \sigma_c$ for fixed ν.

Our numerical solutions indicate that the observations in (5.29) and (5.30) generalize as follows in the small-B (5.14) and large-B (5.15) limits. In the limit $\sigma \to \sigma_c^-$ there are pairs of zeros (in the small-B limit) or poles (in the large-B limit) at

$$\zeta = x_1 + \frac{(2k+1)\pi i}{\nu+n}, \qquad \zeta = x_3 + \frac{(2k+1)\pi i}{\nu+n-2}, \ldots, \zeta = x_{2\lceil n/2\rceil-1} + \frac{(2k+1)\pi i}{\nu+n+2-2\lceil n/2\rceil}, \tag{5.31}$$

and there are pairs of poles (in the small-B limit) or zeros (in the large-B limit) at

$$\zeta = x_2 + \frac{(2k+1)\pi i}{\nu+n-1}, \qquad \zeta = x_4 + \frac{(2k+1)\pi i}{\nu+n-3}, \ldots, \zeta = x_{2\lceil (n-1)/2\rceil} + \frac{(2k+1)\pi i}{\nu+n+1-2\lceil (n-1)/2\rceil} \tag{5.32}$$

where $k \in \mathbb{Z}$. If n is odd, as in Figure 5.8, there is a single vertical row of poles (in the small-B limit) or zeros (in the large-B limit) at

$$\zeta = x_{n+1} + \frac{(2k+1)\pi i}{\nu}, \qquad k \in \mathbb{Z}, \tag{5.33}$$

where $x_1 < \cdots < x_{n+1} < 0$. If n is even, there is a single vertical row of zeros (in the small-B limit) or poles (in the large-B limit) at the points in (5.33). As in Figure 5.8, if $\sigma \to \sigma_c^-$, then $x_1 < \cdots < x_{n+1} \to -\infty$ and if $\sigma \to \sigma_c^+$, then the poles and zeros return from $\mathrm{Re}\,\zeta = -\infty$ and the points at which they reside are as in (5.31), (5.32) and (5.33), except that $(2k+1)$ is replaced by $2k$. The upshot of this is that round$(-\nu)$ poles appear on $\mathbb{R}^+$ in the z-plane as σ increases through σ_c in the small-B and large-B limits.

Theoretical observations

We now attempt to reconcile the observations above with the small-z formulae (5.10)–(5.13). We confine our attention to the positive real axis, $z = x > 0$, or, equivalently, the real ζ-axis. Starting with the observations above: it follows from (5.31), (5.32) and (5.33) that if $\sigma \to \sigma_c^-$, then there are no poles or zeros on the real ζ-axis, see also the left column of Figure 5.8. Since the large-z formula (5.7) is strictly positive on $\mathbb{R}^+$, we conclude that if $\sigma \to \sigma_c^-$, then the solution is strictly positive on $\mathbb{R}^+$. Only when $\sigma > \sigma_c$ do poles or zeros appear on the real ζ-axis (see right column of Figure 5.8). Thus, if $\sigma > \sigma_c$, then the solution changes sign on $\mathbb{R}^+$.

We now consider the small-z expansion (5.10) on the positive real axis. For σ_c defined in (5.14) and (5.15),

$$\sigma < \sigma_c \Rightarrow B(\sigma,\nu) > 0 \qquad \text{and} \qquad \sigma > \sigma_c \Rightarrow B(\sigma,\nu) < 0. \tag{5.34}$$

Thus, if $\sigma \to \sigma_c^-$, then the first two terms of (5.10), Bx^σ and $Bb_{1,1}x$ (see (5.11)), the dominant terms in the limit $x \to 0^+$, are strictly positive, which is consistent with the observations above. In the large-B limit (5.15) with $\sigma \to \sigma_c^+$, we deduce from (5.34) that the leading order term, Bx^σ, is negative, with B arbitrarily large negative, while the large-x formula is positive. This is consistent with the presence of at least one pole on the real ζ-axis, see the second and third rows in the right column of Figure 5.8. In the small-B limit (5.14) with $\sigma \to \sigma_c^+$, the first term of (5.10) is negative; the second term is positive; the third term, $Bb_{1,2}x^{1+2\sigma}$, is negative but negligible, see (5.11), and the fourth term, $Bb_{2,1}x^{2-\sigma}$, is negative and bounded if $n = 0$, see (5.16), and negative but unbounded if $n > 0$, see (5.17). This indicates the presence of at most two zeros and, if $n > 0$, one pole on $\mathbb{R}^+$ in the limit $x \to 0^+$. This is consistent with the observations in (5.31), (5.32) and (5.33) (with $(2k+1)$ replaced by $2k$) according to which a pair of zeros appears on $\mathrm{Im}\,\zeta = 0$ if $n > 0$ and at least one pole appears on $\mathrm{Im}\,\zeta = 0$ if $n > 0$ in the small-B limit (as in the right column of the first row of Figure 5.8).

Suppose $\nu = -n - \frac{\ell}{2m}$, where n, ℓ and m are non-negative integers, ℓ and m are relatively prime and $\nu = -n - \frac{\ell}{2m} \neq -n - \frac{1}{2}$. Then $\sigma_c = (m-\ell)/m$ if $0 < \frac{\ell}{2m} < \frac{1}{2}$ (see (5.14)), and $\sigma_c = (\ell - m)/m$ if $\frac{1}{2} < \frac{\ell}{2m} \leq 1$ (see (5.15) and the comment below (5.20)). This implies that if $\sigma \approx \sigma_c$, then the small-z formula (5.10) is approximately an expansion in powers of $1/m$ and thus the solution behaviour in the limit $z \to 0$ is approximately that of an m-branched solution. If the solution has m distinct branches in the limit $z \to 0$, or equivalently, Re $\zeta \to -\infty$, then the positions of the poles and zeros close to $z = 0$ should repeat every m branches. That is, the sequences (5.31), (5.32) and (5.33) should be $4\pi m$-periodic in the imaginary direction, which is indeed the case[1]. For example, in Figure 5.8 we have, in the first to third rows, respectively, $m \approx 1$, $m = 2$ and $m = 1$. Thus, the positions of the poles and zeros are 4π-periodic in the vertical direction in the first and third rows and 8π-periodic in the second row, which is also evident in (5.29) and (5.30). Recalling that a pole or zero on the lines Im $\zeta = \pm 2\pi$ correspond to a single pole or zero on $\mathbb{R}^-$ in the z-plane since $z = e^{\zeta/2}$, we find that the number of poles and zeros in the left half-plane is conserved in the first and third rows of Figure 5.8 (for example, three poles in the left and right columns of the first row) but not in the second row. This is because $m = 1$ in the first and third rows and $m = 2$ in the second row. However, if one counts the number of poles and zeros in the left half-plane in the second row on $m = 2$ sheets, e.g., on $-2\pi <$ Im $\zeta \leq 6\pi$, then the number of poles and zeros are conserved.

In the limit $\sigma \to \sigma_c$, the poles and zeros at (5.31), (5.32) and (5.33) move infinitely far into the left half-plane, $x_1 < \cdots < x_{n+1} \to -\infty$, which implies that they coalesce in the limit at $z = 0$. Since the pairs of poles and zeros have residues and derivative values, respectively, of opposite signs (see Figure 5.8) they effectively cancel in the limit when they coalesce. This leaves the single vertical row of poles or zeros at (5.33) that coalesce in the limit at $z = 0$ but on different sheets. It follows from (4.5) and (4.6) that if a solution of $\mathrm{P}_{\mathrm{III}}^{(\mathrm{i})}$ with MTW parameters (5.1) admits a pole or zero at $z = 0$, then it has residue or derivative value

$$c_{-1} = -2\nu \qquad \text{or} \qquad c_1 = -\frac{1}{2\nu}. \tag{5.35}$$

This is consistent with the first row of Figure 5.8 in which three poles with $c_{-1} = +1$ coalesce at $z = 0$ in the limit $\sigma \to \sigma_c$, resulting in a pole at $z = 0$ with $c_{-1} = 3 \approx -2\nu = -2(-1.4999)$. Now, the reciprocal of an MTW solution is also an MTW solution, see (5.8). Thus, if n poles

[1] If $\nu < 0$ is irrational so that $\nu \neq -n - \frac{\ell}{2m}$, then the solution has infinitely many distinct branches in the limit $z \to 0$ and thus the pole and zero positions are not periodic in the vertical direction.

with $c_{-1} = +1$ of an MTW solution coalesce at $z = 0$ to form a pole with residue n, as in the first row of Figure 5.8, then the coalescence of n zeros at $z = 0$ must result in a zero at $z = 0$ with $c_1 = 1/n$. Thus, in the third row of Figure 5.8, in which $\nu = -2$ and four zeros with $c_1 = 1$ coalesce, we have $c_1 = 1/n = 1/4$, which is consistent with (5.35) since $c_1 = -\frac{1}{2\nu} = 1/4 = 1/n$. The solution in the second row of Figure 5.8 has two distinct branches ($m = 2$) in the limit $z \to 0$ or $\mathrm{Re}\,\zeta \to -\infty$, thus the positions of the poles and zeros in the left half-plane are 8π-periodic. For this solution, $\nu = -7/4$ and there are seven zeros on two sheets with $c_1 = 1$ that coalesce in the limit $\sigma \to \sigma_c$. If we consider the reciprocal of this solution, then seven poles with $c_{-1} = 1$ coalesce on two sheets and thus the 'residue per sheet' is $7/2 = n/m$, which is the same as the residue of a pole at $z = 0$ on a single sheet in (5.35), i.e., $c_{-1} = -2\nu = 7/2$. Thus, if seven zeros with $c_1 = 1$ coalesce on two sheets we have a 'derivative value per sheet' of $m/n = 2/7$, which is the same as the derivative value of a zero at $z = 0$ on a single sheet in (5.35), $c_1 = -\frac{1}{2\nu} = 2/7$.

Note that the three dislodged rows of poles and zeros of the $\nu = -1.4999$ solution in Figure 5.6 are indistinguishable from the rows of poles and zeros of the solution in the second row of Figure 4.5, for which $\nu = -\frac{3}{2}$. We shall return to this fact in section 5.5.2. Here we note that this observation implies that the pole and zero coalescences in the second row of Figure 4.5 (in the z-plane) and the first row of Figure 5.8 (in the ζ-plane) are virtually the same.

One can use (5.33) to show that the results above generalize as follows for rational ν values. Suppose $\nu = -n - \frac{\ell}{2m} = -\frac{2mn+\ell}{2m}$ and consider the small-B limit (5.14), thus $0 < \frac{\ell}{2m} < \frac{1}{2}$. Then $2mn+\ell$ poles with $c_{-1} = 1$ (if n is odd) or zeros with $c_1 = 1$ (if n is even) coalesce on m sheets, giving a residue per sheet of $\frac{2mn+\ell}{m} = -2\nu$ and a derivative value per sheet of $\frac{m}{2mn+\ell} = -\frac{1}{2\nu}$, which is consistent with (5.35). For the large-B limit (5.15), let $\frac{1}{2} < \frac{\ell}{2m} \leq 1$, then $2mn + \ell$ zeros with $c_1 = 1$ (if n is odd) or poles with $c_{-1} = 1$ (if n is even) coalesce on m sheets, again giving a residue per sheet of $\frac{2mn+\ell}{m} = -2\nu$ and a derivative value per sheet of $\frac{m}{2mn+\ell} = -\frac{1}{2\nu}$, which is again consistent with (5.35).

5.4.3 $|\sigma| > \sigma_c$

Figure 5.9 shows the typical pole dynamics of an MTW solution with $\nu < -\frac{1}{2}$ before and after the round$(-\nu)$ poles first appear on $\mathbb{R}^+$. Except for the rightmost $2\lfloor -\nu \rfloor + 1$ rows of poles that are not aligned with the pole field on the left, the movement of the poles into the right half-

plane and the accumulation of zeros on $\mathbb{R}^+$ when $\lambda > 1/\pi$, or $\sigma = 1 + 2i\mu$, $\mu > 0$, are similar to that of the MTW solutions with $\nu > -\frac{1}{2}$ (cf. Figure 5.2). The bottom frame of Figure 5.9 illustrates that if $\sigma > \sigma_c$, then the small-x and large-x asymptotics of MTW solutions with $\nu < -\frac{1}{2}$ are similar to those of MTW solutions with $\nu > -\frac{1}{2}$ (cf. the bottom-right frame of Figure 5.1), despite the presence of poles on $\mathbb{R}^+$ in MTW solutions with $\nu < -\frac{1}{2}$. This makes the MTW solutions with $\nu < -\frac{1}{2}$ reminiscent of the quasi-Hastings–McLeod solutions of $\mathrm{P_{II}}$, identified in [33]. The asymptotic behaviour of quasi-Hastings–McLeod solutions at $x \to \pm\infty$ is the same as regular Hastings–McLeod solutions, a class of tronquée $\mathrm{P_{II}}$ solutions, despite the presence of a finite number of poles on the real axis.

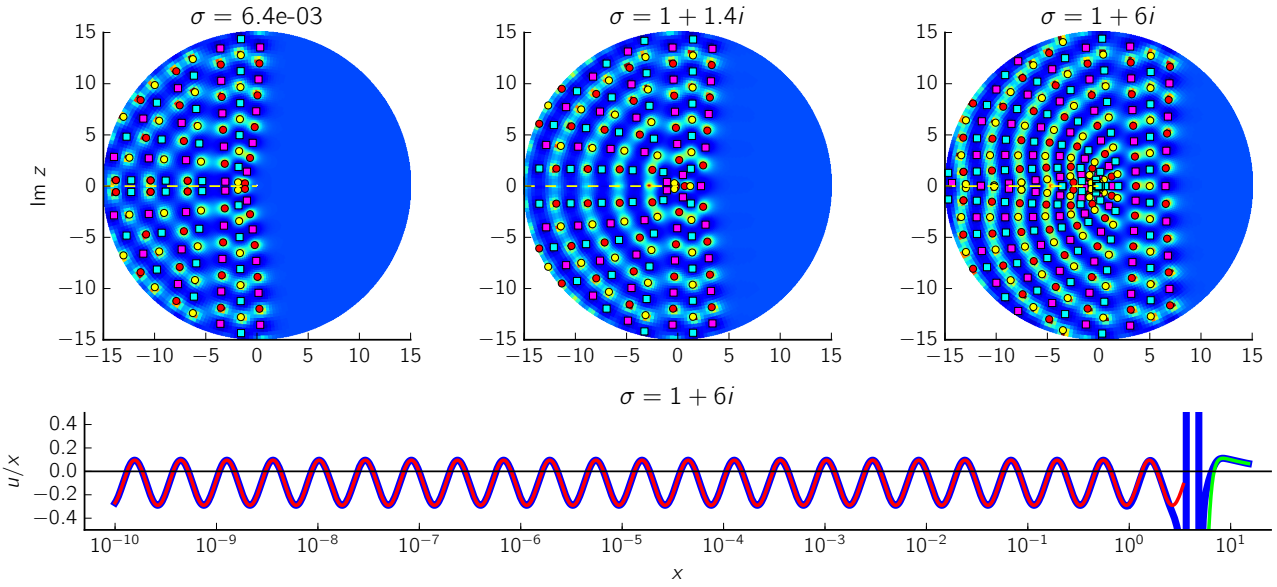

Figure 5.9: The pole fields of an MTW solution with $\nu = -1.75$ before and after the round$(-\nu)$ poles first appear on $\mathbb{R}^+$ (see also the $\nu = -1.75$ solution in Figures 5.6 and 5.8). The bottom frame shows the solution in the rightmost frame on $\mathbb{R}^+$ with its small-x and large-x asymptotic behaviours given by (5.23) and (5.4), respectively, all divided by x (cf. the bottom-right frame of Figure 5.1).

5.5 Limiting MTW solutions with $\nu = -\frac{1}{2} - n$

Although the MTW solutions do not exist when $\nu = -\frac{1}{2} - n$, $n \geq 0$, since then the large-z formula (5.4) is singular, there are two families of solutions that can be viewed as limiting MTW solutions as $\nu \to -\frac{1}{2} - n$. The first family satisfies only the small-x MTW asymptotic formulae: (5.10)–(5.13), (5.18) and (5.23). The second family is the Bessel function one-parameter LDT

solutions with $\nu = -\frac{1}{2} - n$ which were studied in section 4.5.2 and that satisfy the MTW-like large-z expansion (4.74). Since each member of these families satisfies MTW asymptotic formulae only at one end of $\mathbb{R}^+$, we refer to the first family as the left-end MTW solutions and the second family is called the right-end MTW solutions. We denote the left-end MTW solutions by $u(z;\nu,\sigma)$; thus, if $\nu \neq -\frac{1}{2} - n$, then $u(z;\nu,\sigma)$ denotes an MTW solution and if $\nu = -\frac{1}{2} - n$, then $u(z;\nu,\sigma)$ signifies a left-end MTW solution.

5.5.1 The left-end MTW solutions

We know from Figure 5.6 that for an MTW solution with $\nu \approx -\frac{1}{2} - n$, $2\lfloor -\nu \rfloor + 1$ rows of poles are dislodged from the pole field on the left. The left-end MTW solutions are the limiting cases in which these dislodged rows of poles move to $+\infty$, as illustrated in Figure 5.10. The two central frames in Figure 5.10 are phase portraits [88], which depict the phase of the solution u, i.e., $\mathrm{Arg}(u) \in (-\pi, \pi]$, according to the colour wheel above Figure 5.10. All MTW solutions asymptote to positive real values in the right half-plane as $z \to \infty$, see (5.7). However, as ν decreases to the critical value $-\frac{1}{2} - n$, the dislodged poles move infinitely far to the right (thus rendering the large-z formula (5.7) singular) resulting in negative real values in the right half-plane as $z \to \infty$ for the left-end MTW solution, as shown in the third frame of Figure 5.10. As ν decreases through $-\frac{1}{2} - n$, the factor $\Gamma(\nu + \frac{1}{2})$ in (5.7) discontinuously changes sign and the dislodged poles and zeros return into the finite right half-plane as the reciprocals of poles and zeros that exited the finite right-half plane, cf. the leftmost and rightmost frames in Figure 5.10. In the left half-plane, however, there are no perceptible changes in the solution as ν transitions through $-\frac{1}{2} - n$, see Figure 5.10. This is because the small-x formulae (5.10)–(5.13) are continuous functions of ν for fixed $\sigma \neq \sigma_c$, where σ_c is defined in (5.14) and (5.15).

It is shown in Theorem 7 of section 5.8 that the left-end MTW solutions, $u(z;-\nu,\sigma)$, $\nu = n + \frac{1}{2}$, $n \in \mathbb{Z}$, are the negatives of the MTW solutions $u(z;\nu,\sigma)$. Hence, the left-end solution in Figure 5.10 is the negative of the $\nu = 3/2$ solution in Figure 5.4. The large-z behaviour of the left-end MTW solution in Figure 5.10 is therefore given by the negative of the large-z formula (5.7) and thus $u \sim -1$, $z \to \infty$ in the right half-plane.

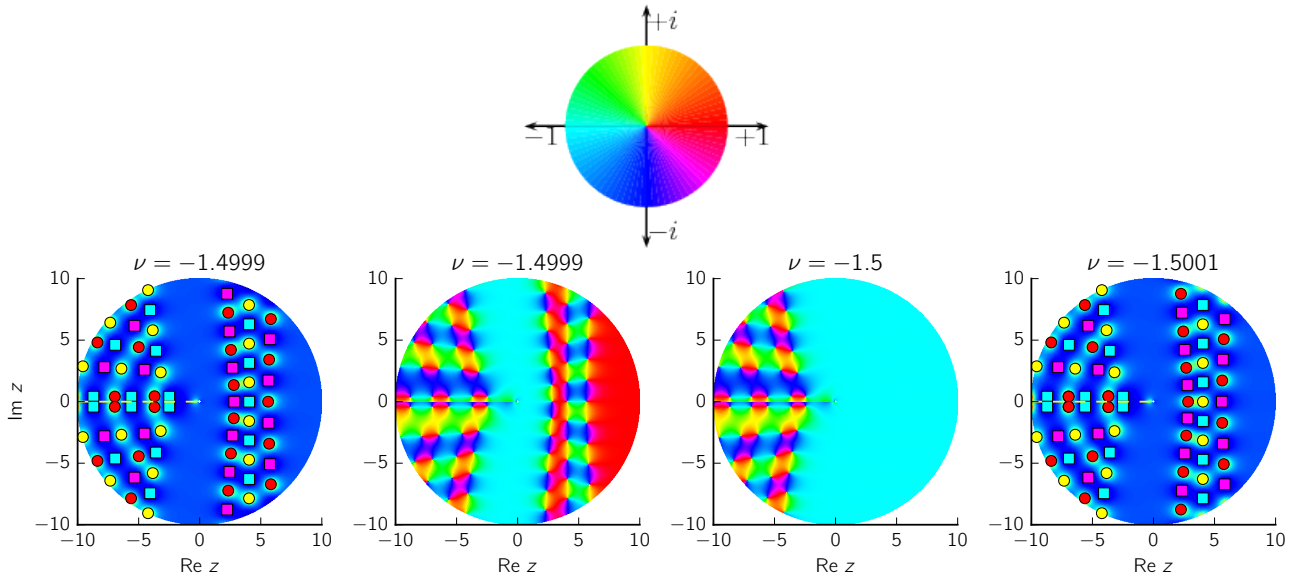

Figure 5.10: A left-end MTW solution (third frame) and two nearby MTW solutions: the leftmost and rightmost frames are modulus plots of the nearby MTW solutions and the second frame is a phase portrait of the solution in the leftmost frame. The only discernible differences between the solutions are in the right half-plane. For these solutions, $\sigma = 1$.

5.5.2 The right-end MTW solutions

Recall from the relationship (4.76) that the Bessel function solutions defined in (4.74) and depicted in Figure 4.5 are one-parameter LDT solutions with $\nu = -\frac{1}{2} - n$ (which are indicated by open circles in the parameter space shown in Figure 4.2), while, according to (5.6), the one-parameter LDT solutions are MTW solutions if $\nu \neq -\frac{1}{2} - n$. Thus, intuitively we expect MTW solutions with $\nu \approx -\frac{1}{2} - n$ to be approximately related to the Bessel function solutions in (4.74). That is, from (4.76) and (5.6) we expect

$$\begin{aligned} u(z; -1-2n, 1+2n, C) &= u^{(0)}\Big(z; -1-2n, 1+2n, \frac{(-4)^n}{n!}C\Big) \\ &\approx u\Big(z; \nu, \frac{(-4)^n}{n!}\frac{C}{2^{-2\nu}\Gamma(\nu+\frac{1}{2})}\Big), \qquad \nu \approx -\frac{1}{2} - n, \end{aligned} \tag{5.36}$$

or

$$u\Big(z; -1-2n, 1+2n, 2^{-2\nu}\Gamma(\nu+\tfrac{1}{2})\frac{n!}{(-4)^n}\lambda\Big) \approx u(z; \nu, \lambda), \qquad \nu \approx -\frac{1}{2} - n. \tag{5.37}$$

Figure 5.11 illustrates the sense in which (5.37) holds: the right-end MTW solutions (the solutions on the left-hand side of (5.37)) are limiting MTW solutions in which the pole-fields in the left half-plane of the nearby MTW solutions exit the finite plane, which leaves the $2n+1$ dislodged rows of poles and zeros in the finite plane. The middle frame depicts the left-hand

side of (5.37) with

$$C = 2^{-2\nu}\Gamma(\nu + \tfrac{1}{2})\frac{n!}{(-4)^n}\lambda, \tag{5.38}$$

(cf. (5.36) and (5.37)), $\nu = -1.4999$, $n = 1$ and $\lambda = 1/\pi$. The left and right frames of Figure 5.11 show nearby MTW solutions, which are examples of the right-hand side of (5.37). The solution in the middle frame of Figure 5.11 is also shown in the second row of Figure 4.5. Since the one MTW solution in Figure 5.11 has $\nu > -\frac{3}{2}$ and the other $\nu < -\frac{3}{2}$, the factor $\Gamma(\nu + \frac{1}{2})$ has opposite signs for the two solutions and thus the signs of λ differ in Figure 5.11 to ensure that (5.37) holds.

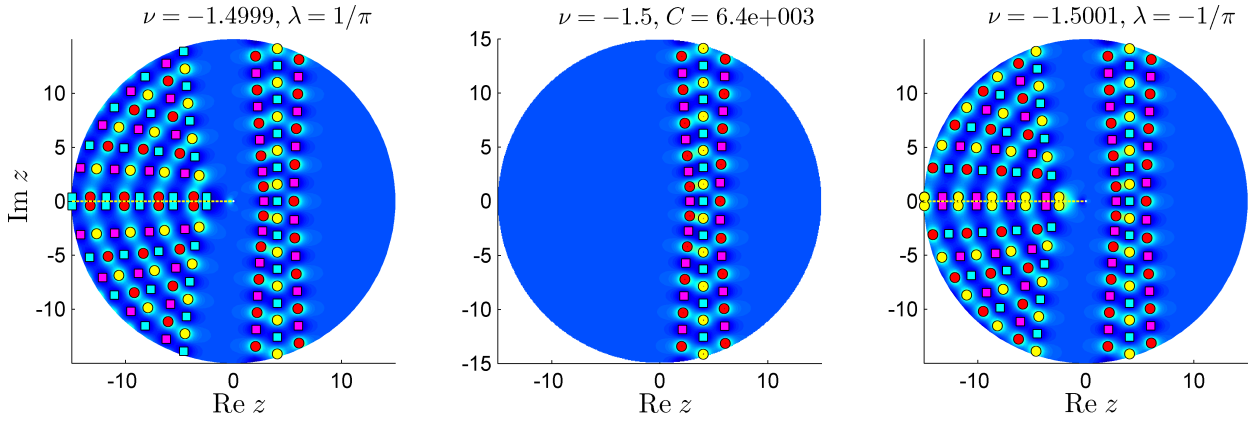

Figure 5.11: The single-valued right-end MTW solution, central frame, can be considered a limiting solution of its two nearby MTW solutions. The parameters of the right-end MTW solution and the nearby MTW solutions, C and λ, respectively, are related according to (5.38) with $n = 1$.

Figure 5.11 is analogous to Figure 5.10: in the latter figure the dislodged rows of poles and zeros move to $+\infty$ and return as reciprocals whereas in Figure 5.11 it is the pole field in the left half-plane that moves to $-\infty$ and returns as its reciprocal as ν decreases through $-\frac{1}{2} - n$. The left-end and right-end MTW solutions constitute the limiting cases in these figures. In Figure 5.10 small changes in the small-z formula lead to significant qualitative differences in the right half-plane. Similarly, in Figure 5.11, small perturbations in the right half-plane result in significant differences in the left half-planes of the solutions.

5.6 The MTW solutions on multiple sheets

The pole field dynamics of the MTW solutions on sheets other than the 0th sheet is very different for the two cases $0 < \sigma < 1$ and $\sigma = 1 + 2i\mu$, $\mu \geq 0$. This can be ascribed to the type of branch point admitted at $z = 0$ in the two cases. We shall find that if σ is a rational number with $0 < \sigma < 1$, then, as suggested by the small-z approximation $u(z/2) \sim Bz^{\sigma}$ (see (5.10)), $z = 0$ is an algebraic branch point and thus the MTW solution has a finite number of distinct branches. It is stated (but not proved) in [56] that algebraic branch points of $\mathrm{P_{III}}$ solutions must have order three. However, as we shall prove in Corollary 2 and as our numerical solutions confirm (e.g., Figure 5.13), MTW solutions with algebraic branch points of any order exist. For the case $\sigma = 1 + 2i\mu$, $\mu \geq 0$, for which the small-x approximations (5.18)–(5.23) are valid, our computations indicate that the MTW solutions have infinitely many distinct branches. The algebraic branch points admitted at $z = 0$ for $0 < \sigma < 1$ imply certain rotational symmetries which lead to the existence of pole-free sectors on sheets neighbouring the 0th sheet that are not present when $\sigma = 1 + 2i\mu$, $\mu \geq 0$. Henceforth we consider only the s-th sheets with $s > 0$ since, as we noted in section 5.2, an MTW solution with real parameters on $\arg z < 0$ is the complex conjugate of the solution on $\arg z > 0$. Thus, the solution features on the $-s$-th sheet are easily deduced from those on the $+s$-th sheet.

5.6.1 Empirical results for $0 < \sigma < 1$

We used the enhanced PFS method to survey the MTW solutions on sheets 0–4. For fixed ν we found that multiple pole-free sectors appear on these sheets as σ is varied between 0 and 1. Table 5.1 describes all the pole-free sectors that we found. All MTW solutions have a pole-free sector on sheet 0, contained in $-\pi/2 < \arg z < \pi/2$, with $u \sim 1$, $z \to \infty$, see (5.7). However, a pole-free sector occurs on sheet s, $s > 0$, only if σ is rational, i.e., $0 < \sigma = \frac{n_1}{n_2} < 1$, where n_1 and n_2 are relatively prime. As we shall prove, it follows from the small-z expansion (5.9) that if $\sigma = \frac{n_1}{n_2}$, then the solution is invariant under rotations through an angle of $2\pi n_2$ and thus we need only consider sheets 0 to $n_2 - 1$, or the region $-\pi/2 < \arg z \leq (2n_2 - \frac{1}{2})\pi$. Table 5.1 shows that if n_1 and n_2 have opposite parity, then MTW solutions with $\nu \in \mathbb{Z}$ have one more pole-free sector than MTW solutions with $\nu \in \mathbb{R} \setminus \mathbb{Z}$: a pole-free sector in a right half-plane with $u \sim -1$ if n_2 is odd, or in a left half-plane with $u \sim 1$ if n_2 is even. If n_1

and n_2 are both odd, then MTW solutions with $\nu \in \mathbb{Z}$ have two more pole-free sectors than their $\nu \in \mathbb{R} \setminus \mathbb{Z}$ counterparts: one contained in an upper or lower half-plane with $u \sim \pm i$ and another contained in a lower or upper half-plane with $u \sim \mp i$.

Table 5.1: The pole-free sectors of MTW solutions $u(z;\nu,\sigma)$ with $0 < \sigma = \frac{n_1}{n_2} < 1$, where the fraction $\frac{n_1}{n_2}$ is expressed to lowest terms. The solution has n_2 distinct branches and thus it suffices to consider the region $-\pi/2 < \arg z \leq (2n_2 - \frac{1}{2})\pi$.

ν	$0 < \sigma = \frac{n_1}{n_2} < 1$	$z \to \infty$	Sector
$\nu \in \mathbb{R} \setminus \mathbb{Z}$	n_1 and n_2 have opposite parity	$u \sim 1$	$-\frac{\pi}{2} < \arg z < \frac{\pi}{2}$
	n_1 and n_2 are odd	$u \sim 1$	$-\frac{\pi}{2} < \arg z < \frac{\pi}{2}$
		$u \sim -1$	$(n_2 - \frac{1}{2})\pi < \arg z < (n_2 + \frac{1}{2})\pi$
$\nu \in \mathbb{Z}$	n_1 and n_2 have opposite parity	$u \sim 1$	$-\frac{\pi}{2} < \arg z < \frac{\pi}{2}$
		$u \sim (-1)^{n_2+1}$	$(n_2 - \frac{1}{2})\pi < \arg z < (n_2 + \frac{1}{2})\pi$
	$n_1 \bmod 4 = 1$ and n_2 is odd	$u \sim 1$	$-\frac{\pi}{2} < \arg z < \frac{\pi}{2}$
		$u \sim (-1)^{\nu} i$	$\frac{n_2-1}{2}\pi < \arg z < \frac{n_2+1}{2}\pi$
		$u \sim -1$	$(n_2 - \frac{1}{2})\pi < \arg z < (n_2 + \frac{1}{2})\pi$
		$u \sim (-1)^{\nu+1} i$	$\frac{3n_2-1}{2}\pi < \arg z < \frac{3n_2+1}{2}\pi$
	$n_1 \bmod 4 = 3$ and n_2 is odd	$u \sim 1$	$-\frac{\pi}{2} < \arg z < \frac{\pi}{2}$
		$u \sim (-1)^{\nu+1} i$	$\frac{n_2-1}{2}\pi < \arg z < \frac{n_2+1}{2}\pi$
		$u \sim -1$	$(n_2 - \frac{1}{2})\pi < \arg z < (n_2 + \frac{1}{2})\pi$
		$u \sim (-1)^{\nu} i$	$\frac{3n_2-1}{2}\pi < \arg z < \frac{3n_2+1}{2}\pi$

We used MATLAB's Parallel Computing Toolbox to parallelize the computation of solutions on sheets 0–4 for fixed ν and different σ values. Then we identified tronquée solutions on sheets 1–4 by observing the movement and orientation of pole fields in animations of solutions in which σ is varied between 0 and 1. As an example, Figure 5.12 shows the pole fields on the first sheet of the MTW solution with $\nu = -1$ as σ increases through the critical value $\sigma = 1/3$. According to the fourth case in Table 5.1, we expect to find two pole-free sectors on the first sheet when $\sigma = 1/3$: within $\pi < \arg z < 2\pi$, on which $u \sim -i$, $z \to \infty$ and within $5\pi/2 < \arg z < 7\pi/2$, on which $u \sim -1$, $z \to \infty$. As σ increases to $1/3$ the pole fields in the upper-left quarter-plane and lower half-plane move towards $z = \infty$, as shown in the first two frames. When $\sigma = 1/3$ the pole fields are out of the finite plane and as the pole fields return from $z = \infty$ for $\sigma > 1/3$ their orientations are changed (cf. the first and second rows).

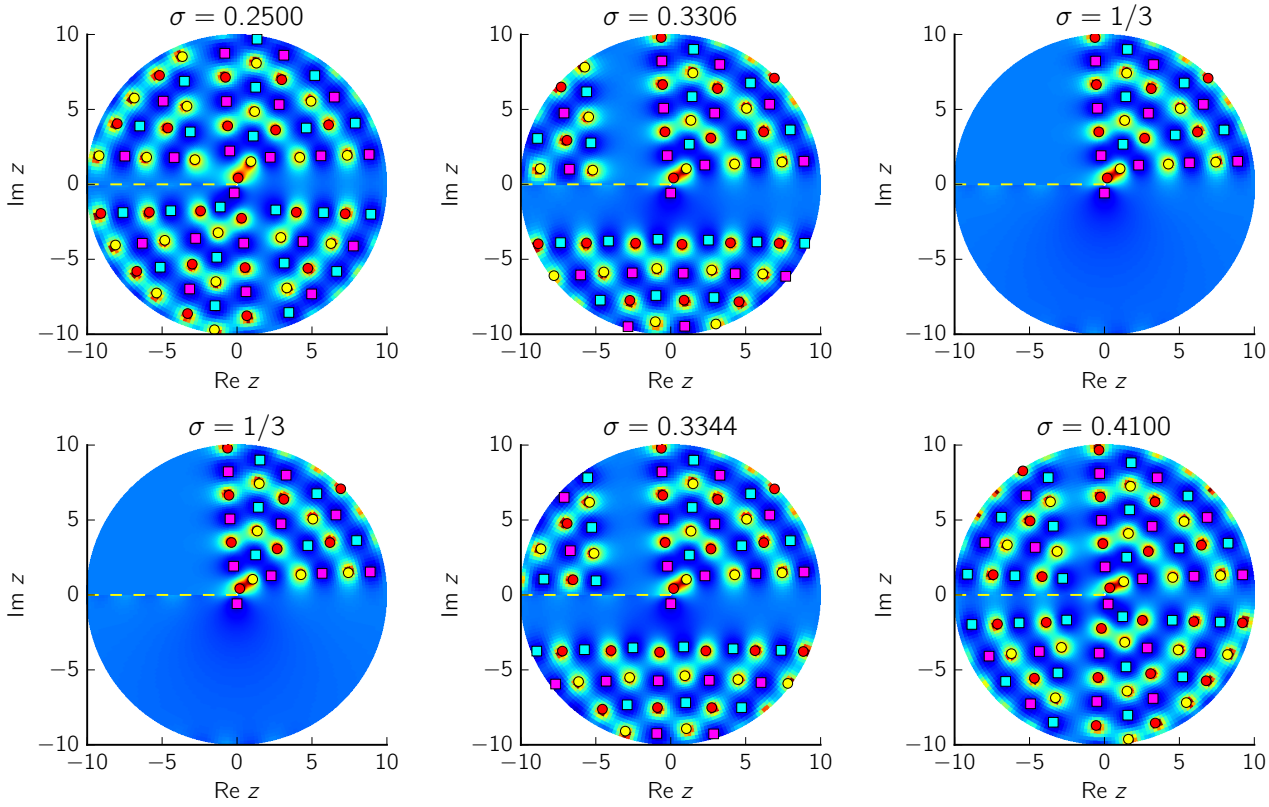

Figure 5.12: The pole fields move out of the finite plane and return with a different orientation as σ transitions through the critical value, $\sigma = 1/3$ in this case. These pole fields are on the first sheet of the MTW solution with $\nu = -1$.

Note the similarities between Figures 5.12 and 5.8. In both figures poles and zeros move out of the finite plane, resulting in a pole-free region, and return differently aligned. In Figure 5.8 the poles and zeros move toward and return from Re $\zeta = -\infty$ (or $z = 0$) and in Figure 5.13

the poles and zeros move toward and return from Re $\zeta = \infty$ (or $z = \infty$).

5.6.2 Analytical results for $0 < \sigma < 1$

To provide further justification for the empirical results in Table 5.1, we will make use of the scaling Bäcklund transformation $T_0(c_1, c_2)$, defined in (4.1)–(4.2). Recall that for solutions of $\mathrm{P}_{\mathrm{III}}^{(\mathrm{i})}$ to be closed under $T_0(c_1, c_2)$, c_1 and c_2 must each be a fourth root of unity, with c_1 and c_2 either both real or both imaginary. Hence, only the scaling transformations (4.7)–(4.10) need to be considered for $\mathrm{P}_{\mathrm{III}}^{(\mathrm{i})}$. Solutions of $\mathrm{P}_{\mathrm{III}}^{(\mathrm{i})}$ with MTW parameters (5.1), however, can only be closed under (4.9) and (4.10) if $\alpha = \beta = 0$, or $\nu = 0$. Thus, we only consider the following special cases of $T_0(c_1, c_2)$ applied to $\mathrm{P}_{\mathrm{III}}^{(\mathrm{i})}$ solutions with MTW parameters (recall that $u(z; \alpha, \beta)$ denotes a generic solution of $\mathrm{P}_{\mathrm{III}}^{(\mathrm{i})}$, whereas $u(z; \nu, \sigma)$ denotes an MTW solution of $\mathrm{P}_{\mathrm{III}}^{(\mathrm{i})}$):

$$T_0((-1)^m, e^{-i\pi m}): \qquad u(z; 2\nu, -2\nu) = (-1)^m u(e^{-i\pi m} z; 2\nu, -2\nu), \tag{5.39}$$

$$T_0((-1)^{m+1}, e^{-i\pi m}): \qquad u(z; -2\nu, 2\nu) = (-1)^{m+1} u(e^{-i\pi m} z; 2\nu, -2\nu), \tag{5.40}$$

$$T_0(-i, ie^{-i\pi m}): \qquad u(z; 0, 0) = iu(ie^{-i\pi m} z; 0, 0), \tag{5.41}$$

$$T_0(i, ie^{-i\pi m}): \qquad u(z; 0, 0) = -iu(ie^{-i\pi m} z; 0, 0). \tag{5.42}$$

Since we are interested in solutions on the s-th sheets with $s > 0$ we let m be an integer with $m \geq 2$. A simple but critical difference between the scaling transformations (4.7)–(4.10) and (5.39)–(5.42) is the additional factor $e^{-i\pi m}$ that rotates z in (5.39)–(5.42). This device will reveal relationships that exist between different Riemann sheets of the *same* solution (in the case of the auto-Bäcklund transformations (5.39), (5.41) and (5.42) that preserve parameter values) or different sheets of *different* solutions (in the case of (5.40) which changes the sign ν, resulting in different solutions on the left and right-hand sides of (5.40) if $\nu \neq 0$). The following results will be used to account for the observations in Table 5.1.

Lemma 3. *Let $T_0(c_1, e^{-i\theta})$ denote any of the transformations (5.39)–(5.42). The MTW solutions with $\nu \in \mathbb{R}$ and $0 < \sigma < 1$, $\sigma \neq \sigma_c$ (see (5.14) and (5.15)) are closed under $T_0(c_1, e^{-i\theta})$, i.e.,*

$$u(z; \widetilde{\nu}, \sigma) = T_0(c_1, e^{-i\theta}) u(z; \nu, \sigma) = c_1^{-1} u(e^{-i\theta} z; \nu, \sigma), \tag{5.43}$$

only if

$$B(\sigma, \widetilde{\nu}) = c_1^{-1} e^{-i\theta\sigma} B(\sigma, \nu), \tag{5.44}$$

where $B(\sigma,\nu)$ is defined in (5.13). If $T_0(c_1,e^{-i\theta})$ denotes the transformation (5.39), then $\widetilde{\nu}=\nu$; if $T_0(c_1,e^{-i\theta})$ is (5.40), then $\widetilde{\nu}=-\nu$ and if $T_0(c_1,e^{-i\theta})$ is (5.41) or (5.42), then $\widetilde{\nu}=\nu=0$.

Proof. As stated in section 5.1.1, a generic $\mathrm{P}_{\mathrm{III}}^{(\mathrm{i})}$ solution with MTW parameters (5.1) has a unique small-z expansion (5.9) for fixed B, ν and σ. What characterizes an MTW $\mathrm{P}_{\mathrm{III}}^{(\mathrm{i})}$ solution for fixed ν and $\sigma\neq\sigma_c$, however, is the coefficient of the leading order term of the unique small-z expansion (5.9): $B=B(\sigma,\nu)$, defined in (5.13). Thus, to prove (5.43), it suffices to show that the coefficients of the leading order terms on the left and right-hand sides of (5.43) match, which is the condition expressed in (5.44).

Alternatively, (5.43) can be proved directly by showing that the small-z expansions on the left and right-hand sides match to all orders. It follows from (5.9)–(5.13) that the small-z asymptotic expansion of the MTW solution on the left-hand side of (5.43) is, for $z\to 0$ and $0<\sigma<1$, $\sigma\neq\sigma_c$,

$$\begin{aligned} u\left(z/2;\widetilde{\nu},\sigma\right) &\sim B(\sigma,\widetilde{\nu})z^{\sigma}\left\{1+\sum_{j=1}^{\infty}\sum_{k=1}^{j+1}b_{j,k}(\sigma,\widetilde{\nu})z^{j-\sigma(j+2-2k)}\right\},\\ &= B(\sigma,\widetilde{\nu})\left[e^{i\theta}\left(e^{-i\theta}z\right)\right]^{\sigma}\left\{1+\sum_{j=1}^{\infty}\sum_{k=1}^{j+1}b_{j,k}(\sigma,\widetilde{\nu})\left[e^{i\theta}\left(e^{-i\theta}z\right)\right]^{j-\sigma(j+2-2k)}\right\}, \end{aligned} \tag{5.45}$$

while that of the scaled and rotated MTW solution on the right-hand side of (5.43) is

$$c_1^{-1}u(e^{-i\theta}z/2;\nu,\sigma)\sim c_1^{-1}B(\sigma,\nu)\left[e^{-i\theta}z\right]^{\sigma}\left\{1+\sum_{j=1}^{\infty}\sum_{k=1}^{j+1}b_{j,k}(\sigma,\nu)\left[e^{-i\theta}z\right]^{j-\sigma(j+2-2k)}\right\}. \tag{5.46}$$

The first few coefficients $b_{j,k}(\sigma,\nu)$ in (5.45) and (5.46) are defined in (5.11) with $B=B(\sigma,\nu)$. Comparing (5.45) and (5.46) we see that the two series coincide only if (5.44) and

$$b_{j,k}(\sigma,\widetilde{\nu})e^{i\theta(j-\sigma(j+2-2k))}=b_{j,k}(\sigma,\nu),\qquad 1\leq k\leq j+1,\qquad j\geq 1, \tag{5.47}$$

are satisfied. □

Theorem 5. *The MTW solutions with $\nu \in \mathbb{R}$ and $0 < \sigma < 1$, $\sigma \neq \sigma_c$ are closed under the transformations (5.39)–(5.42) with $m \geq 2$ only if, respectively,*

$$\nu \in \mathbb{R} \quad \text{and} \quad \sigma = \begin{cases} \dfrac{2n+1}{2k-1} & \text{with} \quad m = 2k-1, \ \text{or} \\ \dfrac{n}{k} & \text{with} \quad m = 2k, \end{cases} \tag{5.48}$$

$$\nu \in \mathbb{Z} \quad \text{and} \quad \sigma = \begin{cases} \dfrac{2n+1}{2k-2} & \text{with} \quad m = 2k-2, \ \text{or} \\ \dfrac{2n}{2k-1} & \text{with} \quad m = 2k-1, \end{cases} \tag{5.49}$$

$$\nu = 0 \quad \text{and} \quad \sigma = \frac{4n+1}{2k-1} \quad \text{with} \quad m = k \quad \text{and} \tag{5.50}$$

$$\nu = 0 \quad \text{and} \quad \sigma = \frac{4n+3}{2k-1} \quad \text{with} \quad m = k, \tag{5.51}$$

where n and k are integers such that $k \geq 2$ and $0 < \sigma < 1$.

Proof. According to Lemma 3, the MTW solutions are closed under the transformations (5.39)–(5.42) only if (5.44) and, for a direct proof, (5.47) are satisfied. For (5.39), $c_1 = (-1)^m$, $c_2 = e^{-i\theta} = e^{-i\pi m}$, $\widetilde{\nu} = \nu$ and thus (5.44) and (5.47) reduce to

$$e^{i\pi m\sigma} = (-1)^m \qquad \text{and} \qquad e^{i\pi m(j-\sigma(j+2-2k))} = 1, \qquad 1 \leq k \leq j+1, \qquad j \geq 1.$$

These equations are satisfied only if $m\sigma\pi = n_1\pi$, i.e., $\sigma = n_1/m$, where n_1 and m are integers with the same parity such that $0 < \sigma < 1$. If m is even, say $m = 2k$, then $\sigma = \frac{n}{k}$ and if m is odd with $m = 2k-1$, then $\sigma = \frac{2n+1}{2k-1}$ where n and k are integers such that $k \geq 2$ and $0 < \sigma < 1$.

For the transformation (5.40), $\widetilde{\nu} = -\nu$, $c_1 = (-1)^{m+1}$ and $c_2 = e^{-i\pi m}$. Thus, (5.44) implies that we require $B(\sigma, -\nu) = \pm B(\sigma, \nu)$ since $B(\sigma, \nu) \in \mathbb{R}$ for $\sigma, \nu \in \mathbb{R}$. According to Lemma 4 of section 5.8, $B(\sigma, -\nu) = B(\sigma, \nu)$ only if $\nu \in \mathbb{Z}$ and $B(\sigma, -\nu) = -B(\sigma, \nu)$ only if $\nu = n + \frac{1}{2}$, $n \in \mathbb{Z}$. However, we need only consider $\nu \in \mathbb{Z}$ since MTW solutions do not exist when $\nu = -n - \frac{1}{2}$, $n \geq 0$.[2] It then follows from the second property of the coefficients in Lemma 5 of section 5.8 that if $\nu \in \mathbb{Z}$, then the equations (5.44) and (5.47) become

$$e^{i\pi m\sigma} = (-1)^{m+1} \qquad \text{and} \qquad e^{i\pi m(j-\sigma(j+2-2k))} = (-1)^j, \qquad 1 \leq k \leq j+1, \qquad j \geq 1, \tag{5.52}$$

if $\nu \neq 0$. If $\nu = 0$, then it follows from the second and fourth properties in Lemma 5 that $b_{j,k}(\sigma, 0) = 0$ if j is odd or if j and k are even and thus (5.52) has to be satisfied only for indices

[2] If $\nu = -n - \frac{1}{2}$, $n \geq 0$, then one set of limiting MTW solutions is the left-end MTW solutions, discussed in section 5.5.1. As pointed out in the final paragraph of that section and in Theorem 7 in section 5.8, the transformation (5.40) with $m = 0$, $u(z; -\nu, \sigma) = -u(z; \nu, \sigma)$, gives the relationship between the left-end MTW solutions and the MTW solutions.

(j,k) with j even and k odd. We conclude that these equations are satisfied only if $m\sigma\pi = n_1\pi$, or, $\sigma = n_1/m$ where n_1 and m are integers with opposite parity such that $0 < \sigma < 1$. If m is even this reduces to $\sigma = \frac{2n+1}{2k-2}$ and if m is odd this reduces to $\sigma = \frac{2n}{2k-1}$ where n and k are integers such that $k \geq 2$ and $0 < \sigma < 1$.

For the transformations (5.41) and (5.42), respectively, $c_1 = \mp i$, $c_2 = ie^{-i\pi m}$ and $\widetilde{\nu} = \nu = 0$. Thus, as above, it follows from the second and fourth properties in Lemma 5 that (5.44) and (5.47) become

$$e^{i\pi(m-\frac{1}{2})\sigma} = \pm i, \qquad e^{i\pi(m-\frac{1}{2})(j-j(\sigma+2-2k))} = 1, \qquad 1 \leq k \leq j+1,\ j \geq 1, \qquad j \text{ even and } k \text{ odd}.$$

For the transformation (5.41), the equations are satisfied only if $(m-\frac{1}{2})\sigma\pi = (n_1-\frac{1}{2})\pi$ with n_1 odd, i.e., only if $\sigma = (2n_1-1)/(2m-1)$, which is equivalent to (5.50). Similarly, for (5.42) the equations are satisfied only if $\sigma = (2n_1-1)/(2m-1)$, with n_1 even, which is equivalent to (5.51). □

Corollary 2. *If $0 < \sigma = \frac{n_1}{n_2} < 1$, $\sigma \neq \sigma_c$, n_1 and n_2 are positive integers and $\frac{n_1}{n_2}$ is reduced to lowest terms, then the MTW solution $u(z;\nu,\sigma)$ is an algebraically branched solution with n_2 distinct branches.*

Proof. This follows from (5.48): setting $m = 2n_2$ in (5.39) we have

$$u(z;\nu,\sigma) = T_0(1, e^{-2i\pi n_2})u(z;\nu,\sigma) = u(e^{-2i\pi n_2}z;\nu,\sigma), \qquad \sigma = \frac{n_1}{n_2}. \tag{5.53}$$

Since $\sigma = \frac{n_1}{n_2}$ is expressed to lowest terms, n_2 is the smallest positive integer for which (5.53) holds and thus the solution has exactly n_2 distinct branches. □

To generate the results in Table 5.1, we shall use repeated applications of the transformations (5.39)–(5.42).

Corollary 3. *For the transformations and values of ν and σ specified in Theorem 5, the MTW solution $u(z;\nu,\sigma)$ is also closed under $T_0^n(c_1, e^{-i\theta})$, $n \geq 1$ and*

$$T_0^n(c_1, e^{-i\theta})u(z;\nu,\sigma) = T_0(c_1^n, e^{-in\theta})u(z;\nu,\sigma) = c_1^{-n}u(e^{-in\theta}z;\nu,\sigma) = u(z;\widehat{\nu},\sigma), \tag{5.54}$$

where $\widehat{\nu} = \nu$ if $T_0(c_1, e^{-i\theta})$ is one of the auto-Bäcklund transformations (5.39), (5.41) or (5.42) and $\widehat{\nu} = (-1)^n\nu$ if $T_0(c_1, e^{-i\theta})$ is the transformation (5.40) that reflects the parameter ν.

Proof. If $u(z;\nu,\sigma)$ is closed under $T_0(c_1,e^{-i\theta})$, then

$$u(z;\widetilde{\nu},\sigma)=T_0(c_1,e^{-i\theta})u(z;\nu,\sigma)=c_1^{-1}u(e^{-i\theta}z;\nu,\sigma). \tag{5.55}$$

If $T_0(c_1,e^{-i\theta})$ denotes (5.39), (5.41) or (5.42), then $\widetilde{\nu}=\nu$ and thus it follows from Theorem 5 that $u(z;\widetilde{\nu},\sigma)$ is also closed under $T_0(c_1,e^{-i\theta})$. If $T_0(c_1,e^{-i\theta})$ denotes (5.40), then $\widetilde{\nu}=-\nu$ and since $\nu\in\mathbb{Z}$, $\widetilde{\nu}\in\mathbb{Z}$ and thus it follows from Theorem 5 that $u(z;\widetilde{\nu},\sigma)$ is also closed under $T_0(c_1,e^{-i\theta})$. Hence, from (5.55) we have

$$\begin{aligned} u(z;\widehat{\nu},\sigma) &= T_0(c_1,e^{-i\theta})u(z;\widetilde{\nu},\sigma)=T_0^2(c_1,e^{-i\theta})u(z;\nu,\sigma)\\ &= T_0(c_1,e^{-i\theta})c_1^{-1}u(e^{-i\theta}z;\nu,\sigma)=c_1^{-2}u(e^{-2i\theta}z;\nu,\sigma)=T_0(c_1^2,e^{-2i\theta})u(z;\nu,\sigma), \end{aligned}$$

where $\widehat{\nu}=\widetilde{\nu}=\nu$ if $T_0(c_1,e^{-i\theta})$ is (5.39), (5.41) or (5.42) and $\widehat{\nu}=-\widetilde{\nu}=-(-\nu)=(-1)^2\nu$ if $T_0(c_1,e^{-i\theta})$ is (5.40). Repeating this argument $n-1$ times, we arrive at the result (5.54). □

In addition to the scaling transformations (5.39)–(5.42), we require the Bäcklund transformation T_ε, defined by (4.61), to account for the results in Table 5.1.

Theorem 6. *For $\nu\in\mathbb{R}$ and $0<\sigma<1$, $\sigma\neq\sigma_c$, the MTW solutions are closed under T_ε, i.e.,*

$$u(z;\nu+\varepsilon,\sigma)=T_\varepsilon u(z;\nu,\sigma),\qquad \varepsilon^2=1,\qquad \nu\neq\frac{1}{2\varepsilon}(\sigma-1). \tag{5.56}$$

Proof. From the definition of the Bäcklund transformation T_ε, the right-hand side of (5.56) is a solution of $\mathrm{P}_{\mathrm{III}}^{(\mathrm{i})}$ and therefore, as stated in section 5.1.1, it has a unique small-z expansion of the form (5.9). To show that this solution is an MTW solution with parameter $\nu+\varepsilon$ and thereby prove the result (5.56), it is sufficient to show, by the same argument given in the first paragraph of the proof of Lemma 3, that the coefficients of the leading order terms of the small-z expansions on the left and right-hand sides of (5.56) match. Substituting the small-z expansion (5.9)–(5.13) into T_ε, we find that the coefficient of the leading order term is

$$\left(\frac{2\varepsilon\nu+1+\sigma}{2\varepsilon\nu+1-\sigma}\right)B(\sigma,\nu). \tag{5.57}$$

The leading order coefficient on the left-hand side of (5.56) is $B(\sigma,\nu+\varepsilon)$ and using (5.13) and the property $\Gamma(z)=(z-1)\Gamma(z-1)$, it follows that

$$B(\sigma,\nu+\varepsilon)=\left(\frac{2\varepsilon\nu+1+\sigma}{2\varepsilon\nu+1-\sigma}\right)B(\sigma,\nu), \tag{5.58}$$

and thus (5.57) and (5.58) match. □

It follows from Theorem 6 that $u(z;\nu+k,\sigma)=T_1^k u(z;\nu,\sigma)$ and $u(z;\nu-k,\sigma)=T_{-1}^k u(z;\nu,\sigma)$ for $\sigma\neq\sigma_c$ and $k\geq 1$, and thus it suffices to apply T_1 only to solutions with $\nu\geq 0$ and T_{-1} only to solutions with $\nu\leq 0$. Hence, the the cases implied by the restriction on ν in (5.56), which follow from the denominator in (5.57)–(5.58), need not arise.

The final results required to generate the empirical results in Table 5.1 using Bäcklund transformations are the large-z behaviours in certain sectors of the solutions $T_0^n(c_1,e^{-i\theta})u(z;\nu,\sigma)$ and the solutions obtained from compositions of T_ε^k with $T_0^n(c_1,e^{-i\theta})u(z;\nu,\sigma)$.

Proposition 1. *For the transformations and values of ν and σ specified in Theorem 5,*

$$u(z;\widehat{\nu},\sigma)=T_0^n(c_1,e^{-i\theta})u(z;\nu,\sigma)=T_0(c_1^n,e^{-in\theta})u(z;\nu,\sigma)=c_1^{-n}u(e^{-in\theta}z;\nu,\sigma)\sim c_1^{-n}, \tag{5.59}$$

and

$$u(z;\widehat{\nu}+k\varepsilon,\sigma)=T_\varepsilon^k u(z;\widehat{\nu},\sigma)=T_\varepsilon^k\circ T_0^n(c_1,e^{-i\theta})u(z;\nu,\sigma)\sim\begin{cases}c_1^{-n}, & \text{if } c_1^{-2n}=1,\\ (-1)^k c_1^{-n}, & \text{if } c_1^{-2n}=-1,\end{cases} \tag{5.60}$$

where (5.59) and (5.60) are valid for

$$z\to\infty,\qquad -\frac{\pi}{2}+n\theta<\arg z<\frac{\pi}{2}+n\theta, \tag{5.61}$$

and where $\epsilon^2=1$, $\widehat{\nu}=\nu$ if $T_0(c_1,e^{-i\theta})$ is (5.39), (5.41) or (5.42) and $\widehat{\nu}=(-1)^n\nu$ if $T_0(c_1,e^{-i\theta})$ is (5.40).

Proof. The result (5.59) follows from Corollary 3 and the large-z formula (5.7):

$$\begin{aligned}u(z;\widehat{\nu},\sigma)=T_0^n(c_1,e^{-i\theta})u(z;\nu,\sigma) &= c_1^{-n}u(e^{-in\theta}z;\nu,\sigma)\\ &\sim c_1^{-n}+\mathcal{O}\left((e^{-in\theta}z)^{-\nu-1/2}\exp[-2e^{-in\theta}z]\right),\end{aligned} \tag{5.62}$$

for $z\to\infty$, $-\frac{\pi}{2}+n\theta<\arg z<\frac{\pi}{2}+n\theta$.

It follows from Theorem 6 that the large-z behaviour of $u(z;\widehat{\nu}+\varepsilon,\sigma)$ on (5.61) can be obtained by substituting (5.62) into (4.61) and letting $z\to\infty$, in which case we find

$$u(z;\widehat{\nu}+\varepsilon,\sigma)=T_\varepsilon u(z;\widehat{\nu},\sigma)=T_\varepsilon\circ T_0^n(c_1,e^{-i\theta})u(z;\nu,\sigma)\sim -c_1^{-n}\frac{\varepsilon(c_1^{-2n}-1)z+(2\varepsilon\widehat{\nu}+1)c_1^{-n}}{\varepsilon(c_1^{-2n}-1)z-(2\varepsilon\widehat{\nu}+1)c_1^{-n}}, \tag{5.63}$$

with the same exponential-order correction term as in (5.62). For the transformations (5.39)–(5.42), $c_1^{-2n}=1$ or $c_1^{-2n}=-1$, hence (5.63) becomes

$$u(z;\widehat{\nu}+\varepsilon,\sigma)=T_\varepsilon u(z;\widehat{\nu},\sigma)\sim\begin{cases}c_1^{-n}+\mathcal{O}\left((e^{-i\theta}z)^{-\nu-1/2}\exp[-2e^{-i\theta}z]\right), & \text{if } c_1^{-2n}=1,\\ -c_1^{-n}+\mathcal{O}\left((e^{-i\theta}z)^{-\nu-1/2}\exp[-2e^{-i\theta}z]\right), & \text{if } c_1^{-2n}=-1,\end{cases} \tag{5.64}$$

for $z \to \infty$, $-\pi/2+n\theta < \arg z < \pi/2+n\theta$, provided $\widehat{\nu} \neq -\frac{1}{2}$ if $\varepsilon = 1$ and $c_1^{-2n} = 1$ and $\widehat{\nu} \neq \frac{1}{2}$ if $\varepsilon = -1$ and $c_1^{-2n} = 1$. However, as noted in the paragraph below the proof of Theorem 6, these cases need not be considered. Hence, the leading order large-z behaviours of $u(z;\widehat{\nu}+\varepsilon,\sigma)$ and $u(z;\widehat{\nu},\sigma)$ are the same on $-\pi/2+n\theta < \arg z < \pi/2+n\theta$ if $c_1^{-2n} = 1$ (cf. (5.64) and (5.62)) but if $c_1^{-2n} = -1$, then the leading order behaviours differ in sign. Note that in both cases, $c_1^{-2n} = 1$ and $c_1^{-2n} = -1$, the correction terms are of the same order in (5.64) and (5.62). Thus, if we apply T_ε to $u(z;\widehat{\nu}+\varepsilon,\sigma)$ on $-\pi/2+n\theta < \arg z < \pi/2+n\theta$, let $z \to \infty$ and use (5.64), then we again arrive at (5.63), with the same correction term as in (5.62), except that $\widehat{\nu}$ is replaced by $\widehat{\nu}+\varepsilon$ in (5.63) and c_1^{-n} is replaced by $-c_1^{-n}$ if $c_1^{-2n} = -1$ in (5.64). We conclude, as before, that the leading order large-z behaviours of $u(z;\widehat{\nu}+2\varepsilon,\sigma)$ and $u(z;\widehat{\nu}+\varepsilon,\sigma)$ are the same on $-\pi/2+n\theta < \arg z < \pi/2+n\theta$ if $c_1^{-2n} = 1$ but if $c_1^{-2n} = -1$, then the leading order behaviours differ in sign. Repeating this argument another $k-2$ times we arrive at the result (5.60). □

Proposition 2. *The empirical results in Table 5.1 follow from the preceding analytical results: Theorem 5, Corollaries 2 and 3 and Proposition 1.*

Proof. Consider the first case in Table 5.1: $\nu \in \mathbb{R} \setminus \mathbb{Z}$ and $0 < \sigma = \frac{n_1}{n_2} < 1$, where the fraction $\frac{n_1}{n_2}$ is expressed to lowest terms and n_1 and n_2 have opposite parity. According to Theorem 5, of the transformations (5.39)–(5.42), $u(z;\nu,\sigma)$ is closed under (5.39) only, with $m = 2n_2$. As shown in the proof of Corollary 2, this transformation maps the solution from sheet s to sheet $s+n_2$. However, according to Corollary 2, the solution has n_2 distinct branches. Thus, henceforth we need not consider the transformation (5.39) with $m = 2n_2$ and we may restrict our attention to sheets 0 to n_2-1, or the region $-\frac{\pi}{2} < \arg z < (2n_2-\frac{1}{2})\pi$. We conclude that the only inference that can be made regarding $u(z;\nu,\sigma)$ based on the transformations (5.39)–(5.42) is that it has n_2 distinct branches. As with all MTW solutions, $u(z;\nu,\sigma)$ has a pole-free sector within $-\pi/2 < \arg z < \pi/2$ on which $u \sim 1$ (see the large-z formula (5.7)). These conclusions are consistent with the results for the first case in Table 5.1.

Now let $\nu \in \mathbb{R} \setminus \mathbb{Z}$ and suppose n_1 and n_2 are both odd (the second case in Table 5.1). Then, of the transformations (5.39)–(5.42), $u(z;\nu,\sigma)$ is closed under (5.39) only, with $m = n_2$ (and $m = 2n_2$ which, as mentioned above, need not be considered). Thus, we set $c_1 = -1$, $c_2 = e^{-i\theta} = e^{-i\pi n_2}$, $\widehat{\nu} = \nu$ and, since we require $-\frac{\pi}{2} < \arg z < (2n_2-\frac{1}{2})\pi$, $n = 1$ in (5.59) and (5.61) and obtain

$$u(z;\nu,\sigma) \sim -1, \qquad z \to \infty, \qquad (n_2-\tfrac{1}{2})\pi < \arg z < (n_2+\tfrac{1}{2})\pi,$$

which is in agreement with the second case in Table 5.1.

Let $\nu \in \mathbb{Z}$ and suppose n_1 and n_2 have opposite parity. Of the transformations (5.39)–(5.42), $u(z;\nu,\sigma)$ is closed under (5.40) only with $m = n_2$. Thus, $c_1 = (-1)^{n_2+1}$, $c_2 = e^{-i\theta} = e^{-i\pi n_2}$, $\widehat{\nu} = -\nu$ and $n = 1$ in (5.59) and (5.61):

$$u(z;-\nu,\sigma) \sim (-1)^{n_2+1}, \qquad z \to \infty, \qquad (n_2 - \tfrac{1}{2})\pi < \arg z < (n_2 + \tfrac{1}{2})\pi,$$

which agrees with the third case in Table 5.1.

Now consider the final two cases in Table 5.1: $\nu \in \mathbb{Z}$ and n_1 and n_2 are odd. Of the transformations (5.39)–(5.42), $u(z;\nu,\sigma)$ is closed under (5.39) and, if $\nu = 0$, (5.41) (if $n_1 \bmod 4 = 1$) or (5.42) (if $n_1 \bmod 4 = 3$). For solutions with $\nu \in \mathbb{Z} \setminus \{0\}$, we also consider compositions of T_ε^k with (5.41) (if $n_1 \bmod 4 = 1$) or (5.42) (if $n_1 \bmod 4 = 3$) applied to $u(z;\nu,\sigma)$ with $\nu = 0$. For the transformations (5.41) and (5.42), respectively, $m = (n_2+1)/2$, $c_1 = \mp i$, $c_2 = e^{-i\theta} = ie^{-i\pi m} = e^{-i\pi n_2/2}$, $\widehat{\nu} = \nu = 0$ and $n = 1, 2, 3$ in (5.60) and (5.61):

$$u(z;k\varepsilon,\sigma) = T_\varepsilon^k \circ T_0^n(\mp i, e^{-i\pi n_2/2})u(z;0,\sigma) \sim \begin{cases} -1 & \text{even } n \\ (-1)^k(\pm i)^n & \text{odd } n \end{cases}, \tag{5.65}$$

$$z \to \infty, \qquad (nn_2 - 1)\tfrac{\pi}{2} < \arg z < (nn_2 + 1)\tfrac{\pi}{2}, \qquad n = 1, 2, 3, \qquad k \geq 0, \tag{5.66}$$

which is equivalent to the results for the fifth and sixth cases in Table 5.1.

For the transformation (5.39), $m = n_2$, $c_1 = -1$, $c_2 = e^{-i\theta} = e^{-i\pi n_2}$ and $n = 1$ in (5.59) and (5.61):

$$u(z;\nu,\sigma) \sim -1, \qquad z \to \infty, \qquad (n_2 - \tfrac{1}{2})\pi < \arg z < (n_2 + \tfrac{1}{2})\pi, \qquad \nu \in \mathbb{Z}. \tag{5.67}$$

However, (5.67) is the same as (5.65) and (5.66) with $n = 2$. The latter observation also follows from the fact that the transformation (5.39) is the same as two applications of (5.41) or (5.42) for the cases under consideration (the final two cases in Table 5.1): $T_0^2(\mp i, e^{-i\pi n_2/2}) = T_0((\mp i)^2, (e^{-i\pi n_2/2})^2) = T_0(-1, e^{-i\pi n_2})$, see (5.54). □

5.6.3 Examples for $0 < \sigma < 1$

Figure 5.13 illustrates solutions described by the third case in Table 5.1: $\nu \in \mathbb{Z}$ and $\sigma = \frac{n_1}{n_2} = \frac{1}{2}$. According to Corollary 2 the solutions in Figure 5.13 have two distinct branches, as can be confirmed by considering the colours above and below the branch cuts in the second row of the

figure. As shown in the proof of Proposition 2, the pole-free sectors of solutions corresponding to the third case in Table 5.1 follow from the transformation (5.40). This transformation is unique among the scaling transformations (5.39)–(5.42) in that it gives the relationship between different regions of different solutions, whereas (5.39), (5.41) and (5.42) describe relationships between different regions of the same solution. Specifically, according to Theorem 5, the relationship between the two solutions in Figure 5.13 is given by

$$u\left(z;-1,\tfrac{1}{2}\right)=T_0(-1,e^{-2i\pi})u\left(z;1,\tfrac{1}{2}\right)=-u\left(e^{-2i\pi}z;1,\tfrac{1}{2}\right). \tag{5.68}$$

Thus, the 0th and 1st sheets of the $\nu=-1$ solution are the negatives of the 1st and 0th sheets, respectively, of the $\nu=1$ solution.

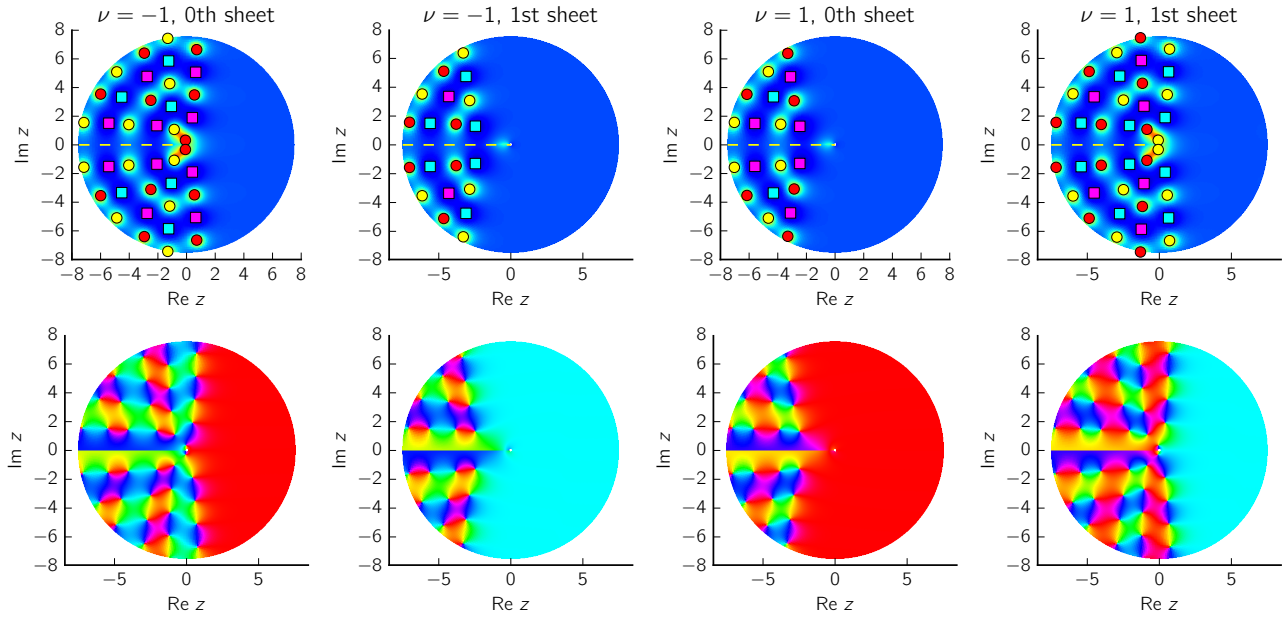

Figure 5.13: Two doubly branched MTW solutions ($\sigma=\frac{1}{2}$) that are related according to (5.68). The second row are phase portraits (see the colour wheel above Figure 5.10) of the corresponding modulus plots in the first row.

Figure 5.14 illustrates solutions corresponding to the fourth case in Table 5.1: $\nu\in\mathbb{Z}$ and $\sigma=\frac{1}{7}=\frac{n_1}{n_2}$. Since the solutions are displayed within $-\pi\le\arg z\le 9\pi$ (and the corresponding region in the ζ-plane, $-2\pi\le\operatorname{Im}\zeta\le 18\pi$), three of the four pole-free regions in Table 5.1 are visible: within $-\pi/2<\arg z<\pi/2$, $3\pi<\arg z<4\pi$ and $13\pi/2<\arg z<14\pi/2$ on which $u\sim 1$, $u\sim(-1)^\nu i$ and $u\sim -1$, respectively, for $z\to\infty$. According to Theorem 5, the solution with $\nu=0$ in the first two columns of Figure 5.14 is closed under $T_0^n(-i,e^{-7i\pi/2})$ and $T_0^n(-1,e^{-7i\pi})$, $n\ge 2$. However, since $T_0^2(-i,e^{-7i\pi/2})=T_0(-1,e^{-7i\pi})$, see (5.54), we need only

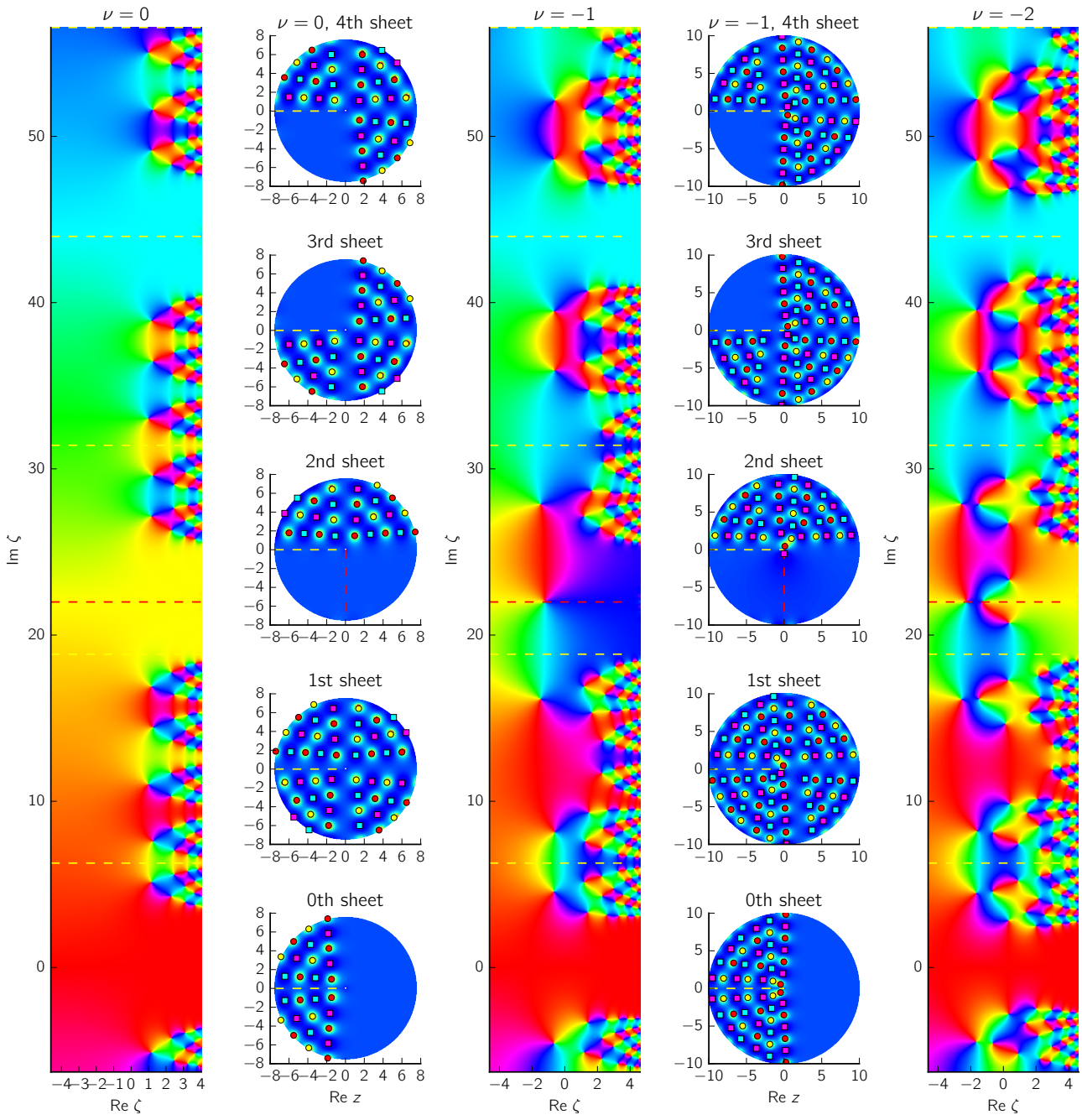

Figure 5.14: MTW solutions with $\nu \in \mathbb{Z}$ and $\sigma = \frac{1}{7}$, corresponding to the fourth case in Table 5.1, on sheets 0 to 4. The second and fourth columns are modulus plots, while the first, third and fifth columns are phase portraits of the solutions that indicate the solution values on the pole-free sectors according to the colour wheel at the top of Figure 5.10. The solutions exhibit certain symmetries and asymmetries in accordance with (5.69)–(5.72). Relationships between (i) the poles and zeros of the same solution and (ii) the poles and zeros of the different solutions are described by (4.14)–(4.15) and (5.73)–(5.74), respectively.

consider $T_0^n(-i, e^{-7i\pi/2})$. Thus,

$$u(z;0,\sigma) = T_0^n(-i, e^{-7i\pi/2})u(z;0,\sigma) = i^n u(e^{-7i\pi n/2}z;0,\sigma), \qquad \sigma = \frac{1}{7}. \tag{5.69}$$

Unlike the $\nu = 0$ solution, the solutions in the third through fifth columns of Figure 5.14 are not closed under $T_0(-i, e^{-7i\pi/2})$ (this follows from Theorem 5):

$$u(z;-k,\sigma) \neq T_0(-i, e^{-7i\pi/2})u(z;-k,\sigma) = iu(e^{-7i\pi/2}z;-k,\sigma), \qquad k = 1,2, \qquad \sigma = \frac{1}{7}. \tag{5.70}$$

However, according to Theorems 5 and 6, the following transformations are applicable to the $\nu \neq 0$ solutions in Figure 5.14:

$$u(z;-k,\sigma) = T_0(-1, e^{-7i\pi})u(z;-k,\sigma) = -u(e^{-7i\pi}z;-k,\sigma), \qquad k = 1,2, \qquad \sigma = \frac{1}{7}, \tag{5.71}$$

and

$$u(z;-k,\sigma) = T_{-1}^k u(z;0,\sigma), \qquad k = 1,2. \tag{5.72}$$

It was shown in Proposition 2 that the pole-free sectors of the solutions in Figure 5.14 follow from the transformations in (5.69), (5.71) and (5.72). Now we also consider the action of these transformations upon the simple poles and zeros of the MTW solutions in the z-plane.

The effect of the scaling transformations (5.69) and (5.71) on the poles and zeros in Figure 5.14 follow from (4.14) and (4.15): Each of the solutions in Figure 5.14 is closed under $T_0(-1, e^{-7i\pi})$, see (5.69) with $n = 2$ and (5.71). Thus, we see in all the columns of Figure 5.14 that $T_0(-1, e^{-7\pi i})$ transforms poles with residue ± 1 and zeros with $u' = \pm 1$ at z_0 to poles and zeros of the same solution at $e^{i\theta}z_0 = e^{7\pi i}z_0$ with residue $\pm c_1^{-1}c_2^{-1} = \pm 1$ and $u' = \pm c_1^{-1}c_2 = \pm 1$, respectively. For the solution in the first two columns we see that $T_0(-i, e^{-7i\pi/2})$ rotates poles and zeros through $\arg e^{i\theta} = \frac{7}{2}\pi$; the residues of the rotated poles are *preserved* since $\pm c_1^{-1}c_2^{-1} = \pm 1$ while the derivative values of the rotated zeros are *reversed* since $\pm c_1^{-1}c_2 = \mp 1$.

To consider the action of T_ε upon the poles and zeros of the MTW solutions, we substitute the two leading order terms of the Laurent expansion about a pole,

$$u(z;\nu,\sigma) = \frac{c}{z - z_0} - \frac{2\nu + c}{2z_0} + \mathcal{O}((z - z_0)), \qquad z \to z_0,\ z_0 \neq 0, \qquad c^2 = 1,$$

and the Taylor expansion about a zero,

$$u(z;\nu,\sigma) = c(z - z_0) + \frac{2\nu + c}{2z_0}(z - z_0)^2 + \mathcal{O}((z - z_0)^3), \qquad z \to z_0,\ z_0 \neq 0 \qquad c^2 = 1,$$

into (4.61). The poles are transformed to

$$u(z;\nu+\varepsilon) = T_\varepsilon u(z;\nu,\sigma) = \begin{cases} -\dfrac{\nu^2+3\varepsilon\nu+\frac{5}{4}+z_0^2}{z_0(4\nu+2\varepsilon)} + \mathcal{O}((z-z_0)), & \text{if } c=\varepsilon, \\ \dfrac{\varepsilon}{z-z_0} - \dfrac{2(\nu+\varepsilon)+\varepsilon}{2z_0} + \mathcal{O}((z-z_0)) & \text{if } c=-\varepsilon, \end{cases} , \varepsilon^2=1, \quad (5.73)$$

and the zeros are transformed to

$$u(z;\nu+\varepsilon) = T_\varepsilon u(z;\nu,\sigma) = \begin{cases} -\dfrac{z_0(4\nu+2\varepsilon)}{-2\nu^2+\frac{1}{2}+z_0^2} + \mathcal{O}((z-z_0)), & \text{if } c=\varepsilon, \\ \varepsilon(z-z_0) + \dfrac{2(\nu+\varepsilon)+\varepsilon}{2z_0}(z-z_0)^2 + \mathcal{O}((z-z_0)^3) & \text{if } c=-\varepsilon. \end{cases} \quad (5.74)$$

Thus, T_ε transforms poles (or zeros) of $u(z;\nu,\sigma)$ with residue $-\varepsilon$ (or $u'=-\varepsilon$) to poles (or zeros) of $u(z;\nu+1,\sigma)$ with residue $+\varepsilon$ (or $u'=+\varepsilon$). This can be confirmed by comparing solutions in Figure 5.14 (and also in Figure 5.4) whose ν-values differ by an integer. The fact that T_ε does not map poles (or zeros) of $u(z;\nu,\sigma)$ with residue ε (or $u'=\varepsilon$) to poles (or zeros) of $u(z;\nu+1,\sigma)$ is most easily seen in Figure 5.4. In the top row of that figure, the poles and zeros that are closest to the imaginary axis, a row of red poles (residue $+1$) and purple zeros ($u'=+1$), are not mapped to poles and zeros at the corresponding points of the solutions in the second row whose ν-values differ by $+1$.

According to (5.69), all the pole-free sectors in the first two columns of Figure 5.14 are scaled and rotated versions of the pole-free sector within $-\pi/2 < \arg z < \pi/2$ on the 0th sheet. Similarly, according to (5.71), the pole-free sector within $-13\pi/2 < \arg z < 14\pi/2$ in the third to fifth columns is rotationally symmetric, up to a scaling factor, to the pole-free sector on the 0th sheet. However, according to (5.70), the pole-free sector within $3\pi < \arg z < 4\pi$ in the third to fifth columns is not a scaled and rotated version of the pole-free sector on the 0th sheet. This asymmetry can be confirmed by comparing the solutions on the centers of these two pole-free sectors: the lines $\arg z = 0$ and $\arg z = \frac{7\pi}{2}$; the latter line is indicated by red dotted lines in Figure 5.14. There is one zero, for the $\nu=-1$ solution, and two zeros, for the $\nu=-2$ solution, on $\arg z = \frac{7\pi}{2}$ whereas $\arg z = 0$ is devoid of zeros for these solutions. Generally, our numerical solutions indicate that on pole-free sectors with $u \sim \pm i$, $z \to \infty$, see Table 5.1, there are $|\nu|$ poles or $|\nu|$ zeros close to $z=0$ in the center of the pole-free sector.

Thus far, we have not considered the application of the Bäcklund transformations $T_0(c_1, e^{-i\theta})$ and T_ε to the MTW solutions for the case $\sigma=\sigma_c$, see (5.14) and (5.15), since then the small-z expansion (5.9), on which our analysis relies, is not valid. We have found numerically that

even if σ_c coincides with one of the values in Table 5.1, then the MTW solution still has n_2 distinct branches and its pole-free sectors are still described by Table 5.1. This observation is consistent with the observation made in section 5.4.2. Namely, if $0 < \sigma_c = \frac{n_1}{n_2} < 1$, then the positions of the poles and zeros in the limit $\sigma \to \sigma_c$, given in (5.31), (5.32) and (5.33), repeat every n_2 sheets, in accordance with what one expects if $z = 0$ is a branch point of order n_2.

We mention one final empirical observation for the MTW solutions on multiple sheets for the case $0 < \sigma < 1$. We found that if $\nu = 0$, then the real and imaginary axes on all the sheets are free of poles and zeros. If $\nu \in \mathbb{Z} \setminus \{0\}$, then there are no poles or zeros on the real axes but there is no restriction on the number of poles or zeros on the imaginary axes. If $\nu \in \mathbb{R} \setminus \mathbb{Z}$, then we found that infinitely many poles or zeros can occur on the real and imaginary axes of sheets other than the 0th sheet.

5.6.4 $\sigma = 1 + 2i\mu,\ \mu \geq 0$

The pole dynamics on sheet $s > 0$ for the case $\sigma = 1 + 2i\mu$, $\mu \geq 0$, when the small-z behaviour on $\arg z = 0$ is given by (5.18)–(5.23), is qualitatively the same for all MTW solutions with $\nu \in \mathbb{R}$. After all the transitions through the σ values in Table 5.1, the poles are aligned along spirals in the z-plane, see Figure 5.15. As μ increases, the spiral arms move closer to each other, the pole density increases rapidly as the sheet index increases and no pole-free sectors are present on sheets other than the 0th sheet. This suggests that the solution is logarithmically branched if $|\sigma| \geq 1$ since every sheet appears to be distinct.

5.7 Conclusions

The MTW solutions were first studied asymptotically on the positive real axis in [59]. Their asymptotics in the right half-plane follow from the recent results in [54]. Our enhanced PFS method completes this progression since it has enabled the study of the MTW tronquée solutions of $\mathrm{P_{III}}$ on multiple Riemann sheets. A new result of this study is the asymptotics of the MTW solutions on multiple Riemann sheets, which follow from Theorems 5 and 6 and which are given in Proposition 1 and Table 5.1.

Our enhanced PFS method has enabled the first computational exploration of tronquée $\mathrm{P_{III}^{(i)}}$ solutions on multiple Riemann sheets. In the process we found solution features that were not

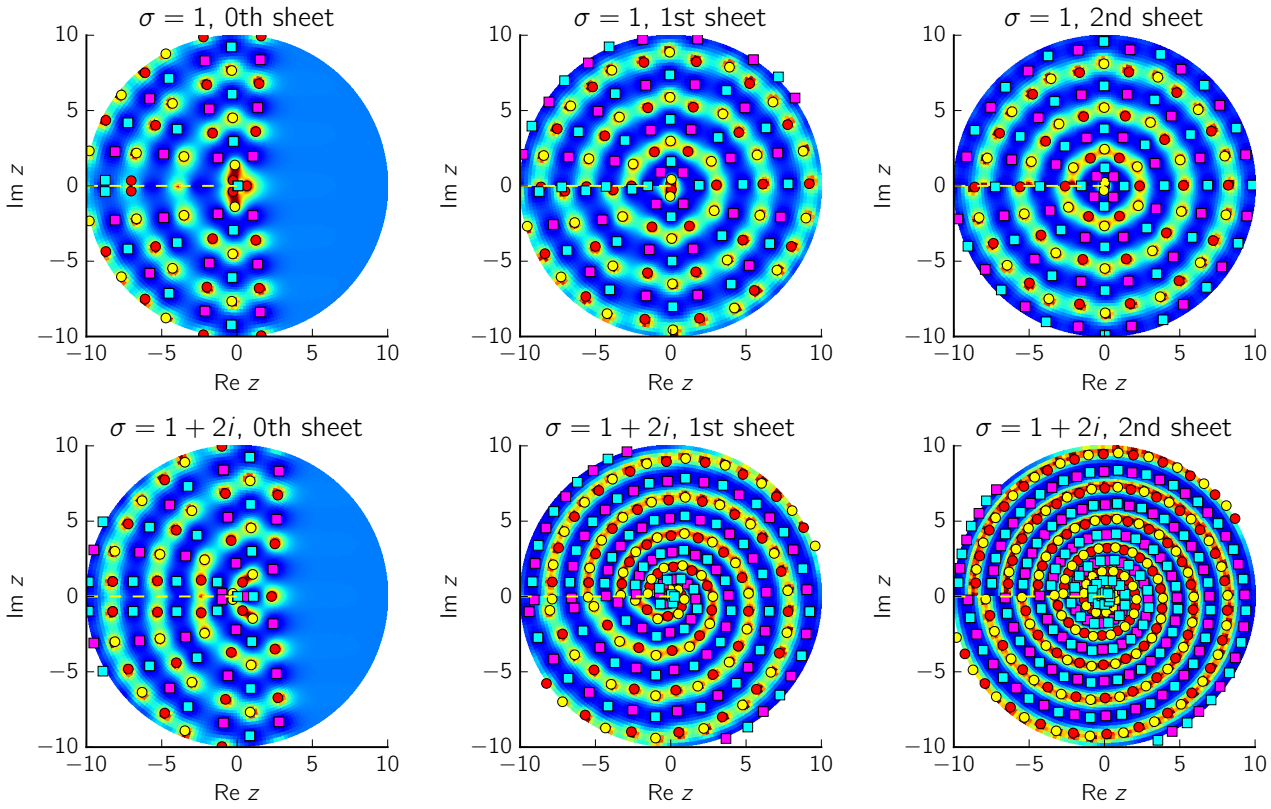

Figure 5.15: The typical pole dynamics of an MTW solution for the case $|\sigma| \geq 1$ on multiple sheets (for this solution $\nu = -5/4$).

seen in the computational studies of the single-valued Painlevé transcendents in [32–34, 76–78]. This is to be expected from the added complexity that the fixed singularity of the $\mathrm{P_{III}}$ equation at $z = 0$ can give rise to: a branch point and thus a possible infinitude of distinct solution branches and a potential limit point of poles or zeros. One basic difference is that poles and zeros of multivalued $\mathrm{P_{III}}$ solutions can enter or leave a bounded region through a branch point and a branch cut as the parameters are varied (see Figures 5.1 and 5.2 for examples). For the class of $\mathrm{P_{III}^{(i)}}$ solutions that we explored, the branch point can be a source of infinitely many poles or zeros on the positive real axis. By contrast, in single-valued solutions, poles and zeros can only enter or exit a bounded region through the boundary of the domain. Transitions through tronquée solutions for large-z with its associated change in pole field alignment, see Figure 5.12, are also features of the meromorphic Painlevé transcendents. However, for $\mathrm{P_{III}}$ solutions tronquée transitions also occur for small z (see Figure 5.8 and recall that $z = e^{\zeta/2}$) during which poles and zeros coalesce at $z = 0$, which is another solution feature that was not observed in the numerical studies of the meromorphic Painlevé transcendents.

We also found symmetries or asymmetries between different sheets of the same solution

(Figure 5.14), the same sheets of different solutions (Figure 5.14) and different sheets of different solutions (Figure 5.13). These global properties of the solutions could be explained using small-z asymptotics and Bäcklund transformations. To our knowledge the pole-free sectors in Table 5.1 have not been noted in the literature before (except for the pole-free sector on the 0th sheet which follows from the results in [54]). We also quantified changes in these pole-free regions as functions of the parameters in sections 5.3.1, 5.3.2 and 5.4.1.

We hope that our analytical and computational results will clear up a misconception in the literature (e.g., in [56, 60]) regarding the order of algebraic branch points that are admitted by $\mathrm{P_{III}}$ at $z = 0$: algebraic branch points of any order, not just order three, are possible (see Corollary 2 and an example in Figure 5.13). triply branched solutions [15,56], special function solutions [60] and generic solutions that fall into none of these categories.

Many types of $\mathrm{P_{III}}$ solutions remain to be explored (not to mention the unexplored solution spaces of $\mathrm{P_V}$ and $\mathrm{P_{VI}}$). These include tronquée solutions for the cases $\gamma\delta \neq 0$, $\alpha \neq -\beta$ and $\gamma = 0$, $\alpha\delta \neq 0$ (see Theorem 2 in [54]); single-valued solutions [36, pp.151–154]; triply branched solutions [15,56], special function solutions [60] and generic solutions that fall into none of these categories.

5.8 Appendix

Lemmata 4 and 5 below give properties of the coefficients in the small-z MTW expansion (5.9)–(5.13) that are used in section 5.1, the proof of Theorem 5 in section 5.6.2 and the proof of Theorem 7, which follows Lemma 5. Although Theorem 7 below is first referred to in section 5.5.1, we recommend that its proof be read in conjunction with the proof of Theorem 5 in the later section 5.6.2 since similar ideas are used.

Lemma 4. *Let $\nu \in \mathbb{R}$ and $0 < \sigma < 1$ or $\sigma = 1 + 2i\mu$, $\mu > 0$, then $B(\sigma, -\nu) = B(\sigma, \nu)$ if and only if $\nu \in \mathbb{Z}$ and $B(\sigma, -\nu) = -B(\sigma, \nu)$ if and only if $\nu = n + \frac{1}{2}$, $n \in \mathbb{Z}$.*

Proof. It follows from the definition of $B(\sigma, \nu)$ in (5.13) and the identity [23]

$$\Gamma(z)\Gamma(1 - z) = \frac{\pi}{\sin(\pi z)},$$

that

$$B(\sigma, \nu) + B(\sigma, -\nu) = 2B(\sigma, \nu)R(\sigma, \nu),$$

where

$$R(\sigma,\nu) := \frac{\cos(\pi\sigma/2)\cos(\pi\nu)}{\cos[\pi(\sigma/2-\nu)]}.$$

For $0<\sigma<1$ or $\sigma = 1+2i\mu$, $\mu>0$, the zeros and singularities of $B(\sigma,\nu)$ occur only at σ_c, defined in (5.14) and (5.15), see (5.13) and (5.22). Hence, we exclude $\sigma=\sigma_c$ in which case $0<|B(\sigma,\nu)|<\infty$. Also note that if $\sigma\neq\sigma_c$, then $\cos[\pi(\sigma/2-\nu)]\neq 0$ and thus $|R(\sigma,\nu)|<\infty$. Hence, for $\nu\in\mathbb{R}$ and $0<\sigma<1$ or $\sigma=1+2i\mu$, $\mu>0$ with $\sigma\neq\sigma_c$ we have

$$B(\sigma,-\nu)=B(\sigma,\nu) \;\Leftrightarrow\; R(\sigma,\nu)=1 \;\Leftrightarrow\; \cos(\pi\sigma/2)\cos(\pi\nu)=\cos[\pi(\sigma/2-\nu)] \;\Leftrightarrow \nu\in\mathbb{Z},$$

and

$$B(\sigma,-\nu)=-B(\sigma,\nu) \;\Leftrightarrow\; R(\sigma,\nu)=0 \;\Leftrightarrow\; \cos(\pi\nu)=0 \;\Leftrightarrow \nu=n+\frac{1}{2},\ n\in\mathbb{Z}.$$

□

Lemma 5. *Let $b_{j,k}(\sigma,\nu)$, $1\le k\le j+1$, $j\ge 1$, with $0<\sigma<1$ or $\sigma=1+2i\mu$, $\mu>0$ and $\sigma\neq\sigma_c$ (see (5.14) and (5.15)) denote the coefficients of the small-z expansion (5.9) of the MTW solutions. The coefficients have the following properties for $1\le k\le j+1$, $j\ge 1$:*

1. *If $j\ge 3$, then $b_{j,1}(\sigma,\nu)=0$.*
2. *If $\nu\in\mathbb{Z}$, then $b_{j,k}(\sigma,-\nu)=(-1)^j b_{j,k}(\sigma,\nu)$.*
3. *If $\nu=n+\frac{1}{2}$, $n\in\mathbb{Z}$, then $b_{j,k}(\sigma,-\nu)=b_{j,k}(\sigma,\nu)$.*
4. *If j and k are both even, then $b_{j,k}(\sigma,0)=0$.*

Proof. We express the MTW small-z expansion (5.9) in powers of $2z$:

$$u(z;\nu,\sigma)\sim\sum_{j=0}^{\infty} C_j(z;\nu,\sigma)(2z)^j, \qquad C_j(z;\nu,\sigma)=B(\sigma,\nu)(2z)^{-\sigma(j-1)}\sum_{k=0}^{j} b_{j,k+1}(\sigma,\nu)(2z)^{2\sigma k},$$

and define $b_{0,1}(\sigma,\nu)=1$ so that $C_0(z;\sigma,\nu)=B(\sigma,\nu)(2z)^{\sigma}$. Henceforth, we shall use the abbreviated notations C_j, B and $b_{j,k}$ for $C_j(z;\sigma,\nu)$, $B(\sigma,\nu)$ and $b_{j,k}(\sigma,\nu)$. Multiplying the $\mathrm{P}_{\mathrm{III}}^{(\mathrm{i})}$ equation with MTW parameters (5.1) by uz, one obtains

$$zu\frac{d^2u}{dz^2}-z\left(\frac{du}{dz}\right)^2+u\frac{du}{dz}-2\nu(u^3-u)-zu^4+z=0. \tag{5.75}$$

We expand every term in (5.75) in powers of $2z$:

$$\sum_{j=-1}^{\infty}\left[D_j-E_j+F_j\right](2z)^j-2\nu\sum_{j=0}^{\infty}\left[C_j^{(3)}-C_j\right](2z)^j-\frac{1}{2}\sum_{j=1}^{\infty}C_{j-1}^{(4)}(2z)^j+\frac{1}{2}(2z)\sim 0, \tag{5.76}$$

where the coefficients in (5.76) are coefficients of the corresponding term in (5.75), e.g., the D_j are the coefficients of the first term in (5.75): $zuu'' \sim \sum_{j=-1}^{\infty} D_j (2z)^j$.

Setting $j = -1$ in (5.76), one obtains an identity:

$$D_{-1} - E_{-1} + F_{-1} = 2B^2(2z)^{2\sigma}\sigma(\sigma-1) - 2B^2(2z)^{2\sigma}\sigma^2 + 2B^2(2z)^{2\sigma}\sigma = 0.$$

For $j = 0$, (5.76) becomes

$$D_0 - E_0 + F_0 - 2\nu\left[C_0^{(3)} - C_0\right] = 2B(2z)^{\sigma}\left[B(\sigma-1)^2 b_{1,1} + \nu\right] + 2B(2z)^{3\sigma}\left[(\sigma+1)^2 b_{1,2} - B\nu\right] = 0,$$

from which it follows that

$$b_{1,1} = -\frac{\nu}{B(\sigma-1)^2}, \qquad \text{and} \qquad b_{1,2} = \frac{B\nu}{(\sigma+1)^2}. \tag{5.77}$$

For $j = 1$, (5.76) simplifies to

$$\left[8B^2(\sigma-1)^2 b_{2,1} + 2\nu B b_{1,1} + \frac{1}{2}\right] + 2B(2z)^{2\sigma}\left[4B b_{2,2} - 3\nu B^2 b_{1,1} + \nu b_{1,2} + 4B\sigma^2 b_{1,1} b_{1,2}\right]$$
$$B^2(2z)^{4\sigma}\left[8(\sigma+1)^2 b_{2,3} - 6\nu B b_{1,2} - \frac{1}{2}B^2\right] = 0,$$

from which we obtain

$$b_{2,1} = \frac{4\nu^2 - (\sigma-1)^2}{16B^2(\sigma-1)^4}, \qquad b_{2,2} = -\frac{\nu^2}{(\sigma+1)(\sigma-1)^2}, \qquad \text{and} \qquad b_{2,3} = \frac{B^2(12\nu^2 + (\sigma+1)^2)}{16(\sigma+1)^4}. \tag{5.78}$$

The formula for the remaining coefficients is

$$b_{j+1,s+1} = \frac{1}{2(\sigma(j+1-2s) - j - 1)^2}\left[T_1 + T_2 + T_3 + T_4\right], \qquad 0 \le s \le j+1, \qquad j \ge 2, \tag{5.79}$$

where

$$T_1 = T_1(\sigma,\nu) = \sum_{k=0}^{j-1} \sum_{r=\max\{0,s-j+k\}}^{\min\{s,k+1\}} K b_{k+1,r+1} b_{j-k,s-r+1}, \qquad 0 \le s \le j+1, \tag{5.80}$$

$$K = 2(\sigma k - 2\sigma r - k - 1)(\sigma(j - 2s - 2k + 4r - 1) - j + 2k + 1), \tag{5.81}$$

$$T_2 = T_2(\sigma,\nu) = 2\nu B \sum_{k_1=0}^{j} \sum_{k_2=0}^{k_1} \sum_{\ell_1=\max\{0,s-1-j+k_1\}}^{\min\{k_1,s-1\}} \sum_{\ell_2=\max\{0,\ell_1-k_1+k_2\}}^{\min\{k_2,\ell_1\}} b_{k_2,\ell_2+1} b_{k_1-k_2,\ell_1-\ell_2+1} b_{j-k_1,s-\ell_1}, \qquad 1 \le s \le j+1, \tag{5.82}$$

$$T_3 = T_3(\sigma,\nu) = -\frac{2\nu}{B} b_{j,s+1}, \qquad 0 \le s \le j, \tag{5.83}$$

$$T_4 = T_4(\sigma,\nu) = \frac{B^2}{2} \sum_{k_1=0}^{j-1} \sum_{k_2=0}^{k_1} \sum_{k_3=0}^{k_2} \sum_{\ell_1=\max\{0,s-1-j+k_1\}}^{\min\{k_1,s-2\}} \sum_{\ell_2=\max\{0,\ell_1-k_1+k_2\}}^{\min\{k_2,\ell_1\}} \sum_{\ell_3=\max\{0,\ell_2-k_2+k_3\}}^{\min\{k_3,\ell_2\}} b_{k_3,\ell_3+1} b_{k_2-k_3,\ell_2-\ell_3+1} b_{k_1-k_2,\ell_1-\ell_2+1} b_{j-1-k_1,s-1-\ell_1}, \qquad 2 \le s \le j+1. \tag{5.84}$$

In the inductive arguments below we will make use of the fact that (5.79) is an explicit formula for the coefficient $b_{j+1,s+1}$. That is, if the coefficients b_{i_1,i_2} with $1 \le i_1 \le j$, $1 \le i_2 \le i_1+1$ are known, then $b_{j+1,s+1}$ can be determined according to (5.79).

To prove the first property of the coefficients, we set $s=0$ in (5.79) and obtain

$$b_{j+1,1} = \frac{1}{2(j+1)^2(\sigma-1)^2}\left[\sum_{k=0}^{j-1} 2(\sigma k - k - 1)(j-2k-1)(\sigma-1) b_{k+1,1} b_{j-k,1} - \frac{2\nu}{B} b_{j,1}\right]. \tag{5.85}$$

Setting $j=2$ and $j=3$ in (5.85) we find, respectively,

$$b_{3,1} = -\frac{b_{2,1}}{9}\left(b_{1,1} + \frac{\nu}{B(\sigma-1)^2}\right), \qquad \text{and} \qquad b_{4,1} = -\frac{b_{3,1}}{16}\left(4b_{1,1} + \frac{\nu}{B(\sigma-1)^2}\right).$$

We conclude from (5.77) that $b_{3,1}=0$, which implies that $b_{4,1}=0$. Thus, for $j \ge 4$ every term in (5.85) is zero and hence $b_{j,1}=0$, $j \ge 3$.

We now prove the second property of the coefficients by induction. It follows from Lemma 4 and equations (5.77) and (5.78) that the coefficients $b_{j,k}$, $1 \le k \le j+1$, $j=1,2$ have the second property. The induction hypothesis is that the coefficients $b_{j,k}$, $1 \le k \le j+1$, $1 \le j \le n$, for some $n > 2$, have the second property. It then follows from the induction hypothesis, Lemma 4 and the formulas (5.80)–(5.84) that

$$T_i(\sigma,-\nu) = (-1)^{j+1} T_i(\sigma,-\nu), \qquad i=1,2,3,4, \qquad \nu \in \mathbb{Z},$$

for each of the s-indices indicated in (5.80)–(5.84). We conclude from (5.79) that

$$b_{j+1,s+1}(\sigma,-\nu) = (-1)^{j+1} b_{j+1,s+1}(\sigma,\nu), \qquad 0 \le s \le j+1,$$

which concludes the proof of the second property.

It follows from Lemma 4 and equations (5.77) and (5.78) that the coefficients $b_{j,k}$, $1 \le k \le j+1$, $j=1,2$ have the third property. We omit the inductive proof of the third property since it is similar to the proof of the second property.

To prove the fourth property of the coefficients, it is sufficient to let j and s be odd in (5.79) and to show that $T_i(\sigma,0)=0$, $i=1,2,3,4$. It follows immediately from (5.82) and (5.83) that $T_2(\sigma,0)=T_3(\sigma,0)=0$. Hence, to complete the proof we are going to prove by induction that $T_1(\sigma,0)=T_4(\sigma,0)=0$ for odd j and s. We observe that the fourth property of the coefficients holds in (5.78). The induction hypothesis is that this property holds for $b_{j,k}$, $1 \le k \le j+1$, $1 \le j \le n$ for some $n \ge 4$. Now consider the summands of $T_1(\sigma,0)$ and $T_4(\sigma,0)$, respectively:

$$K b_{k+1,r+1} b_{j-k,s-r+1}, \qquad \text{and} \qquad b_{k_3,\ell_3+1} b_{k_2-k_3,\ell_2-\ell_3+1} b_{k_1-k_2,\ell_1-\ell_2+1} b_{j-1-k_1,s-1-\ell_1},$$

where K is defined in (5.81). We now argue that if j and s are odd, then every summand of $T_1(\sigma,0)$ and $T_4(\sigma,0)$ is zero and thus $T_1(\sigma,0)=T_4(\sigma,0)=0$. There are two cases to consider: (i) the summand of $T_1(\sigma,0)$ or $T_4(\sigma,0)$ contains at least one coefficient b_{i_1,i_2}, with odd i_1 and (ii) for every coefficient b_{i_1,i_2} in the summand of $T_1(\sigma,0)$ or $T_4(\sigma,0)$, i_1 is even. The second property of the coefficients implies that $b_{i_1,i_2}=0$ if i_1 is odd since $\nu=0$. Thus, in case (i), the summand of $T_1(\sigma,0)$ or $T_4(\sigma,0)$ is zero. To show that the summand of $T_1(\sigma,0)$ or $T_4(\sigma,0)$ is zero in case (ii), it is sufficient to show that it contains at least one coefficient b_{i_1,i_2}, with even i_1 and even i_2, since then $b_{i_1,i_2}=0$ according to the induction hypothesis. Equivalently, we have to show that it is not possible for every coefficient b_{i_1,i_2} in the summand of $T_1(\sigma,0)$ or $T_4(\sigma,0)$ to have indices (i_1,i_2) with i_1 even and i_2 odd. For example, suppose the summand of $T_1(\sigma,0)$, $Kb_{k+1,r+1}b_{j-k,s-r+1}$, is such that $k+1$ is even, $r+1$ is odd, $j-k$ is even and $s-r+1$ is odd. Recalling that s is odd, the supposition that $s-r+1$ is odd implies that r is odd, which contradicts the assumption that $r+1$ is odd. Thus, it is not possible for the summand of $T_1(\sigma,0)$ to contain only coefficients b_{i_1,i_2} with i_1 even and i_2 odd. Letting s and j be odd in the summand of $T_4(\sigma,0)$, one can similarly argue that it is not possible for every coefficient in the summand to be of the form b_{i_1,i_2} with i_1 even and i_2 odd. Thus, in case (ii) the summand of $T_1(\sigma,0)$ or $T_4(\sigma,0)$ is zero. □

Theorem 7. *The left-end MTW solution, $u(z;-\nu,\sigma)$, where $\nu=\frac{1}{2}+n$, $n\geq 0$, and the MTW solution $u(z;\nu,\sigma)$ are related according to*

$$u(z;-\nu,\sigma)=T_0(-1,1)u(z;\nu,\sigma)=-u(z;\nu,\sigma). \tag{5.86}$$

Proof. According to Lemma 3, the result follows if (5.44) and, for a direct proof, (5.47) hold. For the transformation $T_0(-1,1)$, $\widetilde{\nu}=-\nu$, $c_1=-1$ and $c_2=e^{-i\theta}=1$ and thus (5.44) and (5.47) become

$$B(\sigma,-\nu)=-B(\sigma,\nu),\qquad b_{j,k}(\sigma,-\nu)=b_{j,k}(\sigma,\nu),\qquad 1\leq k\leq j+1,\qquad j\geq 1. \tag{5.87}$$

It follows from Lemma 4 and the third property in Lemma 5 that these equations are satisfied for $0<\sigma<1$ or $\sigma=1+2i\mu$, $\mu>0$ only if $\nu=\frac{1}{2}+n$, $n\in\mathbb{Z}$.

For $\sigma=1$, the equations in (5.87) are not valid since $B(\sigma,\nu)$ is undefined according to (5.13). To prove (5.86) for $\sigma=1$, it is sufficient to show (by the same argument used in the first paragraph of the proof of Lemma 3) that the leading order terms of the $\sigma=1$ small-x

expansions on the left and right-hand sides of (5.86) match. We show this as follows. If $\sigma = 1$, then the small-x behaviour of MTW solutions is given by (5.18) and as $x \to 0^+$

$$u(x/2;\nu,\sigma) + u(x/2;-\nu,\sigma) \sim \frac{x}{2}\left[C(\nu) + C(-\nu)\right]\left\{-\ln x + \frac{1}{4\nu}\left[C(\nu) - C(-\nu)\right]\right\}, \qquad \sigma = 1. \tag{5.88}$$

It follows from the definition of $C(\nu)$ in (5.19) and the identities [23]

$$\psi(z+1) = \psi(z) + \frac{1}{z}$$

and

$$\psi(z) - \psi(1-z) = -\frac{\pi}{\tan(\pi z)}$$

that

$$C(\nu) + C(-\nu) = \frac{2\pi\nu}{\tan \pi\nu}, \tag{5.89}$$

which is zero only if $\nu = n + \frac{1}{2}$, $n \in \mathbb{Z}$. Comparing (5.89) and (5.88), we conclude that the leading order terms of $u(z;-\nu,\sigma)$ and $-u(z;\nu,\sigma)$ match as $x \to 0^+$ only if $\nu = n + \frac{1}{2}$, $n \in \mathbb{Z}$. $\square$

Chapter 6

Epilogue

6.1 Contributions and summary of the thesis

- In this thesis and in [27] we presented the first numerical methods that are capable of the efficient and accurate computation of solutions of P_{III}, P_V and P_{VI} on their Riemann surfaces. These solutions are of great interest in modern special function theory and in many physical applications. The main ingredients of the methods are (i) a node placement algorithm for generating a node layout in the complex plane that conforms to the highly non-uniform pole densities of the multivalued Painlevé transcendents, (ii) variable step size Padé methods that automatically select paths that ensure high accuracy and stability and (iii) the navigation of integration paths around branch points onto the desired sheets of the Riemann surfaces.

- We displayed, for the first time, solutions to these equations on multiple Riemann sheets. We depicted these solutions using modulus plots (which indicate the locations and types of poles and zeros) and phase portraits (which indicate complex solution values and the geometry of the Riemann surfaces). These depictions allow one to rapidly apprehend many solution properties.

- Using the new numerical method, we provided evidence for the existence of special solutions to the sixth Painlevé equation that have pole-free sectors, known as tronquée solutions, which appears not to have been identified in the literature before.

- Using the new numerical method, we surveyed and studied a set of multivalued tronquée

solutions of P_{III}. We animated the solutions as functions of the parameters and observed their pole dynamics, which include the creation of an infinity of poles or zeros at the branch point; the passage of poles and zeros between Riemann sheets through their branch cuts; changes in pole-free regions, which were also estimated analytically; the coalescence of poles and zeros at the branch point and the realignment of entire pole fields that recede out of and return into the finite complex plane. The latter two solution features corresponded in some cases to transitions through singularities in the small-z or large-z asymptotic connection formulae. Solutions in these singular limits were also studied and it was shown that one set of limiting solutions is a set of meromorphic solutions that are special cases of solutions that are expressible in terms of Bessel functions.

For the study of the tronquée solutions on multiple Riemann sheets, MATLAB's Parallel Computing Toolbox expedited the computation of solutions that constituted separate frames of the solution animations. Multiple parameter-dependent pole-free sectors were observed which had not been identified in the literature before. A complete analytical account was given of these pole-free sectors. The analysis relied on a small-z connection formula and the symmetries inherent in the P_{III} equation, as expressed through Bäcklund transformations. One consequence of the analysis was the demonstration of the fact that algebraically branched P_{III} solutions can have any number of distinct sheets, not just three, as reported elsewhere in the literature.

We believe that the numerical study of the tronquée solutions illustrates, as did the previous PFS-enabled studies in [32–34, 76–78], that the empirical, or computational, approach to the study of the Painlevé transcendents, which is not a common methodological approach in Painlevé research, can furnish new results for analysis to confirm.

6.2 Possible topics for future research

- Analysis of the convergence, stability and complexity of the enhanced PFS method. Such an analysis could yield optimal choices of the parameters of the method that minimize the execution time for a given level of accuracy.

- In the enhanced PFS method the Stage 1 node set is first generated (based on experimentation or some *a priori* assumption about the unknown pole density of the solution) after

which the Stage 1 Padé paths are run. An alternative approach that could be explored is to generate the Stage 1 node set adaptively at the same time as which the Stage 1 paths are being run. One manner in which this could be achieved is to use, while a path is being run, the Taylor coefficients to estimate the radius of convergence, which can then be used to choose a node separation function with which to generate a local Stage 1 node set. This would generate a Stage 1 node set that conforms to the pole density of the solution but without the need for experimentation or assumptions regarding the pole density of the solution. In addition, if the domain is partitioned, then this approach would be amenable to massive parallelization in the manner described in section 3.1.2.

- Proof of the existence and uniqueness of tronquée solutions of $\mathrm{P_{VI}}$. Our attempt at a proof using Wasow's theorem was unsuccessful, but there may be some reformulation of $\mathrm{P_{VI}}$ that satisfies the conditions of Wasow's theorem. An alternative method of proof is via the isomonodromy method. The proof of these solutions could be complemented by a computational study.

- At the time of writing, methods for the analysis of tronquée solutions of $\mathrm{P_{III}}$ and $\mathrm{P_V}$ in the finite plane are under development by R. Costin and X. Xia [20]. Their analyses could be compared to the estimates we obtained for the changes in the pole-free regions in sections 4.5.3, 5.3.1, 5.3.2 and 5.4.1. Their analytical methods and our computational methods could be combined to explore the possible tronquée solutions of $\mathrm{P_{VI}}$.

- The use of the enhanced PFS method to conduct systematic surveys of the vast unexplored expanses of the solution spaces of $\mathrm{P_{III}}$, $\mathrm{P_V}$ and $\mathrm{P_{VI}}$. For $\mathrm{P_{III}}$ we highlight particular classes of solutions that remain to be surveyed.

  - We explored one-parameter LDT tronquée solutions of $\mathrm{P_{III}^{(i)}}$ that lie on the line $\alpha = -\beta$ in parameter space and which are related to other one-parameter LDT solutions on the lines $\alpha = -\beta$ or $\alpha = \beta$ in parameter space. One-parameter tronquée $\mathrm{P_{III}^{(i)}}$ solutions off these lines remain to be explored, for which small-z connection formulae (which are not available as far as we are aware but which could be derived using the Riemann–Hilbert approach) could prove valuable.

  - The unique, $k = 0$ LDT tronquée solutions of $\mathrm{P_{III}^{(i)}}$, of which we have only explored the solutions on the lines $\alpha \pm \beta = 4n$, $n \in \mathbb{Z}$, which are the rational solutions of $\mathrm{P_{III}^{(i)}}$.

- The Bessel function solutions of $\mathrm{P}_{\mathrm{III}}^{(\mathrm{i})}$, of which we studied only those that intersect the lines $\alpha = -\beta$ or $\alpha = \beta$ in parameter space.
- The one-parameter and unique LDT tronquée solutions of $\mathrm{P}_{\mathrm{III}}^{(\mathrm{ii})}$. An example of the latter type of tronquée solution was given in section 3.3.2. The unique tronquée solutions of $\mathrm{P}_{\mathrm{III}}^{(\mathrm{ii})}$ for the cases $\beta = 2n$, $n \in \mathbb{Z}$ are algebraic solutions that are rational functions of $z^{1/3}$, examples of which are given in [15, 60].
- Meromorphic solutions of $\mathrm{P}_{\mathrm{III}}$ and $\mathrm{P}_{\mathrm{III}}^{(7)}$ (see the final paragraph of section 3.3.2). The expansions about $z = 0$ that characterize these solutions are given in [56] and [36, pp. 151–154].
- The remainder of the solutions spaces of $\mathrm{P}_{\mathrm{III}}^{(\mathrm{i})}$ or $\mathrm{P}_{\mathrm{III}}^{(\mathrm{ii})}$, i.e., their generic solutions.

- Every Painlevé transcendent has an associated tau function that is holomorphic except at the fixed singularities of the associated Painlevé equation [64]. It is often the tau function, instead of the associated Painlevé transcendent, that arises in applications. The computation and exploration of the tau functions could therefore be undertaken in the same spirit as the PFS studies of the Painlevé transcendents in [32–34, 76–78] and in this thesis.

Bibliography

[1] M.J. Ablowitz and H. Segur. Asymptotic solutions of the Korteweg–de Vries equation. *Stud. Appl. Math.*, 57(1):13–44, 1977.

[2] A.A. Abramov and L.F. Yukhno. Numerical solution of the Cauchy problem for the Painlevé I and II equations. *Comput. Math. Math. Phys.*, 52(3):321–329, 2012.

[3] A.A. Abramov and L.F. Yukhno. Numerical solution of the Painlevé IV equation. *Comput. Math. Math. Phys.*, 52(11):1565–1573, 2012.

[4] A.A. Abramov and L.F. Yukhno. Numerical solution of the Cauchy problem for Painlevé III. *Differential Equations*, 48(7):909–918, 2012.

[5] A.A. Abramov and L.F. Yukhno. Numerical solution of the Painlevé V equation. *Comput. Math. Math. Phys.*, 53(1):44–56, 2013.

[6] A.A. Abramov and L.F. Yukhno. Numerical solution of the Painlevé VI equation. *Comput. Math. Math. Phys.*, 53(2):180–193, 2013.

[7] A.A. Abramov and L.F. Yukhno. A method for calculating the Painlevé transcendents. *Appl. Numer. Math.*, 93:262–269, 2015.

[8] M. Abramowitz and I.A. Stegun, editors. *Handbook of Mathematical Functions with Formulas, Graphs, and Mathematical Tables*. U.S. Government Printing Office, Washington, D.C., 1964.

[9] F.V. Andreev and A.V. Kitaev. Exponentially small corrections to divergent asymptotic expansions of solutions of the fifth Painlevé equation. *Math. Res. Lett.*, 4(5):741–759, 1997.

[10] F.V. Andreev and A.V. Kitaev. Connection formulae for asymptotics of the fifth Painlevé transcendent on the real axis. *Nonlinearity*, 13(5):1801–40, 2000.

[11] E. Barouch, B.M. McCoy, and T.T. Wu. Zero-field susceptibility of the two-dimensional Ising model near T_c. *Phys. Rev. Lett.*, 31(23):1409–1411, 1973.

[12] D. Barton, I.M. Willers, and R.V.M. Zahar. The automatic solution of systems of ordinary differential equations by the method of Taylor series. *Comput. J.*, 14(3):243–248, 1971.

[13] A.P. Bassom, P.A. Clarkson, and A.C. Hicks. Numerical studies of the fourth Painlevé equation. *IMA J. Appl. Math.*, 50(2):167–193, 1993.

[14] P. Boutroux. Recherches sur les transcendantes de M. Painlevé et l'étude asymptotique des équations différentielles du second ordre. *Ann. École Norm.*, 30:255–375, 1913.

[15] P.A. Clarkson. The third Painlevé equation and associated special polynomials. *J. Phys. A: Math. Gen.*, 36(36):9507–9532, 2003.

[16] P.A. Clarkson. Painlevé equations–nonlinear special functions. In F. Marcellán and W. van Assche, editors, *Orthogonal Polynomials and Special Functions: Computation and Application*, volume 1883 of *Lecture Notes in Math.*, pages 331–411. Springer, Berlin, 2006.

[17] G.F. Corliss. Integrating ODEs in the complex plane—pole vaulting. *Math. Comp.*, 35(152):1181–1189, 1980.

[18] G.F. Corliss and Y.F. Chang. Solving ordinary differential equations using Taylor series. *ACM Trans. Math. Software*, 8(2):114–144, 1982.

[19] O. Costin, M. Huang, and S. Tanveer. Proof of the Dubrovin conjecture and analysis of the tritronquée solutions of P_I. *Duke Math. J.*, 163(4):665–704, 2014.

[20] R. Costin. Personal communication, 2017.

[21] D. Dai and L. Zhang. On tronquée solutions of the first Painlevé hierarchy. *J. Math. Anal. Appl.*, 368(2):393–399, 2010.

[22] P.A. Deift and X. Zhou. Asymptotics for the Painlevé II equation. *Commun. Pure Appl. Math.*, 48(3):277–337, 1995.

[23] NIST Digital Library of Mathematical Functions. http://dlmf.nist.gov/, Release 1.0.10 of 2015-08-07. Online companion to [70].

[24] B. Dubrovin, T. Grava, and C. Klein. On universality of critical behavior in the focusing nonlinear Schrödinger equation, elliptic umbilic catastrophe and the tritronquée solution to the Painlevé-I equation. *J. Nonlinear Sci.*, 19(1):57–94, 2009.

[25] F.H.L. Essler, H. Frahm, A.R. Its, and V.E. Korepin. Painlevé transcendent describes quantum correlation function of the XXZ antiferromagnet away from the free-fermion point. *J. Phys. A Math. Gen.*, 29(17):5619–5626, 1996.

[26] M. Fasondini, B. Fornberg, and J.A.C. Weideman. A computational exploration of the McCoy–Tracy–Wu solutions of the third Painlevé equation. Submitted, 2017.

[27] M. Fasondini, B. Fornberg, and J.A.C. Weideman. Methods for the computation of the multivalued Painlevé transcendents on their Riemann surfaces. *J. Comput. Phys.*, 344:36–50, 2017.

[28] H. Flaschka and A.C. Newell. Monodromy- and spectrum-preserving deformations. I. *Comm. Math. Phys.*, 76(1):65–116, 1980.

[29] A.S. Fokas and M.J. Ablowitz. On a unified approach to transformations and elementary solutions of Painlevé equations. *J. Math. Phys.*, 23(11):2033–2042, 1982.

[30] A.S. Fokas, A.R. Its, A.A. Kapaev, and V.Y. Novokshenov. *Painlevé Transcendents: The Riemann-Hilbert Approach*, volume 128 of *Mathematical Surveys and Monographs*. American Mathematical Society, Providence, RI, 2006.

[31] B. Fornberg and N. Flyer. Fast generation of 2-D node distributions for mesh-free PDE discretizations. *Comput. Math. Appl.*, 69(7):531–544, 2015.

[32] B. Fornberg and J.A.C. Weideman. A numerical methodology for the Painlevé equations. *J. Comput. Phys.*, 230:5957–5973, 2011.

[33] B. Fornberg and J.A.C. Weideman. A computational exploration of the second Painlevé equation. *Found. Comput. Math.*, 14(5):985–1016, 2014.

[34] B. Fornberg and J.A.C. Weideman. A computational overview of the solution space of the imaginary Painlevé II equation. *Physica D*, 309:108–118, 2015.

[35] V.I. Gromak. Theory of Painlevé's equations. *Differ. Uravn.*, 11(11):373–376, 1975. In Russian. English translation: Differential Equations **11**(11), pp. 285–287.

[36] V.I. Gromak, I. Laine, and S. Shimomura. *Painlevé Differential Equations in the Complex Plane*. Walter de Gruyter, Berlin, 2002.

[37] D. Guzzetti. Tabulation of Painlevé 6 transcendents. *Nonlinearity*, 25(12):3235–3276, 2012.

[38] E. Hille. *Ordinary Differential Equations in the Complex Domain*. Dover Publications, Inc., Mineola, NY, 1997. Reprint of the 1976 original.

[39] A. Hinkkanen and I. Laine. Solutions of the first and second Painlevé equations are meromorphic. *J. Anal. Math.*, 79(1):345–377, 1999.

[40] A. Hinkkanen and I. Laine. Solutions of a modified fifth Painlevé equation are meromorphic. *Report. Univ. Jyväskylä*, 83:133–146, 2001.

[41] A. Hinkkanen and I. Laine. Solutions of a modified third Painlevé equation are meromorphic. *J. Anal. Math.*, 85:323–337, 2001.

[42] P. Holmes and D. Spence. On a Painlevé-type boundary-value problem. *Quart. J. Mech. Appl. Math.*, 37(4):525–538, 1984.

[43] C. Hunter and B. Guerrieri. Deducing the properties of singularities of functions from their Taylor series coefficients. *SIAM J. on Appl. Math.*, 39(2):248–263, 1980.

[44] A.R. Its and A.A. Kapaev. Connection formulae for the fourth Painlevé transcendent; Clarkson–McLeod solution. *J. Phys. A: Math. Gen.*, 31(17):4073–113, 1998.

[45] M. Jimbo, T. Miwa, and K. Ueno. Monodromy preserving deformation of linear ordinary differential equations with rational coefficients: I. General theory and τ-function. *Physica D*, 2(2):306–352, 1981.

[46] N. Joshi. Tritronquée solutions of perturbed first Painlevé equations. *Theoret. and Math. Phys.*, 137(2):1515–1519, 2003.

[47] N. Joshi and A.V. Kitaev. On Boutroux's tritronquée solutions of the first Painlevé equation. *Stud. Appl. Math.*, 107(3):253–291, 2001.

[48] N. Joshi and M. Mazzocco. Existence and uniqueness of tri-tronquée solutions of the second Painlevé hierarchy. *Nonlinearity*, 16(2):427, 2002.

[49] N. Joshi and T. Morrison. Existence and uniqueness of tronquée solutions of the fourth-order Jimbo–Miwa second Painlevé equation. *Proc. Amer. Math. Soc.*, 137(6):2005–2014, 2009.

[50] A.V. Kashevarov. The second Painlevé equation in the electrostatic probe theory: Numerical solutions for the partial absorption of charged particles by the surface. *Technical Physics*, 49(1):1–7, 2004.

[51] A.V. Kitaev and A.H. Vartanian. Connection formulae for asymptotics of solutions of the degenerate third Painlevé equation: I. *Inverse Problems*, 20(4):1165–1206, 2004.

[52] A.V. Kitaev and A.H. Vartanian. Connection formulae for asymptotics of solutions of the degenerate third Painlevé equation: II. *Inverse Problems*, 26(10):105010, 2010.

[53] D. Levi and P. Winternitz, editors. *Painlevé Transcendents: Their Asymptotics and Physical Applications*, volume 278. Springer Science & Business Media, 2013.

[54] Y. Lin, D. Dai, and P. Tibboel. Existence and uniqueness of tronquée solutions of the third and fourth Painlevé equations. *Nonlinearity*, 27(2):171–186, 2014.

[55] N.A. Lukashevich. Elementary solutions of certain Painlevé equations. *Differential Equations*, 1:561–564, 1965.

[56] N.A. Lukashevich. On the theory of the third Painlevé equation. *Differential Equations*, 3:994–999, 1967.

[57] S.L. Lukyanov. Critical values of the Yang–Yang functional in the quantum sine-Gordon model. *Nucl. Phys. B*, 853(2):475–507, 2011.

[58] B.M. McCoy and S. Tang. Connection formulae for Painlevé functions. *Physica D*, 18(1-3):190–196, 1986.

[59] B.M. McCoy, C.A. Tracy, and T.T. Wu. Painlevé functions of the third kind. *J. Math. Phys.*, 18(5):1058–1092, 1977.

[60] A.E. Milne, P.A. Clarkson, and A.P. Bassom. Bäcklund transformations and solution hierarchies for the third Painlevé equation. *Stud. Appl. Math.*, 98:139–194, 1997.

[61] J.M. Myers. Wave scattering and the geometry of a strip. *J. Math. Phys.*, 6(11):1839–1846, 1965.

[62] K. Nishioka. A note on the transcendency of Painlevé's first transcendent. *Nagoya Math. J.*, 109:63–67, 1988.

[63] V.Y. Novokshenov. Padé approximations for Painlevé I and II transcendents. *Theor. Math. Phys.*, 159(3):853–862, 2009.

[64] K. Okamoto. Polynomial Hamiltonians associated with Painlevé equations, I. *Proc. J. Acad., Ser. A*, 56(6):264–268, 1980.

[65] K. Okamoto. Studies on the Painlevé equations. III. Second and fourth Painlevé equations, P_{II} and P_{IV}. *Math. Ann.*, 275(2):221–255, 1986.

[66] K. Okamoto. Studies on the Painlevé equations. I. Sixth Painlevé equation P_{VI}. *Ann. Mat. Pura Appl. (4)*, 146:337–381, 1987.

[67] K. Okamoto. Studies on the Painlevé equations. II. Fifth Painlevé equation P_{V}. *Japan. J. Math. (N.S.)*, 13(1):47–76, 1987.

[68] K. Okamoto. Studies on the Painlevé equations. IV. Third Painlevé equation P_{III}. *Funkcial. Ekvac.*, 30(2-3):305–332, 1987.

[69] F.W.J. Olver. *Asymptotics and Special Functions*. A. K. Peters, Wellesley, MA, 1997. Reprint, with corrections, of original Academic Press edition, 1974.

[70] F.W.J. Olver, D.W. Lozier, R.F. Boisvert, and C.W. Clark, editors. *NIST Handbook of Mathematical Functions*. Cambridge University Press, New York, NY, 2010. Print companion to [23].

[71] S. Olver. Numerical solution of Riemann-Hilbert problems: Painlevé II. *Found. Comput. Math.*, 11(2):153–179, 2011.

[72] P. Painlevé. Sur les équations différentielles du second ordre et d'ordre supérieur don't l'intégrale générale est uniforme. *Acta Math.*, 25(1):1–85, 1902.

[73] L. Peltonen. Numerical solution of ODEs with poles. Master's thesis, Worcester College, University of Oxford, 2011.

[74] S. Persides and B.C. Xanthopoulos. Some new stationary axisymmetric asymptotically flat space-times obtained from Painlevé transcendents. *J. Math. Phys.*, 29(3):674–680, 1988.

[75] E. Picard. Mémoire sur la théorie des fonctions algébriques de deux variables. *J. de Math.*, 5(4):135–320, 1889.

[76] J.A. Reeger. *A Computational Study of the Fourth Painlevé Equation and a Discussion of Adams Predictor-Corrector Methods.* PhD thesis, University of Colorado, 2013.

[77] J.A. Reeger and B. Fornberg. Painlevé IV with both parameters zero: A numerical study. *Stud. Appl. Math.*, 130(2):108–133, 2013.

[78] J.A. Reeger and B. Fornberg. Painlevé IV: A numerical study of the fundamental domain and beyond. *Physica D*, 280–281:1–13, 2014.

[79] N. Seiberg and D. Shih. Flux vacua and branes of the minimal superstring. *J. High Energy Phys.*, 2005. Electronic. E-print number: hep-th/0412315. 38 pp.

[80] L.F. Shampine and M.K. Gordon. *Computer Solution of Ordinary Differential Equations.* W.H. Freeman, San Francisco, 1975.

[81] S. Shimomura. Truncated solutions of the fifth Painlevé equation. *Funkcialaj Ekvacioj*, 54(3):451–471, 2011.

[82] N. Steinmetz. On Painlevé's equations I, II and IV. *J. Anal. Math.*, 82(1):363–377, 2000.

[83] Y. Tourigny and M. Grinfeld. Deciphering singularities by discrete methods. *Math. Comput.*, 62(205):155–169, 1994.

[84] H. Umemura. On the irreducibility of the first differential equation of Painlevé. In *Algebraic Geometry and Commutative Algebra*, volume 2, pages 771–789. Kinokuniya, Tokyo, 1988.

[85] H. Umemura. Second proof of the irreducibility of the first differential equation by Painlevé. *Nagoya Math. J.*, 117:125–171, 1990.

[86] M. Van Barel, G. Heinig, and P. Kravanja. A stabilized superfast solver for nonsymmetric Toeplitz systems. *SIAM J. Matrix Anal. Appl.*, 23(2):494–510, 2001.

[87] W. Wasow. *Asymptotic Expansions for Ordinary Differential Equations*. Dover, 1987.

[88] E. Wegert. *Visual Complex Functions: An Introduction with Phase Portraits*. Birkhäuser/ Springer Basel AG, Basel, 2012.

[89] J.A.C. Weideman and S.C. Reddy. A MATLAB differentiation matrix suite. *ACM TOMS*, 26(4):465–519, 2000.

[90] I.M. Willers. A new integration algorithm for ordinary differential equations based on continued fraction approximations. *Comm. ACM*, 17:504–508, 1974.

[91] T.T. Wu, B.M. McCoy, C.A. Tracy, and E. Barouch. Spin-spin correlation functions for the two-dimensional Ising model: Exact theory in the scaling region. *Phys. Rev. B*, 13:316–374, 1976.

[92] P. Wynn. The epsilon algorithm and operational formulas of numerical analysis. *Math. Comp.*, 15(74):151–158, 1961.

[93] A.B. Zamolodchikov. Painlevé III and 2D polymers. *Nuclear Phys. B*, 432(3):427–456, 1994.